Identification and estimation of the extent of factors influencing maize production using images from Unmanned Aerial Systems

Z Labuschagne



orcid.org/0000-0001-6355-165X

Dissertation accepted in partial fulfilment of the requirements for the degree *Master of Science in Computer Science* at the North-West University

Supervisor:	Mr H Foulds
Assistant Supervisor:	Prof L Drevin

Graduation May 2021

23585137

Acknowledgements

I would like to thank my supervisors, Mr. Henry Foulds and Prof. Lynette Drevin, for their guidance and patience during my studies. I would like to acknowledge our friendly and caring research director, Prof. Magda Huisman for preparing us for what was laying ahead. The lecturers who taught me most of what I know today, need to know that they are immensely appreciated. Finally I would like to thank my family for the unconditional support during my academic time.

Samevatting

Daar is 'n toename in die toepassing van presisie-landbou; van geoutomatiseerde besproeiingstelsels tot geoutomatiseerde insekdoderverspreiding met behulp van hommeltuie, asook trekker-gemonteerde kameras, om sodoende data-beramings te verkry. Hommeltuie is 'n toenemend algemene en gerieflike manier om inligting in te samel oor gewasse. Inligting wat verkry word vanaf hommeltuie word egter steeds handmatig geïnterpreteer deur middel van visuele inspeksie op die ingesamelde beelde. Hierdie studie ondersoek die uitvoerbaarheid van die outomatisering van die identifikasie, asook die bepaling van die omvang van skade op voedselgewasse deur middel van hommeltuie. Hierdie studie fokus op mielie-oeste, en die omvang van waterskade op voedselgewasse. Ander tipes skade word ook ondersoek, maar vorm nie deel van die spesifieke studie nie. Stilbeelde word geneem en aanmekaar geweef deur die kalibrasie van GPS-koördinate en kamera-parameters. 'n Oorsigtelike ondersoek word gedoen op die onderwerp van beeldwefing wat begelei word deur die data-bevindings. Die beeldwefing-proses word gevolg deur 'n ondersoek en eksperimentering op plantegroei-segmentasie. Ten slotte bied eksperimente op 'n neurale-netwerk ondersteuning tot die klassifikasie van gewas-areas as 'beskadig' of 'gesond'.

Sleutelwoorde: Presisie-landbou, Hommeltuig, Beeldwefing, Klassifikasie, Masjienleer.

Abstract

Precision agriculture is becoming increasingly popular. From the use of automated irrigation systems to automated pesticide distribution using drones (Unmanned Aerial Systems (UASs)) spanning to yield-estimation through the use of image sensors mounted on tractors. UASs are becoming an increasingly common and convenient way of obtaining information about crops. However, the information gathered from these UASs is still manually interpreted utilising visual inspection of the images. This study investigates the possible automation of identification and estimation, of the extent of damages on food crops using UASs. This study focuses on maize as a food crop, and water stress as primary means of damage. Other types of damage are also investigated, however, they are not included in this experiment. Still images are captured and stitched together using GPS-coordinates and camera parameters. A brief investigation on the topic of image stitching is provided with findings on the particular method(s) used. Following the stitching process, investigation and experimentation on vegetation segmentation are discussed along with the findings of this particular case. Finally, a neural network is experimented with to classify crop areas as 'damaged' or 'healthy'.

Keywords: Precision Agriculture, UAS, Image Mosaicing, Anomaly Classification, Machine Learning.

Contents

Acknowledgements . . . . . **i**

Samevatting . . . . . **ii**

Abstract . . . . . **iii**

Acronyms . . . . . **vi**

List of figures **1**

List of tables **1**

1 Introduction **2**

1.1 Project description 2

1.2 Problem description 3

1.3 Problem statement 6

1.4 Aims and objectives 6

1.5 Scope 7

1.6 Risks 8

1.7 Document structure 8

2 Literature study **10**

2.1 The maize plant 10

2.2 Methods of observation 17

2.3 Image processing techniques 22

2.4 Summary 26

3 Experimental setup **27**

3.1 Ethical and legal implications 27

3.2 Development environment . . . 29
3.3 Environment . . . 30
3.4 Data acquisition . . . 30
3.5 Data processing . . . 34
3.6 Summary . . . 40

4 Results . . . 42
4.1 Mosaicing results . . . 42
4.2 Classification results . . . 48
4.3 Summary . . . 52

5 Evaluation . . . 54
5.1 Evaluation of the mosaicing algorithm . . . 54
5.2 Evaluating the classification . . . 55
5.3 Summary . . . 57

6 Conclusion . . . 59
6.1 Summary of findings . . . 59
6.2 Revisiting aims and objectives . . . 60
6.3 Contributions . . . 62
6.4 Limitations . . . 62
6.5 Future work . . . 63

References . . . 70

A Telemetry data extract . . . 71

B EXIF data example . . . 72

C Additional results . . . 77
C.1 DroneDeploy classification results . . . 77
C.2 Stitched image classification results . . . 109

Acronyms

AGL Above ground level.

AVIRIS Airborne Visible InfraRed Imaging Spectrometer.

CTSD Standard Deviation of Canopy Temperature.

CWSI Crop Water Stress Index.

DACT Degrees Above Canopy Threshold.

DANS Degrees Above Non-Stressed.

EXIF Exchangeable Image File Format.

FIR Far-infrared.

FOV Field of view.

IIR Intermediate infrared.

InSAR Interferometric synthetic aperture radar.

IPM Integrated pest management.

ISO International Organization For Standardization.

LWIR Long-wavelength infrared.

MIR Mid-infrared.

MWIR Mid-wavelength infrared.

NIR Near-infrared.

RGB Red, green and blue.

ROC Receiver operating characteristic.

RPAS Remotely piloted aircraft systems.

SACAA South African Civil Aviation Authority.

SAMAA South African Model Aircraft Association.

SAR Synthetic aperture radar.

SOP Standard operating procedure.

SPOT Système Pour I'Observation De La Terre.

SWIR Short-wavelength infrared.

TIR Thermal infrared.

UAS Unmanned Aerial System.

UASs Unmanned Aerial Systems.

VNIR Visible and near-infrared.

List of figures

1.1 Successful IPM program implementation approach [19] 4

2.1 Representation of a mature maize plant [18] 11
2.2 Schematic of precision agriculture workflow and parameters [42] 17
2.3 SAR signal penetration on vegetation by sensor wavelength [23] 20
2.4 SAR signal penetration on earth surfaces by sensor wavelength [23] . . 21
2.5 Schematic sketch of the three main scattering types considered for SAR data [23] 21

3.1 Calculating distances within an image using geometry and trigonometry *(Triangles are not drawn to scale)* 37
3.2 The summation of each discretely computed Euclidean distance from the centre of the shifted Fourier transform of a 7x7 matrix, each represented by a different colour 39
3.3 Ground truth data obtained from an insurance assessor for both images 40

4.1 Stitched image using DroneDeploy third party software 43
4.2 Stitched image using algorithm as described in section 3.5.1 44
4.3 Stitched image using algorithm as described in section 3.5.1, but skipping every second image. This image was also scaled down to 40% of the original 45
4.4 Stitched image using algorithm as described in section 3.5.1, but skipping every third image. This image was scaled down to 70% of the original . 45
4.5 Stitched image using algorithm as described in section 3.5.1, but skipping every fourth image. This image was scaled down to 80% of the original 46
4.6 Stitched image using algorithm as described in section 3.5.1, but skipping every second image and every second row. This image was scaled down to 80% of the original 46

4.7 Close-up comparison of both methods. 47
4.8 Classification results of using a window size of 45x45 pixels, having the first 4 summations of the computed Fourier coefficients of the red, green, blue and ExR components in the feature vector. This is a an extraction from FIGURE C.54 50
4.9 Classification results of using a window size of 45x45 pixels, having the first 8 summations of the computed Fourier coefficients of the red, green, blue, hue, saturation, value and ExR components in the feature vector. This is a an extraction from FIGURE C.24 52

List of tables

2.1 Commonly used electromagnetic spectrum wavelengths according to Byrnes [7] unless cited otherwise 18
2.2 Infrared subdivisions' electromagnetic spectrum wavelengths as defined by the ISO 19

3.1 Specifications and parameters of the DJI Phantom 3 Professional camera [12] 31
3.2 Specifications and parameters of the DJI Mavic Pro camera [11] 32
3.3 Specifications and parameters of the DJI Zenmuse X7 camera with 35mm lens and 3:2 still image setting as used on the DJI Inspire II UAS [10] . 32
3.4 Specifications and parameters of the DJI Inspire II and DJI Zenmuse X7 with 35mm lens and 3:2 still image setting [10] 35

4.1 Key results from the unbiased classification confusion matrices. 53

A.1 Extract of telemetry data recorded using DroneDeploy 71

Chapter 1

Introduction

The purpose of this study is to propose a method for identifying factors influencing maize production by using Unmanned Aerial Systems (UASs) and to evaluate the possibility of implementing such a system. These factors can range from diseases and pests to factors caused by weather conditions. For this study, the scope will be limited to water stress only; an accurate description of the scope of this study is covered in section 1.5.

The main contribution of this study is a set of computational operations with specific parameters to be completed on images of maize crops. This would in turn yield an indication of the areas influenced by the factors chosen as part of the scope of the study.

1.1 Project description

This study consists of three phases. The first phase is a literature survey of methods required to achieve the goal of this study, and these methods include image mosaicing, vegetation segmentation and classification using an artificial neural network. The second phase is acquiring images using a UAS. The last phase applies image processing techniques and artificial neural network methods to images to identify affected areas and estimate the extent of the damage identified.

1.2 Problem description

Diseases, pests, and extreme weather have a substantial influence on **food security** [9]. Some of these factors are seasonal, with the degree of damage varying each year [9]. Managing these influences is crucial to improve food security. **Precautionary methods** used to manage diseases, pests and plagues include biological controls, cultural controls, mechanical (technical or physical) controls and chemical controls [49, 45]. Some of the aforementioned controls such as chemical controls and mechanical controls can be also used as aftercare measures; for example, chemical controls such as pesticides and herbicides [45, 49] can be used once pests and weeds have been spotted either directly or by their evidence of presence. Fertilisation is also a chemical control that can mitigate the negative influences of weeds and pests once damages are already done. Weeds can also be mechanically removed using physical equipment, which is an example of a mechanical control being implemented [49] as an aftercare measure. Biological controls such as introducing insects in the vicinity that are natural enemies, predators, parasites, pathogens and competitors to pests but not to the crop [49] is an example of a precautionary control. Examples of precautionary cultural controls are crop rotation [56, 45, 37], pruning [37], usage of perennial cultivars [56] and the use of a cultivar that is resistant to an influence that is commonly found in the environment [49] such as a specific fungus. Integrated pest management (IPM) is a precautionary method [49] that includes more than one of the aforementioned controls [20]. One implementation of this is to set sticky paper traps (physical control) with a pheromone inside (chemical control) that attracts one gender of a pest. The pests are stuck to the sticky paper for the rest of their lives. The scarcity of one gender causes a decline in mating which results in a smaller population of a pest. Some influencing factors can be controlled by more than one control as mentioned before with weeds as an example. Some influences can only be controlled by a specific control and some can by managed be IPM, which is usually a better option when taking the environment into consideration [49].

Figure 1.1 illustrates the cycle of IPM. Shown in Figure 1.1, the first objective in managing influences is to identify the influence, which is where the implementation of this study can provide support. The implementation of this study might also provide

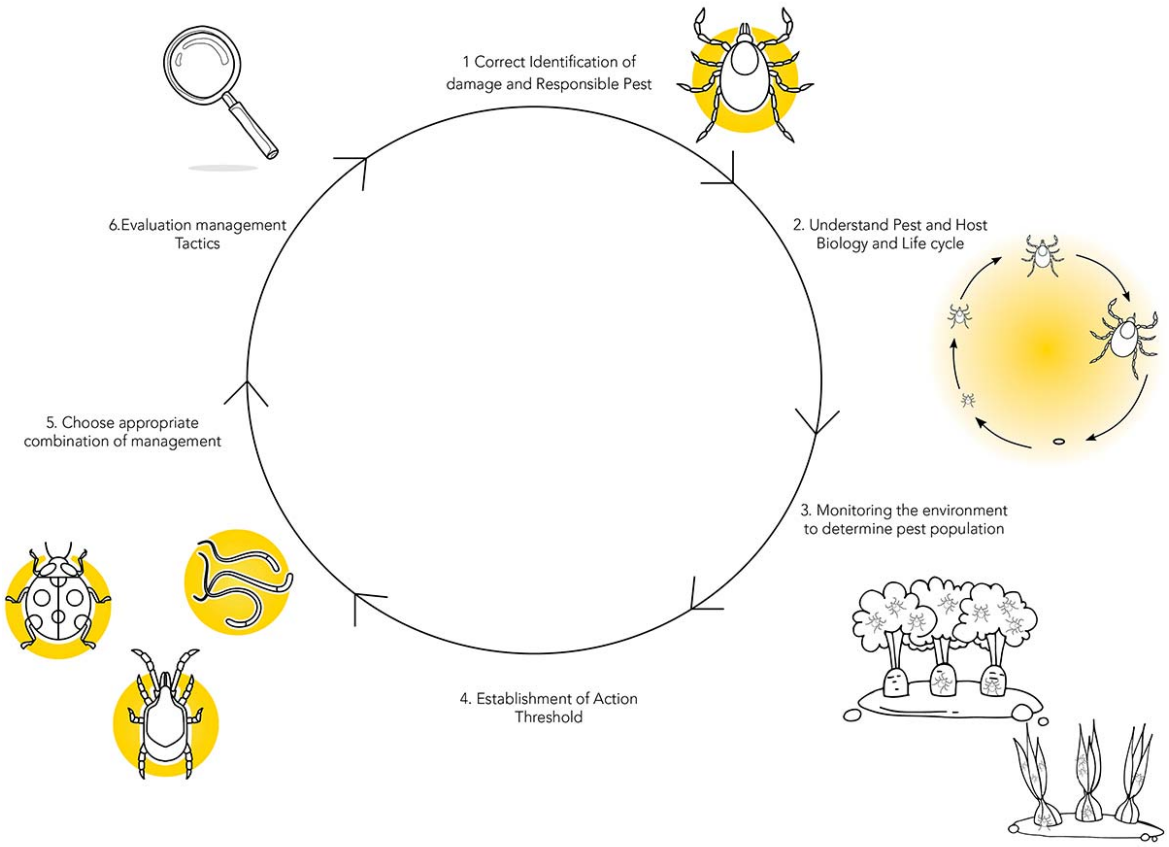


FIGURE 1.1: Successful IPM program implementation approach [19]

support for step 3, the monitoring of the population of the influence, which also requires the estimation of the extent of the influence. The process shown in FIGURE 1.1 relies on timely and accurate identification and estimation of the extent of the influence. The use of a UAS can be an appropriate platform for this implementation, because data are acquired within an hour, whereas with satellite imagery, the data are acquired after a few weeks at best, revisiting frequencies are insufficient and the spatial and spectral resolution is inadequate [26, 3]. The shortcomings of satellite imagery may be overcome by using traditional aerial photography, but requests are still limited and production costs are higher compared to a UAS [52].

Research is also conducted on scenarios where the focus shifts from the factors causing damage to estimating and analysing the **post-disaster** damage [21]. Traditional methods used for data acquisition and analysis employ space **remote sensing** solutions such as satellite imagery, although UAS sensing solutions are increasingly being used [43].

1.2.1 Background

Interest was expressed by botanists to evaluate the possibility of using images obtained from UAS to identify the presence of Fall Armyworm and estimate the extent of the damage caused. Unfortunately, it quickly became clear during the initial investigation and preliminary experimentation that it would not be possible to directly identify Armyworm on maize crop. Visual inspection on maize crop infected with Fall Armyworm indicated that the worms are not always directly visible on the plant, as it hides within the leaves of the plant. One should be able to detect the aftermath of Armyworm damage using visual spectrum cameras, but the lack of cases where maize production is influenced by the Armyworm in the near vicinity, despite the reports of farmers, led to a more general identification and damage estimation of influences on maize crop instead. This means that the final solution might lead to a two pronged-approach, possibly involving manual verification of the damage, and using remote sensing to estimate the extent of the damage caused. It was also learnt during this initial experiment that it is also possible to do secondary identification of an influence through the damages caused by this influence instead of observing the presence of the influence directly.

The interest in using a UAS platform in this study instead of a space remote sensing or aerial photography solution is justified by the timeliness and costs of obtaining equivalent data without compromising on accuracy that is inherently decreased by the delay of space remote sensing and aerial photography solutions. A farmer can easily instruct a UAS to capture a very specific area and have the data in less than an hour; whereas with satellite imagery, the farmer is not in control and waits for weeks to get the data. Using a UAS, the farmer can respond timely and be better prepared or even contain the damage in cases of pest influence, for example.

1.2.2 Rationale

Current methods of detecting influences (that exhibit symptoms within the visible spectrum) on maize production include manual visual inspection, microscopic evaluation of morphology features and microbiological diagnostic techniques [5, 47], which are not

consistent as many human raters are subjective [1] and their conclusions are subject to their experience [42]. Raters also lose accuracy due to tiring and loss of concentration over time [1]. Visual cues used to identify a disease can include lesions, blight, galls, tumors, cankers, wilts and rots [42]. Other autonomous solutions might include space remote sensing and aerial photography, but as stated before, these options are not as accurate, timely and economical. The application of precision agriculture and automation which includes the use of UAS, is also increasing to aid in optimised food production [63].

1.3 Problem statement

A UAS can be used to automate [31] the search for damaged areas in crops [62]. Research in this study focuses on identifying factors influencing maize production from anomalies detected, as well as the estimation of the extent of these factors. Section 1.1 shed light on a problem that can be addressed by utilising the available technologies mentioned in section 1.2.2, however, it is not known how accurately one can detect factors that are influencing maize production, using UASs.

The research question is: "How accurately can image processing techniques, applied to images obtained from a UAS, identify factors influencing maize production, and estimate the extent of this influence?"

1.4 Aims and objectives

The aim of this study is to explore and evaluate image processing techniques to support sustainable food security using remote sensing implemented on a UAS platform. The focus of the implementation of the image processing techniques in this study will be on identifying factors influencing maize production from a list of possible factors being considered and also to determine the extent of the influence.

In order to achieve the above aim, the following objectives are set:

1. Performing an introductory survey of factors influencing maize production, and how these factors can be detected and studied. Appropriate factors for further analysis in this study will be chosen after this survey. Surveys will also include conventional methods used to detect and determine damage on maize used in practice by botanists and insurance assessors.

2. Investigate image processing techniques that can be used to identify and classify factors influencing maize production. Additional image processing techniques will also be studied to aid in determining the extent of the influence caused by these factors.

3. Explore remote sensing techniques in literature to identify appropriate data acquisition methods. These remote sensing techniques will include satellite and UAS approaches to optical and multi-spectral data acquisition.

4. Acquire data using chosen methods on healthy maize and maize influenced by factors. Images will be acquired by flying a UAS over farm land after receiving consent. All South African Civil Aviation Authority (SACAA) regulations will be followed as discussed in the standard operating procedure (SOP) for UAS Equipment" document. Ground truth data are also recorded during this objective.

5. Process the images to identify anomalies in maize fields and match the anomalies to possible factors influencing maize production, using image processing and popular pattern recognition techniques. The extent of the anomalies will also be calculated from the images.

6. Evaluate the accuracy of the approach using ground truth data.

1.5 Scope

The influences on maize production to be identified are limited to water damages (drowning). Other influences are not covered because of the lack of cases in the near

vicinity, and therefore the range of influences covered is determined by what the data can provide.

In addition to the identification of the influences, the extent of the influences is also determined to provide an indication of the severity of the damages.

1.6 Risks

Risks that are concerned with this study include the safety of people and the environment where the flight of the UAS takes place. To mitigate this risk, an SOP is followed throughout all flights. This standard operating procedure (SOP) adhere to the standards set by the SACAA to ensure proper safety rules.

There is also the risk of damaging the UAS, which could have a significant impact on this study as this study relies on quality equipment such as the DJI Inspire II UAS. There are reserve UASs available such as the DJI Phantom 3 and DJI Mavic Pro. The camera of the DJI Phantom 3 is sufficient; however, the telemetry is not as accurate as desired. The DJI Mavic Pro has an inferior camera and is smaller, which results in a steep degrade of image quality, but still adequate. The telemetry of this UAS is also adequate making, the DJI Mavic Pro a suitable reserve UAS. The DJI Phantom 3 and DJI Mavic Pro UAS are not property of the university, but private property of an employee partaking in this study who is permitting the usage of the DJI Phantom 3 Professional and DJI Mavic Pro for this study.

1.7 Document structure

This document is divided into the following chapters:

1. **Introduction:** The introduction includes a description of the project, the aim of the study along with the objectives to be completed in order to achieve the aims of this study. The introduction section also includes a background and a

rationale. The methods of investigation, scope and constraints of this project are also discussed in this chapter.

2. **Literature study:** This chapter contains all literature reviewed relevant to this study.

3. **Experimental Setup:** This chapter contains information about how the UASs is set up and utilised, the remote sensing methods used and the processing done to produce the results pertaining to the influenced area detected and the degree of influence.

4. **Results:** The results of this research study are discussed in this chapter.

5. **Evaluation:** This chapter contains an evaluation of the results and judge the performance of the research outcome. Aspects evaluated includes the classification of damaged areas as well as the accuracy of areas identified to be damaged areas.

6. **Conclusion:** The conclusion to this study is discussed in the final chapter.

Chapter 2

Literature study

Key publications in this study are divided into three categories. The first category, agriculture, contains the following topics: the maize plant itself [18, 35], factors influencing maize production including pests and diseases [48, 45, 34], and precision agriculture [42, 63]. The second category, image processing, includes image processing techniques applicable to analysing vegetation, including vegetation indices [8], colour space transforms [50], vegetation segmentation [6], and colour segmentation [9]. The last category, image acquisition, covers the following topics: hyperspectral and multispectral remote sensing [9], thermal remote sensing [40], photogrammetry and mapping using UASs [9].

2.1 The maize plant

This section will cover literature on the maize plant and crop. Topics covered are some background on the plant itself followed by influences on its production.

2.1.1 The anatomy of a maize plant

This subsection is an overview of the anatomy of the corn plant, which familiarises the reader with the terminology used in the literature following this subsection. Figure 2.1

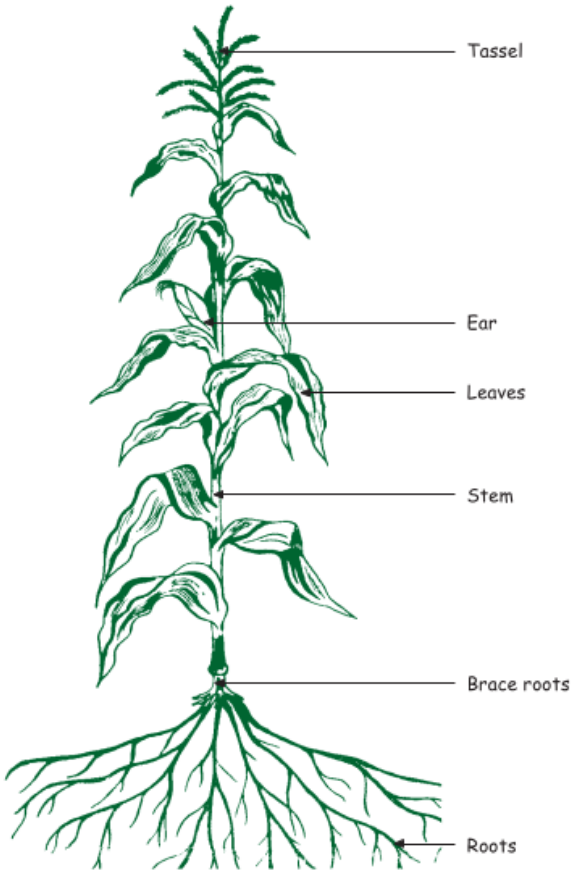


FIGURE 2.1: Representation of a mature maize plant [18]

shows a mature maize plant with labels indicating its main parts. Become familiar with the terminology in order to follow the literature in the subsections that follow.

2.1.2 Stages in the life-cycle of maize

According to Hanway [35] and Du Plessis [18], the maize plant has 11 stages of growth, as explained below.

Stage 0: Plant emergence from soil This stage lasts from the moment the seed is planted up to the point where the seedling is barely visible above the soil, which should be in between four to ten days after planting in a warmer climate such as South Africa. The stems are around 25 to 40 mm below the soil surface and ideal ambient temperatures at this stage range from 20 to 30°C with 60% moisture content of the soil.

Stage 1: Four leaves completely unfolded Two leaves should be completely unfolded one week after stage 0, with four leaves completely unfolded two weeks after stage 0.

Stage 2: Eight leaves completely unfolded Six leaves should be completely unfolded three weeks after stage 0, with eight leaves completely unfolded four weeks after stage 0. The plant absorbs more nutrients during this stage and is susceptible to rootworms. Since the leaves are rapidly growing during this stage, it is also a time where the leaves are starting to get eaten by pests.

Stage 3: Twelve leaves completely unfolded Ten leaves should be completely unfolded five weeks after stage 0, with 12 leaves completely unfolded six weeks after stage 0. The tassel starts to develop during this stage if it has not yet started to develop during the end of the previous stage. Water damage is less of a concern from this stage and onwards. Nutrient deficiencies will begin to influence the development of the ears during this stage. The moisture content of the soil also has great influence on the absorption of nutrients during this stage. The maize plant in this stage is also very susceptible to hail or other physical damage.

Stage 4: Sixteen leaves completely unfolded Fourteen leaves should be completely unfolded seven weeks after stage 0, with 16 leaves completely unfolded eight weeks after stage 0. The stem is rapidly elongating during this stage along with the growth of the tassel, ears and silks. Moisture stress or nutrient deficiencies will show during this stage, with higher intensities in the bottom of the plant. It is interesting to note that physical damages such as hail to the leaves would result in a 25 to 30% yield loss if half of the leaves are destroyed.

Stage 5: Silk appearance and pollen shedding The tassel is completely developed, all leaves unfolded and the stem stops elongating at this stage. The plant is very susceptible to nutrient deficiency and moisture stress, the susceptibility of the plant to nutrient damage increases as the plant grows [35]. The silks are susceptible to corn rootworm beetles from this stage.

Stage 6: Green mealie stage The ear and cob should be fully developed at this stage and there should be a rapid increase in grain dry weight.

Stage 7: Soft dough stage This stage shows an increase in grain, and sugars are converted into starch.

Stage 8: Hard dough stage Nutrient deficiencies and lack of moisture have a great influence in the kernel development during this stage and the previous.

Stage 9: Maturity The kernel reaches maximum dry weight.

Stage 10: Kernel drying Some of the leaves are no longer green, the kernel stops increasing in grain dry weight and harvest commences after drying of which the rate varies depending on the conditions of the field and environment.

2.1.3 Factors influencing maize production

This section contains literature reviewed about the factors that influence maize production such as natural influences (weather), pests and diseases. According to a survey by Oerke [48], almost one third of attainable maize production was lost due to the influences of pests, weeds and pathogens.

Temperature stress

Maize is grown in areas where the average temperature is above 19°C. Frost can damage the plants during any of the growth stages discussed above and a period of 120 to 140 days with no frost is required in order to prevent damage to the maize plants. Frost damage is not critical while the growth point is below the soil surface, because new leaves will grow, but the leaves of mature plants are much more susceptible to frost damage [18].

Water stress

350 to 450 mm of rain per annum is required in order to produce a good yield of 3152 kg/ha. If no moisture stress is exhibited on the plant, it will use a total of 250 ℓ water throughout its lifetime [18].

Water stress can be identified by monitoring the canopy temperature of the maize crop using thermal imagery [34], but more on this topic regarding image processing techniques used to identify water stress in section 2.3.3.

Diseases

Diseases threatening maize production include ear rot, maize streak virus disease, grey leafspot, rust, cob-and-tassel smut, stemrot and rootrots. The susceptibility of the maize plant to these diseases depends on its cultivar; a cultivar is usually selected that is the least susceptible to the most common disease in the area [18].

Fungal diseases causing ear, stalk and root rot are considered to have the greatest influence on maize production economically [45]. Fungal diseases are most commonly treated by utilising chemical controls such as using fungicides, but since many of the fungal diseases infect plants through feeding wounds caused by arthropod pests such as corn borers, one can also approach this influence with biological controls or other chemical controls such as insecticides [45] as explained in section 2.1.3. The influence of fungal diseases in Europe can be managed by utilising cultural controls such as early

planting and crop rotation. When the plant is planted earlier, it matures earlier and avoids time spent in high moisture seasons; otherwise, the plant is very susceptible to fungal disease in its mature stages [45]. One can also use a cultivar that has a shorter life span instead of planting early [45]. Endophytic bacterium can also be used as a biological control measure to manage the influence of fungal disease [45].

Nutrient deficiencies

Fertilisation includes the following basic elements:

- Nitrogen
- Phosphorus
- Potassium
- Zinc

A nitrogen deficiency is indicated by a pale light green or yellow colour in young plants. Mature plants shows nitrogen deficiency in their leaves by having a yellow colour. A deficiency in phosphorus is more common in young plants under cool and wet conditions and is indicated by having dark green leaves with a reddish-purple colour around the edges of the leaf. A potassium deficiency is indicated by yellow colour around the edges of the leaves, initially starting at the bottom leaves and progressing to the top leaves. A zinc deficiency is indicated by light bands between the veins on the leaf; this symptom is easier to identify in overcast weather. [18]

Weeds

Weeds have the greatest influence on maize crop [48]. The influence is the most significant during the first six to eight weeks of development as it is very competitive for nutrients, water and sunlight [18]. Weeds are generally controlled by using herbicide to eradicate the weeds within the maize crop. [45]. The utilisation of herbicide is a chemical control and is considered as an after care control. The use of chemical

controls, which are unhealthy for the environment, can be reduced by using integrated weed control, a component of IPM. Integrated weed control can consist of cultural and mechanical controls [45].

Pests

Pests can be controlled by using pesticide or by utilising IPM solutions and vary according to the specific pests being targeted. IPM methods can be divided into categories such as preventative control, cultivation control, biological control, insect resistant plants and chemical control [18]. Just as mentioned in weed control, one can utilise IPM methods to reduce the use of pesticides and insecticides [45]. A common control to use in IPM is biological controls [45], which is usually more sustainable and causes less harm to the environment. One can also utilise cultural controls to manage the influences of pests such as crop rotation, early or late planting, irrigation and fertilisation, which are effective against the Western corn worm because these control measures strengthen the roots of the plant [45]. Mechanical (technical or physical) controls such as mowing stalks or ploughing can be used to mange the influence of corn borers, cutworms and maybe wireworms [45]. Another IPM example is to use synthetically produced sex pheromones that disrupt mating of stem borers [45], which is considered a biological control. Scouting can be performed to use pesticides and insecticides at an applicable level and only when economic threshold levels are exceeded [45].

2.1.4 Managing factors influencing maize production

Influences and threats to maize production can be managed by utilising biological controls, chemical controls and technical controls [45]. Many of the mentioned threats have measures to control their influences on maize production but the farmer is in many cases restricted to use a limited amount only if at all of some control measure. Some of these control measures are managed by governing bodies and law to protect the environment, and a balance between the amount of control and crop loss is maintained in order to maximise income [45]. Some control measures are only suitable for certain

environments as one control measure might have consequences for other pest complexes and result in a new, possibly worse, problem than initially [45].

2.2 Methods of observation

Precision agriculture is a technology– and information– based domain where a collection of sensors is used to obtain data on an agricultural crop, which is, in turn, used to manage the agricultural development by solving challenges such as diagnosing and detecting plant diseases [42]. Precision agriculture involves real-time processing of data to aid in timely decisions, and mapping systems for crop and soil as seen in FIGURE 2.2 [42].

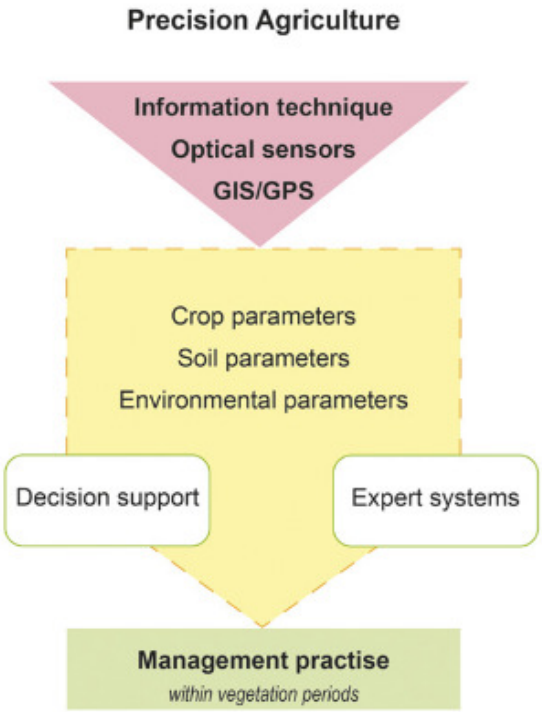


FIGURE 2.2: Schematic of precision agriculture workflow and parameters [42]

Symptoms to leverage in optical sensors can include tissue colour, leaf shape, transpiration rate, canopy morphology and vegetation density [42, 60]. According to Mahlein [42] and Franke and Menz [24], optical sensing techniques in combination with advanced methods of data analysis can aid in targeted pest management for sustainable crop production. These sensors can not only observe the visual spectrum in which

humans make observations, but also in ranges beyond that, such as the ones being investigated here [42].

Methods of observation can be categorised according to the platform used for observation, spectrum band or range, or the method of data acquisition. Platforms used for earth remote sensing include satellites, conventional aircraft and UAS [39]. Electromagnetic spectra (also known as bands or ranges) used for remote sensing include the visible spectrum [2], Near-infrared (NIR) [2], Short-wavelength infrared (SWIR) [28], Mid-wavelength infrared (MWIR) [28, 4], Long-wavelength infrared (LWIR) [7], and synthetic aperture radar (SAR) [23]. See TABLE 2.1 for the properties of each of these spectra. The method of data acquisition can be either by means of passive sensing or active sensing [59]; SAR would be an example of active sensing where the observation requires an emission of energy in order to observe a reflection or in other cases a difference (CT scans) of the emitted energy.

Spectrum	**Wavelength**	**Frequency**
Visible (RGB)	400–700 nm [36]	430–790 THz[36]
NIR	0.75–1.4 μm	214–400 THz
SWIR	1.4–3 μm	100–214 THz
MWIR	3–8 μm	37–100 THz
LWIR	8–15 μm	20–37 THz
FIR	15–1000 μm	0.3–20 THz
SAR	2.4–100 cm [23]	0.3–12 GHz [23]

TABLE 2.1: Commonly used electromagnetic spectrum wavelengths according to Byrnes [7] unless cited otherwise

The distinctions in the divisions of the spectra listed in TABLE 2.1 are loosely defined with more or less the same margins, they vary across different fields like astronomy and telecommunication. TABLE 2.2 shows how the International Organization for Standardization (ISO) defines the subdivisions of infrared, but unfortunately, are not defined as granular as they are used in practice.

Spectrum	Wavelength
NIR	0.78–3 μm
MIR	3–50 μm
FIR	50–1000 μm

TABLE 2.2: Infrared subdivisions' electromagnetic spectrum wavelengths as defined by the ISO [38]

The visible spectrum is what is observable by the human eye [28, 4], some animals can observe energy outside of this range [4]. Most cameras capture energy in this range as the objective is to capture a moment as one have observed it and is the most familiar to humans. However, it is in many cases beneficial to capture images in the spectra outside of the visible spectrum.

The average consumer grade camera and most cameras onboard UASs have image sensors responding to the visible light spectrum. Some UASs, like the DJI Matrice 210 and DJI Matrice 600, allow for custom cameras and equipment to be fitted. Thermal and infrared cameras with standard mounting solutions like the DJI Zenmuse XT range for most DJI UAS are also obtainable. [15, 14, 16]

2.2.1 Infrared imaging

Imaging in the NIR band is useful for shoreline mapping and biomass mapping [28] and estimation [51, 53]. A range used in practice but not listed in the spectra tables is Visible and near-infrared (VNIR) [2], it is not listed as this range is not a distinct division. VNIR includes both the visible spectrum and the NIR spectrum [2]. MWIR, also known as Intermediate infrared (IIR) [7], is useful for the observation of moisture content in soil and vegetation [28]. Gonzalez and Woods consider the Thermal infrared (TIR) band, having a wavelength of 10.4 μm to 12.5 μm, to be useful for soil moisture estimation and thermal mapping [28]. According to Birchfield, TIR and FIR are used interchangeably [4]. SWIR [28] and VNIR [59] are both useful for mineral mapping. FIR is a prominent spectrum used in the field of astronomy [4].

2.2.2 Synthetic aperture radar imaging

As stated before, SAR is an active sensing solution and requires the emission of energy before being able to observe [4, 23]. SAR is a radar imaging solution, and therefore uses radio waves reflected from a surface for observation [4, 23]. Radar uses much longer wavelengths that have the property to propagate through clouds and weather resulting in radar being able to observe reflections without weather conditions being an influential factor [23]. Much like the infrared spectra, SAR can be divided into bands. Bands Ka (0.8–1.1 cm, 27–40 GHz), K (1.1–1.7 cm, 18-27 GHz) and Ku (1.7–2.4 cm, 12–18 GHz) are rarely used and are used for airport surveillance, water absorption and satellite alimentary, respectively [23]. The X band at wavelength 2.4–3.8 cm and 8–12 GHz is used for urban monitoring and can be used for ice and snow mapping [23]. The C band at wavelength 3.8–7.5 cm and 4–8 GHz is used for global mapping, change detection, ice and maritime navigation [23]. The S band at wavelength 7.5–15 cm and 2–4 GHz is not as popular, but gaining popularity in earth observation for agriculture monitoring [23]. The L band at wavelength 15-30cm and 1–2 GHz is used for geophysical monitoring, biomass and vegetation mapping [23]. The L band is also used in interferometric synthetic aperture radar (InSAR), which is used to map and analyse the earth's topography and surface deformations by exploiting the difference between the phase signals of repeated SAR acquisitions [23]. The P band at wavelength 30–100 cm and 0.3–1 GHz is used to estimate biomass, and map and assess vegetation [23]. Figures 2.4 and 2.3 illustrate how the different SAR bands can be used to map different environments. Figure 2.5 illustrates how SAR can be used to map different environments by also looking at the scatter patterns.

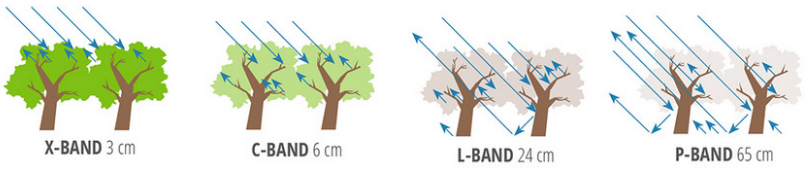


Figure 2.3: SAR signal penetration on vegetation by sensor wavelength [23]

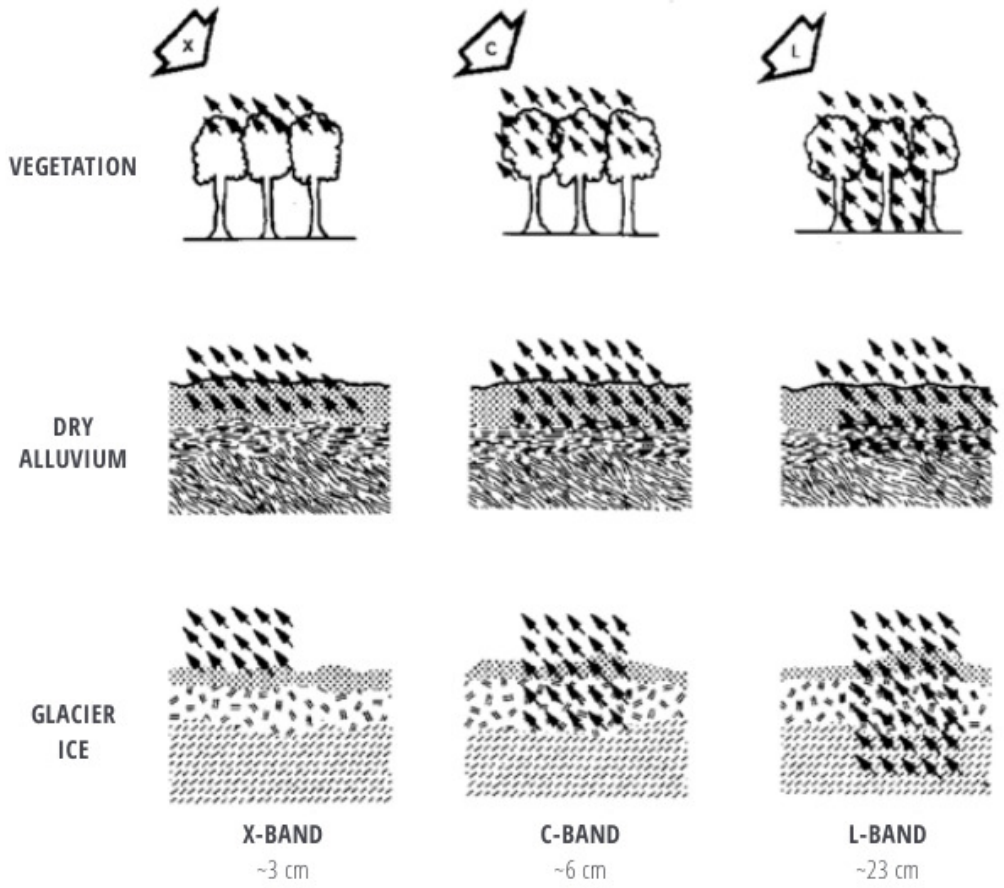


FIGURE 2.4: SAR signal penetration on earth surfaces by sensor wavelength [23]

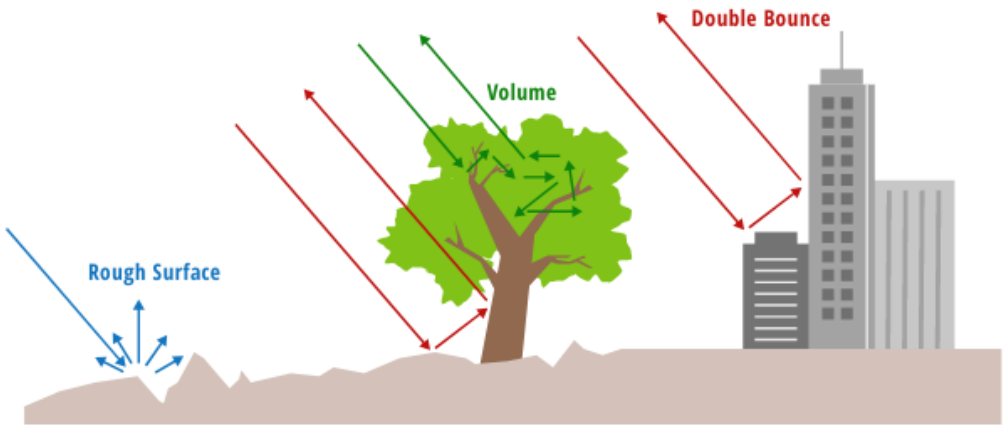


FIGURE 2.5: Schematic sketch of the three main scattering types considered for SAR data [23]

2.2.3 Remote sensing in general

Remote sensing has applications in meteorology, agriculture, surveillance and geology and is achieved by utilising satellite or aircraft [4, 28]. These images are obtained using image sensors spanning over multiple spectra, and are therefore called a multispectral sensor, or hyperspectral sensor if a wider range of spectra is covered [4]. Examples of multispectral satellite remote sensing solutions include the LANDSAT program of NASA covering eight spectral bands, Système Pour l'Observation de la Terre (SPOT) covering five spectral bands [4]. An example of a hyperspectral remote sensing solution attached to an aircraft is the Airborne Visible InfraRed Imaging Spectrometer (AVIRIS), which covers 224 contiguous spectral bands from 400 to 2500 nm [4]. Remote sensing solutions tend to include spectrum bands across the visual spectrum and infrared spectra [28].

2.3 Image processing techniques

This section starts with a literature survey on image processing techniques used to prepare the UAS images for further processing such as image mosaicing and segmentation. This is followed by a literature study on image processing techniques that can be used to identify anomalies in maize crops.

2.3.1 Image mosaicing

Image mosaicing is a process of aligning and stitching a set of images, each representing a partial view of a 3D scene, to form a single composition representing the same 3D scene but having a larger field of view in order to capture the 3D scene as a composite image [27, 57]. This process is a linear transformation of the projective space captured (the three dimensional scene represented in two dimensions), which is called a collineation or homography [22, 64]. Image mosaicing can be done in planar or panoramic views [58]; this study is only concerned with planar mosaicing. Planar mosaicing is the reconstruction of a scene using images captured from different locations

(such as a moving UAV), where panoramic mosaicing is the reconstruction of a scene using images captured from a single stationary point of view having only rotational movement around one axis [58, 64].

The UAS captures a number of still images in JPG format of the area scanned. These images can be merged or stitched together using image mosiacing to create one large image of the entire area, which is easier to interpret than a set of separate images. Since this is a bit off–topic for this study and only part of the preprocessing stage, only elementary methods for image mosaicing were considered. Methods that contain techniques based on blending, frequency domain or features are not considered elementary methods, because it could turn into a separate study on its own. Instead, this study only looks at image mosaicing methods that are based on registration and georeferencing, because the images used in the dataset contain information such as GPS data and camera parameters on which linear algebra and trigonometry operations can be performed to determine the location of the images captured relative to each other.

Almost all literature surveyed was found to utilise either advanced image processing techniques or ground control points in cases similar to this research, while very few were found that use georeferencing and trigonometry, which were the researchers' first idea of a probable solution. The attempted solutions for the image mosaicing in the case of this study are explained in detail in section 3.5.1.

2.3.2 Vegetation segmentation

This section contains literature reviewed on segmenting vegetation in images. The literature reviewed is applied to perspective images or frames from videos captured from a moving ground vehicle and processed in real time. However, these techniques are still useful for UAS applications as they have the same goal except for real-time processing, which is not relevant in the case of this study. The segmentation of the vegetation is necessary to provide information on the leaf mass and to eliminate pixels not pertaining to plants as this study focuses on the identification of influences on maize production.

Guijarro *et al.* [30] propose a method, called the combined approach (COM), for the automatic segmentation of relevant textures in agricultural images. This method is favoured because it is proven to yield satisfactory performances in applications of maize crop and weed detection [29]. The first step is colour space normalisation, applied to an image in the RGB colour space, which is achieved by calculating the normalised spectral r, g and b components ranging in $[0, 1]$ as demonstrated in equation 2.1. The values of R, G and B in equation 2.2 should be in the range of $[0, 1]$; if it is not the case, the values need to be normalised using equation 2.1.

$$R' = \frac{R}{R_{max}}, \quad G' = \frac{G}{G_{max}}, \quad B' = \frac{B}{B_{max}} \tag{2.1}$$

Where $R_{max} = G_{max} = B_{max}$ denotes the maximum value for a pixel, *e.g.* 255 for a 24-bit RGB image.

$$r = \frac{R'}{R' + G' + B'}, \quad g = \frac{G'}{R' + G' + B'}, \quad b = \frac{B'}{R' + B' + G'} \tag{2.2}$$

According to Gée *et al.* [25] the normalisation scheme in 2.2 is usually applied in argonomic image segmentation. Following colour space normalisation comes indices computation where the excess red (ExR), green (ExG), blue (ExB) and excess red subtracted from excess green ($ExGR$) indices are calculated as seen in equation 2.3.

$$ExR = 1.4r - g, \quad ExG = 2g - r - b, \quad ExB = 1.4b - g, \quad ExGR = ExG - ExR \tag{2.3}$$

The excess red (ExR) formula can be used to identify green areas in an image as proposed by Meyer *et al.* [46], but Hamuda *et al.* [33] found that it was not as accurate as ExG. The excess green (ExG) formula was proposed by Woebbecke *et al.* [61] to separate plants from non-plants and is used commonly [33] throughout applications where vegetation segmentation is required.

The indices computation continues in equations 2.4 and 2.5 where the colour index of vegetation extraction ($CIVE$) [41] and vegetative index (VEG) are calculated.

$$CIVE = 0.441r - 0.811g + 0.385b + 18.78745 \tag{2.4}$$

$$VEG = \frac{g}{r^a b^{1-a}}, \qquad a = 0.667 \tag{2.5}$$

The value of a is set to 0.667 in accordance with Hague *et al.* [32] and Guijarro *et al* [30]. Following indices computation is combining the green indices from the four images (ExG, $ExGR$, $CIVE$, VEG) specifically oriented towards the determination of the greenness as calculated in the previous step. The combining of the greenness is shown in equation 2.6, which represents a fused grayscale image from the four previously mentioned images.

$$COM = \sum_{\Omega} w_{G_k} G_k, \qquad \Omega = \{G_k | k \equiv ExG, ExGR, CIVE, VEG\} \tag{2.6}$$

w_{G_k} is a weight calculated from either the entropy of the green indices or the uniformity, Guijarro *et al* [30] found that there is an insignificant difference between using entropy and uniformity leading to the preference for the uniformity approach because of its simplicity in terms of computing. Guijarro *et al.* found that averaged values of 0.25, 0.30, 0.33 and 0.12 should be used for w_{ExG}, w_{ExGR}, w_{CIVE} and w_{VEG}, respectively, which, in turn, leads to equation 2.7.

$$COM = 0.25ExG + 0.30ExGR + 0.33CIVE + 0.12VEG \tag{2.7}$$

Guerrero *et al.* [29] proposed an upgrade on the COM method by introducing $COM2$ as seen in equation 2.8. The normalised difference index and $ExGR$ were excluded because soil regions and plant shadows was classified as part of the plant. It is also important to note that this method was proposed for the analysis of maize plants.

$$COM2 = 0.36ExG + 0.47CIVE + 0.17VEG \tag{2.8}$$

The final step of the COM method is to binarise the grayscale image to indicate which pixels belong to a representation of a plant and which do not. The most common binarisation algorithm used in the literature was found to be Otsu's binarisation algorithm, which is a fairly old algorithm, but well proven.

2.3.3 Estimating water stress

Han *et al.* [34] proposes a method for determining water stress in order to efficiently manage water usage during irrigation. This approach uses thermal imagery to monitor the canopy temperature of maize crop. Han *et al.* [34] indicate that the monitoring of canopy temperature has long been recognized as an indicator of plant stress and that several indices of water stress on crop have been developed. Examples of the before-mentioned crop water stress indices are Crop Water Stress Index (CWSI), Degrees Above Non-Stressed (DANS) index and Degrees Above Canopy Threshold (DACT) index. Han *at al.* [34] developed a solution called Standard Deviation of Canopy Temperature (CTSD) to obtain canopy temperature distribution from thermal imagery. The advantage of this method over the others is that it requires less parameters to indicate water stress from imagery, but still requires more field testing to prove itself [34].

2.4 Summary

This chapter was introduced with a literature review on the maize plant, influences on maize plants, and the management of these influences. This was followed by a literature review on various methods of observation, which was in turn followed by image processing techniques. It was seen that there are numerous image processing techniques that can be very useful in this study, the estimation of water stress that was briefly discussed in section 2.3.3 looks very interesting and promising, but requires thermal imagery which is out of the scope of this study. In the next chapter the experimental setup will be presented.

Chapter 3

Experimental setup

This chapter contains information about how the UAS is set up and utilised, the remote sensing methods used, and the processing done to produce the results pertaining to the influenced area detected.

3.1 Ethical and legal implications

There are some ethical risks impacting the farmer such as disclosing the state of a farm; the owner of the farm from where the data are recorded is not of concern, nor is the name or absolute location, and therefore none of these details will not be disclosed.

Licenses for the software used are all obtained legally. A student license of MathWorks Matlab® R2018 and R2019 is used. A free but limited license of DoneDeploy is used for the third party software to control the UAS. Windows is used on some personal computers having a legal license; other personal computers in use run Linux distributions, which have free and legal licenses. Documentation is developed using either Microsoft Office 360 with a legally obtained license or LaTeX, which is free to use. All C++ libraries used are distributed freely, such as OpenCV, to give an example.

3.1.1 UAS regulations

The body governing the safety and security of civil aviation in South Africa is called the South African Civil Aviation Authority (SACAA). All experiments were conducted within the borders of South Africa and followed the regulations as set out by the SACAA for remotely piloted aircraft systems (RPAS) [54]. SACAA defines RPAS as an unmanned aircraft piloted remotely from a pilot station, with the exception to non-human-carrying model and toy aircraft used exclusively for sport, display and recreational purposes or for children to play with. It is also noted that the director of Civil Aviation has designated an external organisation to oversee the operations of recreational aviation called the South African Model Aircraft Association (SAMAA) [55]. The guidelines specified by SACAA for RPAS are somewhat meager and therefore the guidelines as set out by SAMAA are followed to complement the guidelines of SACAA as the guidelines set out by SAMAA are more complete and descriptive. SACAA mandates to adhere to the following rules:

1. Fly/operate RPAS, or toy aircraft in a safe manner, at all times.
2. Remotely piloted aircraft or toy aircraft should remain within the visual line of sight at all times.
3. Fly/operate RPAS in daylight and clear weather conditions.
4. Inspect your aircraft before each flight.

SACAA prohibits operation of any RPAS or toy aircraft 50 m or closer to any person or group of people, and property without consent from the property owner. The following conditions are not to be met unless approved by SACAA:

1. Near manned aircraft.
2. 10km or closer to an aerodrome (airport, helipad, airfield)
3. Weighing more than 7kg.
4. In controlled airspace.

5. In restricted airspace.

6. In prohibited airspace.

3.2 Development environment

The environment in which this study is performed is of scientific nature, data are gathered by measurements in the form of images, and image processing techniques will be performed on the data, which is transparently presented. More information on the physical environment where the experiments are undertaken is provided in section 3.4.

3.2.1 Hardware

Personal computers are used for research and development. DJI UAS is used with the focus on the DJI Inspire II as the main UAS because of the quality of the images its camera produces and the accuracy of its telemetry. No custom software is developed for any UAS. This study only utilises the UAS as a method of data acquisition. In addition to the DJI Inspire II, the DJI Mavic Pro and DJI Phantom 3 Professional are also used as reserves in the cases where the Inspire would not be available. A DJI Zenmuse X7 camera with a 35mm lens was mounted on the DJI Inspire II UAS and the stock cameras of the DJI Phantom 3 Professional and DJI Mavic Pro were used on those UASs.

3.2.2 Software

A computing environment, MathWorks Matlab®, is used for prototyping, which includes toolboxes such as the image processing and computer vision toolbox, mapping toolbox and the neural network toolbox. C++ is also used in addition for cases where Matlab's processing speed fall short of what is desired. C++ is preferred in almost all cases because of its increased execution speed in comparison with higher-level environments such as Matlab and Python; however, time constraints may restrict some of the

implementations to the Matlab environment. Documentation is presented in Portable Document Format (PDF), because it is a portable format and highly compatible with many systems. A third party application is used for piloting the UAS, DroneDeploy [17], its online software is also used to create a stitched image of the whole area scanned, if necessary.

3.3 Environment

The first set of flights were flown using both a DJI Inspire II and a DJI Phantom Pro 3, at a research farm (Agriculture Research Council) in Potchefstroom, North-West Province. This study is mainly concerned with the data obtained from the second set of flights over a farm in the Free State Province that consisted of better quality maize, much closer to what you would encounter on an actual maize farm with the aim to produce food crop. The images were captured on a maize farm near the end of the maize season during June of 2019. The maize crop was in the mature phase ready for harvesting and grew in the Free State Province of South Africa. The UAS used was a DJI Inspire II with a Zenmuse X7 camera mounted on the drone; see TABLE 3.4 for the specifications of this UAS. The table also contains the relevant parameters for the flight that took place on 2019/06/01 at around 16:20. Two flights were flown during the experiments, the first at around 14:00 at an altitude of approximately 45 m above ground level (AGL) and the second between 16:00 and 17:00 at an altitude of approximately 30 m AGL.

3.4 Data acquisition

The data used in this study can be divided into three categories; the first is the digital images captured by the camera on board the UAS, the second is the telemetry data of the flight captured by the application used to operate the UAS, and the third is the EXIF data embedded within the images.

3.4.1 Images

DJI Phantom 3

The DJI Phantom 3 Professional images, which were used for the preliminary investigation, have a Sony Cyber–Shot DSC-HX400V Basic Compact camera. The specifications of the image data acquired from this UAS and camera are presented in TABLE 3.1. These specifications are essential in the calculations used to perform image mosaicing.

Effective image resolution	4000x3000 pixels
Physical sensor dimensions	8.8x6.6 mm
Actual focal distance	3.6 mm
35 mm equivalent focal distance (stills)	20 mm
Field of view	94x70.5°[12] (84x63°)
Image bit depth	8 bits

TABLE 3.1: Specifications and parameters of the DJI Phantom 3 Professional camera [12]

DJI specifies [12, 11] the sensor size of the camera on the DJI Phantom 3 and Mavic Pro as 1/2.3". The exact dimensions of the sensor can be calculated from that diagonal size and the ratio of the images (3:4). This yields a diagonal length of 11 mm as presented in equation 3.1, while the dimensions are calculated as 8.8 mm wide and 6.6 mm high.

$$\begin{aligned} d &= 1/2.3 \text{ in} * 25.4 \text{ mm}, \quad \text{convert inches to mm} \\ \therefore d &= 11 \text{ mm} \end{aligned} \tag{3.1}$$

DJI Mavic Pro

The DJI Mavic Pro, like the Phantom 3, was also used for preliminary investigation. The DJI Mavic Pro has a Sony IMX377 camera integrated into the UAS. The specifications of the image data acquired from this UAS and camera are presented in TABLE 3.2.

According to the manufacturer, DJI [11], the FOV is 78.8° horizontally, but according to the EXIF data and mathematically calculated FOV, the FOV is actually 69.4°

Effective image resolution	4000x3000 pixels
Physical sensor dimensions	8.8x6.6 mm
Actual focal distance	4.7 mm
35 mm equivalent focal distance (stills)	26 mm
Field of view	78.8x59.1°[11] (69.4x52.1°)
Image bit depth	8 bits

TABLE 3.2: Specifications and parameters of the DJI Mavic Pro camera [11]

horizontally. DJI specifies [11] the sensor size of the camera on the DJI Mavic Pro as 1/2.3". The dimensions of the sensor can be calculated from that diagonal size and the ratio of the images (3:4) as explained before. These values are the same since the diagonal size of the image sensor is the same for both the Mavic Pro and Phantom 3 Professional. This discrepancy in the FOV may be accounted for by arguing that optical zoom was applied either by DroneDeploy or by the camera firmware to focus the lens.

DJI Inspire II with Zenmuse X7 and 35mm Camera

The specifications of image data acquired from the DJI Inspire II with the DJI Zenmuse X7 camera and 35mm lens mounted are presented in TABLE 3.3.

Effective image resolution	5248x3936 pixels
Physical sensor resolution	6016x4008 pixels [13]
Physical sensor dimensions	23.5x15.7 mm
Actual focal distance	35 mm
35 mm equivalent focal distance (stills)	54 mm
Field of view	37.1x25.3°
Image bit depth	8 bits

TABLE 3.3: Specifications and parameters of the DJI Zenmuse X7 camera with 35mm lens and 3:2 still image setting as used on the DJI Inspire II UAS [10]

3.4.2 Telemetry

The telemetry recorded is in csv format and provided by the DroneDeploy application [17], which includes data about the aircraft itself, radio control, gimbal and camera. This data contains all necessary telemetry for this study such as altitude, GPS data and camera parameters to name a few relevant columns, as well as superfluous data not of interest in this study. The telemetry data are captured at a frequency of roughly 8 Hz and an extract of relevant columns can be seen in TABLE A.1 in Appendix A. The csv file also contains general information about the flight such as devices and equipment used during flight, battery and firmware information and camera serial number.

The EXIF data contains data similar to the data in the log file discussed previously. In the experiments where the DJI Inspire II was used, it is more accurate to use the EXIF data because the data are attached to the image file itself while the log file only indicates that images were captured at the time of the log entry, it then becomes difficult to attach a specific log entry or entries to a specific image. For example the column in the log file (see Appendix A) labeled `Aircraft Camera Single Capture` indicates whether or not an image is being captured, if so the row will have `1` entered in that column, if not, the value would be `0`. The `Aircraft Camera Storing Photo` column follows the same principle, where, the value `1` would indicate that a photo is currently being written to permanent storage in that moment, while `0` would indicate otherwise. The images of the DJI Inspire II are of higher resolution resulting in larger files, which take a longer time to write to storage, yielding the value `1` for all entries for that column throughout the log file. The DJI Phantom and Mavic log files have a few `0` entries in the log file in the `Aircraft Camera Single Capture` column, which is a more reliable indication of when an image was captured. An example of EXIF data read from an image is given in Appendix B.

3.4.3 Experiment

An iOS application, DroneDeploy, was used to automate the flight and capture the images, the same parameters except for the altitude and exact area to scan were used for both of the flights. The camera parameters of interest for both flights were as follows: spatial effective image resolution of 5248x3936 (20.7 MP), 35 mm lens, 54 mm focal length (35 mm equivalent), a field of view of 37.1° and physical sensor dimensions of 23.5x15.7 mm consisting of 6016x4008 pixels. The first experiment consists of 50 JPG images and a DroneDeploy csv log file, while the second experiment consists of 199 JPG images and a DroneDeploy log csv log file. All images have the metadata embedded in exchangeable image file format (EXIF). Both experiments have an overlap of 80%. Overlap is a parameter that can be configured on the UASsoftware, this is the amount by which the images should overlap when captured. Section 4.1.2 shows images that are stitched together, one can see discontinuities at the edges of each image and see that they are placed quite close together and run over each other, this is due to the overlap. With an overlap of 0% one should, in a perfect environment, have the images placed exactly next to each other without any gaps and without any overlap. Due to changes in wind the UAS will not fly perfectly, it will not only deviate from its path, but the pitch and yaw will also be influenced causing the images captured by the UAS to not be in the position and angle that was aimed for. This might result in missed areas and result in an image visually similar to FIGURE 4.5 for example. To ensure that the entire area is captured, the overlap was set to 80%. The weather was clear with few clouds in sight and mild wind with no gusts.

3.5 Data processing

The images and embedded image data are processed using quantitative methods applied using MathWorks Matlab ® R2019a and R2019b, and the accompanying neural network toolbox for the classification.

Altitude	45 m
Overlap	80%
Effective image resolution	5248x3936 pixels
Physical sensor resolution	6016x4008 pixels [13]
Physical sensor dimensions	23.5x15.7 mm
Actual focal distance	35 mm
35 mm equivalent focal distance (stills)	54 mm
Field of view	37.1x25.3°
Image bit depth	8 bits

TABLE 3.4: Specifications and parameters of the DJI Inspire II and DJI Zenmuse X7 with 35mm lens and 3:2 still image setting [10]

3.5.1 Image mosaicing

The first phase is to stitch or "merge" the images together using a mosaicing algorithm. It was decided very early in the study that mosaicing algorithms utilising techniques based on feature detection, registration, blending and frequency domain operations would not be used because of their complexity and not being the focus of this study, but merely a preprocessing step. Instead, elementary methods will be looked at and attempted, if unsuccessful a third party application or service would be used for the stitching of the images. A few approaches were attempted using the GPS coordinates, camera specifications and telemetry data. The final attempt made will be discussed as it was found to be the only approach viable to use in this study. All processing that follows is done on both the resulting image of the stitching algorithm as described in this section (FIGURE 4.2) and the resulting image obtained from third party software (FIGURE 4.1), DroneDeploy. The reason for exploring an alternative stitching algorithm to the image obtained from third party software is to preserve the resolution of the original images obtained from the UAS.

The stitching algorithm used in this study starts with reading EXIF data from the image files, the following key entries are extracted from each image's EXIF data: latitude, longitude, relative altitude, camera yaw, pitch and roll. The pitch and roll of the camera are only used to identify the cause for some of the excessive rotational factors of outlier images; this defect might also be due to sensor inaccuracy or interference. For

optimal results, the roll, pitch and yaw of the camera gimbal must be kept as stable as possible, but given weather influences such as wind, this is not always achievable. This is followed by operations to calculate the range of the coordinates. The range calculated is converted to meters and pixels to be used later to create a mesh grid to place (plot) the images as texture maps on the mesh grid. The dimensions in meters of each image are calculated using the specifications and parameters of the camera and lens as given in TABLE 3.4 and illustrated in FIGURE 3.1 using equation 3.4. The top triangle would be the inside of the camera where c denotes the effective length of image sensor, calculated in equation 3.2, f denotes the focal length, which is in this case 35 mm as mentioned in TABLE 3.4, θ is the field of view that can be either 37.1° or 25.3° depending on which dimension of the image you are calculating, again as mentioned in TABLE 3.4. The field of view (θ) can also be calculated for both dimensions using equation 3.3. The bottom triangle is the field of view from the camera. The altitude is denoted by h, which is slightly different for every image as the drone tried to maintain altitude above ground level, while the contour of the land varied slightly. The altitude is retrieved from the EXIF data, and l the length of one of the dimensions of the image. l can alternatively be calculated using equation 3.5.

$$\begin{aligned} c_l &= 23.5 * (5248/6016) \\ c_b &= 15.7 * (3936/4008) \end{aligned} \tag{3.2}$$

$$\begin{aligned} \theta_l &= \arctan((c_l/2)/f) * 2 \\ \theta_b &= \arctan((c_b/2)/f) * 2 \end{aligned} \tag{3.3}$$

$$\begin{aligned} l_l &= h/f * c_l \\ l_b &= h/f * c_b \end{aligned} \tag{3.4}$$

$$\begin{aligned} l_l &= \tan((\theta_l/2)) * h * 2 \\ l_b &= \tan((\theta_b/2)) * h * 2 \end{aligned} \tag{3.5}$$

The edge points of each image are calculated using equations 3.2 to 3.5 before being placed (plotted) on a mesh grid as a texture map. Immediately after placement, the image is rotated in order for the top of the image to face North by using the camera yaw values retrieved from the EXIF data. The yaw is in some cases inaccurate, it could

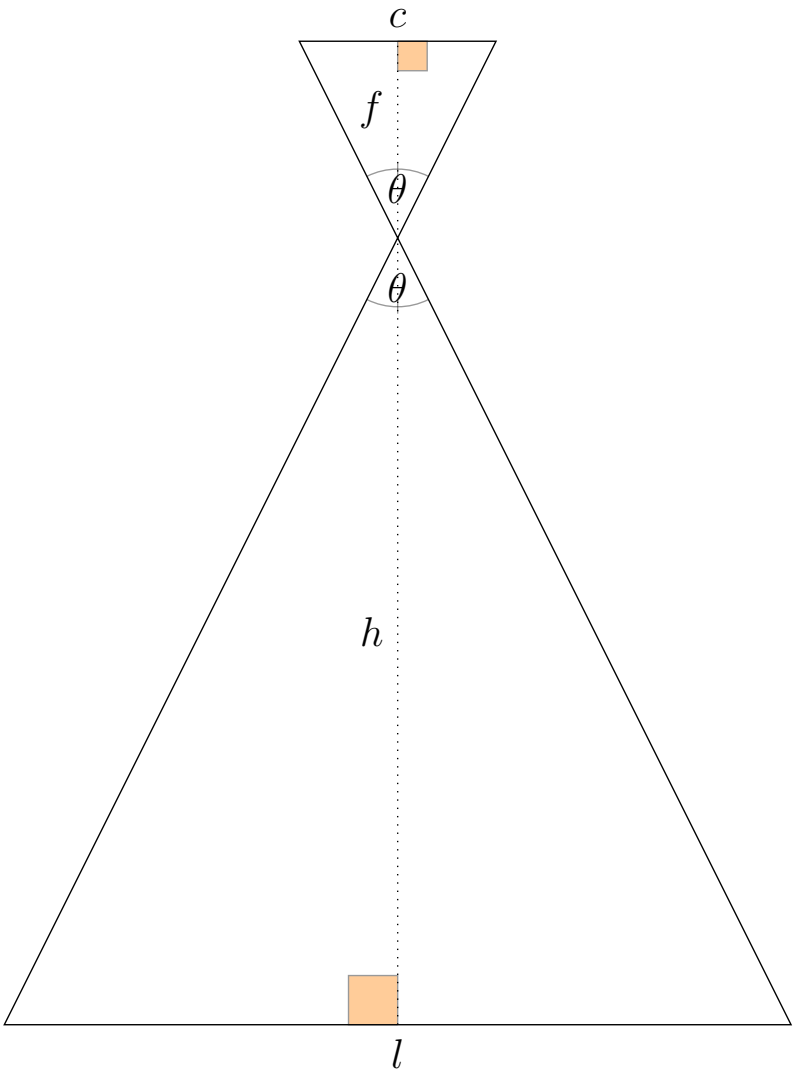


FIGURE 3.1: Calculating distances within an image using geometry and trigonometry *(Triangles are not drawn to scale)*

be that the camera was rotated in flight by the automated software (this seems an unlikely case), or a misreading on the sensor caused by interference or inaccuracy on the electronics. This stitching algorithm as described thus far is not very considerate of memory usage as all the images are being stored in RAM during processing. To provide some perspective, 26 GiB of memory was available, this was also used for system resources such as the operating system and user applications *etc.* The memory usage was monitored while the algorithm was running, up to a point where the development environment would come to a halt when the memory available has exhausted. The earlier C++ implementation could not compile due to the matrix used to store the image taking up too much memory. To address this issue, the images are scaled down

and written to disk after the placement of each image before processing the remaining higher resolution images. The factor by which the images were scaled down was kept to a minimum in order to preserve image resolution as far as possible. The factor by which the images were scaled down to was experimented with, and since the overlap of the images was quite significant, it was possible to skip one or two images before processing another, which made it possible to reduce the factor by which the images were scaled down to, to 80%. By skipping images, more discontinuities among the placement of the images were introduced, so it was decided to rather not skip images and to increase the downscaling factor to 40%. The resulting image of this algorithm is compared to the image from the third party application, DroneDeploy in Chapter 4.

3.5.2 Vegetation segmentation

Some of the techniques discussed in literature in 2.3.2 are implemented on the resulting image of the stitching algorithm, as well as the result from the third party software. The results of these techniques are then used as components in the feature vector for classification.

The RGB values are normalised as explained in the literature survey through equations 2.1 and 2.2. This is followed by calculating the vegetation indices as described in section 2.3.2. The excessive red, excessive green, excessive blue and excess red subtracted from excess green indices were calculated using equation 2.3. In addition, the HSV colour components were also used as inputs in the feature vector.

3.5.3 Damage classification using artificial neural network

As mentioned earlier Matlab's neural network toolbox was used, more specifically a pattern recognition neural network. According to Matlab's documentation [44], this is a two-layered feed-forward network with sigmoid hidden and softmax output neurons. The network is trained with scaled conjugate gradient backpropagation. The following parameters are experimented with: window size, number of Fourier summations to include in the feature vector, and the results of the techniques that were discussed in

section 3.5.2 were experimented with. The colour components and vegetation indices described in section 3.5.2 were first experimented with individually to observe the effect they each have on the classification result in isolation. This followed by adding the vegetation indices and/or colour components that showed promising results as components to the feature vector. These components are not used in their raw form as discussed in detail below, the word "component" from here on refers to a member of the feature vector.

Following the mosaicing process, the resulting images of the stitching algorithm and from the third party software representing the entire area scanned are now prepared for identification of influences. The image is resized to the largest size possible, while being a multiple of the window size being experimented with, for example 7, which will be used as an example. The image is then broken up into small 7x7 segments, windows or matrices and stored as a collection of small matrices, which is a collineation of the previous result. Each matrix of the collection is processed to provide a feature vector for the neural network. A subset, 70%, of the collection is used to train the neural network, while the remaining elements in the collection are used to identify influencing factors, 15% for testing and 15% for validation. The feature vector consists of the summations of the Fourier coefficients of each component participating in the experiment. A sum exists for each discretely computed Euclidean distance from the center of the shifted Fourier transform of the 7x7 matrix as depicted in FIGURE 3.2. The feature vector also includes the average of the Fourier image, and may also include a combination of multiple instances for the different components being evaluated such as red, green, blue, ExR *etc.*

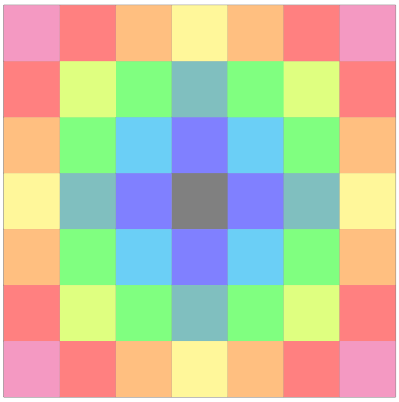
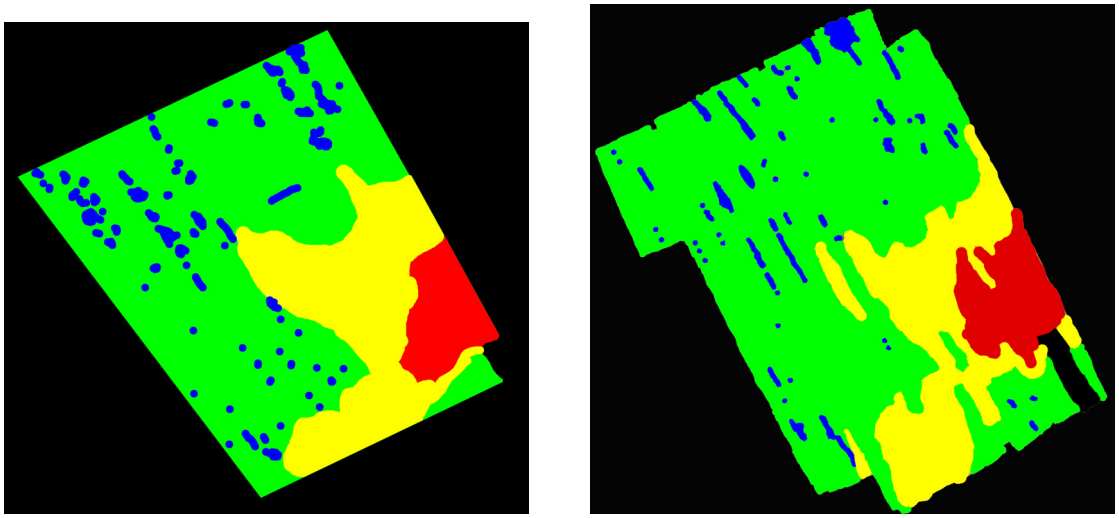


FIGURE 3.2: The summation of each discretely computed Euclidean distance from the centre of the shifted Fourier transform of a 7x7 matrix, each represented by a different colour

3.5.4 Ground truth data

The ground truth data was obtained by providing an insurance assessor with the stitched images, who, in turn, marked the influenced areas according to their damage and degree of damage where applicable using 4 categories. The categories are: Very bad water damage, water damage, healthy and unknown damage. See FIGURE 3.3 for the colour coded ground truth data visualizing the 4 categories. The areas highlighted by green are classified as healthy, yellow is classified as water damage, and the red is classified as severe water damage. The blue areas (see FIGURE 3.3) are damages that are not directly related to water damage, the assessor has indicated that it might be from something such as a planting error but it is still very uncertain. The black areas are not considered or processed in the classification as it covers either an unmapped area or maize that has been cut by the farm owner as these images were taken at the end of the maize season.



(A) Ground truth on the stitched image obtained from DroneDeploy

(B) Ground truth on the stitched image obtained from the novel algorithm described in section 3.5.1

FIGURE 3.3: Ground truth data obtained from an insurance assessor for both images

3.6 Summary

In this Chapter, the environment in which this study took place, the method of data acquisition, image mosaicing and the classification were presented. There were some

difficulties with the image mosaicing process due to memory limitations as discussed before and will be evaluated in more depth in section 5.1. More difficulties were experienced with the accuracy of the mosaicing process when using the DJI Matrice and the DJI Phantom due to insufficient accuracy on the location and other telemetry data, but this was resolved with the DJI Inspire II. The mosaicing process was not supposed to be such a big part of this study, but the opportunity and need for it was recognised during the initial experimentation. The next chapter will show the results of the methodology that was applied in this chapter.

Chapter 4

Results

The results of this research study are presented in this chapter. The first section focuses on the results of the mosaicing process, followed by the results of the pattern recognition process used to classify anomalies found on the image.

4.1 Mosaicing results

This section covers the results of the mosaicing process. The novel mosaicing algorithm, utilising the methods as discussed in section 3.5.1 was evaluated against the result obtained from third party software, DroneDeploy.

4.1.1 DroneDeploy result

FIGURE 4.1 is the result obtained by using DroneDeploy software.

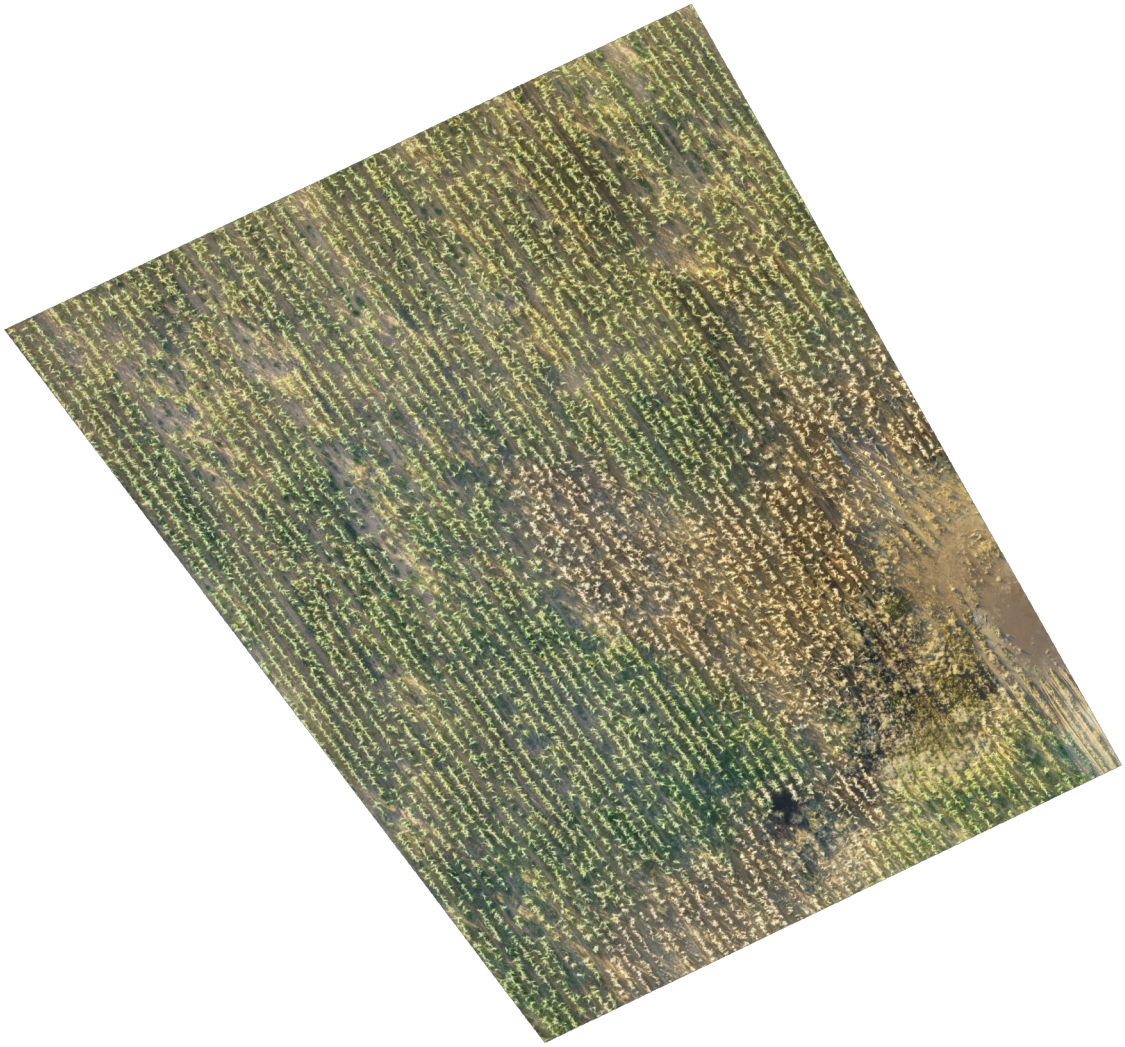


FIGURE 4.1: Stitched image using DroneDeploy third party software

Using this result as input for the neural network, the evaluation is discussed in Chapter 5, followed by the Conclusions drawn in chapter 6.

4.1.2 Mosaicing result

FIGURE 4.2 is the result obtained by using the novel algorithm as described in Chapter 3.

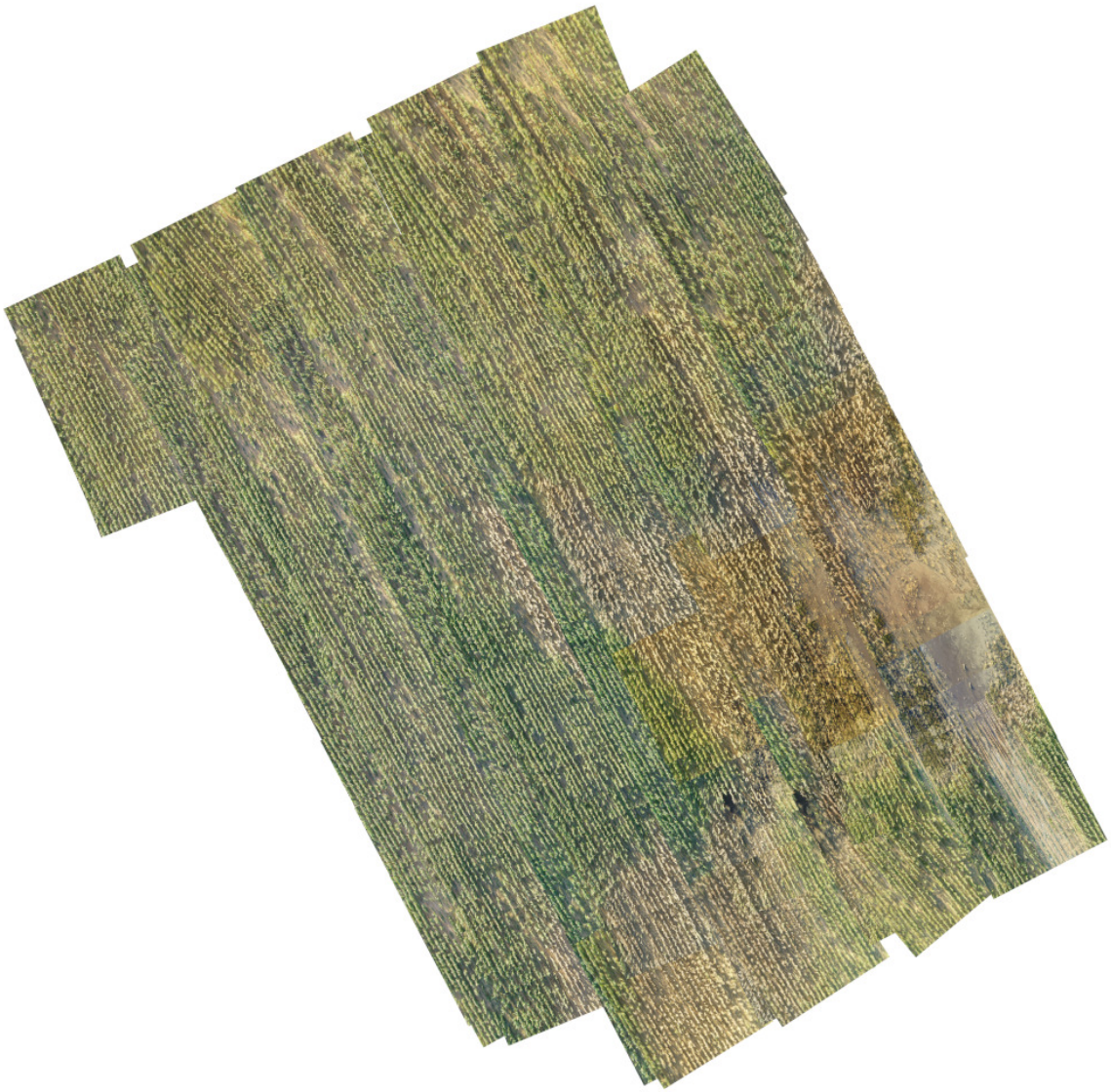


FIGURE 4.2: Stitched image using algorithm as described in section 3.5.1

This result used in further processing is the image represented in FIGURE 4.2, which is scaled down to 40% of the original scale due to processing limitations as previously discussed in section 3.5.1. In addition to implementing an algorithm for mosaicing, some aspects were tweaked such as skipping every second image and/or row, for example; this had a significant influence on the resulting image (see FIGURES 4.3–4.6).

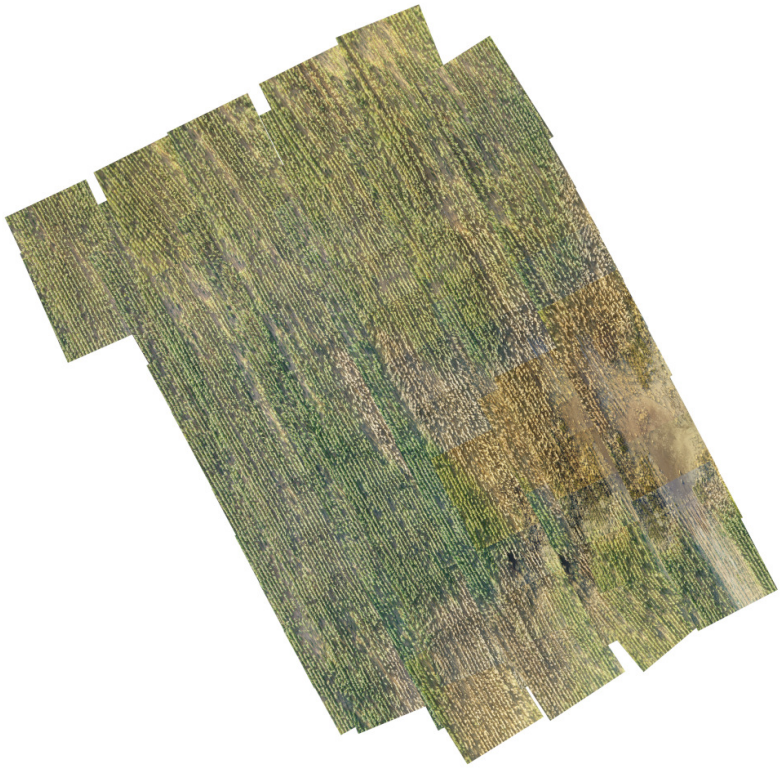


FIGURE 4.3: Stitched image using algorithm as described in section 3.5.1, but skipping every second image. This image was also scaled down to 40% of the original

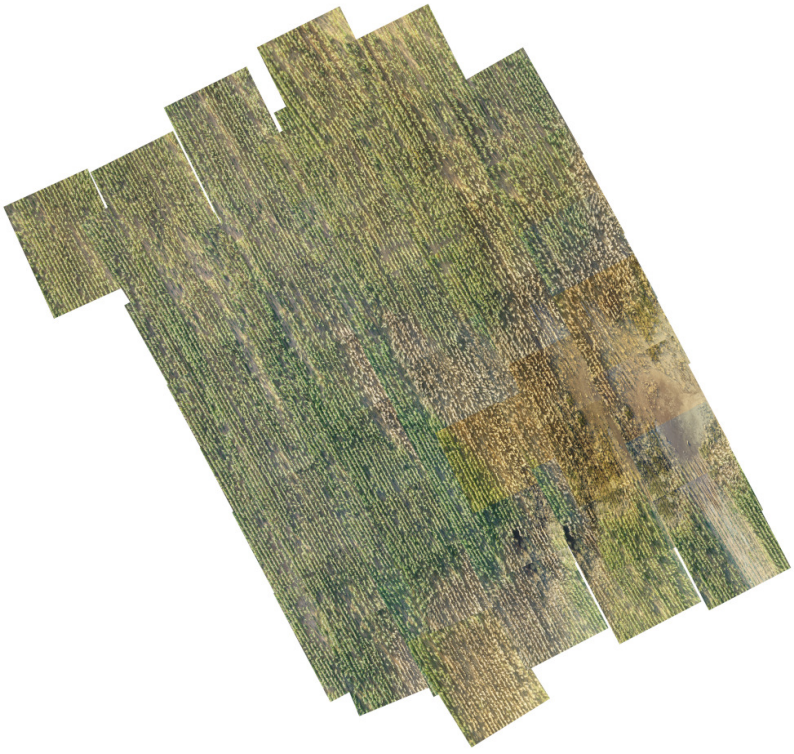


FIGURE 4.4: Stitched image using algorithm as described in section 3.5.1, but skipping every third image. This image was scaled down to 70% of the original

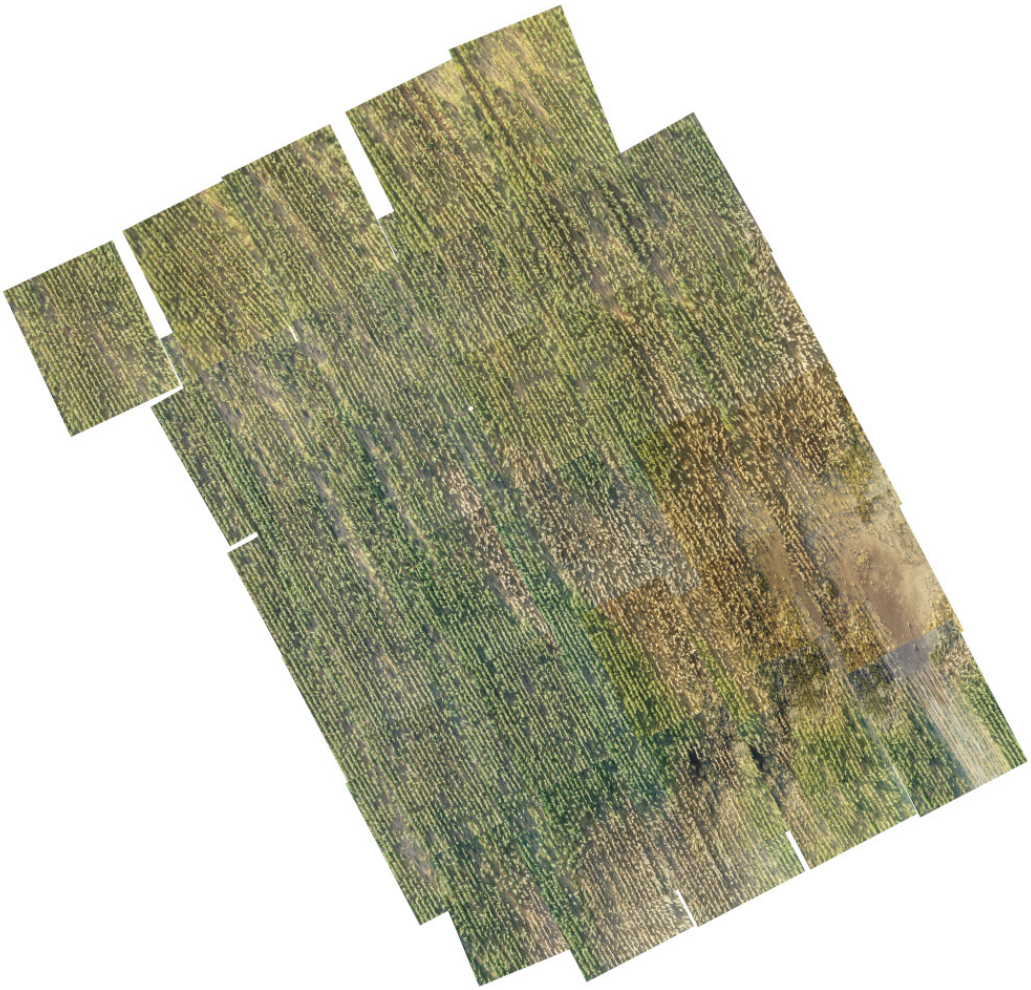


FIGURE 4.5: Stitched image using algorithm as described in section 3.5.1, but skipping every fourth image. This image was scaled down to 80% of the original

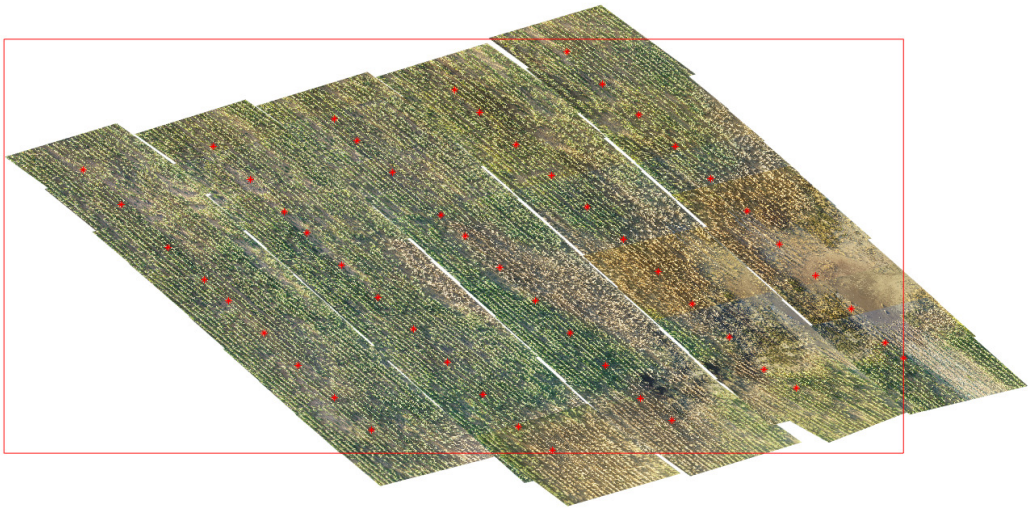
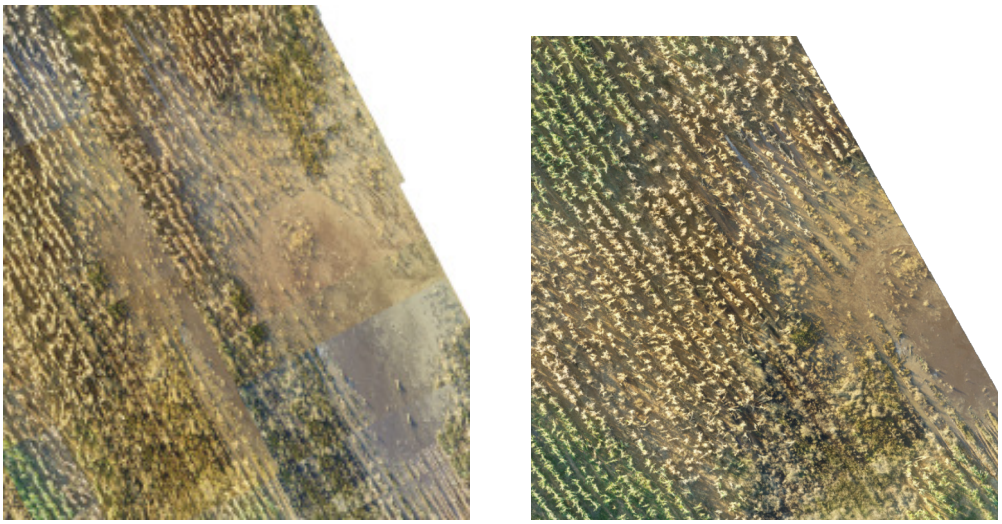


FIGURE 4.6: Stitched image using algorithm as described in section 3.5.1, but skipping every second image and every second row. This image was scaled down to 80% of the original



(A) Novel mosaicing algorithm result. (B) DroneDeploy result.

FIGURE 4.7: Close-up comparison of both methods.

In FIGURE 4.7 one can see the discontinuities formed by the novel mosaicing algorithm when compared to the DroneDeploy results. More than one type of discontinuity can be observed here, the first is the discontinuity in the spatial placement of the originally captured images, the second being a discontinuity in the colour.

4.2 Classification results

This section presents the results obtained by using the classification methods as described in section 3.5.3. Results of the classification are presented in confusion matrices indicating the true positive classifications and the incorrect classifications. Alongside the confusion matrices, are the corresponding ROC graphs as they are a popular measure of neural network performance and accuracy. The results in sections 4.2.2 and C.1 are obtained using the image acquired from the DroneDeploy third party software (FIGURE 4.1) and the results in sections 4.2.1 and C.2 are obtained by using the stitched image (FIGURE 4.2) resulting from the algorithm as described in section 3.5.1. Both the aforementioned sections contain results obtained by using different feature vectors for the classification process. These results are evaluated and discussed in Chapter 5.

The format of the results is represented in two sets of results. The first set is a confusion matrix representing correct classifications on the diagonal (green) of the matrix and the incorrect classifications on the off-diagonal (red) indices, the rows correspond to the predicted class (Output Class) and the columns correspond to the true class (Target Class) from the ground truth data, *e.g.* the first column and third row represent the number of classifications that were incorrectly classified as class 3, but should have been correctly classified as class 1. The column on the far right corresponds to the percentage of the classifications that were assigned to that class, the green percentages being the percentage of classifications correctly assigned to that class and the red the incorrect classification percentage for that class. The bottom row represents the percentages of all classifications that should have been assigned to that class and that are correctly classified (green percentages) and incorrectly classified (red percentages). The cell in the bottom right represents the overall accuracy. The second set is a receiver operating characteristic (ROC) curve, this graph shows the accuracy of the classification at all thresholds. The true positive and true negative rates are calculated using equation 4.1. The ideal ROC result would be to have as many true positive rates as possible and have the false positive rates at a minimum, meaning all the points are plotted in the upper left corner. Each of these results has a confusion

matrix and an ROC curve associated.

$$TPR = \frac{TP}{TP + FN}$$
$$FPR = \frac{FP}{FP + TN} \tag{4.1}$$

Each of the aforementioned sets of results has four components, going from left to right and top to bottom:

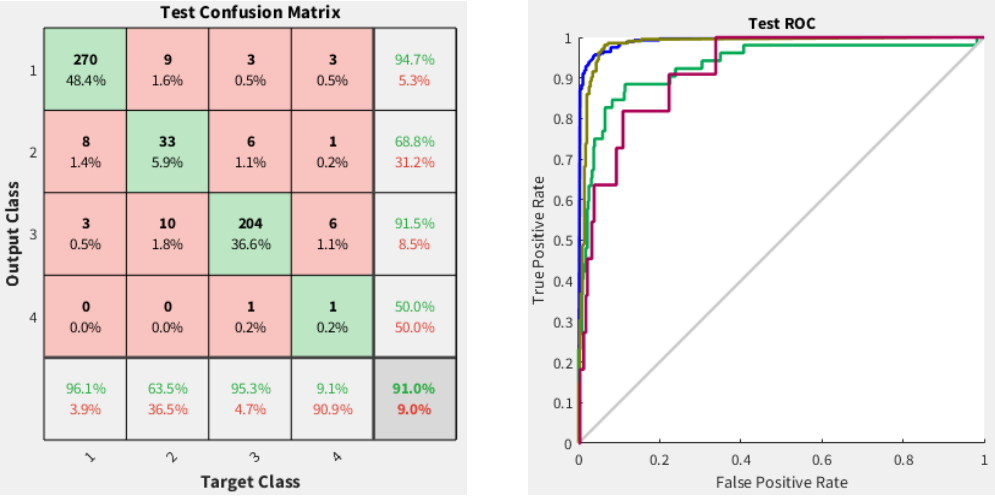
1. **Training:** Training data used to determine the weights of the neural network.
2. **Validation:** Data used to validate the training results.
3. **Test:** Unbiased performance estimate.
4. **All:** Represents the summation of the training, validation and test results previously obtained.

The result of interest is the **Test** results which, represent the unbiased classification results. As stated in 3.5.3, key elements that were experimented with are: the window size of the segments the image is divided into, the number of Fourier summations included in the feature vector as well as the selection of components to include in the feature vector such as red, green, blue and vegetation indices. The classes are defined as follows:

1. Severe water damage.
2. Water damage.
3. Healthy.
4. Unknown damage.

4.2.1 Classification results from stitched image

FIGURES C.32 to C.62 are the results obtained from the classification applied on the image constructed from the mosaicing algorithm described in section 3.5.1. FIGURE 4.8 is an extract showing only the test results. This result was found to have the highest unbiased true positive and true negative classifications as indicated by the far lower right cell. This cell indicates the total true positive classifications to be 91%, and the total true negative classification to be 9%. As explained earlier in section 4.2 the cells on the diagonal (green) are the percentages of the true positive classifications. In this particular case, the classifications that were correctly classified as class 1 (severe water damage) made up 270 samples which is 48.4% of the total samples used for unbiased testing, which in turn was 15% of the entire sample set obtained from the images as stated in section 3.5.3. As already explained in section 4.2.1, the cell in the third column and second row for example indicates that 6 samples, which is 1.1% of the total samples used for unbiased testing, was incorrectly classified as class 2 (water damage), where they should have been classified as class 3 (healthy).



(A) Confusion matrix. (B) ROC.

FIGURE 4.8: Classification results of using a window size of 45x45 pixels, having the first 4 summations of the computed Fourier coefficients of the red, green, blue and ExR components in the feature vector. This is a an extraction from FIGURE C.54

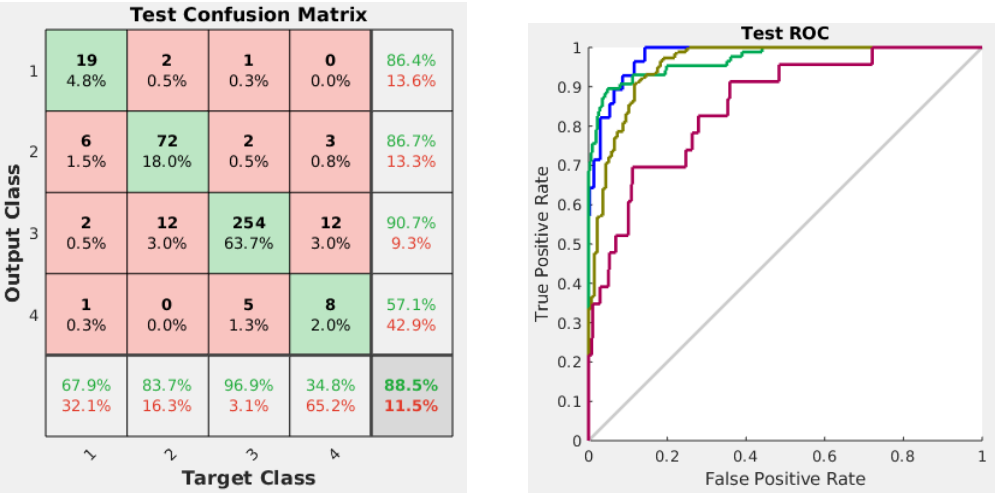
The ROC graph was already introduced in section 4.2, the graph shows the true positive rate on the y-axis and the false positive rate on the x-axis as indicated by the

axis labels. The graph legend is defined on the original results (see FIGURE C.54). The result in FIGURE 4.8 in particular indicates poor unbiased classification performance for classes 4 (unknown damage) and 2 (water damage). Classes 1 and 3 on the other hand have good unbiased classification performance, although more points closer to the upper left corner at (0,1) is preferred.

4.2.2 Classification results from DroneDeploy image

FIGURES C.1 to C.31 are the results obtained from the classification applied on the image obtained from DorneDeploy. FIGURE 4.9 is an extract showing only the test results. This result was found to have the highest unbiased true positive and true negative classifications out of the all the classification results obtained from using the DroneDeploy image. As indicated by the far lower right cell. This cell indicates the total true positive classifications to be 88.5%, and the total true negative classification to be 11.5%. For this case, the classifications that were correctly classified as class 1 (severe water damage) made up 19 samples which is 4.8% of the total samples used for unbiased testing. The cell in the third column and second row for example indicates that 2 samples, which is 0.5% of the total samples used for unbiased testing, was incorrectly classified as class 2 (water damage), where they should have been classified as class 3 (healthy).

This ROC graph (FIGURE 4.9) in particular indicates poor unbiased classification performance for class 4 (unknown damage). Classes 1, 2 and 3 have better unbiased classification performance but still not good enough, more points closer to the upper left corner at (0,1) is preferred.



(A) Confusion matrix. (B) ROC.

FIGURE 4.9: Classification results of using a window size of 45x45 pixels, having the first 8 summations of the computed Fourier coefficients of the red, green, blue, hue, saturation, value and ExR components in the feature vector. This is a an extraction from FIGURE C.24

4.3 Summary

This chapter showed some key results to be evaluated in the next chapter. The complete results can be found in Appendix C. A summary of the key results are presented in TABLE 4.1. The first column are references to the figures showing the complete results. The "Feature Vector" column shows which components were included in the feature vector. The "Fourier Coefficients" column shows how many summed coefficients of each component were included in the feature vector as explained in section 3.5.1. The "DroneDeploy" columns shows the classification results obtained by performing the classification on the DroneDeploy image. The "Mosaic" columns shows the results obtained from performing the classification on the image that resulted from the novel mosaicing algorithm. The columns labeled "TP %" shows the percentage of true positive classifications. The columns labeled "TN %" shows the percentage of true negative classifications. In the next chapter the evaluation phase of the study is presented.

Figures		Feature Vector	Window Size	Fourier Coefficients	DroneDeploy		Mosaic	
					TP %	TN %	TP %	TN %
C.21	C.54	R,G,B, ExR	45	4	82.7	17.3	91.0	9.0
C.24	C.56	R,G,B, H,S,V, ExR	45	8	88.5	11.5	90.7	9.3
C.23	C.55	R,G,B, H,S,V, ExR	45	6	86.5	13.5	90.5	9.5
C.8	C.52	R,G,B, H,S,V ExR	45	4	82.7	17.3	88.4	11.6
C.29	C.60	R,G	45	9	82.5	17.5	89.4	10.6
C.22	C.53	R,G	45	4	81.7	18.3	87.1	12.9
C.19	C.50	R,G	27	4	79.6	20.4	89.4	10.6
C.16	C.47	R,G	55	4	78.7	21.3	88.8	11.2
C.26	C.58	ExR	45	9	70.9	29.1	84.8	15.2
C.25	C.57	ExG	45	9	67.9	32.1	81.5	18.5

Table 4.1: Key results from the unbiased classification confusion matrices.

Chapter 5

Evaluation

This section contains the evaluation of the results and judges the performance of the research outcome. Aspects evaluated include the evaluation of the mosaicing results and classification of damaged areas.

5.1 Evaluation of the mosaicing algorithm

In the mosaicing algorithm, the images were scaled down to 40% of the original due to processing limitations, which still is a higher resolution image than that obtained from DroneDeploy. The resolution could be increased by skipping every second, third or even fourth image due to the large overlap as demonstrated in section 4.1.2, this allowed for a resolution increase of up to 80% to that of the original image in the case of skipping every fourth image or skipping every second image and every second row of images. However, skipping images caused even more discontinuities and gaps within the image, which is of course not desired. However, since the techniques used in the image mosaicing algorithm only employed elementary mathematical techniques, it was not nearly as accurate in terms of visual presentation, based on the gaps and overlap discontinuities, as it could be when compared to the image of DroneDeploy, even when skipping no images. It is unknown which image processing techniques were employed by the DroneDeploy software, but as seen in the literature in section 2.3.1, it would at least include more advanced image processing algorithms such as blending

and registration. As a result, the mosaicing algorithm yielded many discontinuities and was only able to place the image in the vicinity of its GPS coordinates. More critique on the mosaicing algorithm is that some images were captured at a roll and/or pitch that is not insignificant, which was not corrected in the algorithm, only the yaw was used to rotate the image to its correct orientation. This algorithm is also very sensitive to inaccuracies in the flight telemetry as was observed when using the DJI Phantom 3 Pro and DJI Mavic when compared to the DJI Inspire II. The mosaicing algorithm is considered a novel algorithm because no literature could be found that uses this same method to stitch images together, except for few similar methods that were using ground reference points in addition to the methods used in this study.

It is important to note that the stitched image used in the classification experiments were scaled down even more after mosaicing to allow for easier management on lower end computers, especially when the ground truth was constructed by colour coding the image using image manipulation software by an agricultural insurance assessor. The resulting stitched image ended up having a resolution of 2810x2727, whereas the image obtained from DroneDeploy has a resolution of 3454x3254.

5.2 Evaluating the classification

Evaluation of the success of the classification is done by comparing the confusion matrices of each experiment. The **test confusion matrix** in particular is of interest because it is the true indication of how successful the unbiased classification was. Surprisingly, it is observed that the classification is on average more accurate when performed on the stitched image using the algorithm described in section 3.5.1. FIGURES C.32 to C.62 show increased classification accuracy when compared to the results obtained from the DroneDeploy image in FIGURES C.1 to C.31. The evaluation and remarks that follow regarding the construction of the feature vector are for both cases the novel stitching algorithm and for the classification done using the image obtained from DroneDeploy.

5.2.1 Feature vector construction

It is also apparent that the way the feature vector is constructed significantly influences the classification results. One of the observations made was that including the blue component of the RGB colour space in the feature vector yields no improvement in classification. This is probably due to the lack of blue colour in a natural vegetation setting. As expected, including the green component of the RGB colour space in the feature vector has a significant influence on the classification. At first, it was a surprise that the red component of the RGB colour space had such a tremendous influence on the classification, but after giving it some thought, it started to make sense. This was also pointed out by Meyer *et al.* [46] who proposed the excess red index for vegetation segmentation in plant species identification. The colour of the soil (usually brown) is far closer to the red colour of the RGB colour space than green and blue, and since the absence of vegetation would show more soil, it makes sense that red would have a considerable impact on the classification and therefore would be a good component to include in the feature vector as FIGURES C.18 *vs* C.19, C.20 *vs* C.22, C.27 *vs* C.28 and C.29 indicate. The results obtained by the mosaiced image counterparts support this observation as well as indicated by FIGURES C.49 *vs* C.50, C.51 *vs* C.53, C.59 *vs* C.60. Given that red has such a great influence it could also be expected that the ExR, or excessive red, vegetation index would be a valuable component to include in the feature vector. The results from the classification that utilised the ExR vegetation index showed an increase in classification accuracy as can be seen in FIGURES C.8, C.23 and C.24 for the DroneDeploy image and FIGURES C.52, C.54, C.55, C.56 and C.58 for the novel mosaicing algorithm.

Another interesting observation is that for both the DroneDeploy image and the image constructed using the mosaicing algorithm from section 3.5.1 the classifications utilising the excessive red vegetation index (ExR) performed better than the excessive green vegetation index. FIGURES C.25 *vs* C.26 and FIGURES C.57 *vs* C.58 support this statement. This result could be due to the colour of the maize plants being of a more yellowish hue than green, in which case the ExR vegetation index would perform better than the ExG vegetation index as the absence of both green and yellow vegetation would show more red colours.

5.2.2 Window size

The window size used to segment the image for classification also has an impact on the results; a smaller window size can give more data for the classification neural network, which is preferable, but too small would result in windows being too small to contain informative information. A larger window size can give more information that can be used for classification, but reduces the total number of classifications that can be made, reducing the training, validation and testing datasets. A comparison between FIGURE C.51 and FIGURES C.61 and C.62 shows what happens when the window size gets too big. One can see when looking at the ROC graphs that class 4 (being the smallest set) starts to become more jagged as the amount of data reduces. The same comparison can be made with FIGURE C.20 and FIGURES C.30 and C.31. Smaller window sizes seem to be beneficial for the classification as it provides more data to train and test with but FIGURES C.17 and C.18 shows a reduction in classification accuracy when compared to FIGURE C.20. This is probably because the window size is getting too small to contain informative information. Looking at their counterparts applied on the stitched image (FIGURES C.48 and C.49 *vs* C.51), one can see not just an increase in classification accuracy, but classification accuracy is increasing as the window size gets smaller than what was found to be the optimal in the experiments performed on the DroneDeploy image, which was 45x45. This observation suggests that the accuracy of the classification can be increased by constructing the same feature vector that was found to have the best classification results for a window size of 45x45, and apply it on data that is segmented into window sizes that are smaller than 45x45.

5.3 Summary

In this chapter the evaluation of results was discussed. It could be seen that there should be a good balance between the window size and number of windows, more windows are more data but windows that are too small does not contain as much information. It is also apparent that the classification, while utilising the novel algorithm used for the stitching of the images, outperforms the classification while using the DroneDeploy

image instead. Another interesting observation mentioned earlier in section 5.2.1, is that the red colour component generally provides a better indication of maize crop health than the green component. In the next chapter the conclusions of the study are given and the aim and objectives are revisited.

Chapter 6

Conclusion

6.1 Summary of findings

Looking at the mosaicing in isolation, the result is nothing more than what was expected, imperfect yet acceptable considering no ground reference points nor advanced image processing techniques were implemented. However, when viewing the classification results, it proved to yield results with increased accuracy, although it would have been preferable to use a full resolution image. To leverage the potential of this novel mosaicing algorithm for classification of influences on maize crop, or any other purpose, it needs improvements on numerous aspects which will be discussed in the future work section (section 6.5).

The classification demonstrated positive results with a classification accuracy of as high as 91.0% (see FIGURE C.54); the case, however, is very specific and it would have been more favourable to have a greater variety of influences on the maize crop than just water damage. The parameters such as the length of the feature vector and window size might change as one starts experimenting with other influences, but the elements to include in the feature vector will probably remain the same as what was found optimal in this study: ExR, red, green and blue. If the feature vector needs to be trimmed, it is expected that the blue component would be the least significant, and the most significant components would be ExR, red, and green.

6.2 Revisiting aims and objectives

The aim of this study was to explore and evaluate image processing techniques to support sustainable food security using remote sensing implemented on a UAS. The focus of the image processing techniques to be used was directed towards identifying influencing factors on maize production with an additional objective of determining the extent of the influence. This study concluded with a possible solution that needs further exploration. The solution utilises a pattern recognition neural network to classify influences on maize crop, while the study proposes a set of image processing techniques to include in the feature vector to be used by the neural network. As for the extent of the influence on maize crop, the main influence present in the data available to this study (water damage), was divided into two classes as discussed in section 4.2.1. The objectives that were set out for this study is discussed below.

1. The first objective was to perform an introductory survey of factors influencing maize production, as well as how those factors can be detected. This survey was to provide a suitable candidate (influence) to investigate that would yield the most preferable results from using image processing techniques, however, the influence to be focussed on was eventually determined by what was available at the time, water damage.

2. The second objective was to investigate image processing techniques that can aid in identifying and classifying influencing factors on maize production. Section 2.3 shows the techniques that have been researched, of which some were implemented in this study. There are techniques that are far more superior that those that were implemented in this study and deserves more research and experimentation, see section 2.3.3 to name one, but requires specialised cameras which were not available.

3. The third objective was to explore remote sensing techniques, because as mentioned in the previous paragraph, there are superior image processing techniques that can be used when utilising the infra-red spectrum for example. Section 2.2 explores various methods of observation that can be performed that may produce

improved results, or may not be adequate for the solution applied in this study. This survey also serves a purpose to shed some light on the shortcomings of satellite remote sensing, and justifies using UASs as opposed to satellite remote sensing.

4. The fourth objective was to acquire the data on maize crop that contained both healthy maize and maize that are influenced by one or more factors. Section 3.4 describes how the data was acquired.

5. The fifth objective was to process the data (images) to identify anomalies and match these anomalies to factors influencing maize production. Section 3.5 describes how this was done. The estimation of the extent of the damage was done by having different classes for the different levels of extent, of which in this case there were only two classes of one influence.

6. The sixth objective was to evaluate the accuracy of the proposed solution using ground truth data obtained from an insurance assessor. This objective was completed in Chapter 5. Both the image mosaicing approach and the classification were evaluated.

As stated in section 1.3, the research question this study aimed at answering is "How accurately can image processing techniques, applied to images obtained from a UAS, be used to identify factors influencing maize production, and estimate the extent of this influence?" The answer to the first part of this question is that the image processing techniques applied in this study is able to identify factors influencing maize production such as water damage. Other influences are to be experimented with and many aspects of the approach used has room for improvement. To answer the second part of the question regarding the extent of the influence, when the extent of the damage can be visually differentiated, as with this case, then one can accurately determine the extent of the influence.

6.3 Contributions

This study provides an approach to identify influencing factors on maize crop that is accurate enough to be useful, and also reveals opportunities for more research. Research in specific topics, such as the ones discussed in section 6.5, can lead to significant improvements to the approach demonstrated in this study. The approach followed in this study demonstrated which image processing techniques are promising to use as feature vector elements for a neural network. Another contribution from this study, which was unplanned, is the novel mosaicing algorithm described in section 3.5.1. During the literature survey, it was found that performing mosaicing by only using camera specifications and telemetry data, and without the aid of ground referencing points, is not that common.

6.4 Limitations

There are a number of limitations that placed constraints on this study. The ones that had the greatest impact was the memory usage of the mosaicing algorithm and the portability of the resulting image. The purpose of implementing a mosaicing algorithm was to ensure a full resolution image of the area captured. It became clear that more computational resources, especially memory, would be needed in order to achieve this result. On top of the difficulty of producing the full resolution image came the handling and management of the image; because of the amount of data it contains it proved difficult to handle as a portable image and therefore also difficult to manipulate with image processing software to get a high resolution ground truth image from the insurance assessor.

This study was also limited to the data that was available, water damage, it would be beneficial to experiment with other types of influences as well. There was also only an optical camera available to this study, as mentioned in section 2.2, other types of cameras and remote sensing techniques can open doors to a greater variety of image processing techniques for an improved feature vector to be used in classification.

Existing research on specific topics as mentioned in section 6.5 with the purpose of aiding in identification of influences on maize crop.

6.5 Future work

This study is only a stepping stone to ones to follow to eventually reach a practical implementation. This study indicates points of interest, areas to focus future research on, and sheds light on key topics paramount in the solution to this problem. Key topics are: image mosaicing without the use of ground reference points, vegetation segmentation on images captured from UASs, and classification of maize crop damage using images captured from UASs. Research on damage classification on maize from microscopic and close-up images is plentiful, as well as phenotyping using satellite images, but research on damage classification on images obtained from UASs is still very scarce. This study only skimmed the surfaces of these topics using only elementary techniques from each. However, a more thorough investigation into each with the end goal being identification of influences on maize crop would probably reveal many opportunities for improvement to aid in the classification and the approach to solving this problem as a whole.

Bibliography

[1] Jayme Garcia Arnal Barbedo. Digital image processing techniques for detecting, quantifying and classifying plant diseases. *SpringerPlus*, 2(1):660, 2013.

[2] Juliane Bendig, Kang Yu, Helge Aasen, Andreas Bolten, Simon Bennertz, Janis Broscheit, Martin L Gnyp, and Georg Bareth. Combining uav-based plant height from crop surface models, visible, and near infrared vegetation indices for biomass monitoring in barley. *International Journal of Applied Earth Observation and Geoinformation*, 39:79–87, 2015.

[3] Jose AJ Berni, Pablo J Zarco-Tejada, Lola Suárez, and Elias Fereres. Thermal and narrowband multispectral remote sensing for vegetation monitoring from an unmanned aerial vehicle. *IEEE Transactions on Geoscience and Remote Sensing*, 47(3):722–738, 2009.

[4] Stan Birchfield. *Image processing and analysis*. Cengage Learning, 2016.

[5] CH Bock, GH Poole, PE Parker, and TR Gottwald. Plant disease severity estimated visually, by digital photography and image analysis, and by hyperspectral imaging. *Critical Reviews in Plant Sciences*, 29(2):59–107, 2010.

[6] Petra Bosilj, Tom Duckett, and Grzegorz Cielniak. Connected attribute morphology for unified vegetation segmentation and classification in precision agriculture. *Computers in Industry*, 98:226–240, 2018.

[7] James Byrnes. *Unexploded ordinance detection and mitigation*. Springer Science & Business Media, 2008.

[8] Toby N Carlson and David A Ripley. On the relation between ndvi, fractional vegetation cover, and leaf area index. *Remote Sensing of Environment*, 62(3):241–252, 1997.

[9] Sukumar Chakraborty and Adrian C Newton. Climate change, plant diseases and food security: an overview. *Plant Pathology*, 60(1):2–14, 2011.

[10] DJI. *ZENMUSE X7 User Manual*. DJI.

[11] DJI. MAVIC PRO SPECS, 2019.

[12] DJI. PHANTOM 3 PROFESSIONAL SPECS, 2019.

[13] DJI. ZENMUSE X7 Cinematic Vision Rising, 2019.

[14] DJI. Drone solutions for a new generation of work, 2020.

[15] DJI. Professional aerial & ground imaging, 2020.

[16] DJI. Zenmuse xt, 2020.

[17] DroneDeploy. The leading drone software that elevates your business, 2019.

[18] Jéan Du Plessis. *Maize production*. Department of Agriculture Pretoria, South Africa, 2003.

[19] Dudutech. Integrated pest management, 2019.

[20] Lester E Ehler. Integrated pest management (IPM): definition, historical development and implementation, and the other IPM. *Pest Management Science*, 62(9):787–789, 2006.

[21] Carlos Alphonso F Ezequiel, Matthew Cua, Nathaniel C Libatique, Gregory L Tangonan, Raphael Alampay, Rollyn T Labuguen, Chrisandro M Favila, Jaime Luis E Honrado, Vinni Canos, Charles Devaney, et al. UAV aerial imaging applications for post-disaster assessment, environmental management and infrastructure development. In *2014 International Conference on Unmanned Aircraft Systems (ICUAS)*, pages 274–283. IEEE, 2014.

[22] Olivier Faugeras. *Three-dimensional computer vision: a geometric viewpoint*. MIT press, 1993.

[23] Africa Ixmuca Flores-Anderson, Kelsey E Herndon, Rajesh Bahadur Thapa, and Emil Cherrington. The sar handbook: Comprehensive methodologies for forest monitoring and biomass estimation. 2019.

[24] Jonas Franke and Gunter Menz. Multi-temporal wheat disease detection by multi-spectral remote sensing. *Precision Agriculture*, 8(3):161–172, 2007.

[25] Ch Gée, Jérémie Bossu, Gawain Jones, and Frederic Truchetet. Crop/weed discrimination in perspective agronomic images. *Computers and Electronics in Agriculture*, 60(1):49–59, 2008.

[26] Caroline M Gevaert, Juha Suomalainen, Jing Tang, and Lammert Kooistra. Generation of spectral–temporal response surfaces by combining multispectral satellite and hyperspectral UAV imagery for precision agriculture applications. *IEEE Journal of Selected Topics in Applied Earth Observations and Remote Sensing*, 8(6):3140–3146, 2015.

[27] Debabrata Ghosh and Naima Kaabouch. A survey on image mosaicing techniques. *Journal of Visual Communication and Image Representation*, 34:1–11, 2016.

[28] Rafael C Gonzalez and Richard E Woods. *Digital Image Processing*. Pearson, 2018.

[29] José Miguel Guerrero, José Jaime Ruz, and Gonzalo Pajares. Crop rows and weeds detection in maize fields applying a computer vision system based on geometry. *Computers and Electronics in Agriculture*, 142:461–472, 2017.

[30] Marıa Guijarro, Gonzalo Pajares, Isabel Riomoros, PJ Herrera, XP Burgos-Artizzu, and Angela Ribeiro. Automatic segmentation of relevant textures in agricultural images. *Computers and Electronics in Agriculture*, 75(1):75–83, 2011.

[31] Suraj G Gupta, Mangesh M Ghonge, and PM Jawandhiya. Review of unmanned aircraft system (uas). *International Journal of Advanced Research in Computer Engineering & Technology (IJARCET)*, 2(4):1646–1658, 2013.

[32] T Hague, ND Tillett, and H Wheeler. Automated crop and weed monitoring in widely spaced cereals. *Precision Agriculture*, 7(1):21–32, 2006.

[33] Esmael Hamuda, Martin Glavin, and Edward Jones. A survey of image processing techniques for plant extraction and segmentation in the field. *Computers and Electronics in Agriculture*, 125:184–199, 2016.

[34] Ming Han, Huihui Zhang, Kendall C DeJonge, Louise H Comas, and Thomas J Trout. Estimating maize water stress by standard deviation of canopy temperature in thermal imagery. *Agricultural Water Management*, 177:400–409, 2016.

[35] John J Hanway. How a corn plant develops. 1966.

[36] William M Haynes. *CRC handbook of chemistry and physics*. CRC press, 2014.

[37] Stuart B. Hill. Cultural methods of pest, primarily insect, control, 1989.

[38] ISO Central Secretary. Optics and photonics – spectral bands. Standard ISO/IEC TC 20473:2007, International Organization for Standardization, Berlin, DE, 2007.

[39] Ramia Jannoura, Katja Brinkmann, Daniel Uteau, Christian Bruns, and Rainer Georg Joergensen. Monitoring of crop biomass using true colour aerial photographs taken from a remote controlled hexacopter. *Biosystems Engineering*, 129:341–351, 2015.

[40] HG Jones and P Schofield. Thermal and other remote sensing of plant stress. *General and Applied Plant Physiology*, 34(1-2):19–32, 2008.

[41] Takashi Kataoka, Toshihiro Kaneko, Hiroshi Okamoto, and S Hata. Crop growth estimation system using machine vision. In *Proceedings 2003 IEEE/ASME International Conference on Advanced Intelligent Mechatronics (AIM 2003)*, volume 2, pages b1079–b1083. IEEE, 2003.

[42] Anne Katrin Mahlein. Plant disease detection by imaging sensors–parallels and specific demands for precision agriculture and plant phenotyping. *Plant Disease*, 100(2):241–251, 2016.

[43] Alessandro Matese, Piero Toscano, Salvatore Filippo Di Gennaro, Lorenzo Genesio, Francesco Primo Vaccari, Jacopo Primicerio, Claudio Belli, Alessandro Zaldei, Roberto Bianconi, and Beniamino Gioli. Intercomparison of uav, aircraft and

satellite remote sensing platforms for precision viticulture. *Remote Sensing*, 7(3):2971–2990, 2015.

[44] MathWorks. Classify patterns with a shallow neural network, 2021.

[45] M Meissle, P Mouron, T Musa, F Bigler, X Pons, VP Vasileiadis, S Otto, Daniele Antichi, J Kiss, Z Pálinkás, et al. Pests, pesticide use and alternative options in european maize production: current status and future prospects. *Journal of Applied Entomology*, 134(5):357–375, 2010.

[46] George E Meyer, Timothy W Hindman, and Koppolu Laksmi. Machine vision detection parameters for plant species identification. In *Precision Agriculture and Biological Quality*, volume 3543, pages 327–335. International Society for Optics and Photonics, 1999.

[47] Forrest W Nutter Jr, Paul S Teng, and Matthew H Royer. Terms and concepts for yield, crop loss, and disease thresholds. *Plant Disease*, 77:211, 1993.

[48] EC Oerke. Crop losses to pests. *The Journal of Agricultural Science*, 144(1):31–43, 2006.

[49] University of California. What is integrated pest management (IPM)?, 2018.

[50] Isabelle Philipp and Thomas Rath. Improving plant discrimination in image processing by use of different colour space transformations. *Computers and Electronics in Agriculture*, 35(1):1–15, 2002.

[51] Jiaguo Qi, Abdelghani Chehbouni, Alfredo R Huete, Yann H Kerr, and Soroosh Sorooshian. A modified soil adjusted vegetation index. *Remote Sensing of Environment*, 48(2):119–126, 1994.

[52] Catur Aries Rokhmana. The potential of UAV-based remote sensing for supporting precision agriculture in indonesia. *Procedia Environmental Sciences*, 24:245–253, 2015.

[53] JW Rouse, RH Haas, JA Schell, and DW Deering. Monitoring vegetation systems in the great plains with erts proceeding. In *Third Earth Reserves Technology Satellite Symposium, Greenbelt: NASA SP-351*, volume 30103017, 1974.

[54] SACAA. About us, 2017.

[55] SAMAA. The South African Model Aircraft Association, 2020.

[56] Götz Schroth, Ulrike Krauss, Luadir Gasparotto, JA Duarte Aguilar, and Katrin Vohland. Pests and diseases in agroforestry systems of the humid tropics. *Agroforestry Systems*, 50(3):199–241, 2000.

[57] Richard Szeliski. Image mosaicing for tele-reality applications. In *Proceedings of 1994 IEEE Workshop on Applications of Computer Vision*, pages 44–53. IEEE, 1994.

[58] Richard Szeliski and Sing Bing Kang. Direct methods for visual scene reconstruction. In *Proceedings IEEE Workshop on Representation of Visual Scenes (In Conjunction with ICCV'95)*, pages 26–33. IEEE, 1995.

[59] Freek D Van der Meer, Harald MA Van der Werff, Frank JA Van Ruitenbeek, Chris A Hecker, Wim H Bakker, Marleen F Noomen, Mark Van Der Meijde, E John M Carranza, J Boudewijn De Smeth, and Tsehaie Woldai. Multi-and hyperspectral geologic remote sensing: A review. *International Journal of Applied Earth Observation and Geoinformation*, 14(1):112–128, 2012.

[60] Jonathan S West, Cedric Bravo, Roberto Oberti, Dimitrios Moshou, Herman Ramon, and H Alastair McCartney. Detection of fungal diseases optically and pathogen inoculum by air sampling. In *Precision crop protection-the challenge and use of heterogeneity*, pages 135–149. Springer, 2010.

[61] D Woebbecke, A Al-Faraj, and GE Meyer. Calibration of large field-of-view thermal and optical sensors for plant and soil measurements. *Transactions of the ASAE*, 37(2):669–677, 1994.

[62] Stephen L Young and Francis J Pierce. *Automation: The Future of Weed Control in Cropping Systems*. Springer, 2013.

[63] Chunhua Zhang and John M Kovacs. The application of small unmanned aerial systems for precision agriculture: a review. *Precision agriculture*, 13(6):693–712, 2012.

[64] Imad Zoghlami, Olivier Faugeras, and Rachid Deriche. Using geometric corners to build a 2d mosaic from a set of images. In *Proceedings of IEEE Computer Society Conference on Computer Vision and Pattern Recognition*, pages 420–425. IEEE, 1997.

Appendix A: Telemetry data extract

Date/Time (UTC)	Aircraft Latitude (Degrees)	Aircraft Longitude (Degrees)	Aircraft Barometric Altitude (ft)	Aircraft GPS Signal	Gimbal Pitch (Degrees)	Gimbal Roll (Degrees)	Gimbal Yaw (Degrees)	Aircraft Camera Single Capture	Aircraft Camera Storing Photo
06/01/2019 11:52:00	-27.801612738666865	26.265180390953734	151.246724	Very Strong	-90	0	-166.8	0	0
06/01/2019 11:52:00	-27.801612564622001	26.265182090128299	151.574808	Very Strong	-90	0	-166.8	1	1

TABLE A.1: Extract of telemetry data recorded using DroneDeploy

Appendix B: EXIF data example

ExifTool Version Number	: 11.59
File Name	: DJI_0017.JPG
Directory	: .
File Size	: 8.9 MB
File Modification Date/Time	: 2019:10:09 13:11:12+02:00
File Access Date/Time	: 2019:10:09 13:36:44+02:00
File Inode Change Date/Time	: 2019:10:09 13:11:12+02:00
File Permissions	: rwxr-xr-x
File Type	: JPEG
File Type Extension	: jpg
MIME Type	: image/jpeg
Exif Byte Order	: Little-endian (Intel, II)
Image Description	: DCIM\100MEDIA\DJI_0017.JPG
Camera Model Name	: FC6540
Orientation	: Horizontal (normal)
X Resolution	: 72
Y Resolution	: 72
Resolution Unit	: inches
Software	: v01.09.2222
Modify Date	: 2019:06:01 16:23:38
Y Cb Cr Positioning	: Centered
Exposure Time	: 1/40
F Number	: 5.6
Exposure Program	: Program AE
ISO	: 100
Exif Version	: 0230
Date/Time Original	: 2019:06:01 16:23:37

Create Date	: 2019:06:01 16:23:37
Components Configuration	: -, Cr, Cb, Y
Compressed Bits Per Pixel	: 3.505833814
Shutter Speed Value	: 1/60
Aperture Value	: 5.6
Exposure Compensation	: 0
Max Aperture Value	: 2.8
Subject Distance	: 0 m
Metering Mode	: Center-weighted average
Light Source	: Fluorescent
Flash	: No flash function
Focal Length	: 16.0 mm
Warning	: [minor] Possibly incorrect maker notes offsets (fix by 1783?)
Make	: DJI
Speed X	: -3.30
Speed Y	: +1.60
Speed Z	: +0.00
Pitch	: -4.70
Yaw	: +152.90
Roll	: -0.30
Camera Pitch	: -90.00
Camera Yaw	: +151.90
Camera Roll	: +0.00
Flashpix Version	: 0010
Color Space	: sRGB
Exif Image Width	: 5248
Exif Image Height	: 3936
Interoperability Index	: R98 - DCF basic file (sRGB)
Interoperability Version	: 0100
Exposure Index	: undef
File Source	: Digital Camera
Scene Type	: Directly photographed

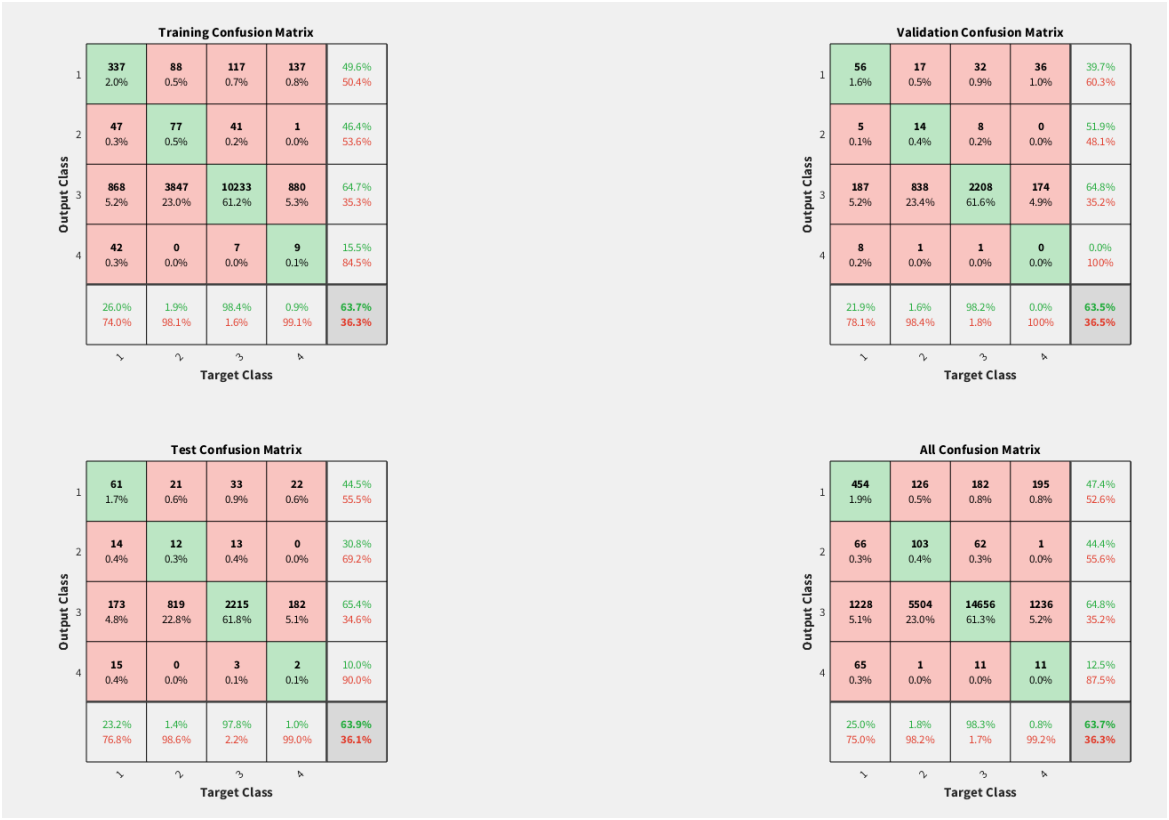
Custom Rendered	: Normal
Exposure Mode	: Auto
White Balance	: Auto
Digital Zoom Ratio	: undef
Focal Length In 35mm Format	: 24 mm
Scene Capture Type	: Standard
Gain Control	: None
Contrast	: Normal
Saturation	: Normal
Sharpness	: Hard
Subject Distance Range	: Unknown
Serial Number	: 20160411015b6c4c4d923352540ee744
Lens Make	: Panasonic
Lens Model	: DJI DL-S 16mm F2.8 ND ASPH
GPS Version ID	: 2.3.0.0
GPS Latitude Ref	: South
GPS Longitude Ref	: East
GPS Altitude Ref	: Above Sea Level
XP Comment	: Type=N, Mode=P, DE=None
XP Keywords	: v01.09.2222;0.0.1;v1.0.0
Compression	: JPEG (old-style)
Thumbnail Offset	: 10240
Thumbnail Length	: 11221
About	: DJI Meta Data
Format	: image/jpg
Absolute Altitude	: +1222.47
Relative Altitude	: +27.20
Gimbal Roll Degree	: +0.00
Gimbal Yaw Degree	: +151.90
Gimbal Pitch Degree	: -90.00
Flight Roll Degree	: -0.30
Flight Yaw Degree	: +152.90

Flight Pitch Degree	: -4.70
Cam Reverse	: 0
Gimbal Reverse	: 0
Self Data	: Undefined
Calibrated Focal Length	: 4092.071533
Calibrated Optical Center X	: 2624.000000
Calibrated Optical Center Y	: 1968.000000
Rtk Flag	: 0
Version	: 7.0
Has Settings	: False
Has Crop	: False
Already Applied	: False
MPF Version	: 0010
Number Of Images	: 2
MP Image Flags	: Dependent child image
MP Image Format	: JPEG
MP Image Type	: Large Thumbnail (VGA equivalent)
MP Image Length	: 270154
MP Image Start	: 9081916
Dependent Image 1 Entry Number	: 0
Dependent Image 2 Entry Number	: 0
Image UID List	: (Binary data 66 bytes, use -b option to extract)
Total Frames	: 1
Image Width	: 5248
Image Height	: 3936
Encoding Process	: Baseline DCT, Huffman coding
Bits Per Sample	: 8
Color Components	: 3
Y Cb Cr Sub Sampling	: YCbCr4:2:2 (2 1)
Aperture	: 5.6
Image Size	: 5248x3936
Megapixels	: 20.7

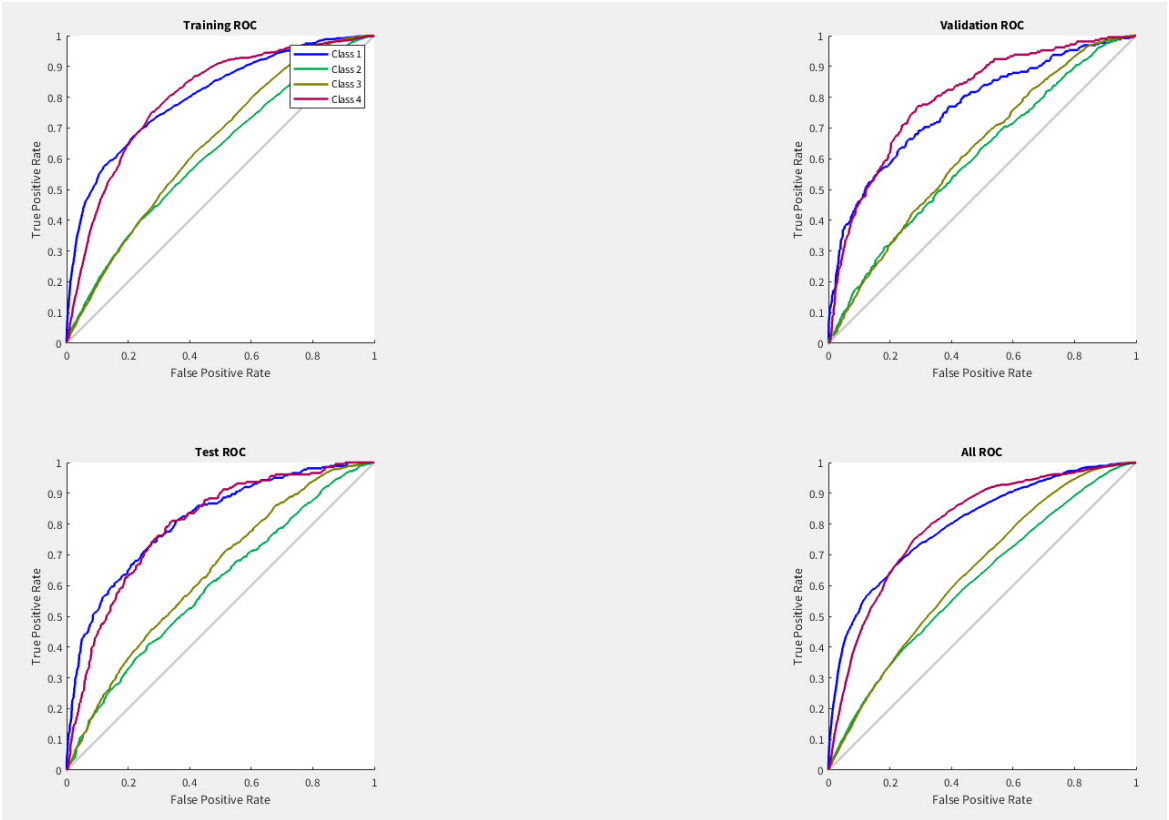
Scale Factor To 35 mm Equivalent	: 1.5
Shutter Speed	: 1/40
Thumbnail Image	: (Binary data 11221 bytes, use -b option to extract)
GPS Altitude	: 1222.4 m Above Sea Level
GPS Latitude	: 27.800266583333332 Degrees S
GPS Longitude	: 26.265022166666668 Degrees E
Preview Image	: (Binary data 270154 bytes, use -b option to extract)
Circle Of Confusion	: 0.020 mm
Field Of View	: 73.7 deg
Focal Length	: 16.0 mm (35 mm equivalent: 24.0 mm)
GPS Position	: 27.800266583333332 Degrees S, 26.265022166666668 Degrees E
Hyperfocal Distance	: 2.28 m
Light Value	: 10.3

Appendix C: Additional results

C.1 DroneDeploy classification results

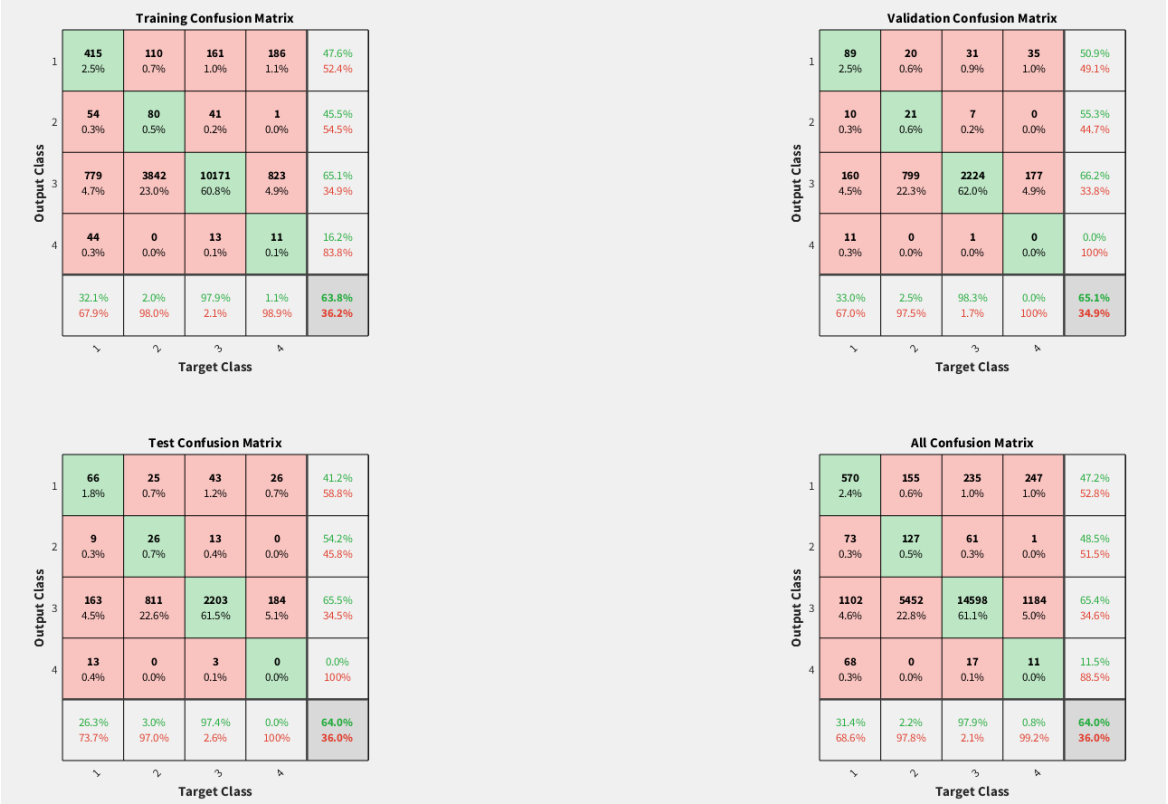


(A) Confusion matrix.

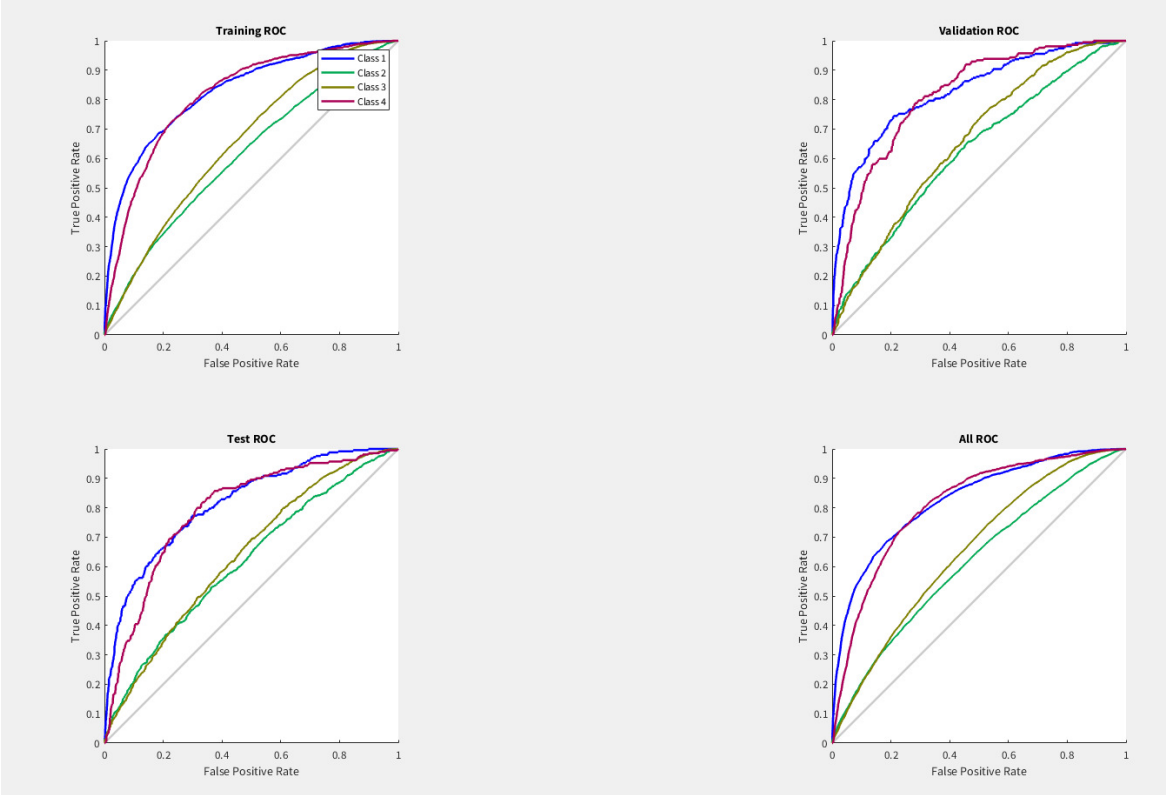


(B) ROC.

FIGURE C.1: Classification results of using a window size of 15x15 pixels, having the first 9 summations of the computed Fourier coefficients of the green component in the feature vector

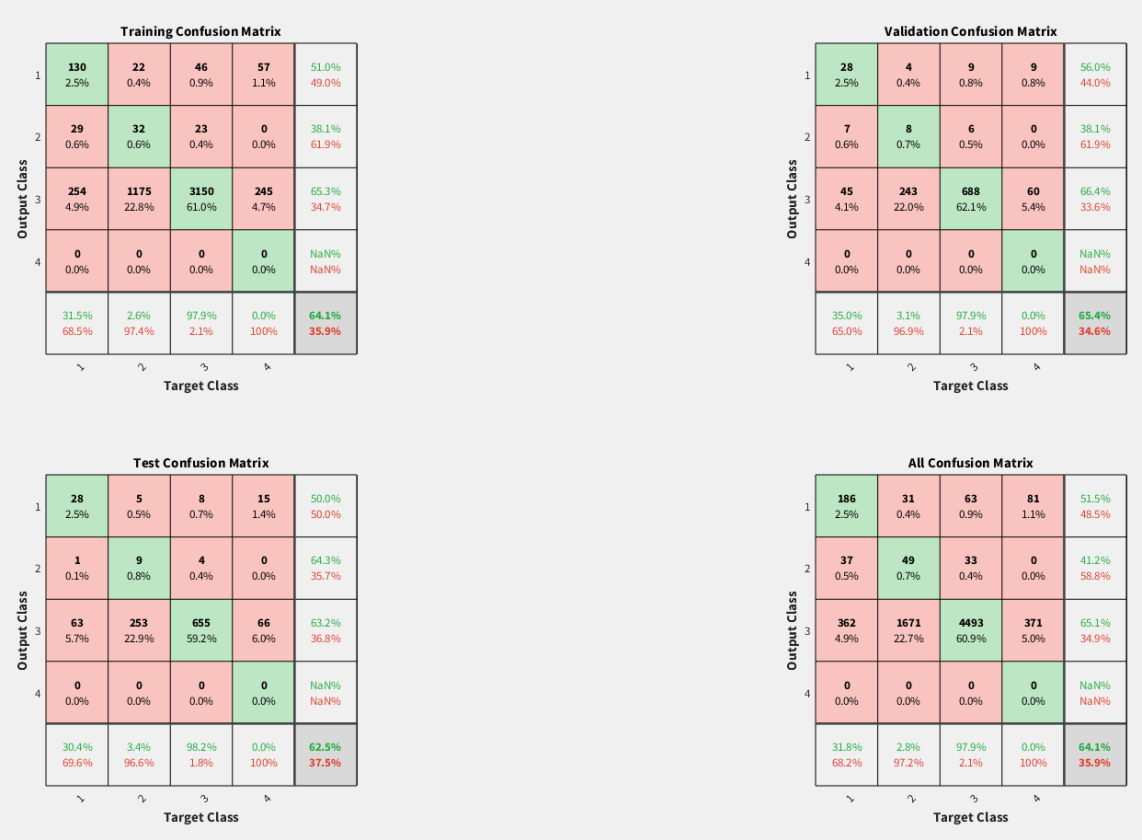


(A) Confusion matrix.

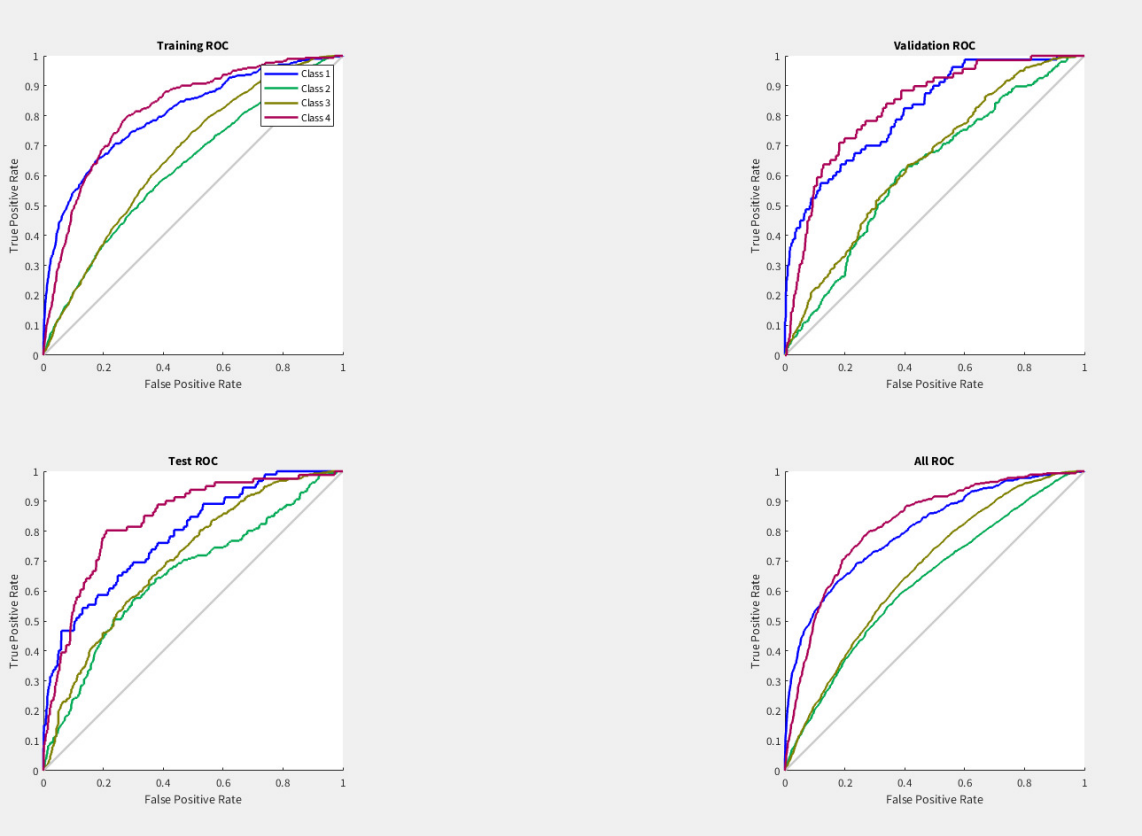


(B) ROC.

FIGURE C.2: Classification results of using a window size of 15x15 pixels, having the first 19 summations of the computed Fourier coefficients of the green component in the feature vector

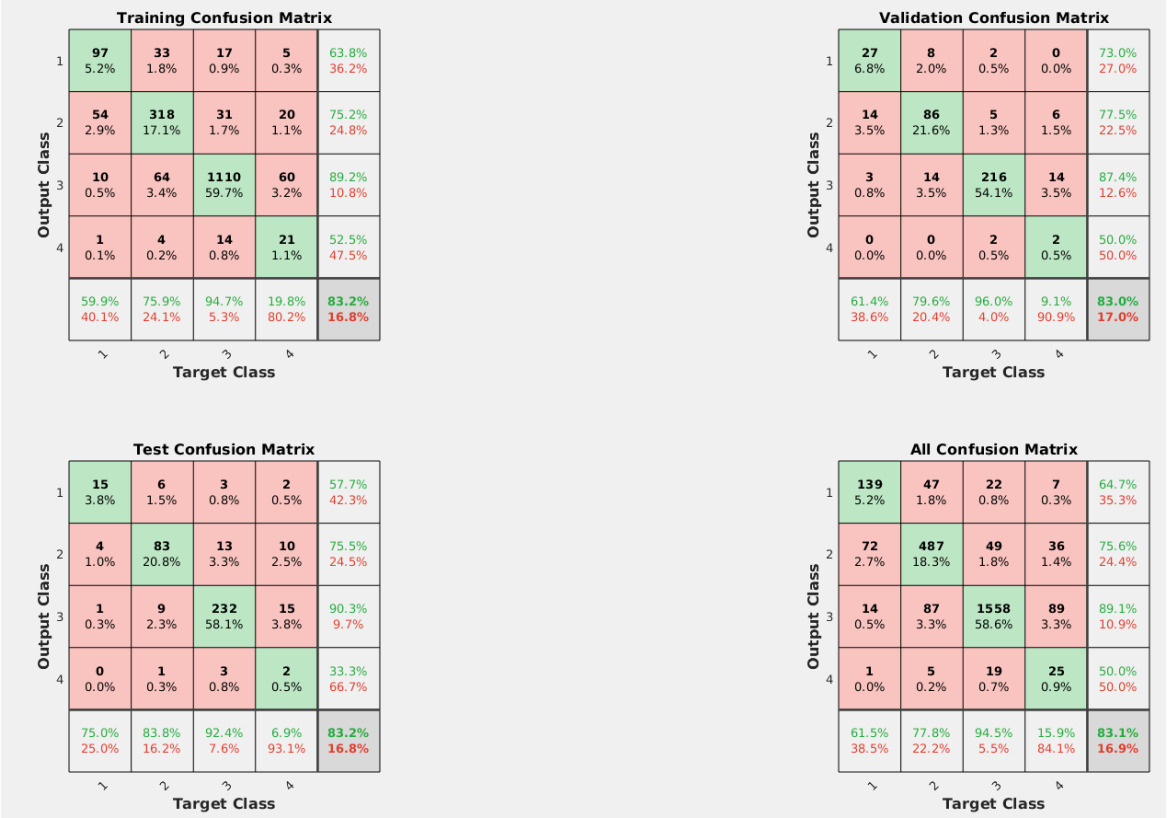


(A) Confusion matrix.

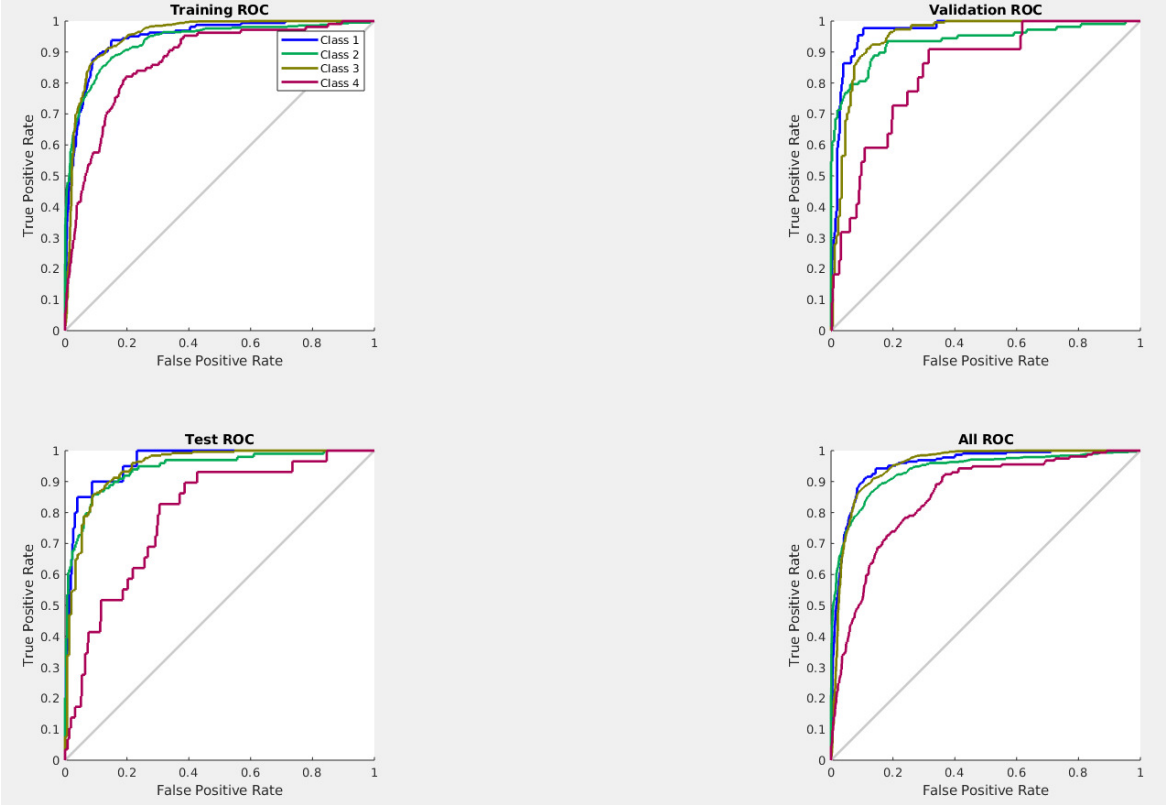


(B) ROC.

FIGURE C.3: Classification results of using a window size of 27x27 pixels, having the first 9 summations of the computed Fourier coefficients of the green component in the feature vector

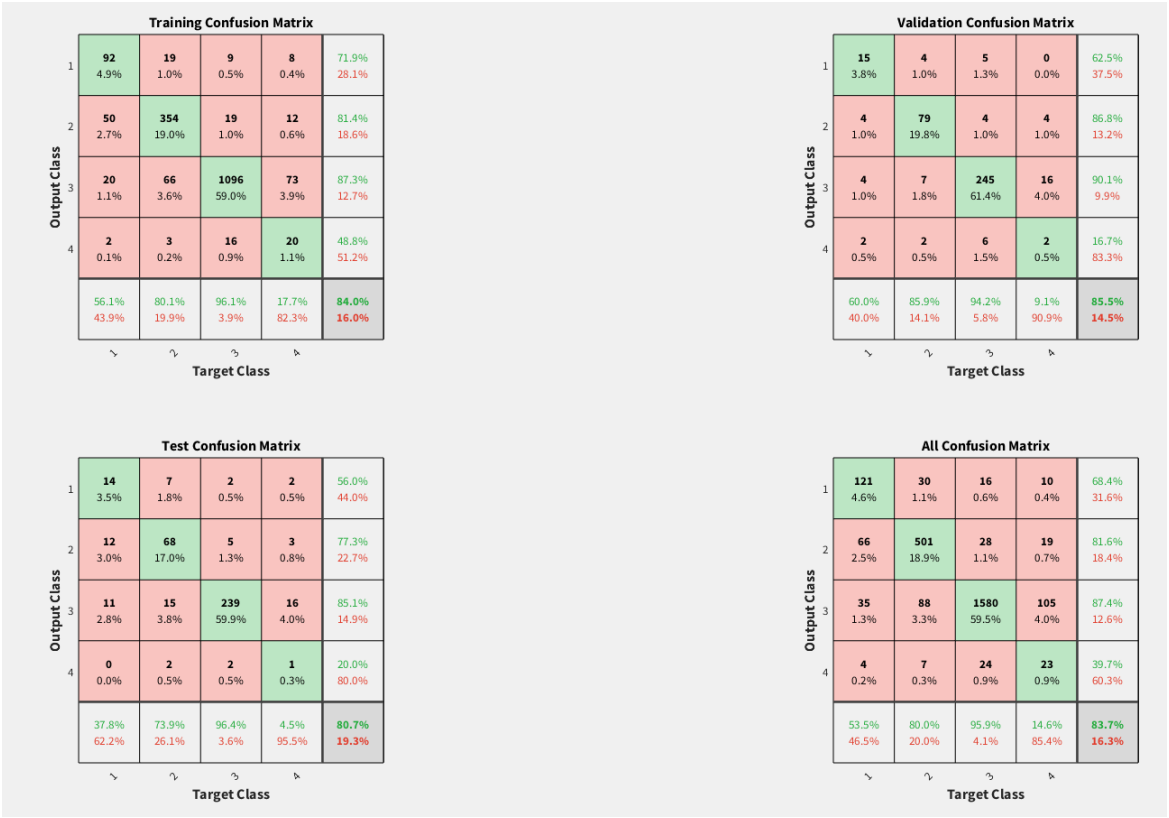


(A) Confusion matrix.

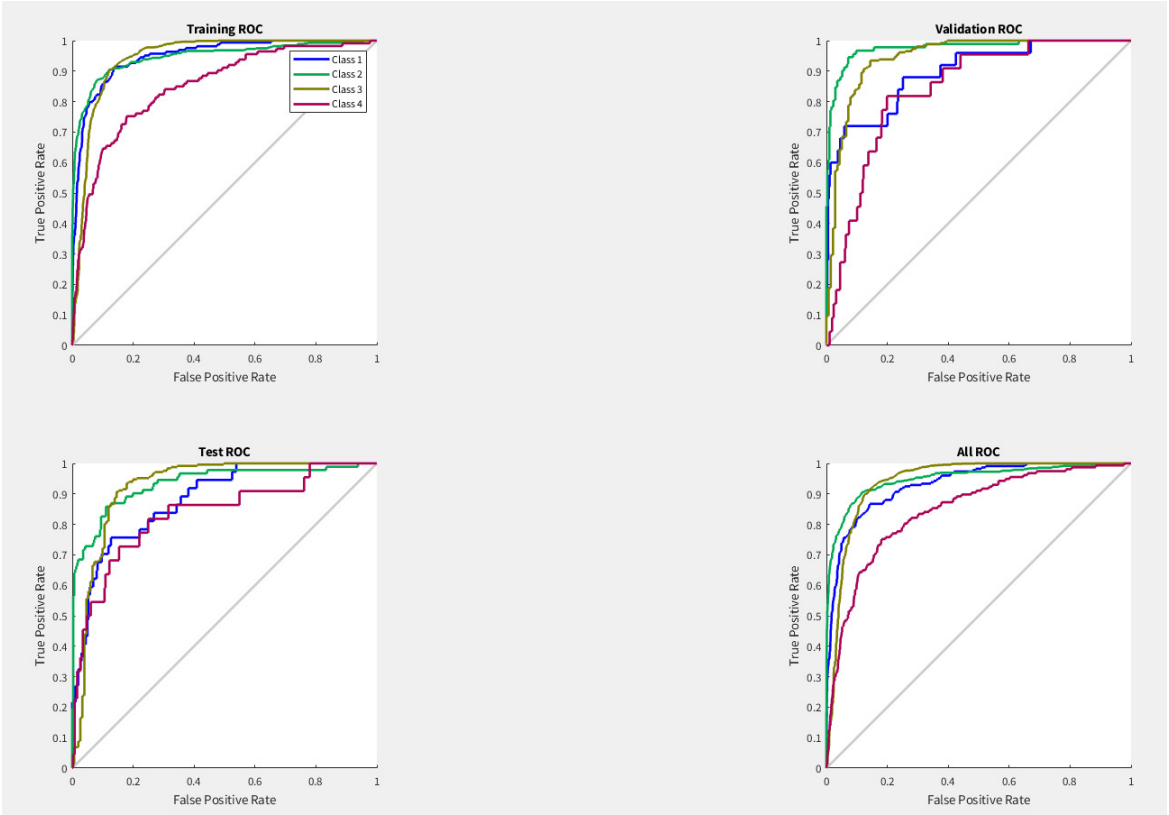


(B) ROC.

FIGURE C.4: Classification results of using a window size of 45x45 pixels, having the first 3 summations of the computed Fourier coefficients of the hue, saturation, value, red, green and blue components in the feature vector

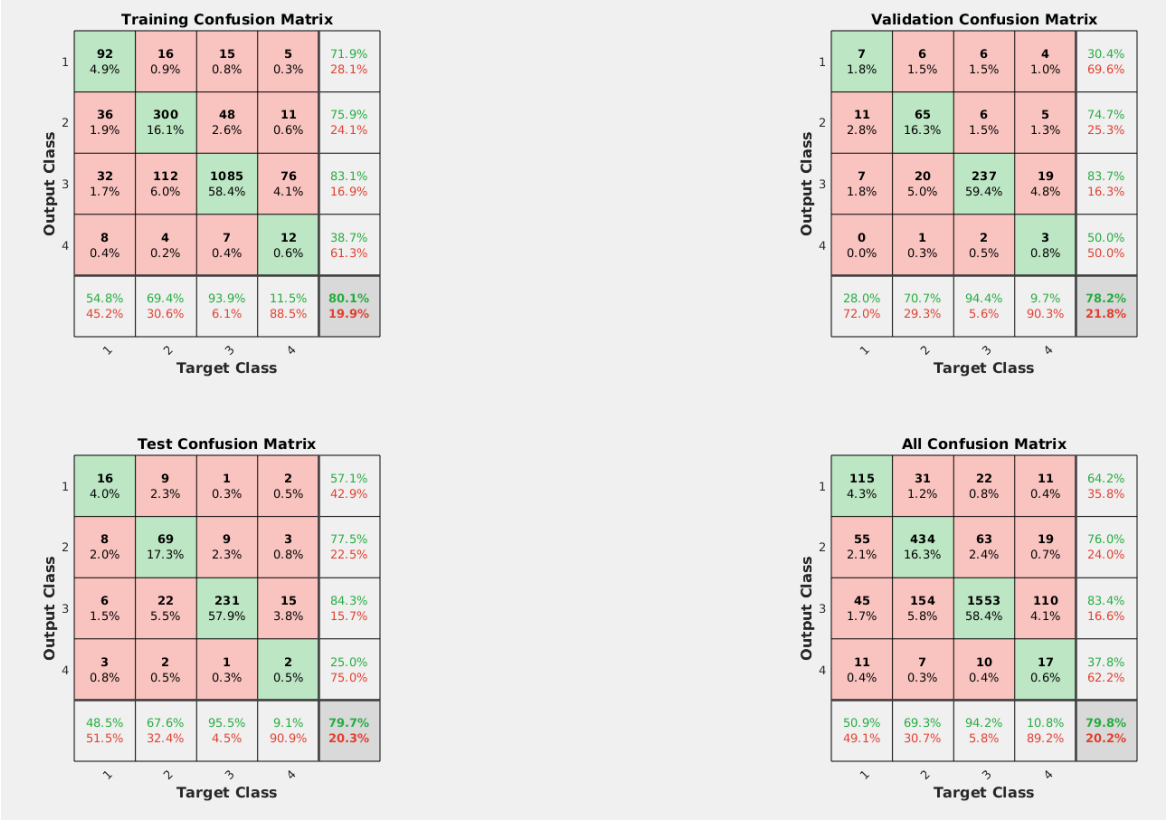


(A) Confusion matrix.

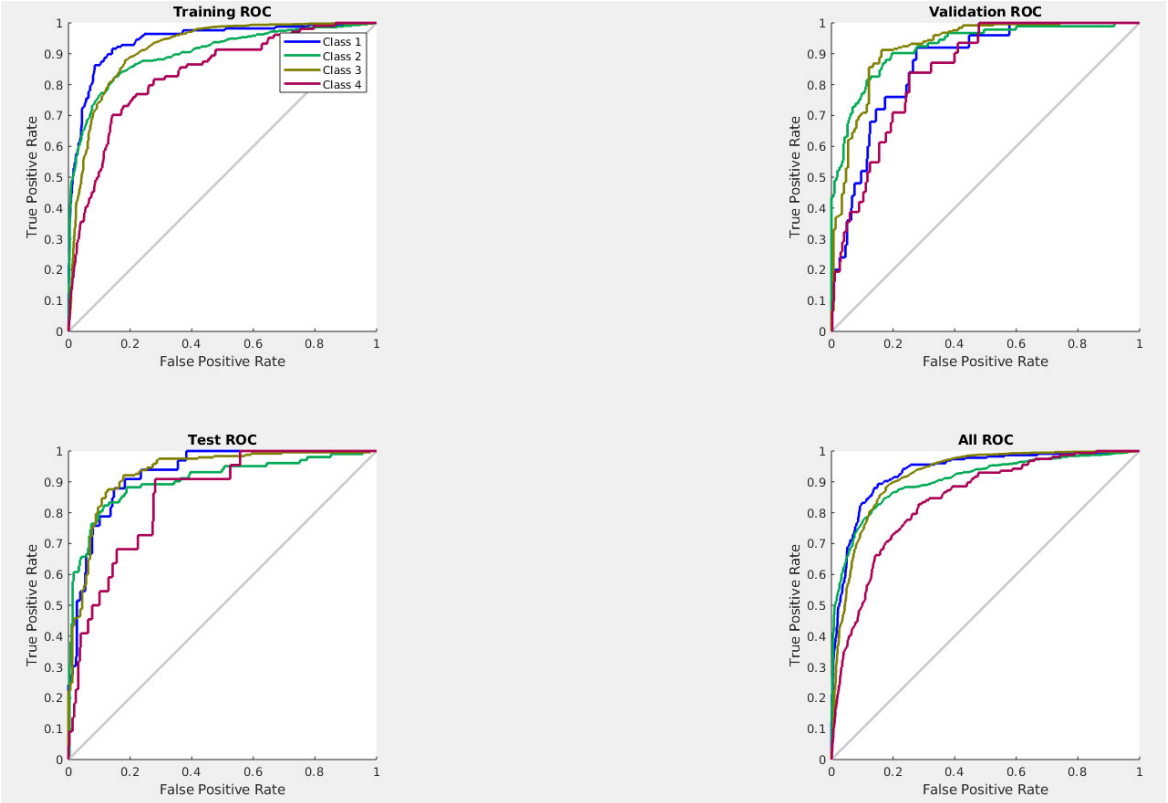


(B) ROC.

FIGURE C.5: Classification results of using a window size of 45x45 pixels, having the first 4 summations of the computed Fourier coefficients of the green and blue components, and the ExR index in the feature vector

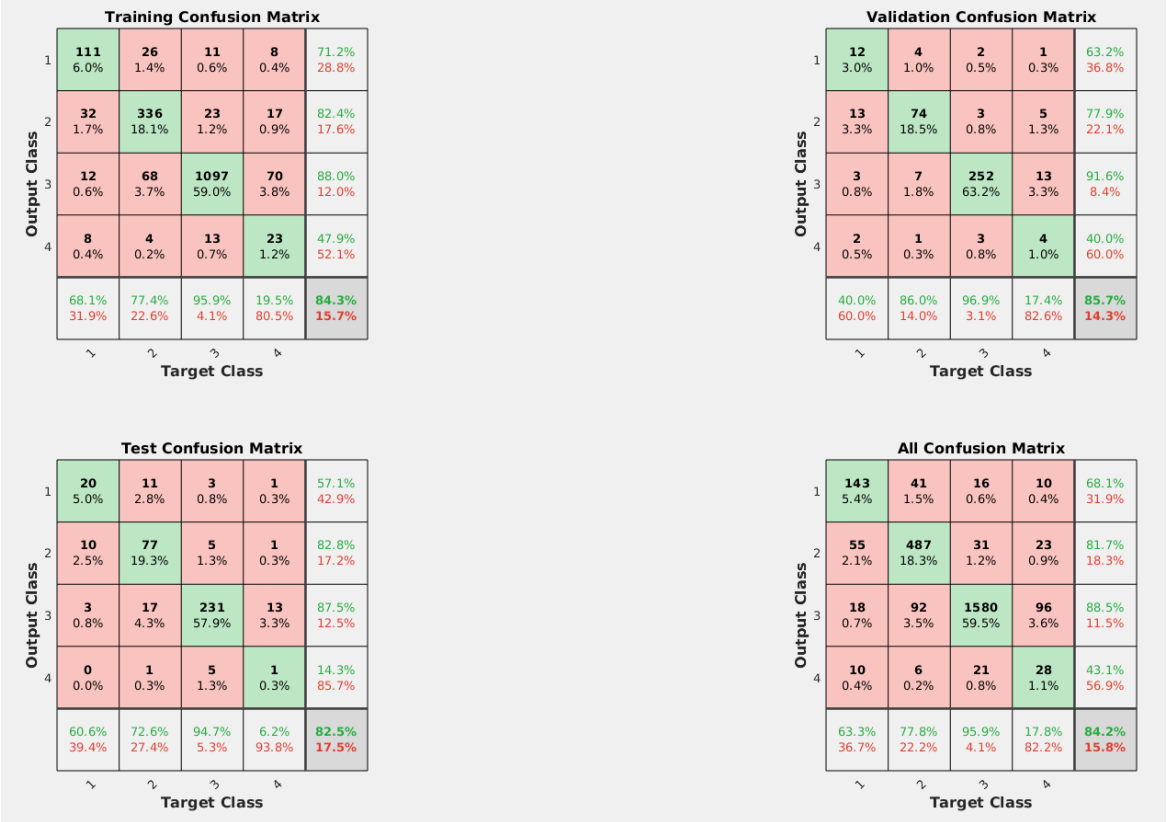


(A) Confusion matrix.

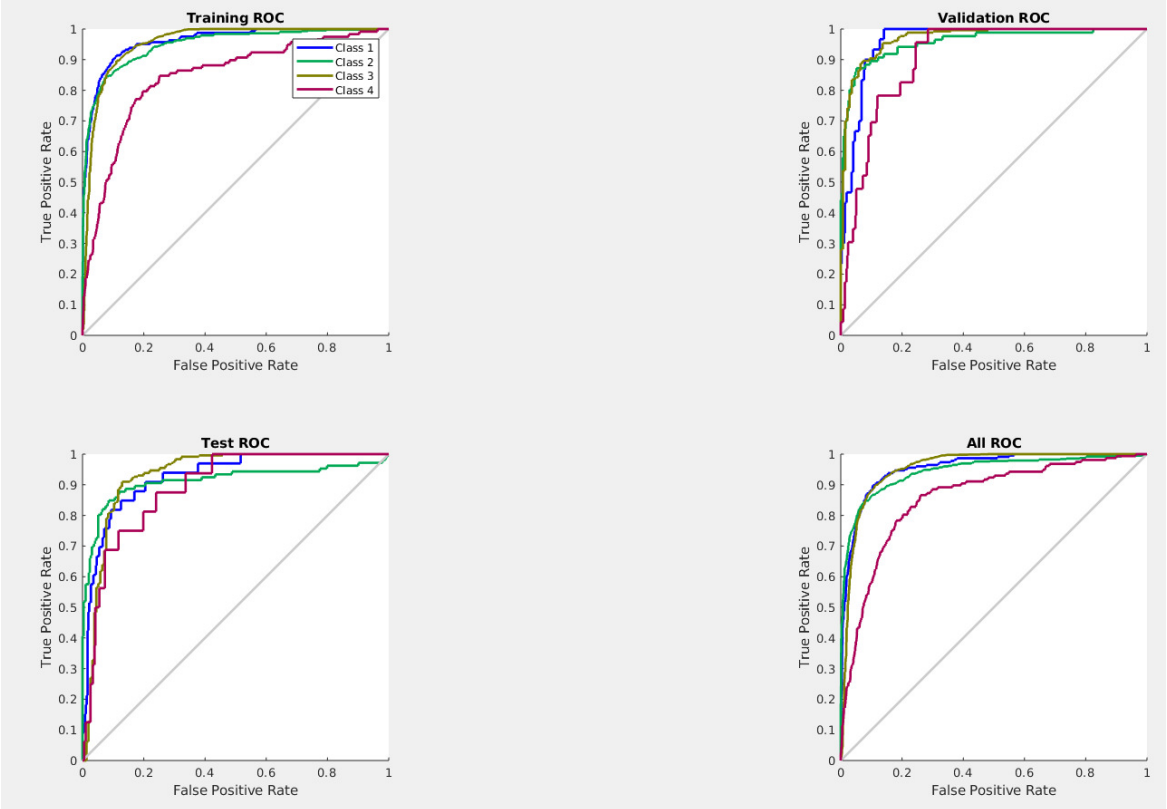


(B) ROC.

FIGURE C.6: Classification results of using a window size of 45x45 pixels, having the first 4 summations of the computed Fourier coefficients of the hue, saturation and value components in the feature vector

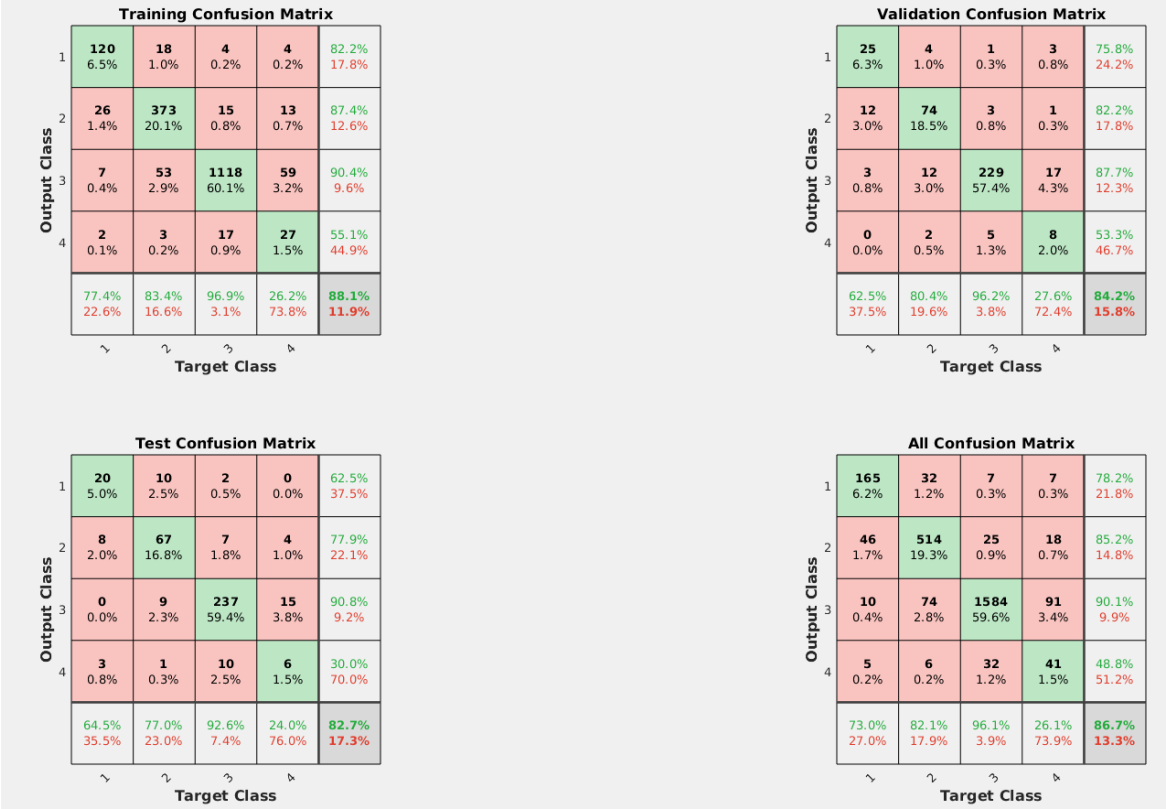


(A) Confusion matrix.

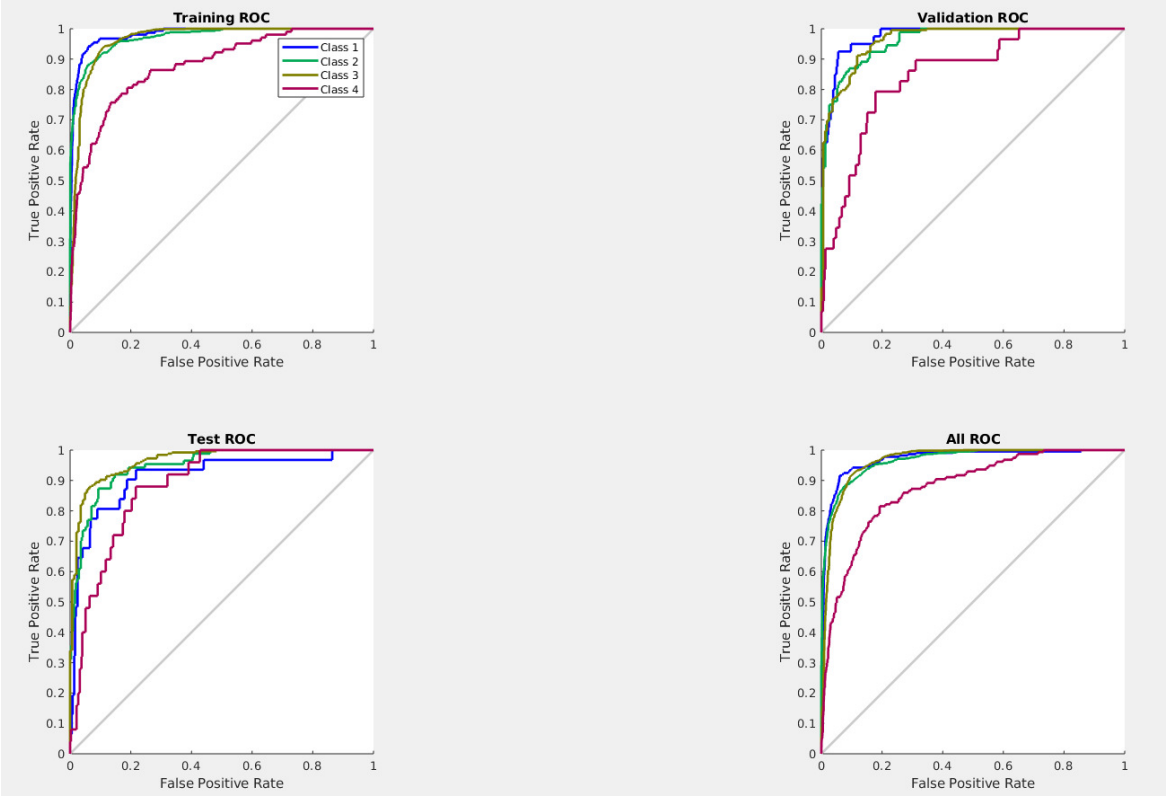


(B) ROC.

FIGURE C.7: Classification results of using a window size of 45x45 pixels, having the first 4 summations of the computed Fourier coefficients of the hue, saturation, value, red, green and blue components in the feature vector

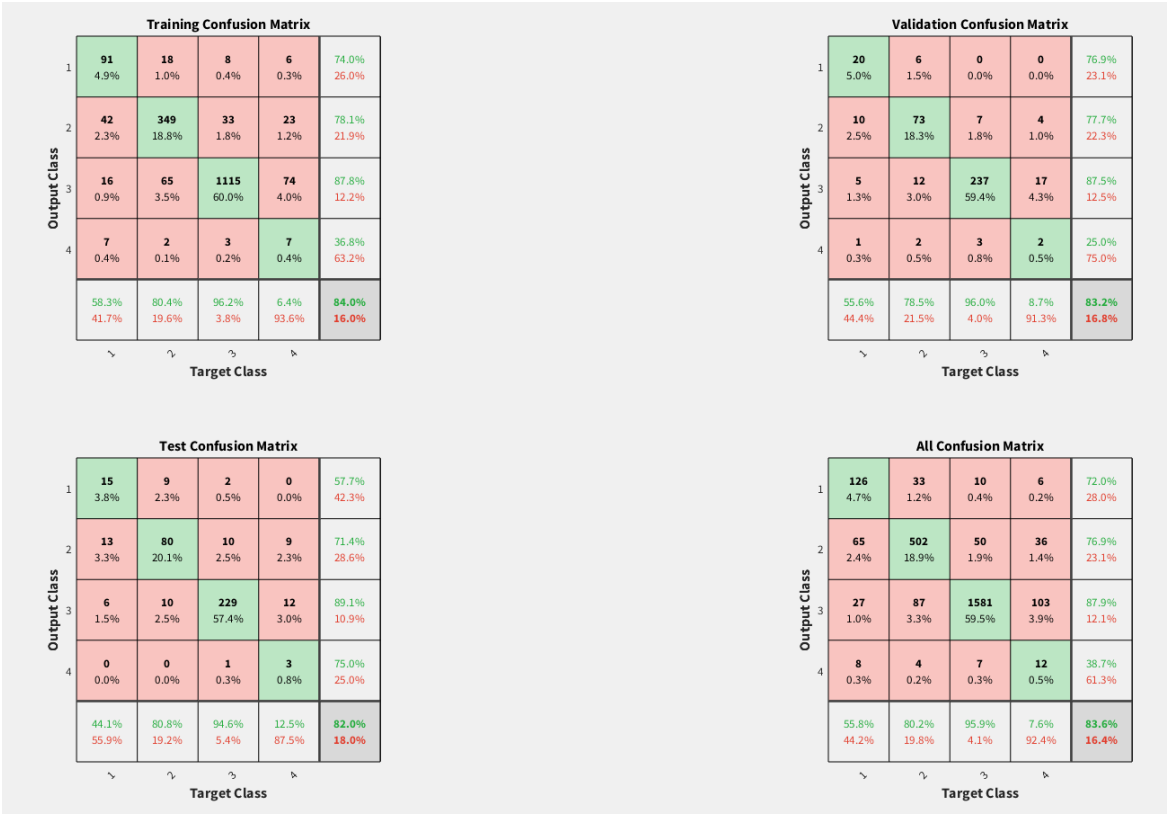


(A) Confusion matrix.

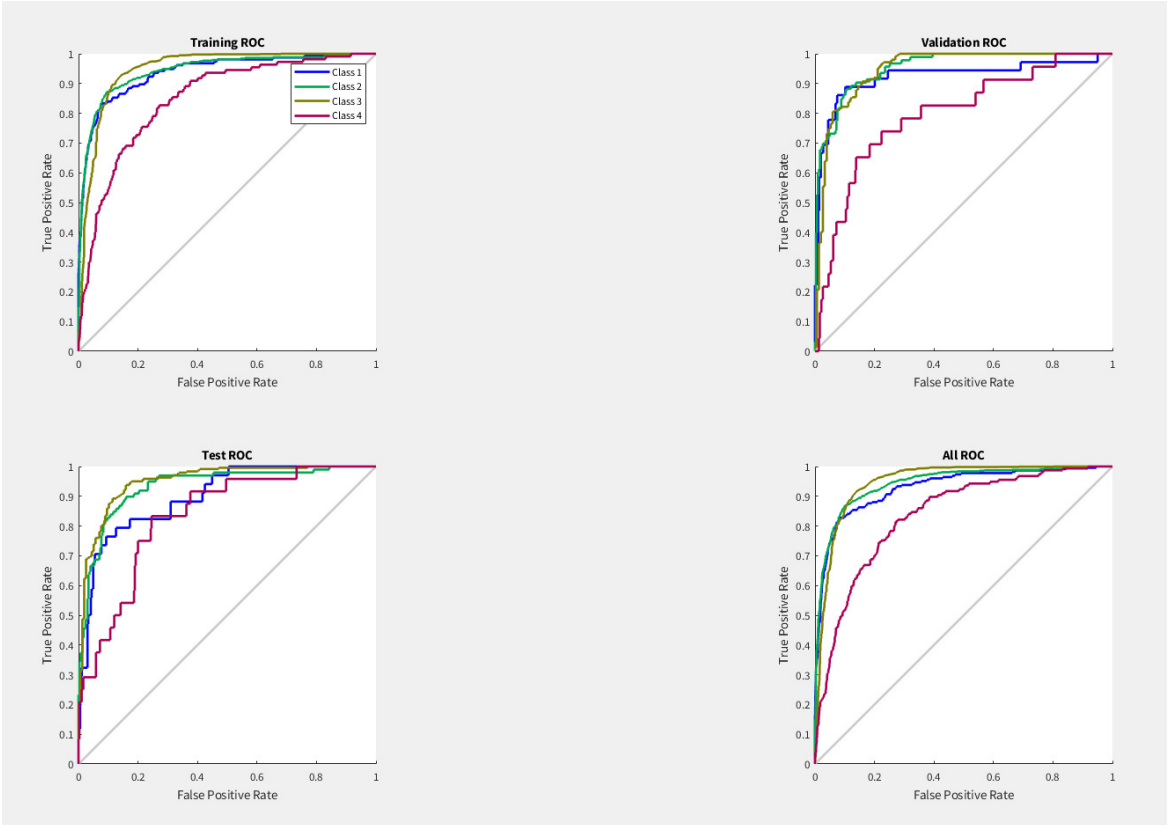


(B) ROC.

FIGURE C.8: Classification results of using a window size of 45x45 pixels, having the first 4 summations of the computed Fourier coefficients of the hue, saturation, value, red, green and blue components, and the ExR index in the feature vector

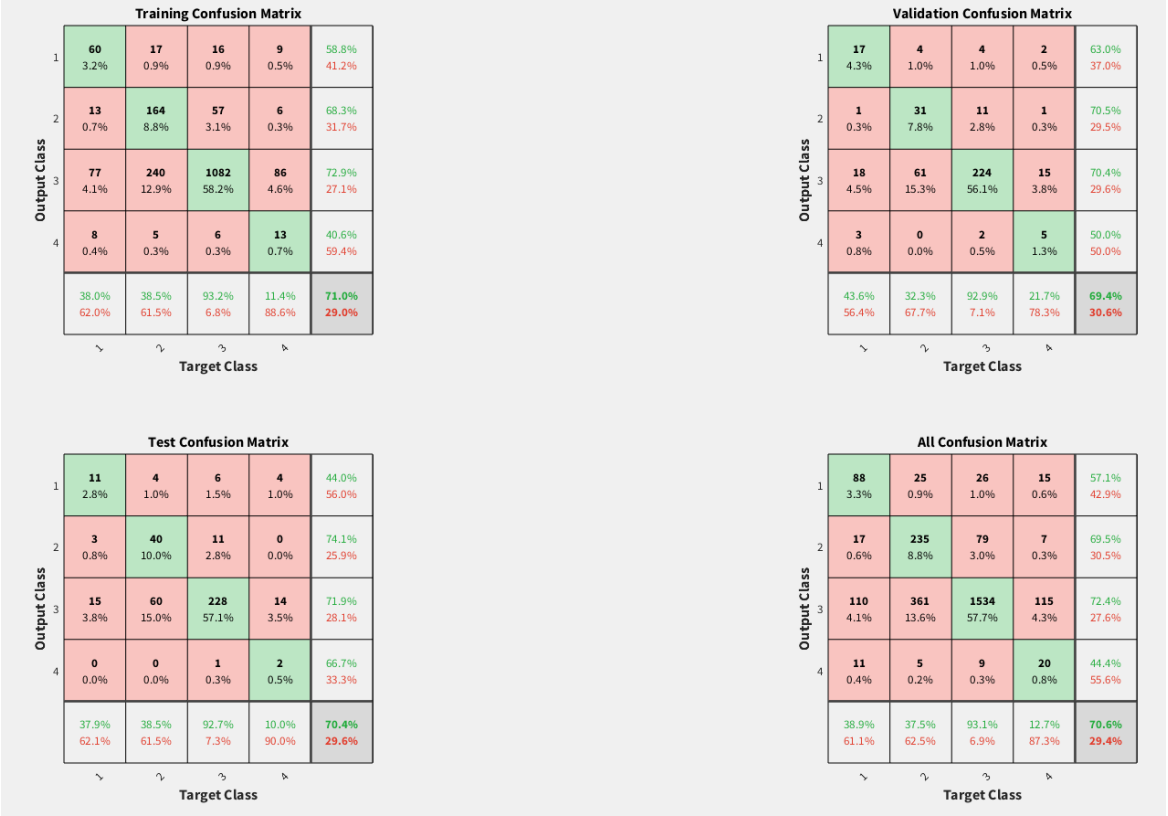


(A) Confusion matrix.

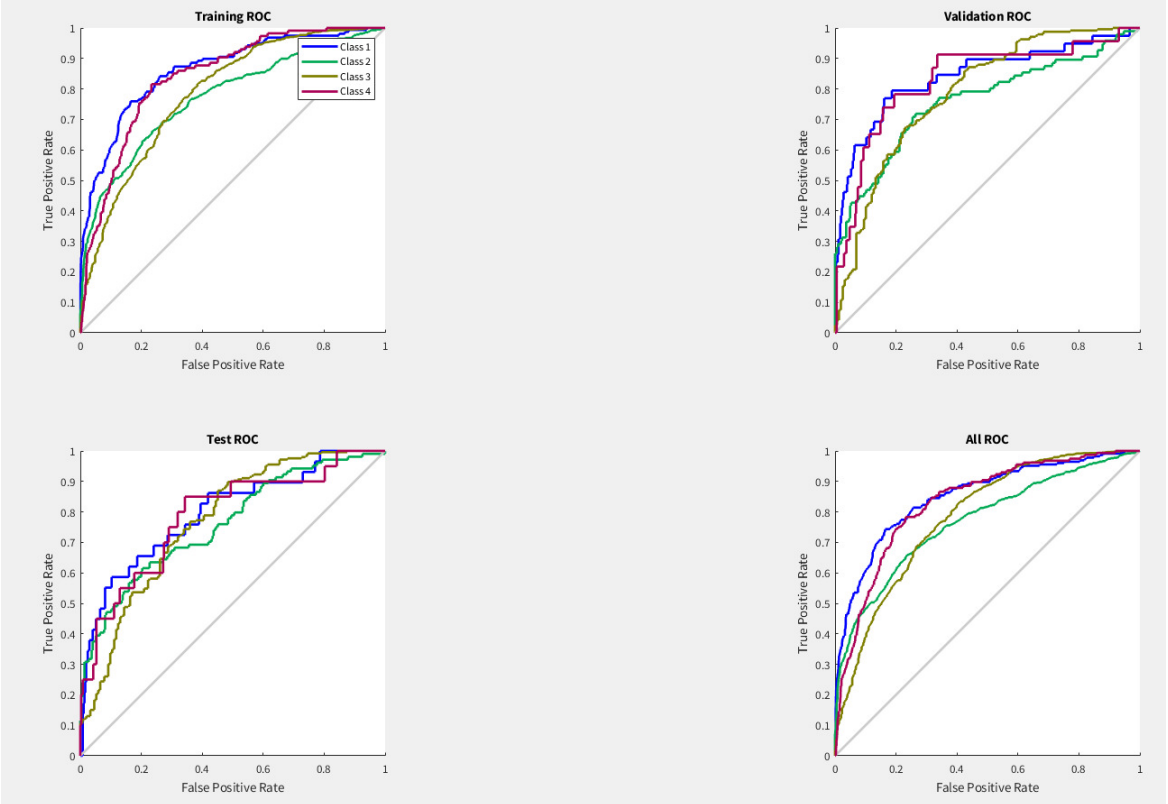


(B) ROC.

FIGURE C.9: Classification results of using a window size of 45x45 pixels, having the first 4 summations of the computed Fourier coefficients of the red, green and blue components in the feature vector

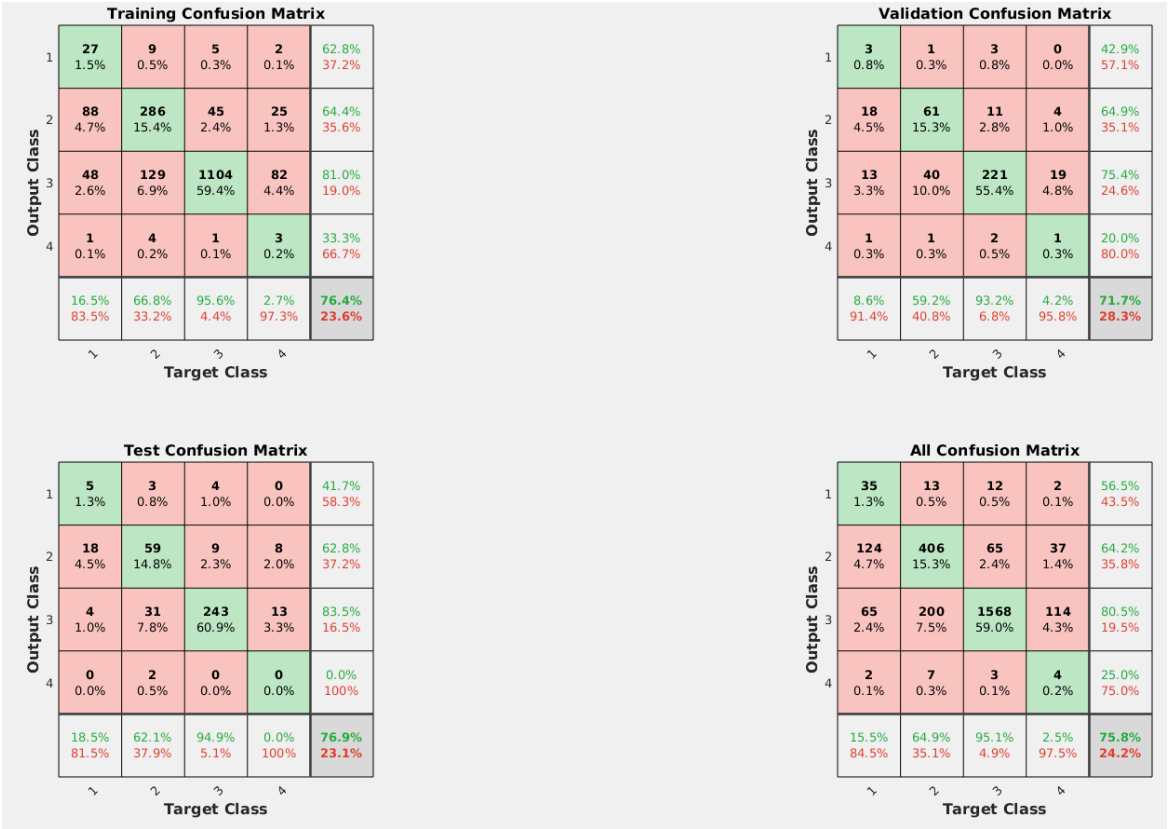


(A) Confusion matrix.

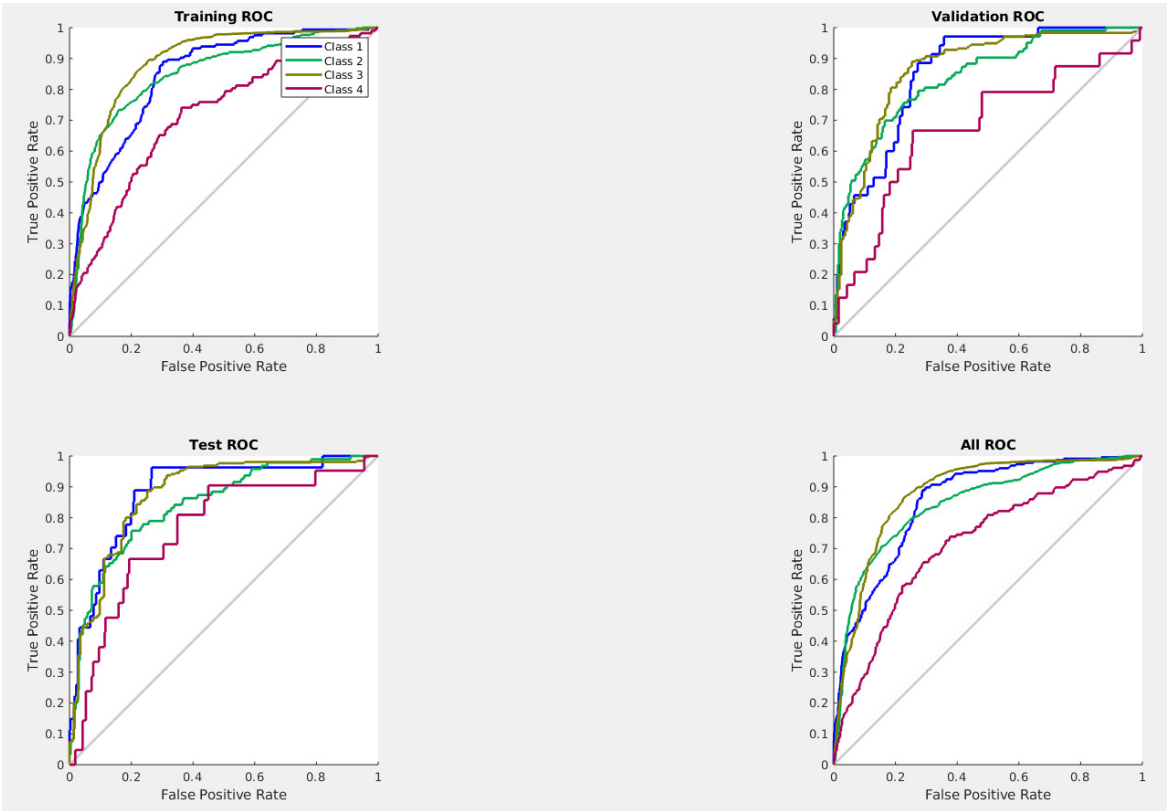


(B) ROC.

FIGURE C.10: Classification results of using a window size of 45x45 pixels, having the first 9 summations of the computed Fourier coefficients of the blue component in the feature vector

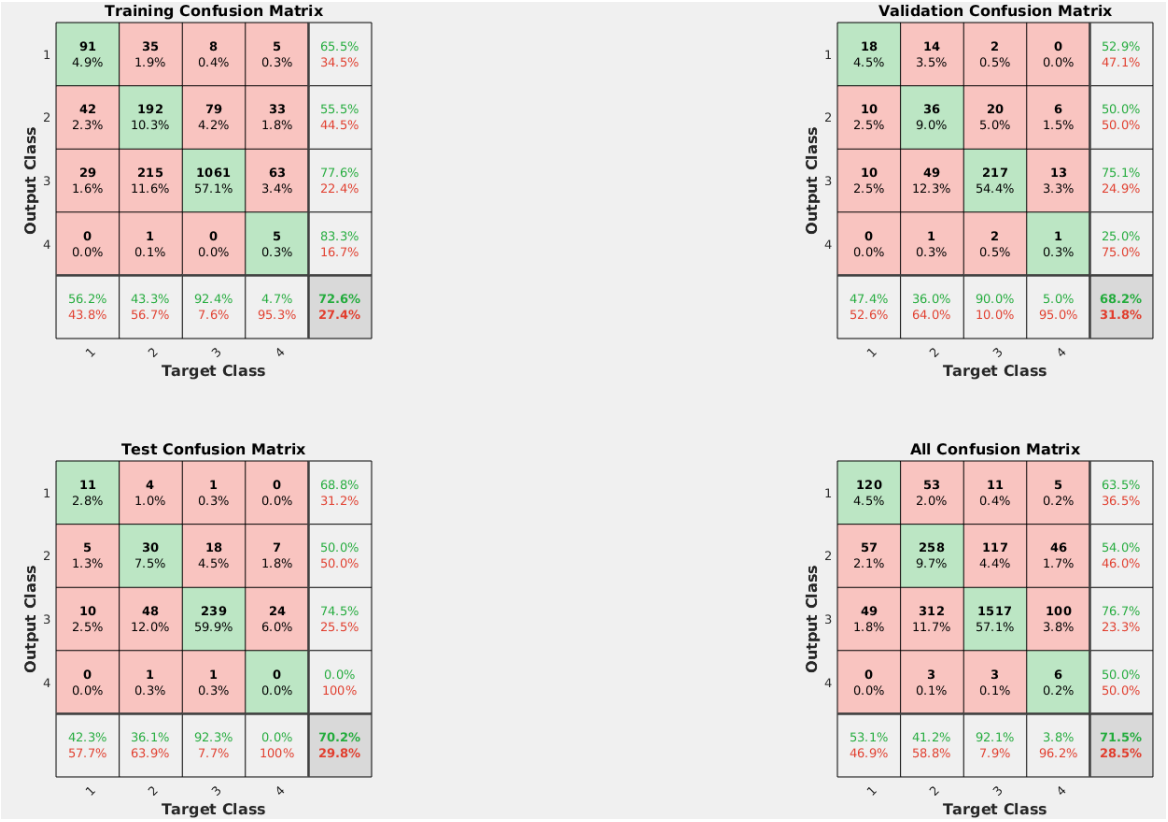


(A) Confusion matrix.

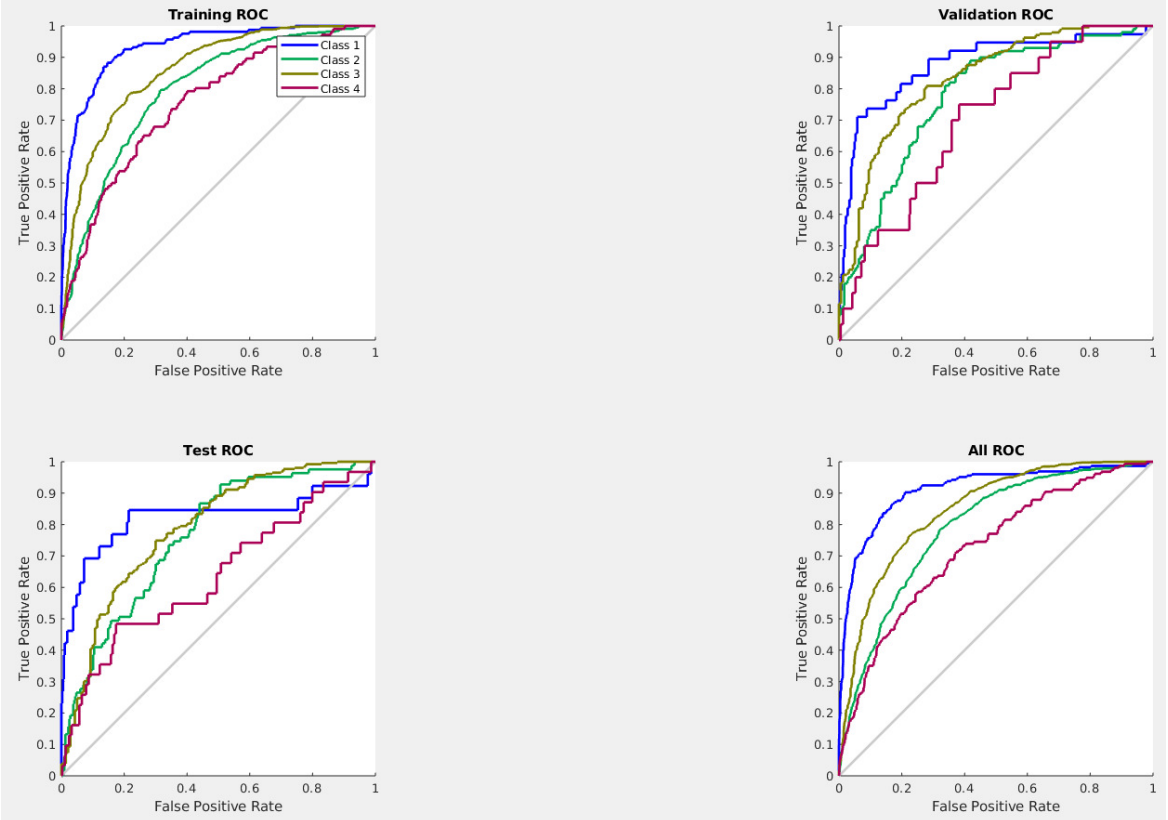


(B) ROC.

FIGURE C.11: Classification results of using a window size of 45x45 pixels, having the first 9 summations of the computed Fourier coefficients of the hue component in the feature vector

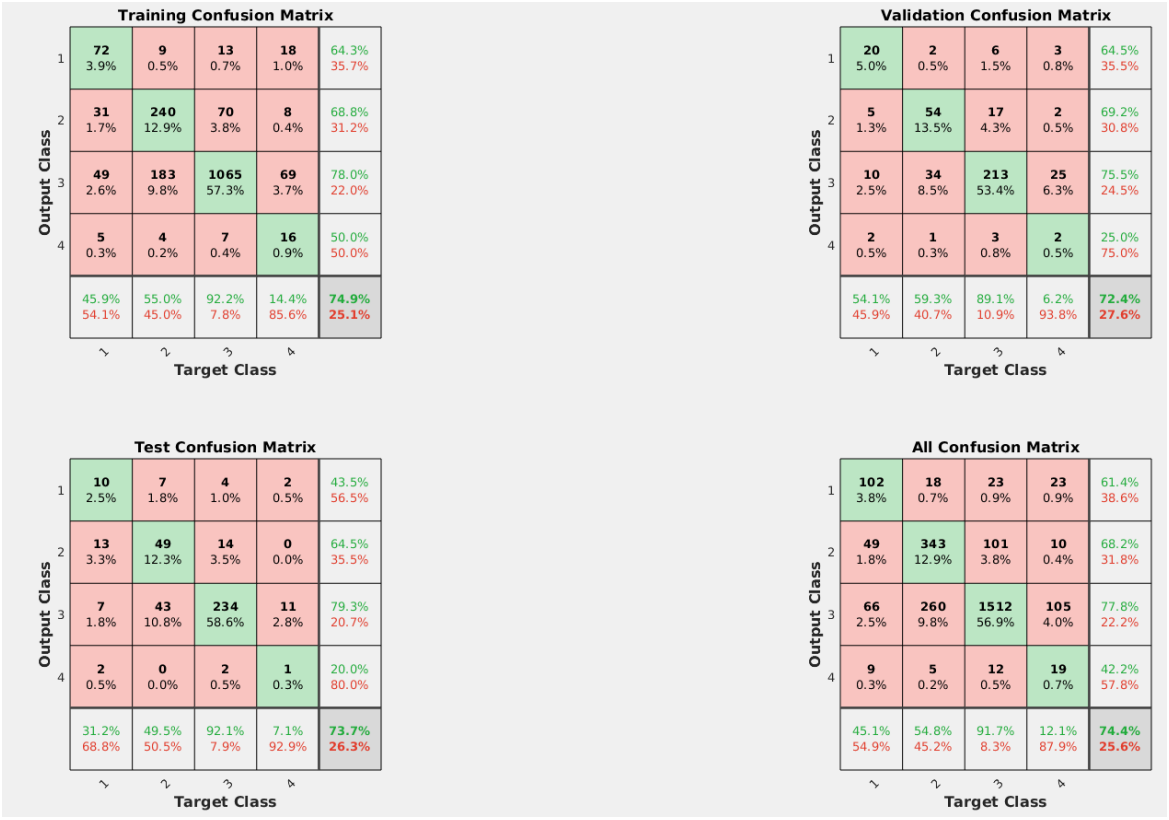


(A) Confusion matrix.

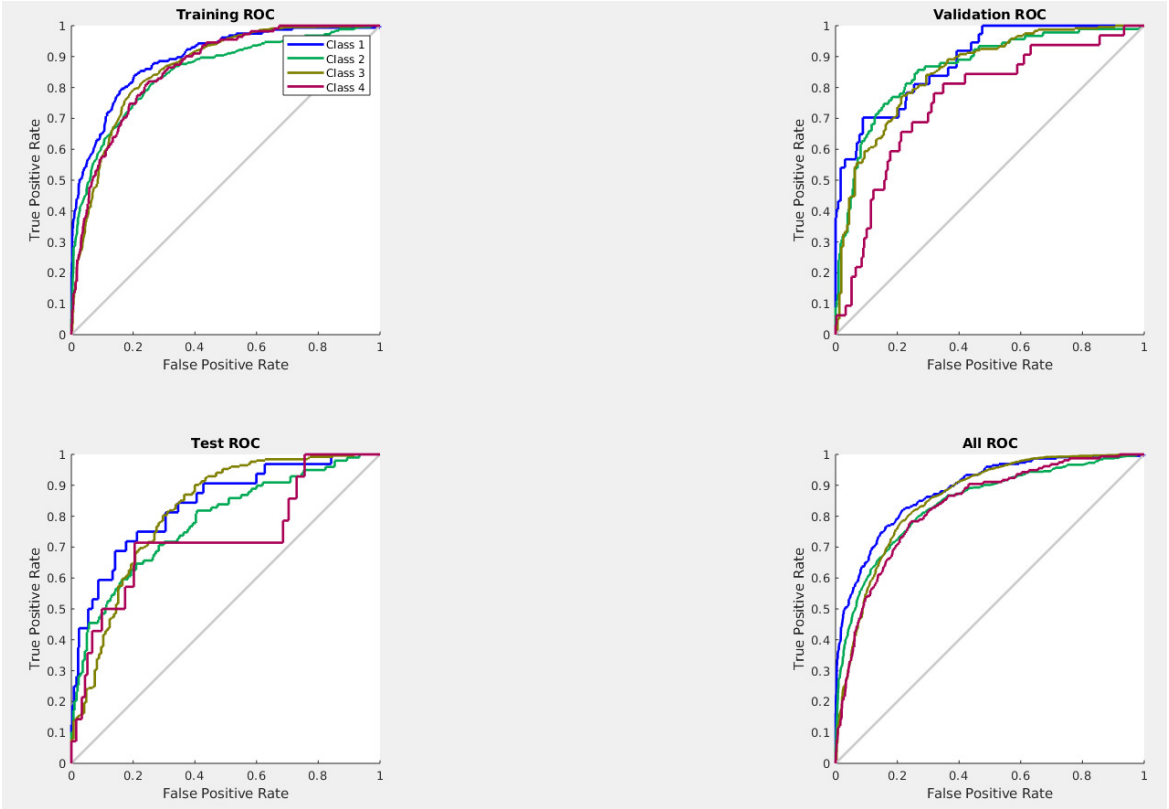


(B) ROC.

FIGURE C.12: Classification results of using a window size of 45x45 pixels, having the first 9 summations of the computed Fourier coefficients of the saturation component in the feature vector

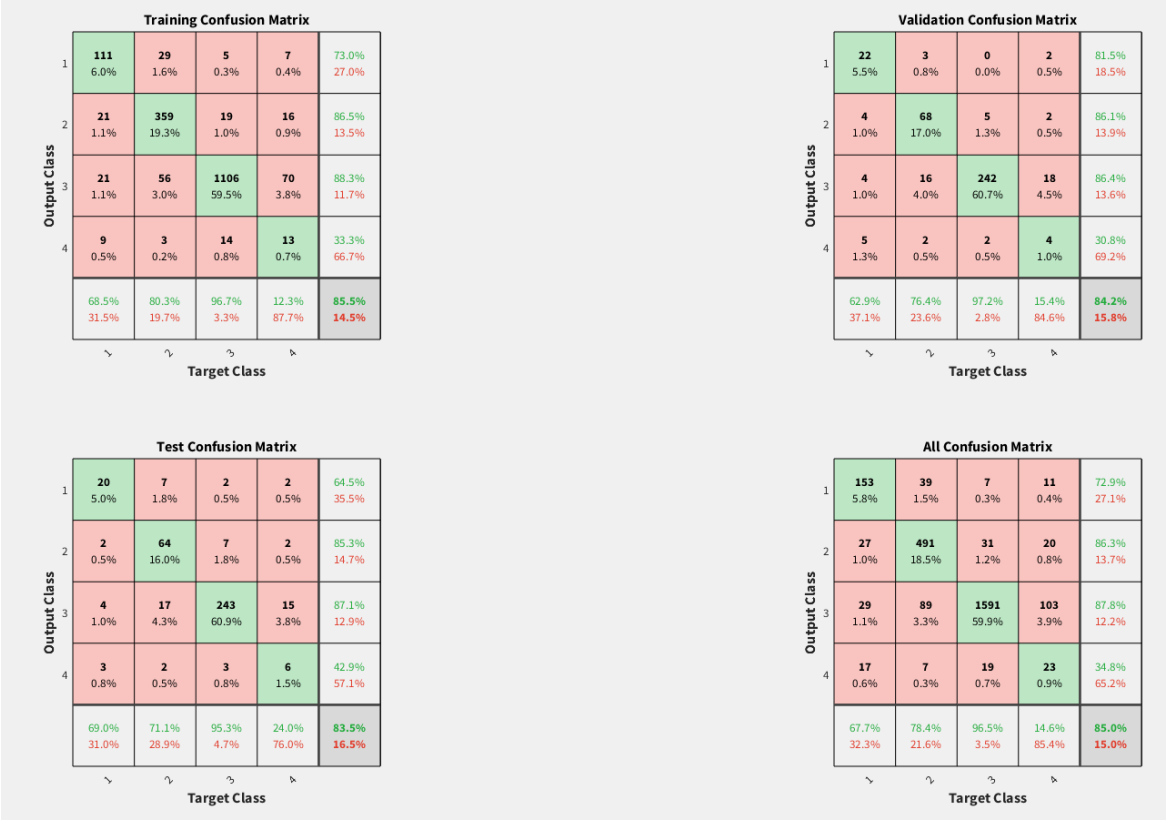


(A) Confusion matrix.

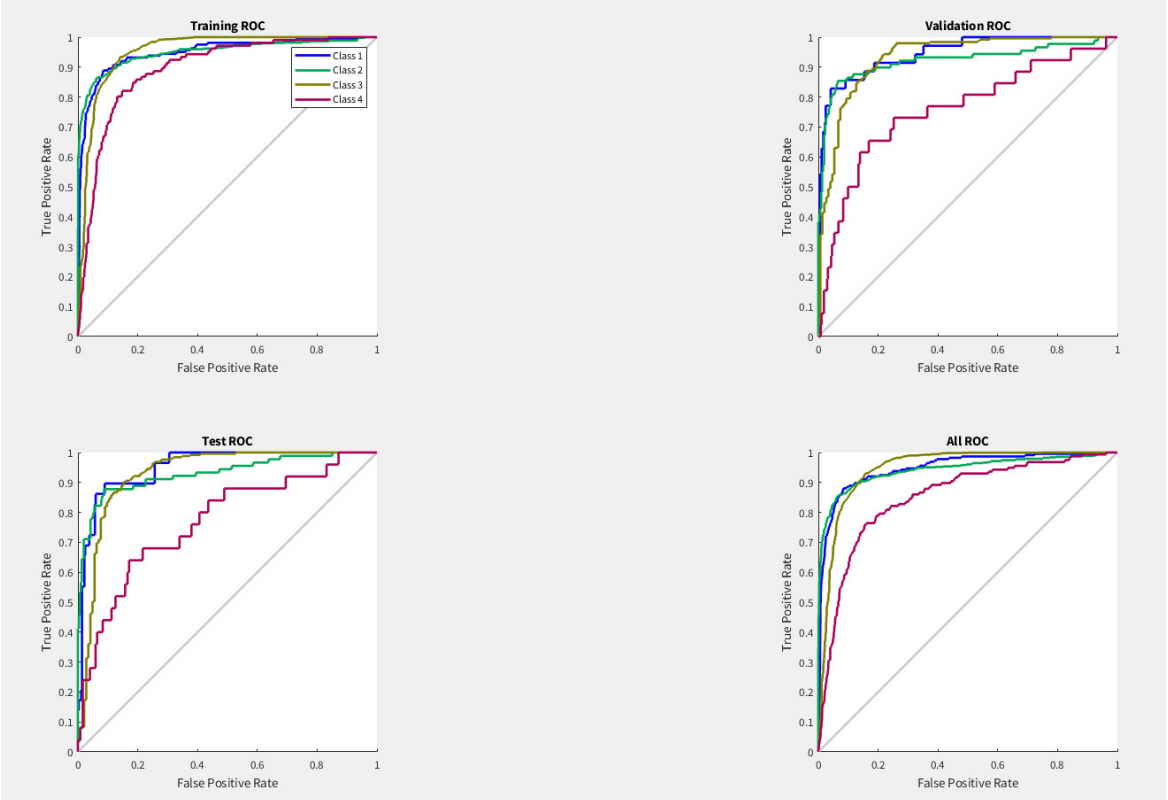


(B) ROC.

FIGURE C.13: Classification results of using a window size of 45x45 pixels, having the first 9 summations of the computed Fourier coefficients of the value component in the feature vector

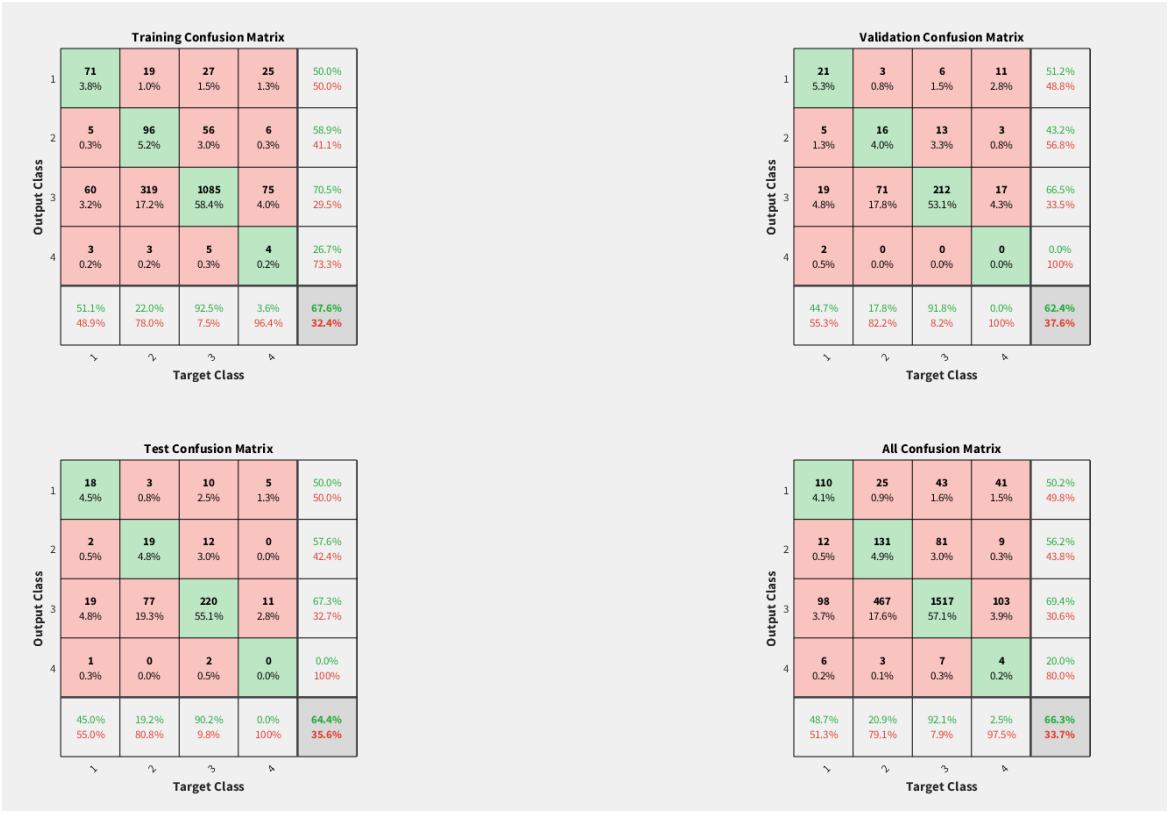


(A) Confusion matrix.

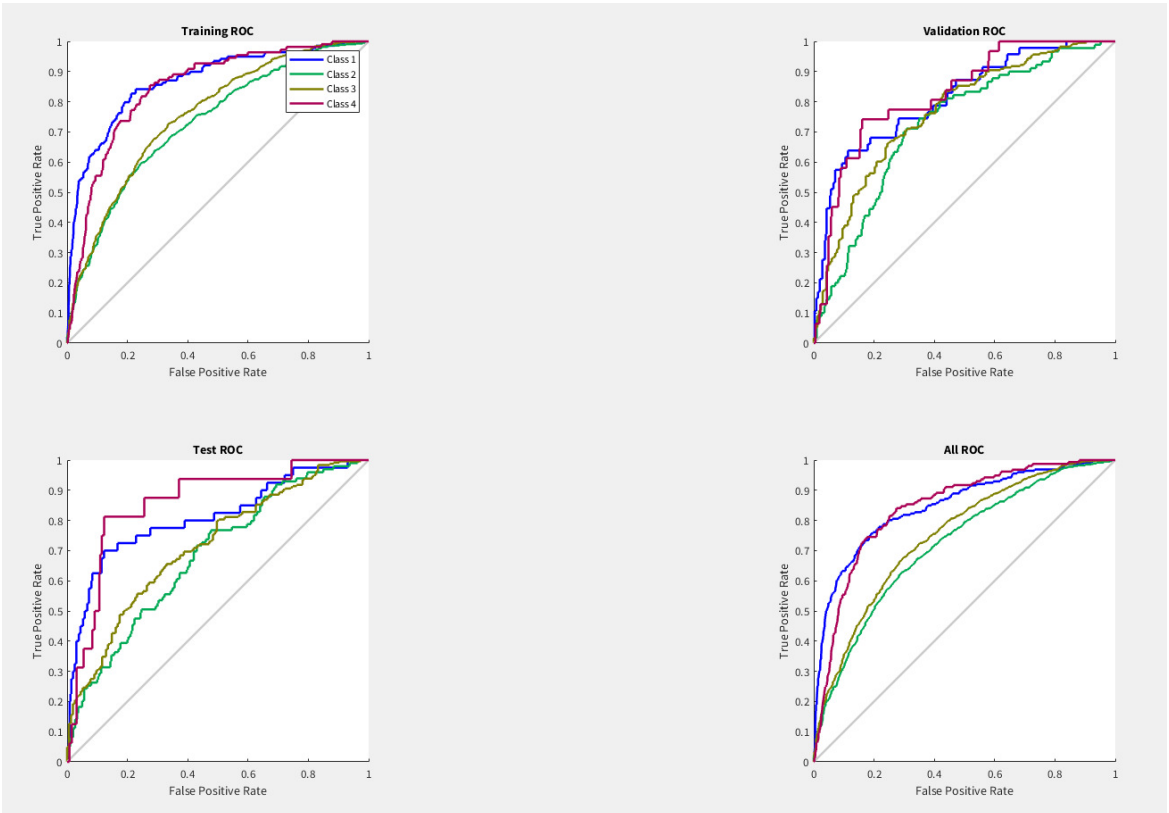


(B) ROC.

FIGURE C.14: Classification results of using a window size of 45x45 pixels, having the first 9 summations of the computed Fourier coefficients of the red, green and blue components in the feature vector

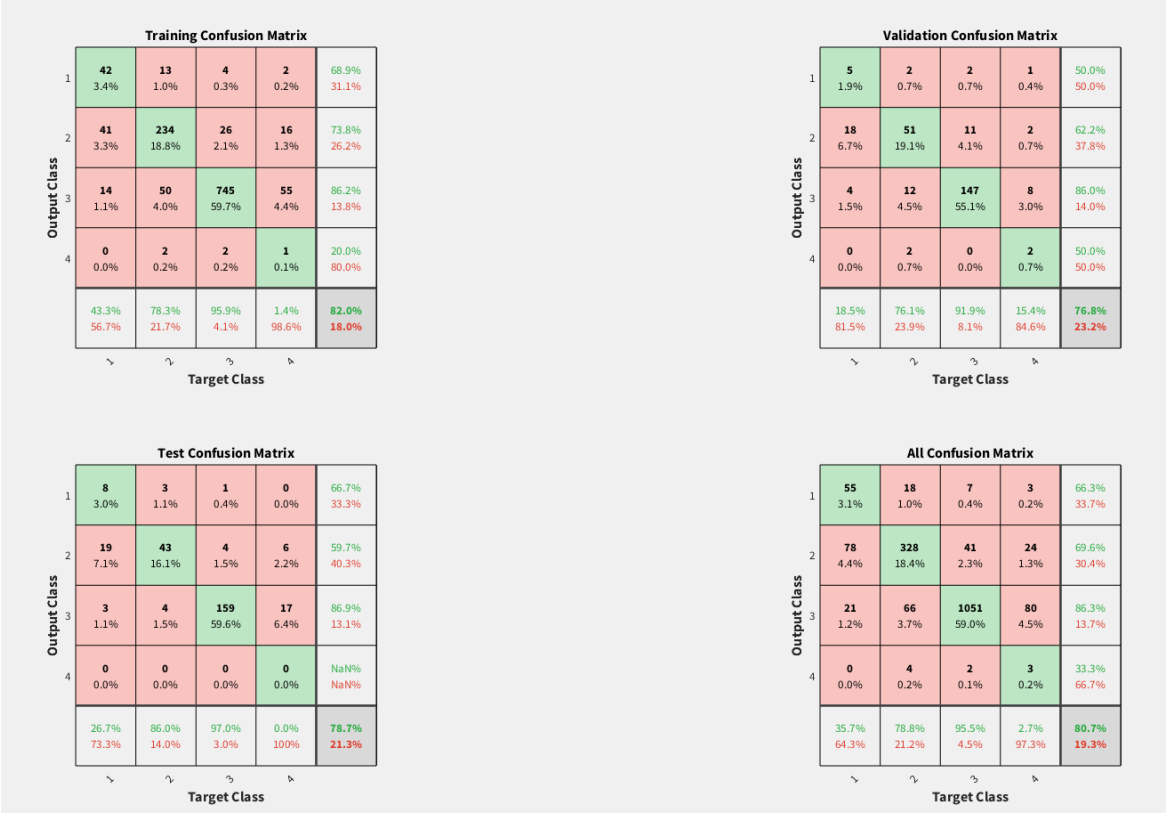


(A) Confusion matrix.

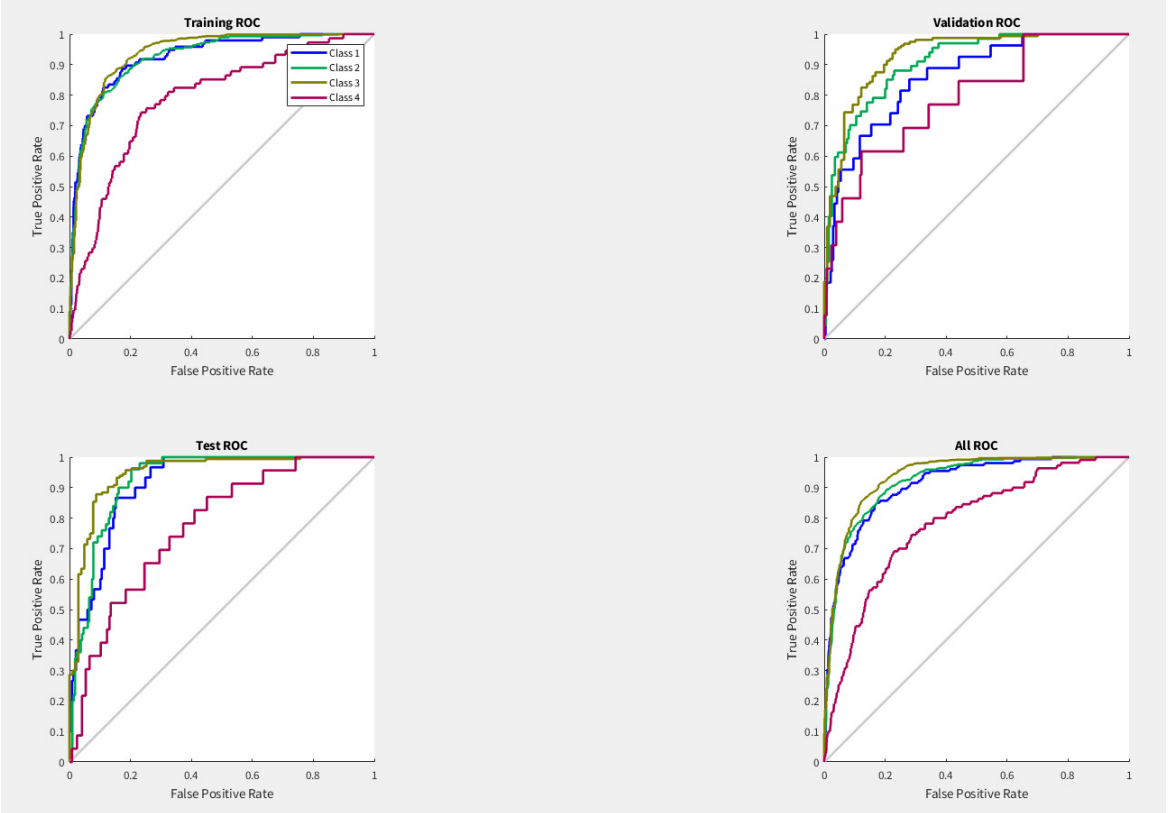


(B) ROC.

FIGURE C.15: Classification results of using a window size of 45x45 pixels, having the first 19 summations of the computed Fourier coefficients of the green component in the feature vector

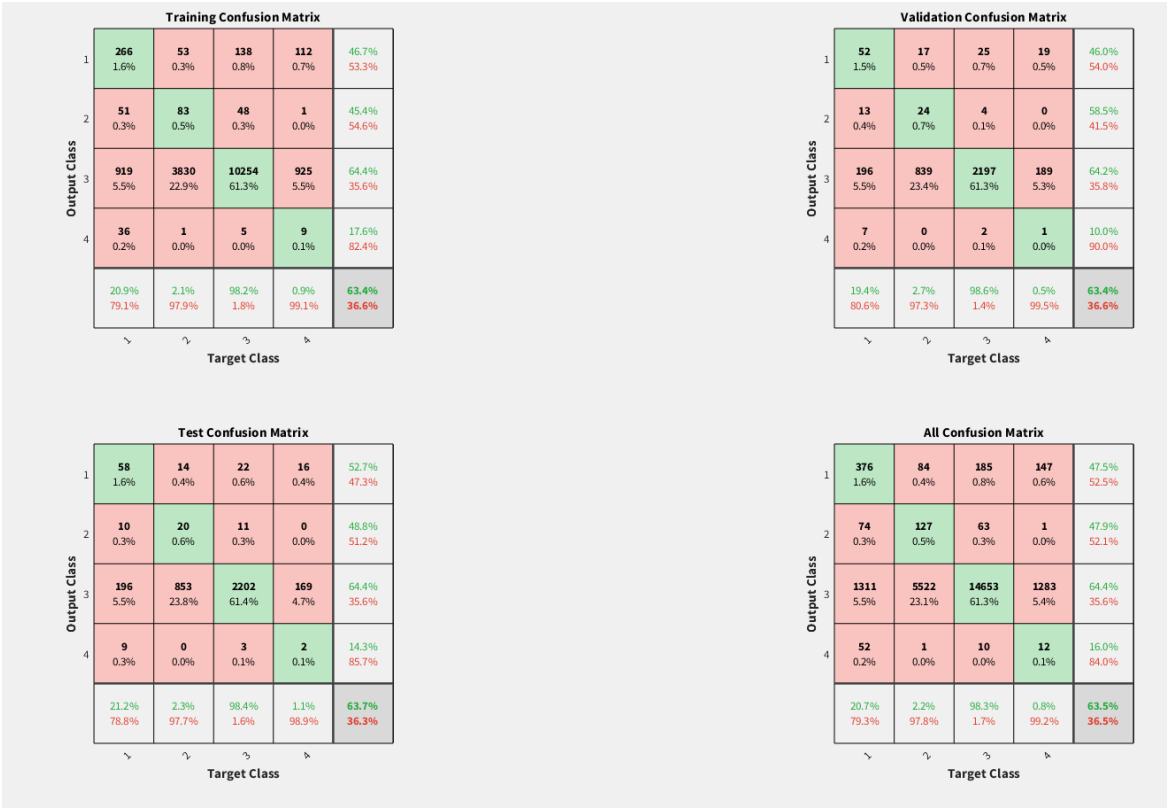


(A) Confusion matrix.

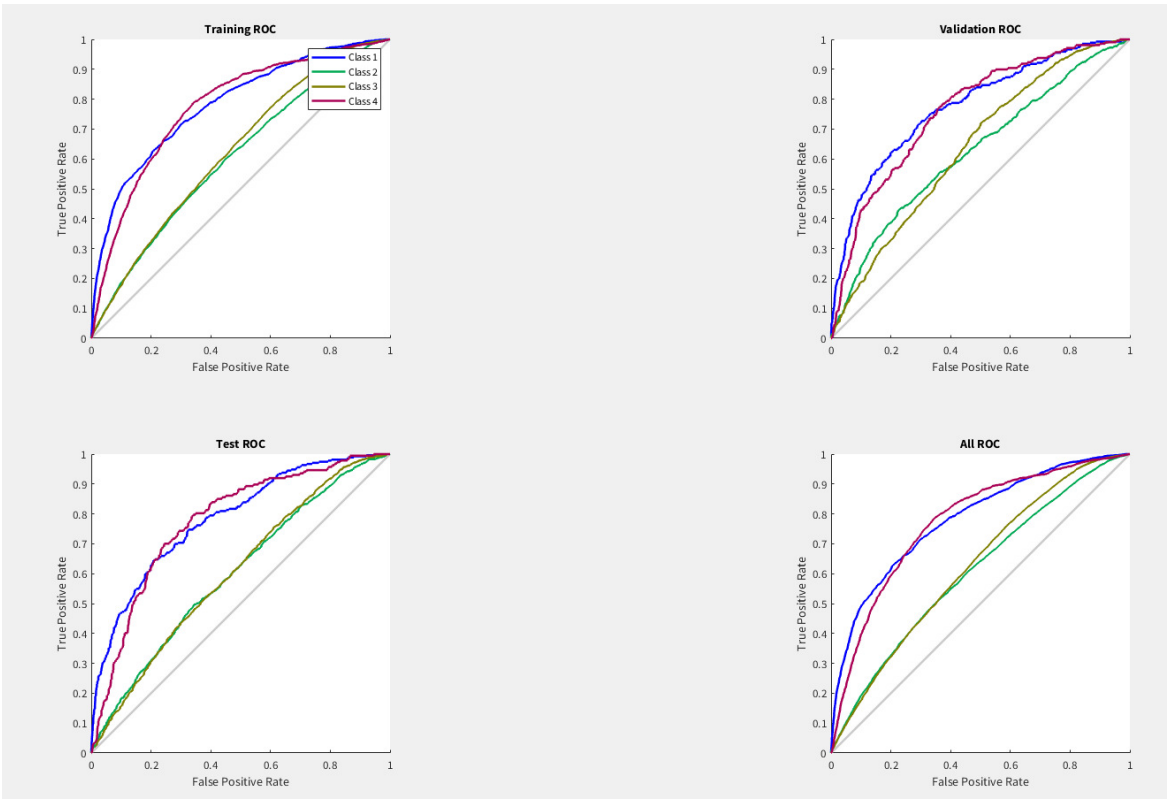


(B) ROC.

FIGURE C.16: Classification results of using a window size of 55x55 pixels, having the first 4 summations of the computed Fourier coefficients of the red and green components in the feature vector

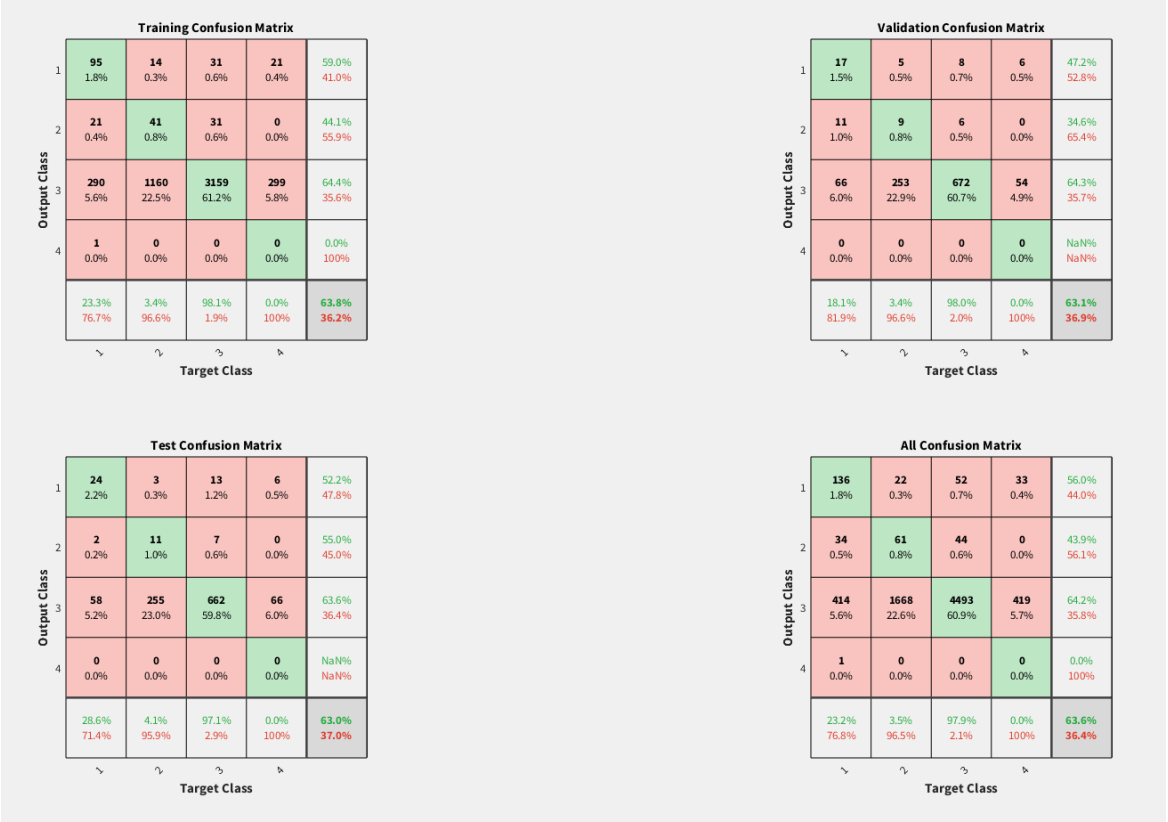


(A) Confusion matrix.

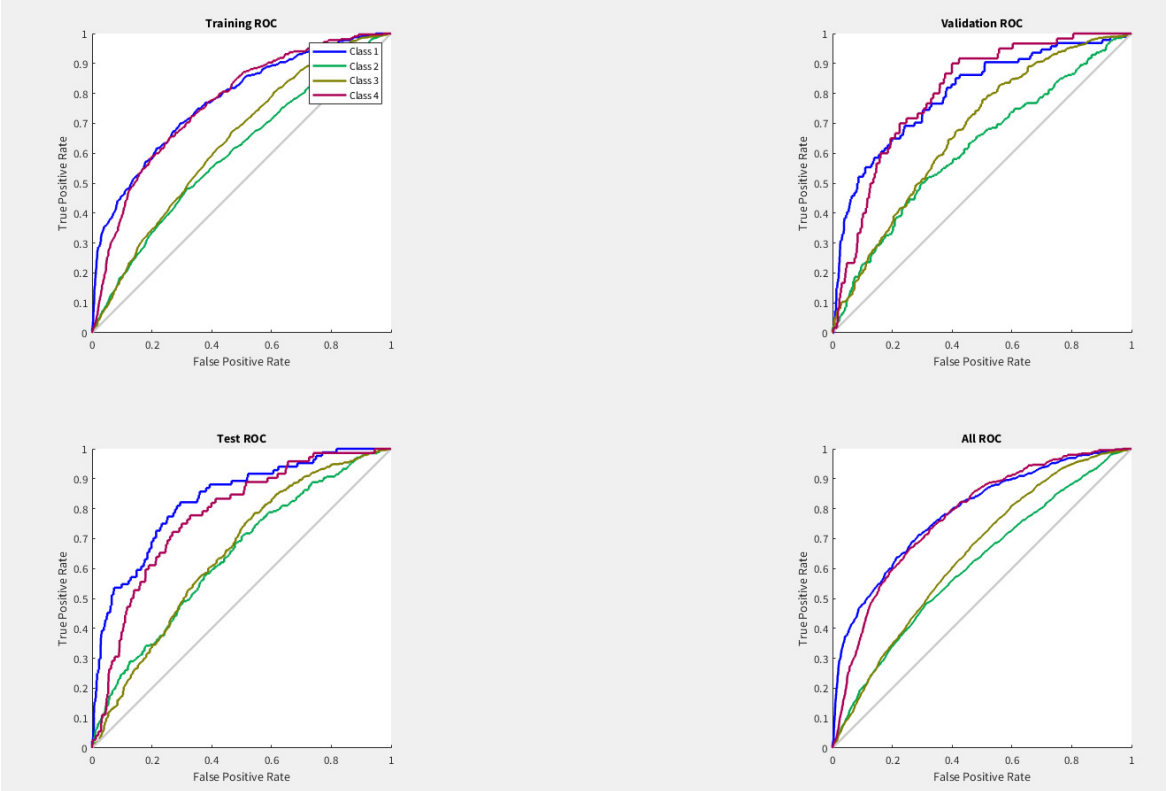


(B) ROC.

FIGURE C.17: Classification results of using a window size of 15x15 pixels, having the first 4 summations of the computed Fourier coefficients of the green component in the feature vector

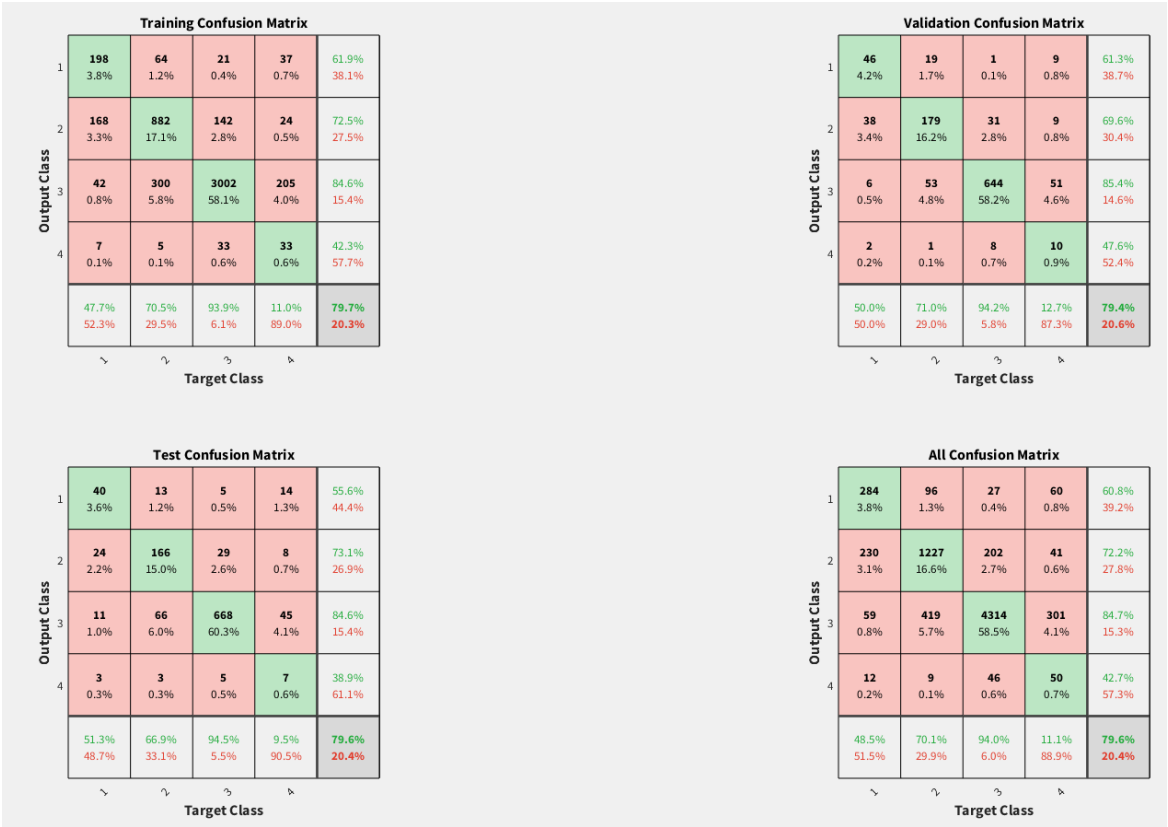


(A) Confusion matrix.

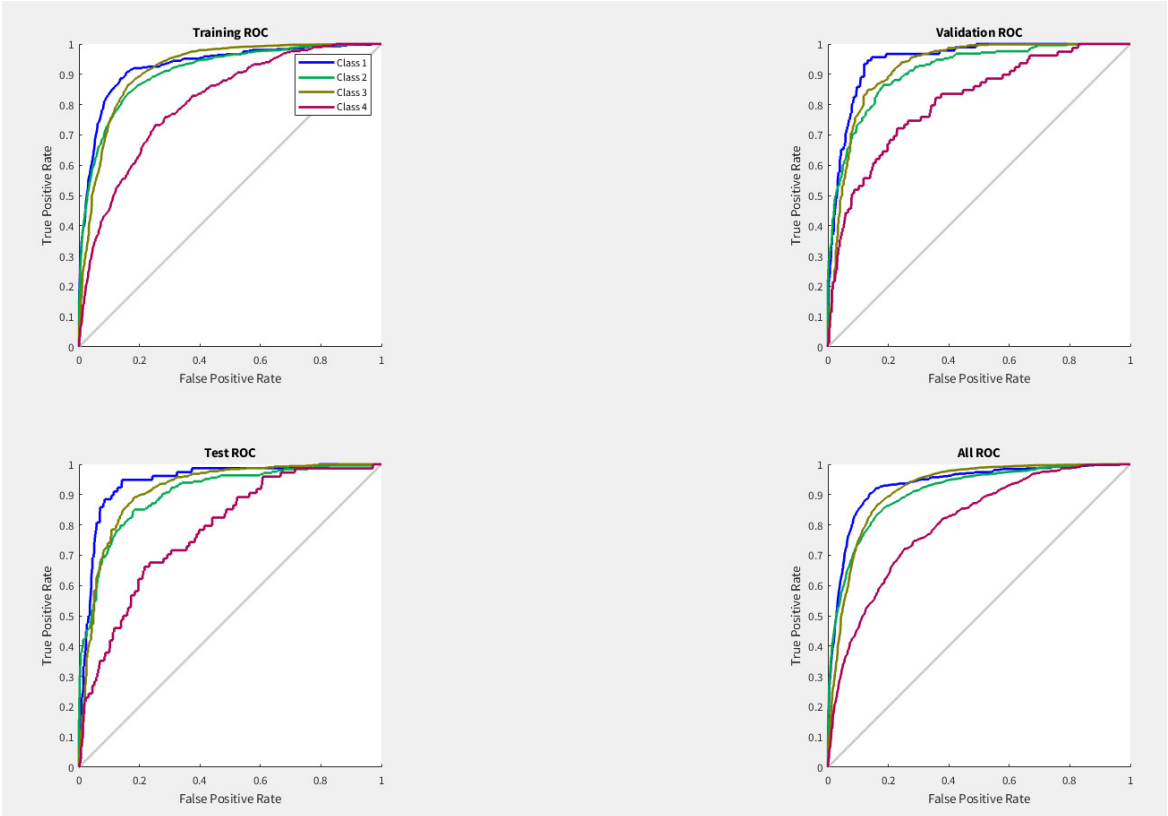


(B) ROC.

FIGURE C.18: Classification results of using a window size of 27x27 pixels, having the first 4 summations of the computed Fourier coefficients of the green component in the feature vector

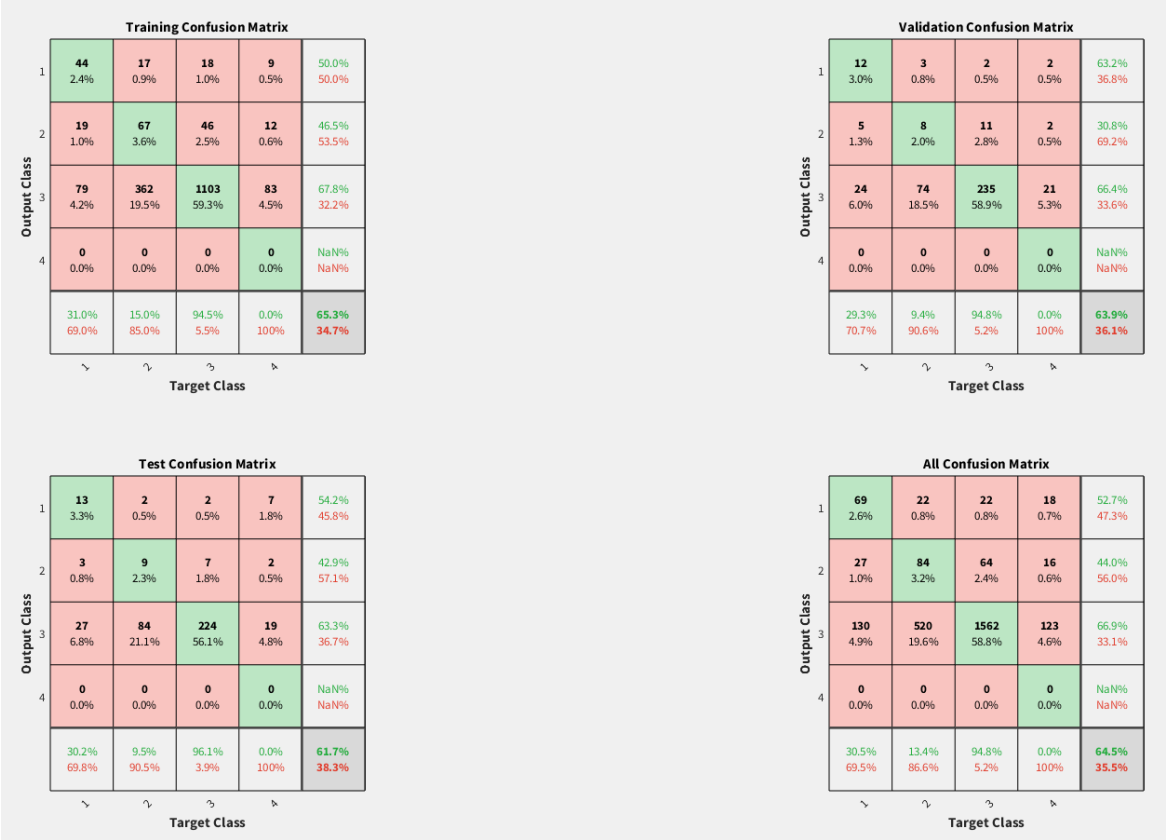


(A) Confusion matrix.

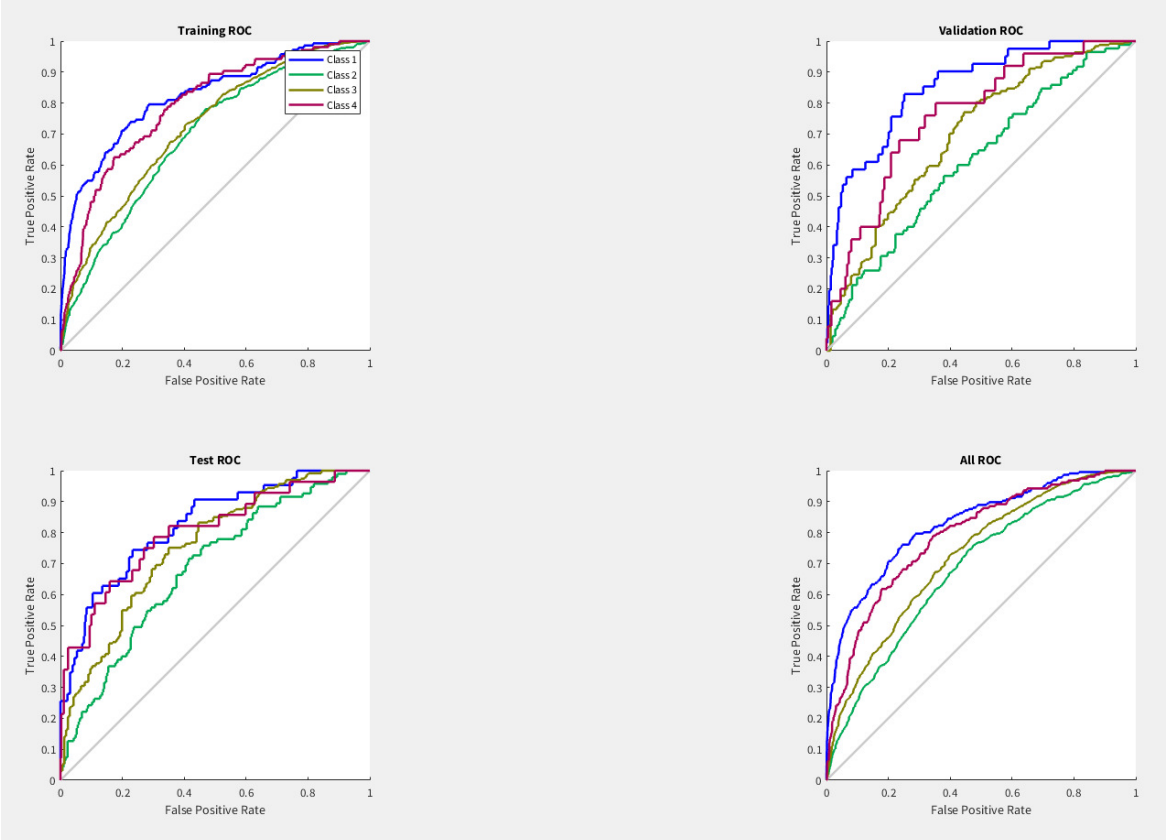


(B) ROC.

FIGURE C.19: Classification results of using a window size of 27x27 pixels, having the first 4 summations of the computed Fourier coefficients of the red and green components in the feature vector

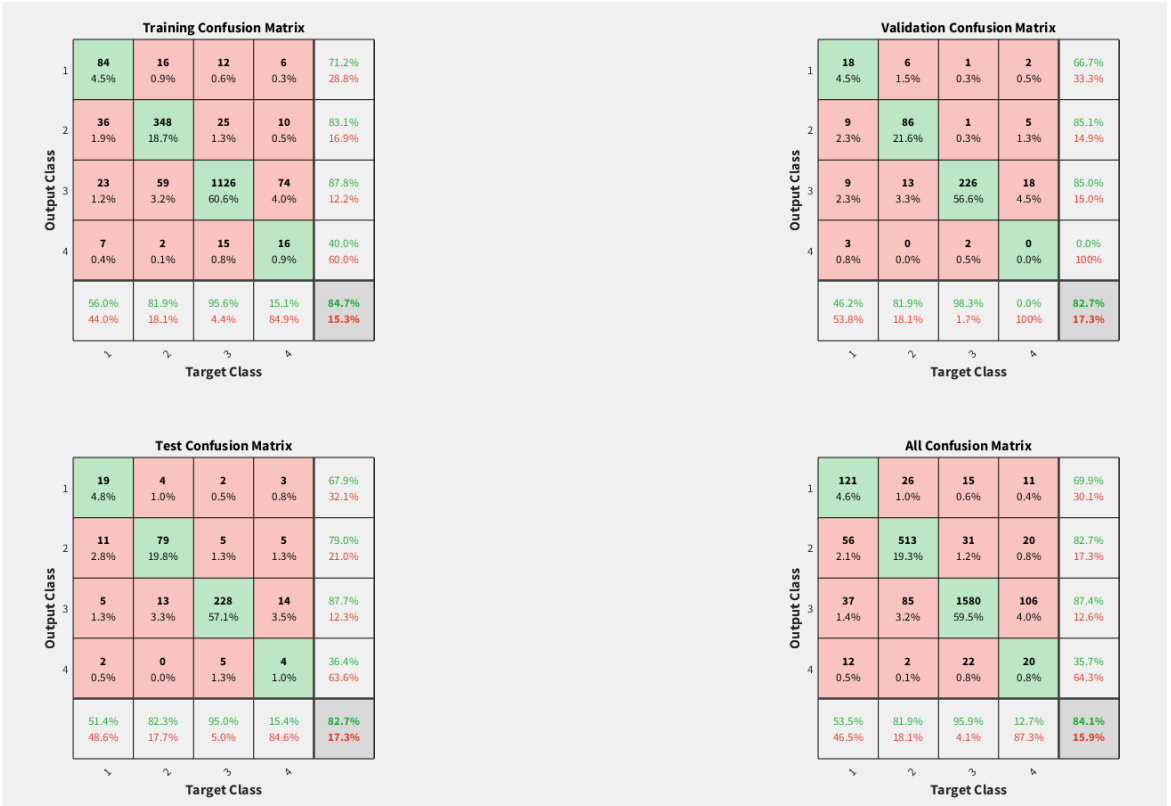


(A) Confusion matrix.

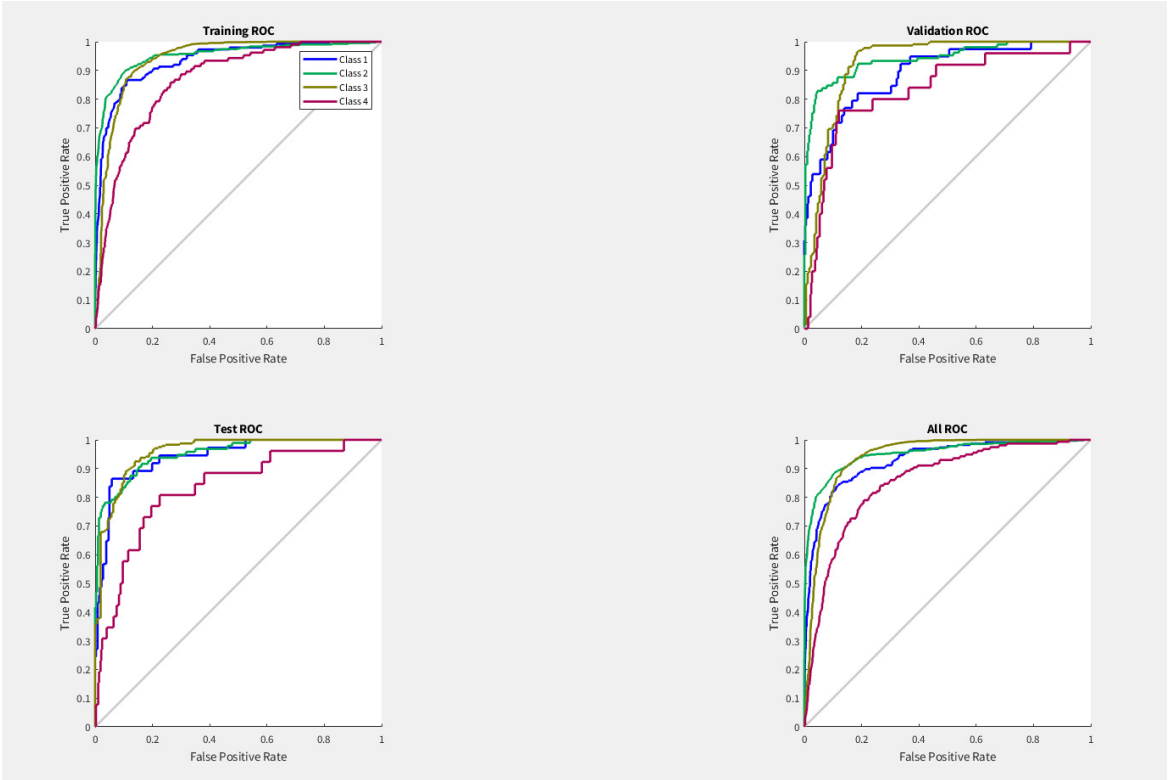


(B) ROC.

FIGURE C.20: Classification results of using a window size of 45x45 pixels, having the first 4 summations of the computed Fourier coefficients of the green component in the feature vector

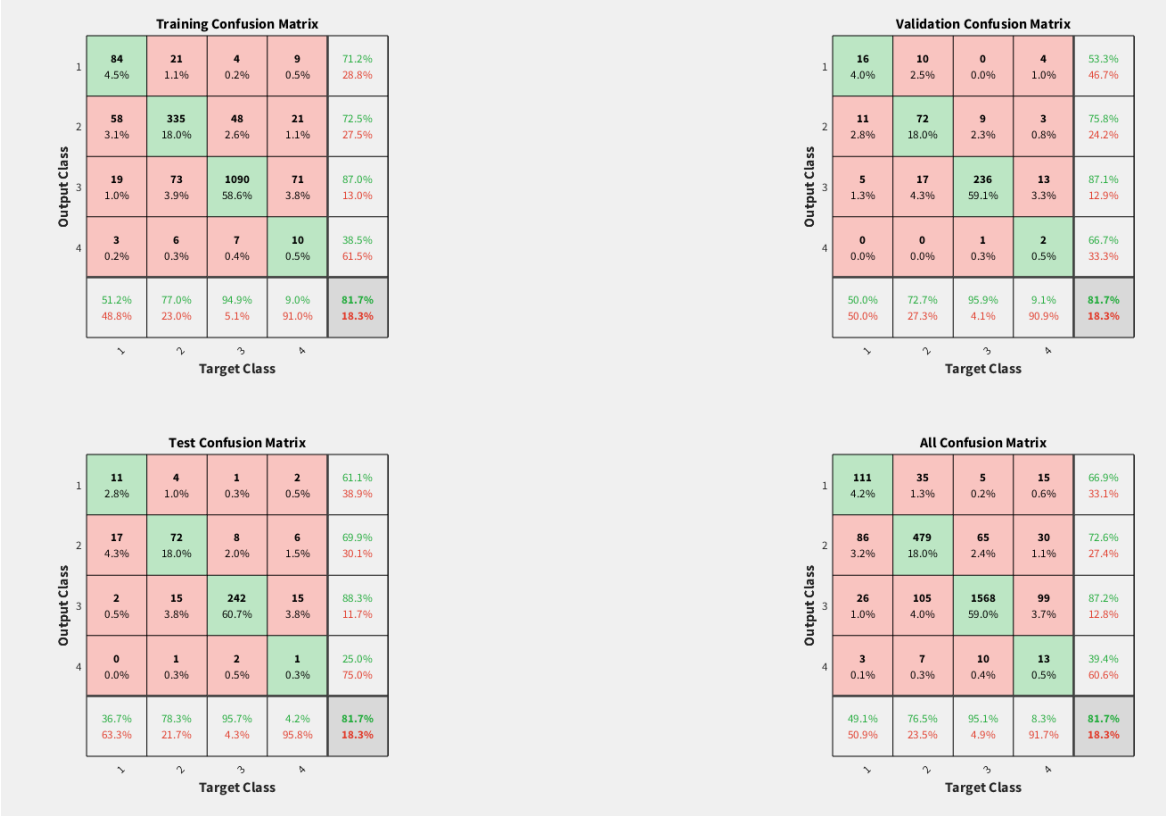


(A) Confusion matrix.

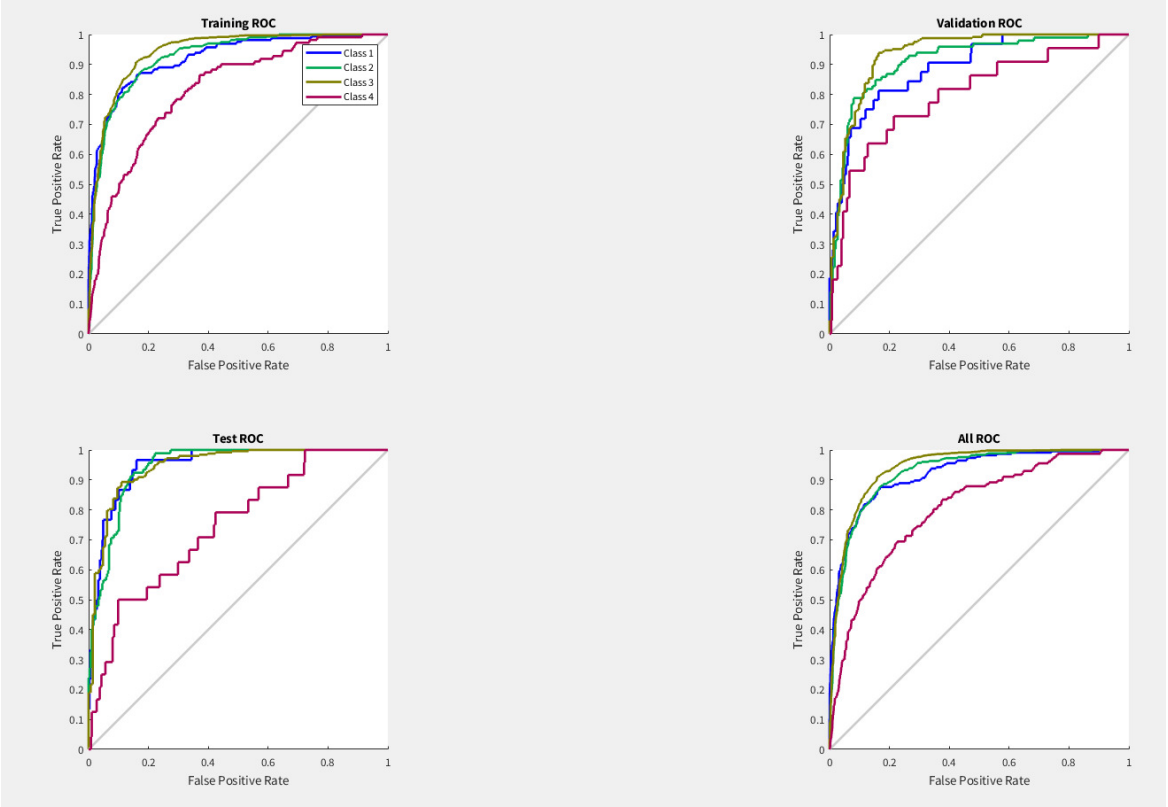


(B) ROC.

FIGURE C.21: Classification results of using a window size of 45x45 pixels, having the first 4 summations of the computed Fourier coefficients of the red, green and blue components, as well as the ExR in the feature vector

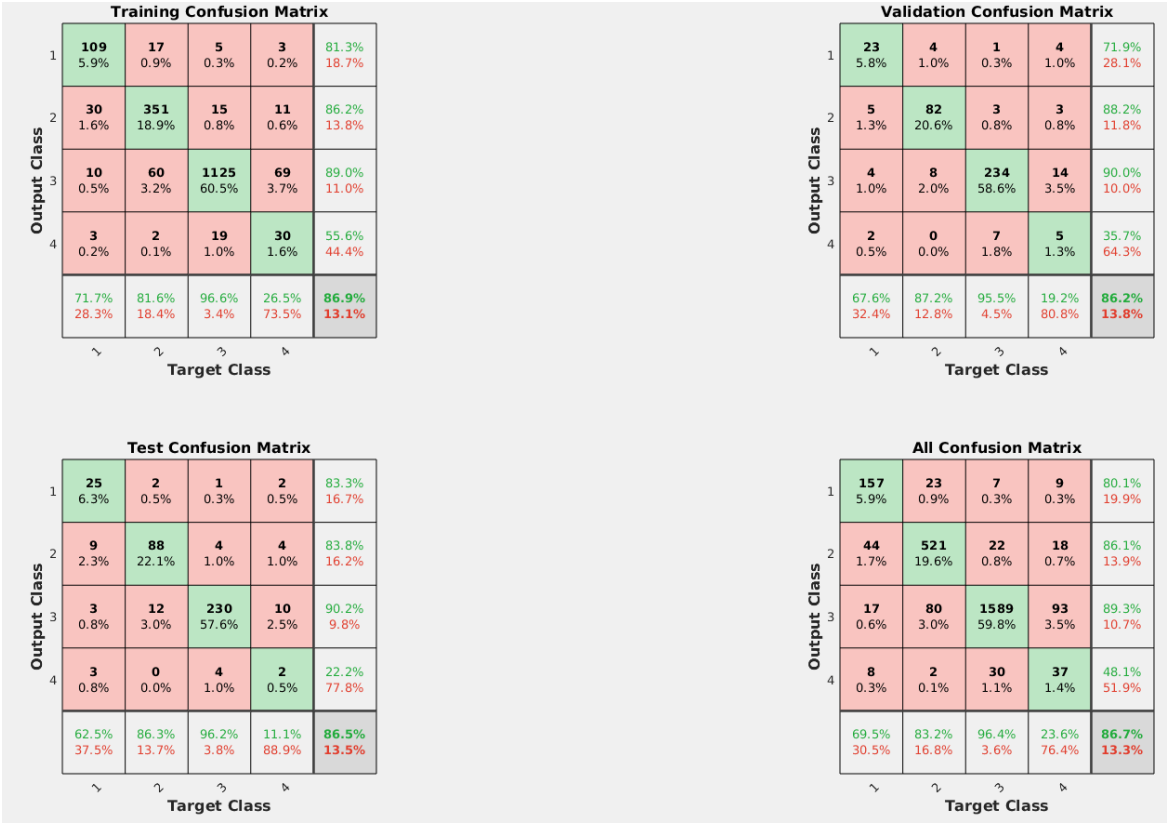


(A) Confusion matrix.

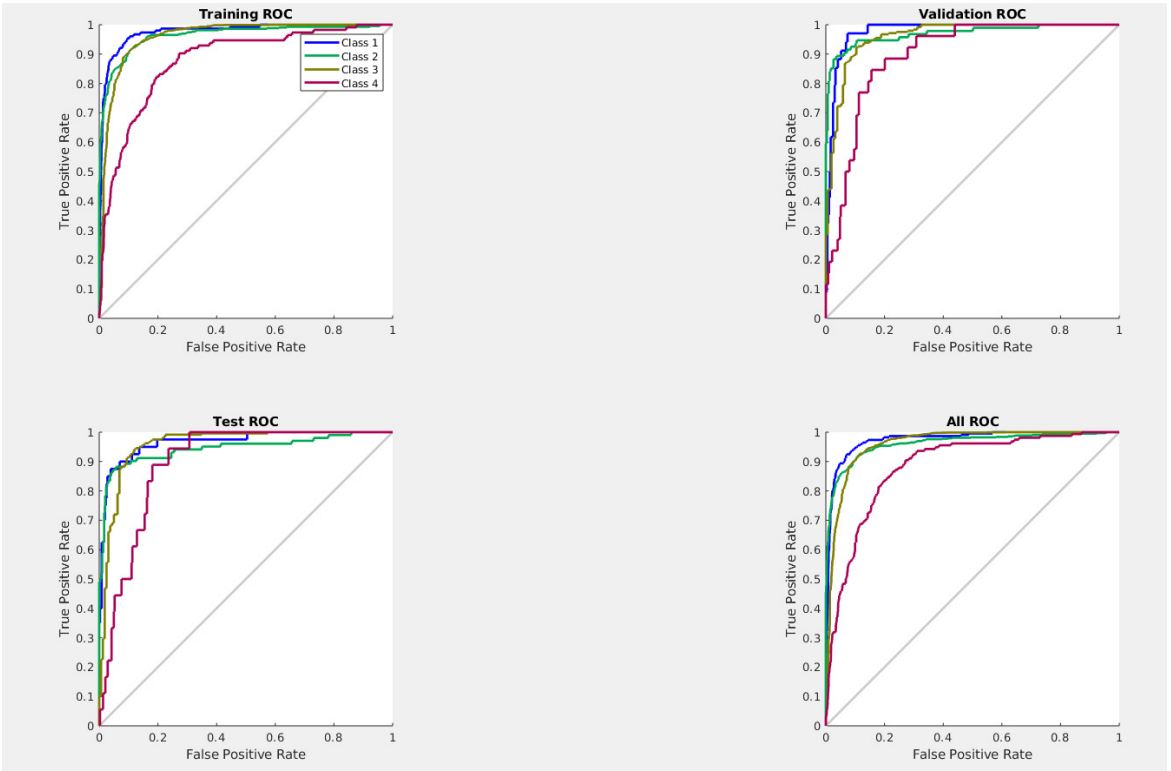


(B) ROC.

FIGURE C.22: Classification results of using a window size of 45x45 pixels, having the first 4 summations of the computed Fourier coefficients of the red and green components in the feature vector

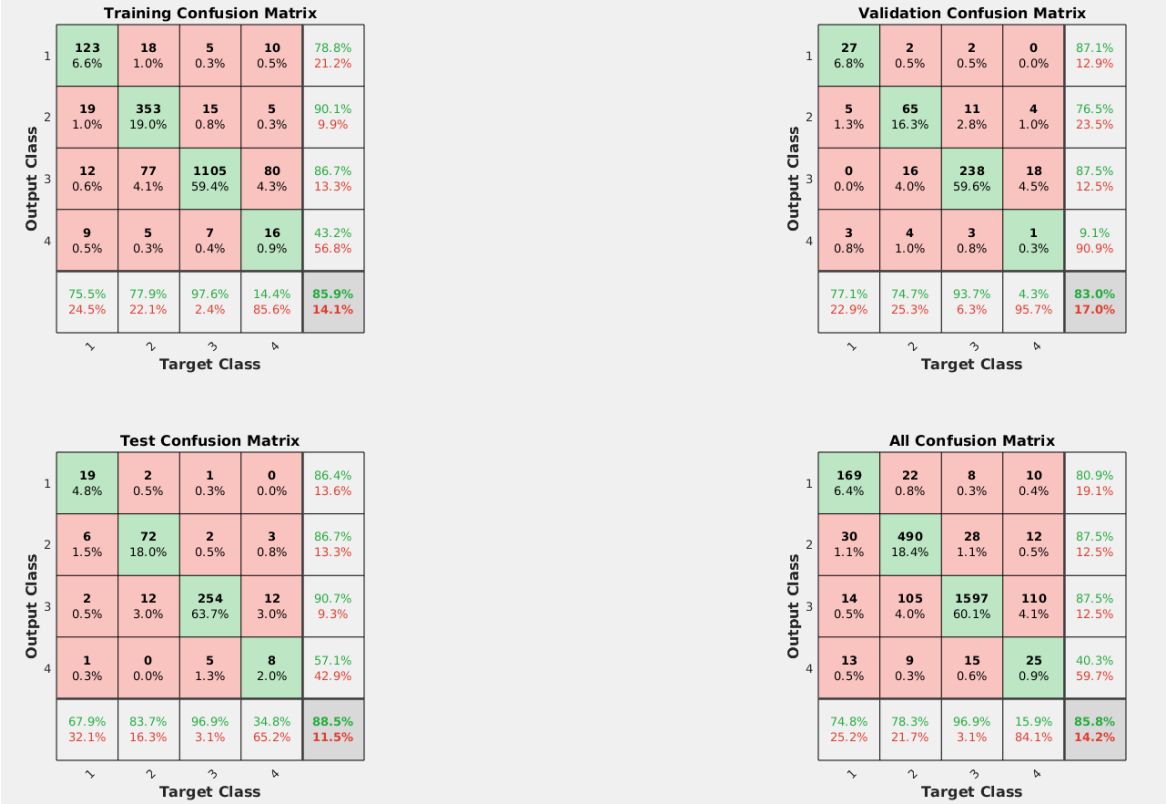


(A) Confusion matrix.

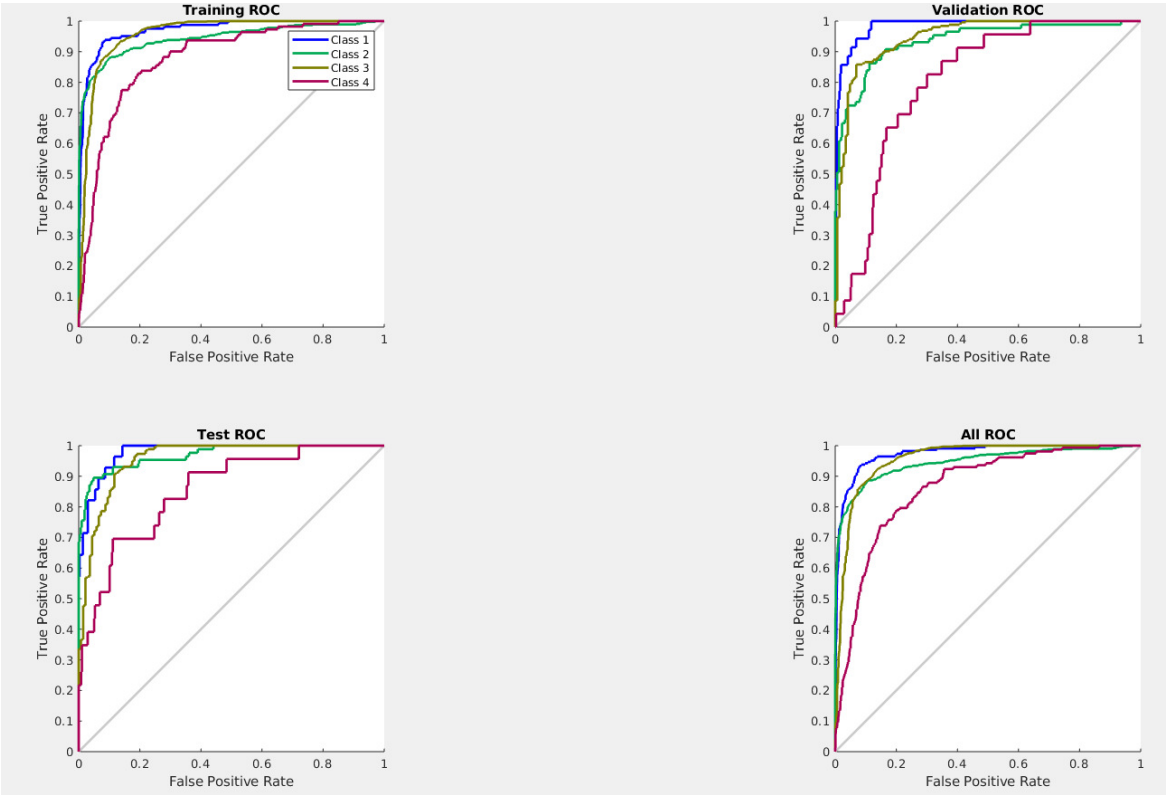


(B) ROC.

FIGURE C.23: Classification results of using a window size of 45x45 pixels, having the first 6 summations of the computed Fourier coefficients of the red, green, blue, hue, saturation and value components, as well as the ExR in the feature vector

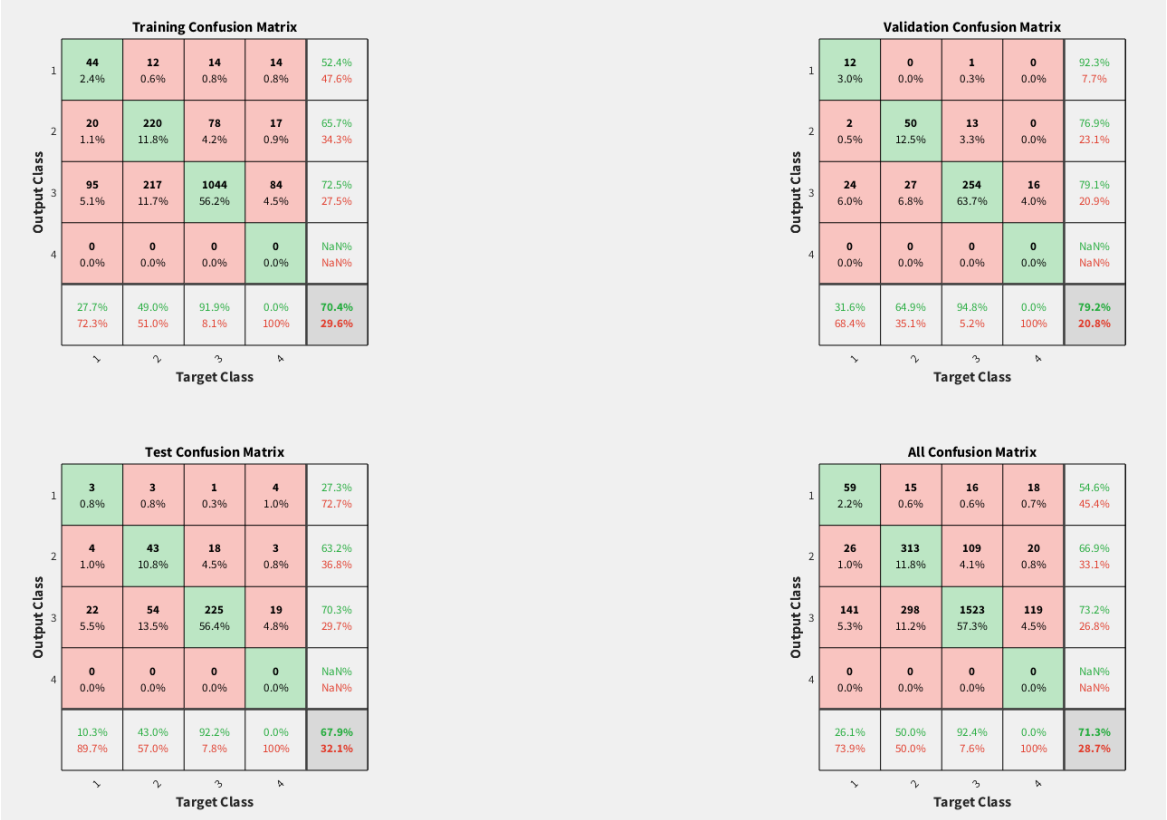


(A) Confusion matrix.

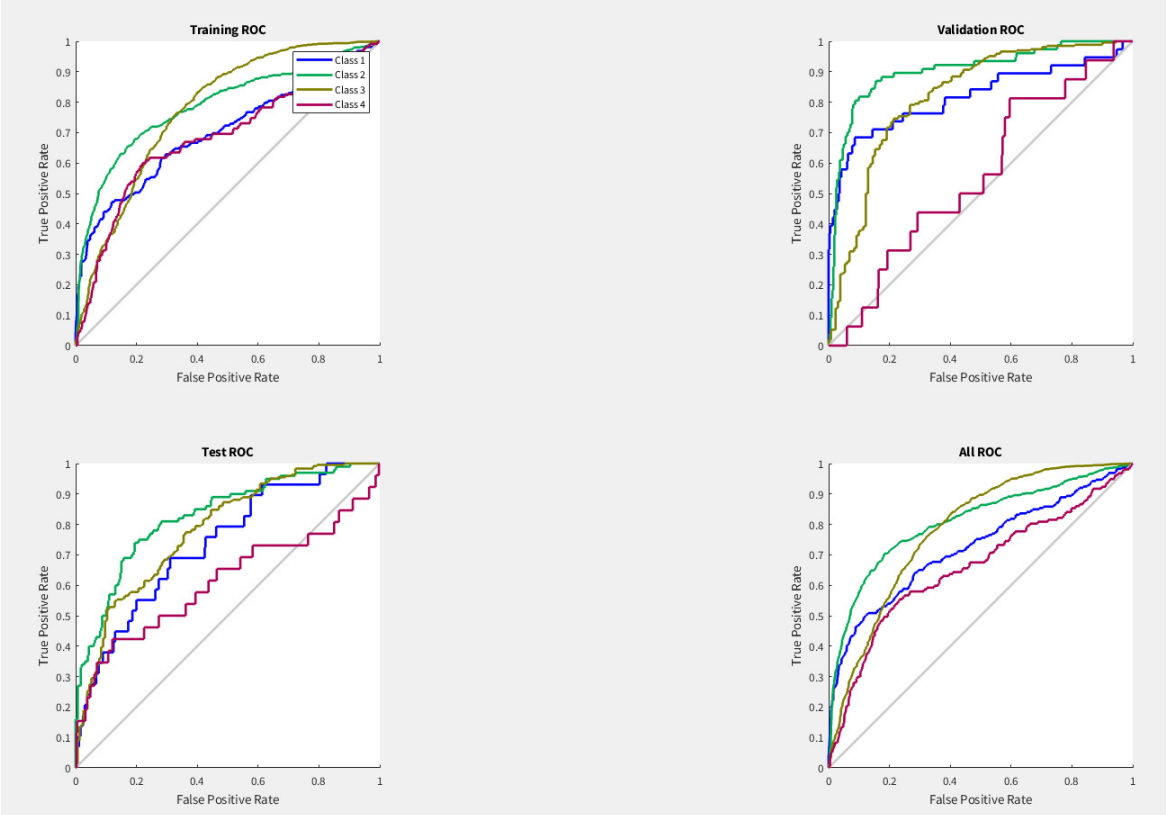


(B) ROC.

FIGURE C.24: Classification results of using a window size of 45x45 pixels, having the first 8 summations of the computed Fourier coefficients of the red, green, blue, hue, saturation and value components, as well as the ExR in the feature vector

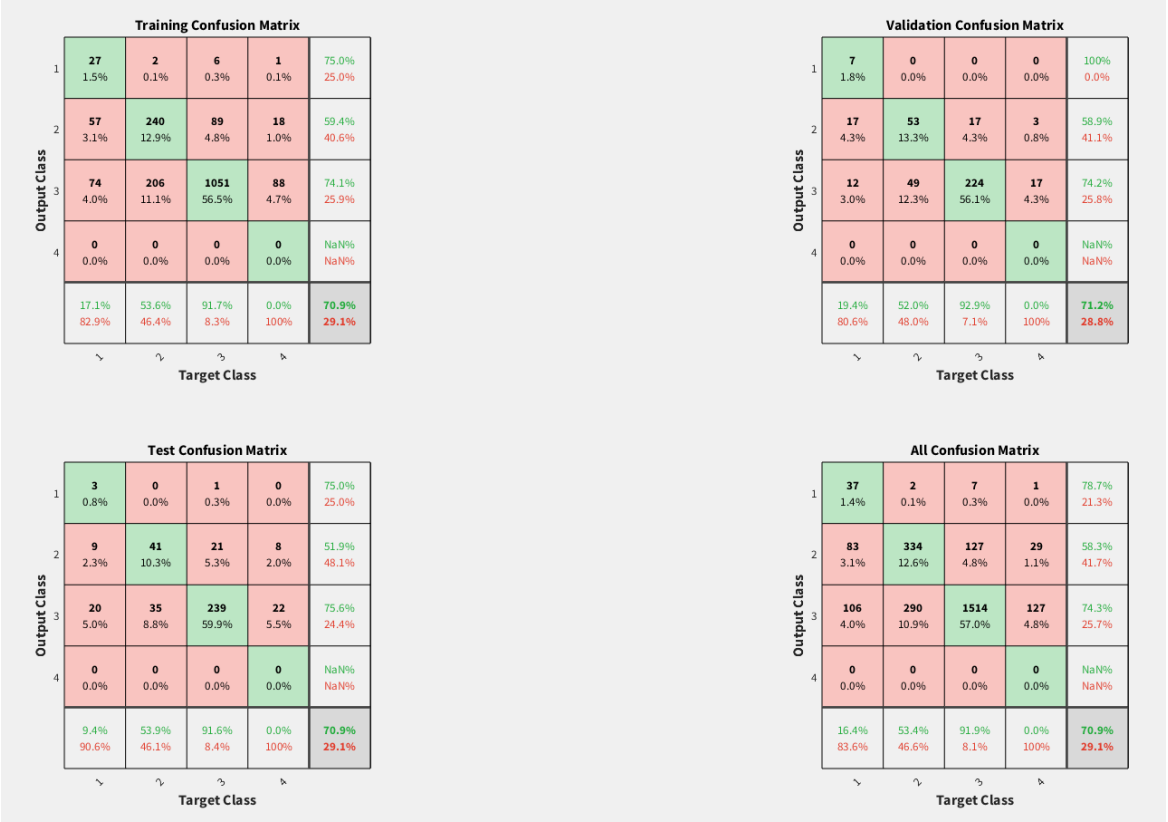


(A) Confusion matrix.

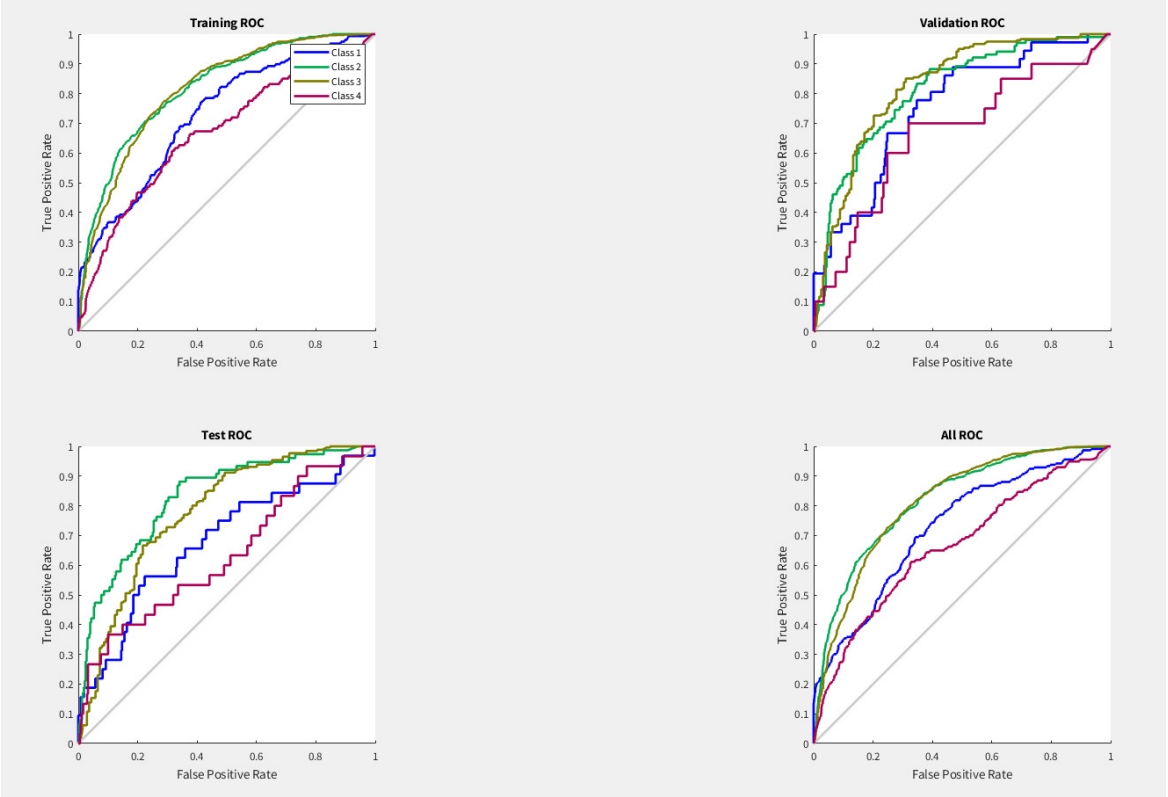


(B) ROC.

FIGURE C.25: Classification results of using a window size of 45x45 pixels, having the first 9 summations of the computed Fourier coefficients of the ExG index in the feature vector

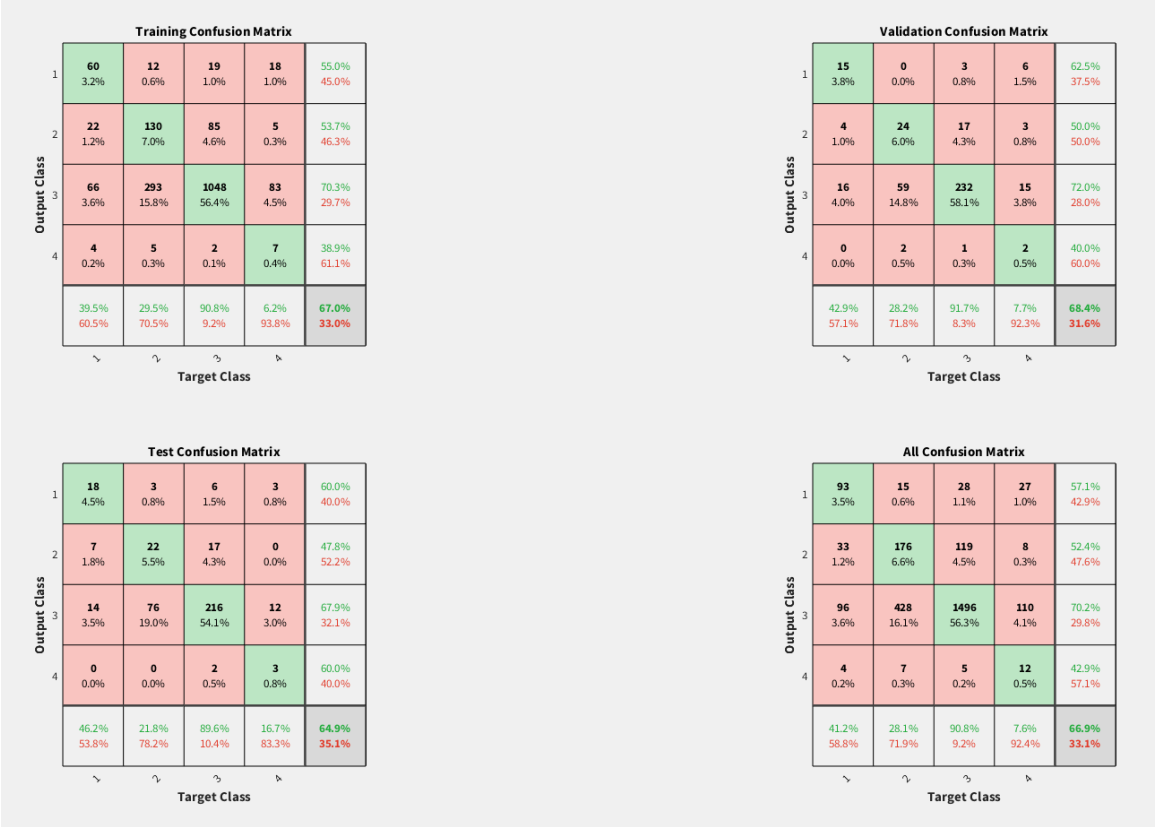


(A) Confusion matrix.

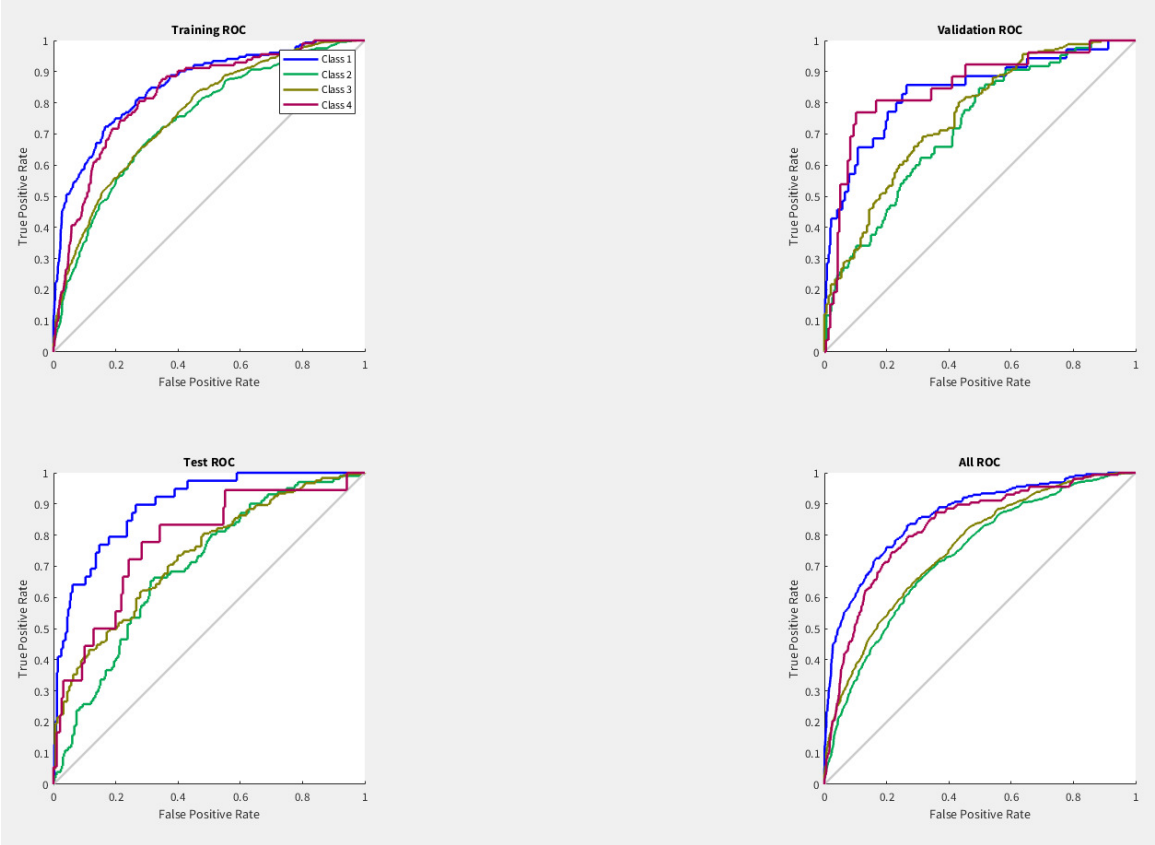


(B) ROC.

FIGURE C.26: Classification results of using a window size of 45x45 pixels, having the first 9 summations of the computed Fourier coefficients of the ExR index in the feature vector

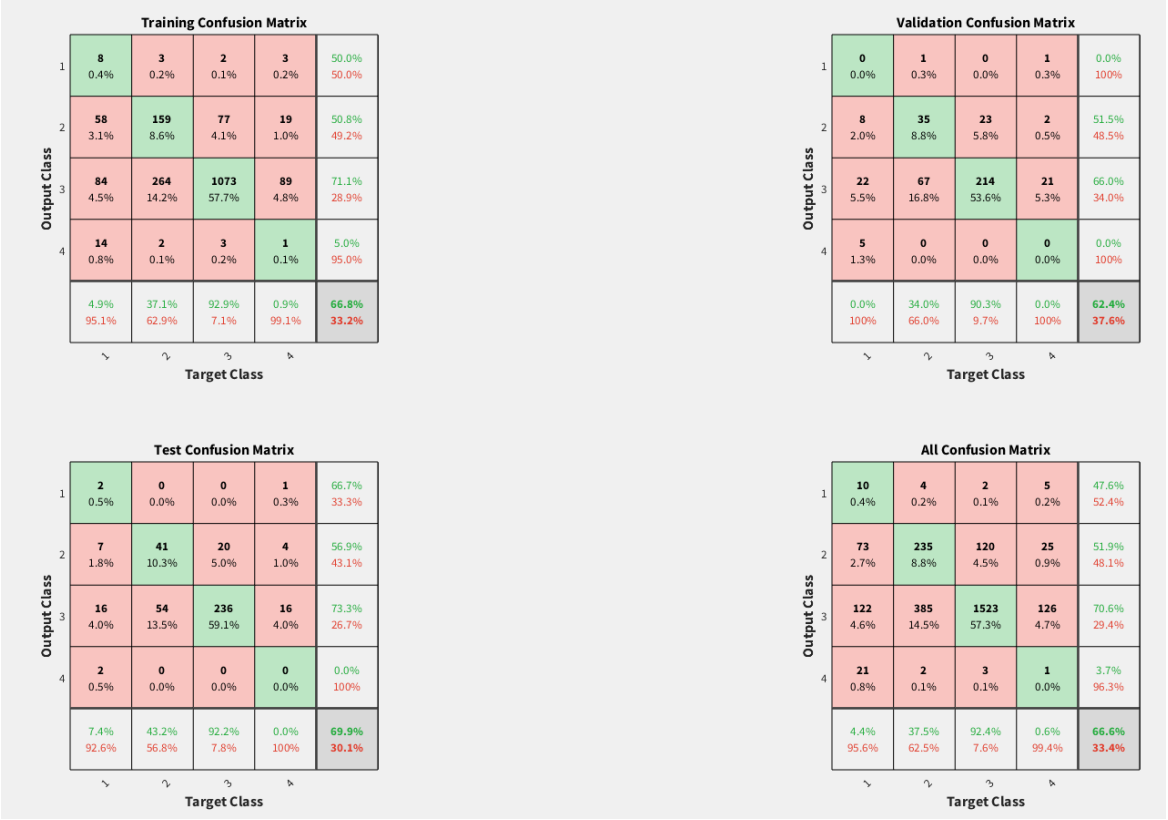


(A) Confusion matrix.

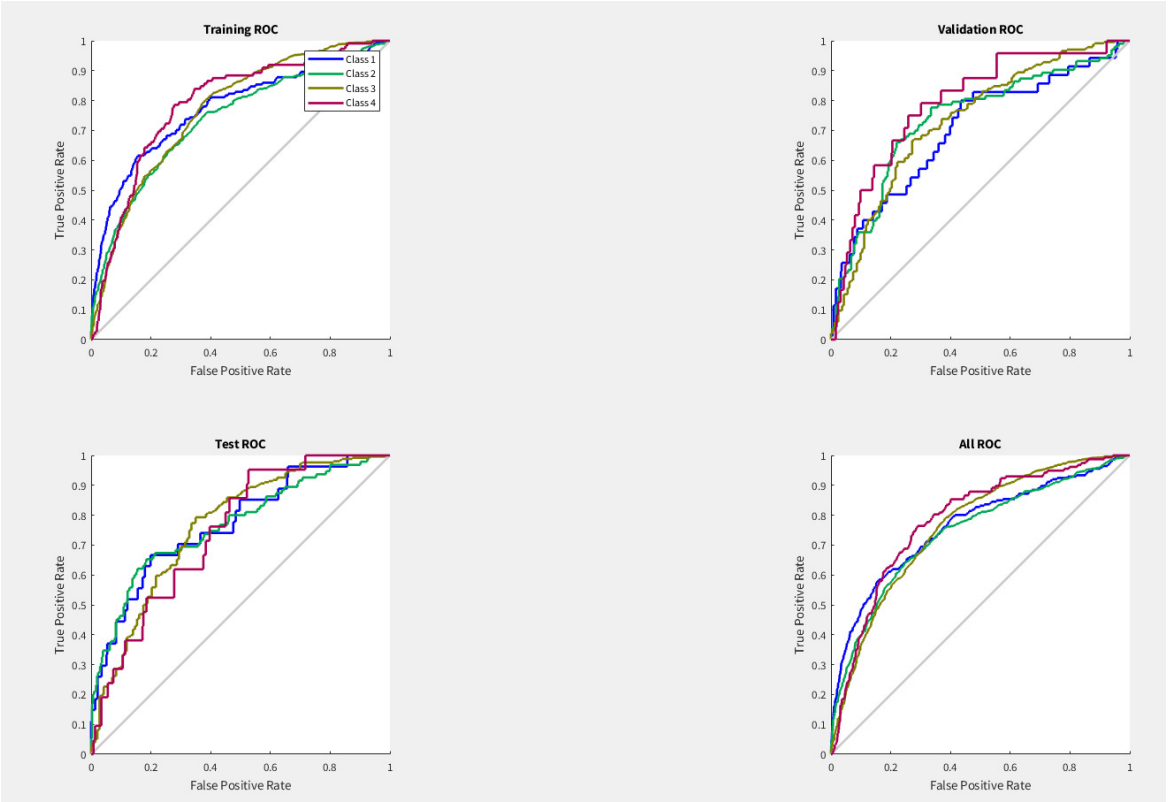


(B) ROC.

FIGURE C.27: Classification results of using a window size of 45x45 pixels, having the first 9 summations of the computed Fourier coefficients of the green component in the feature vector

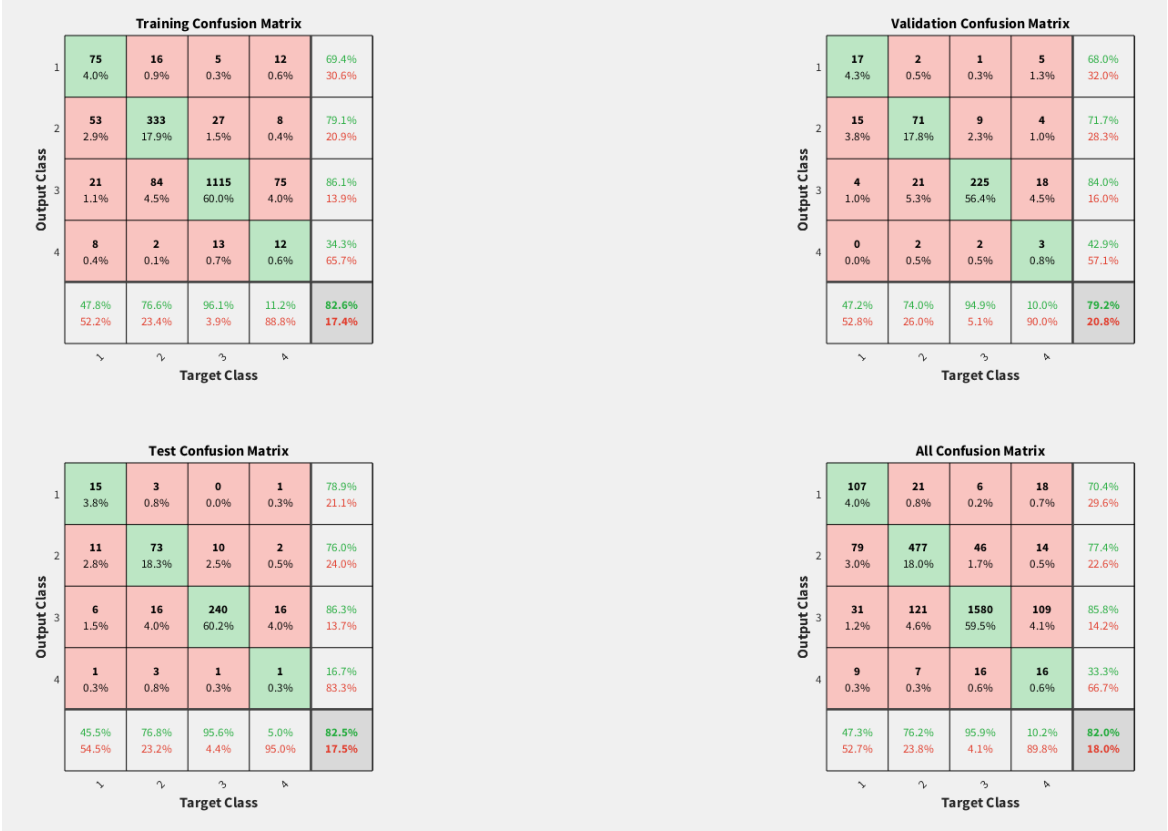


(A) Confusion matrix.

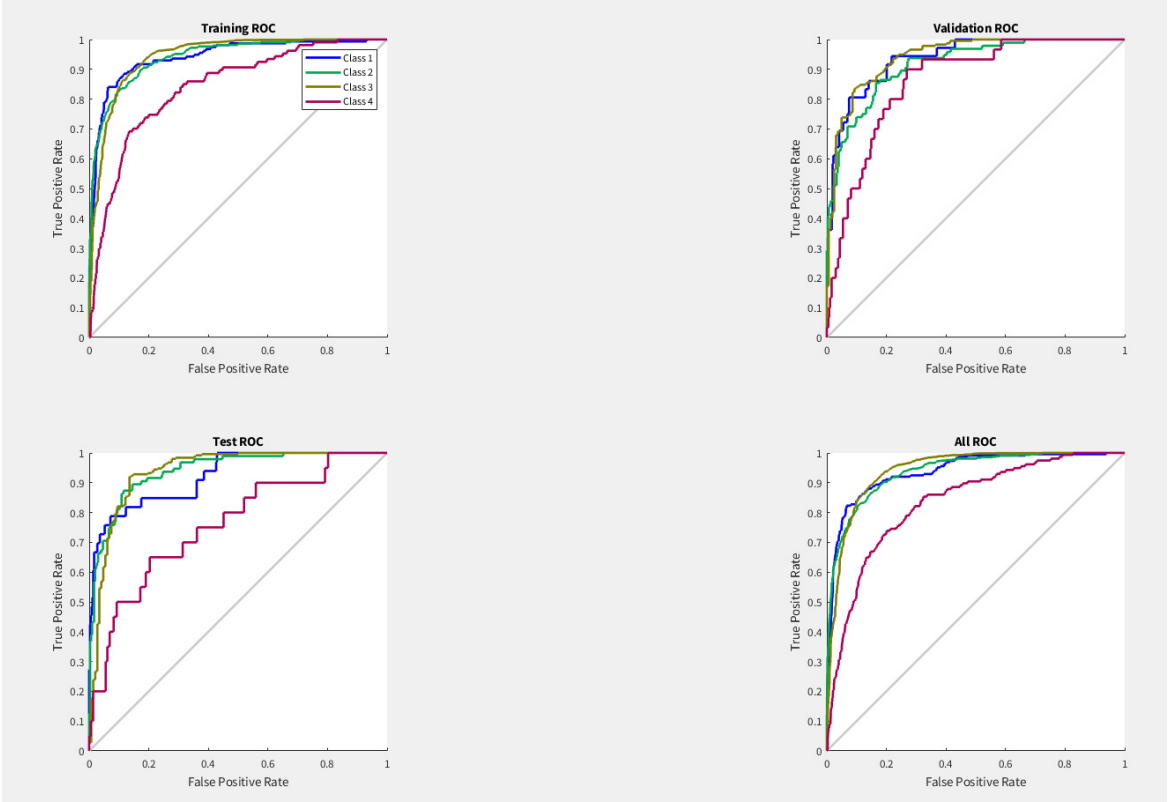


(B) ROC.

FIGURE C.28: Classification results of using a window size of 45x45 pixels, having the first 9 summations of the computed Fourier coefficients of the red component in the feature vector

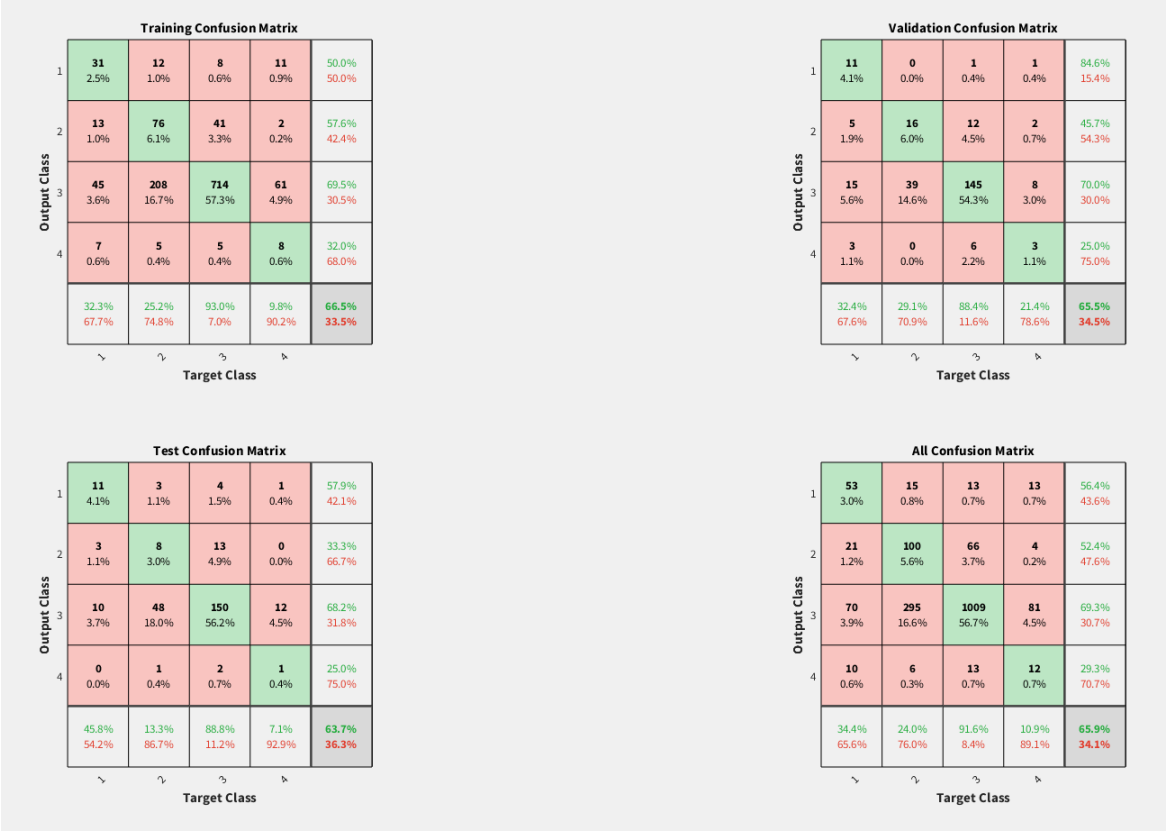


(A) Confusion matrix.

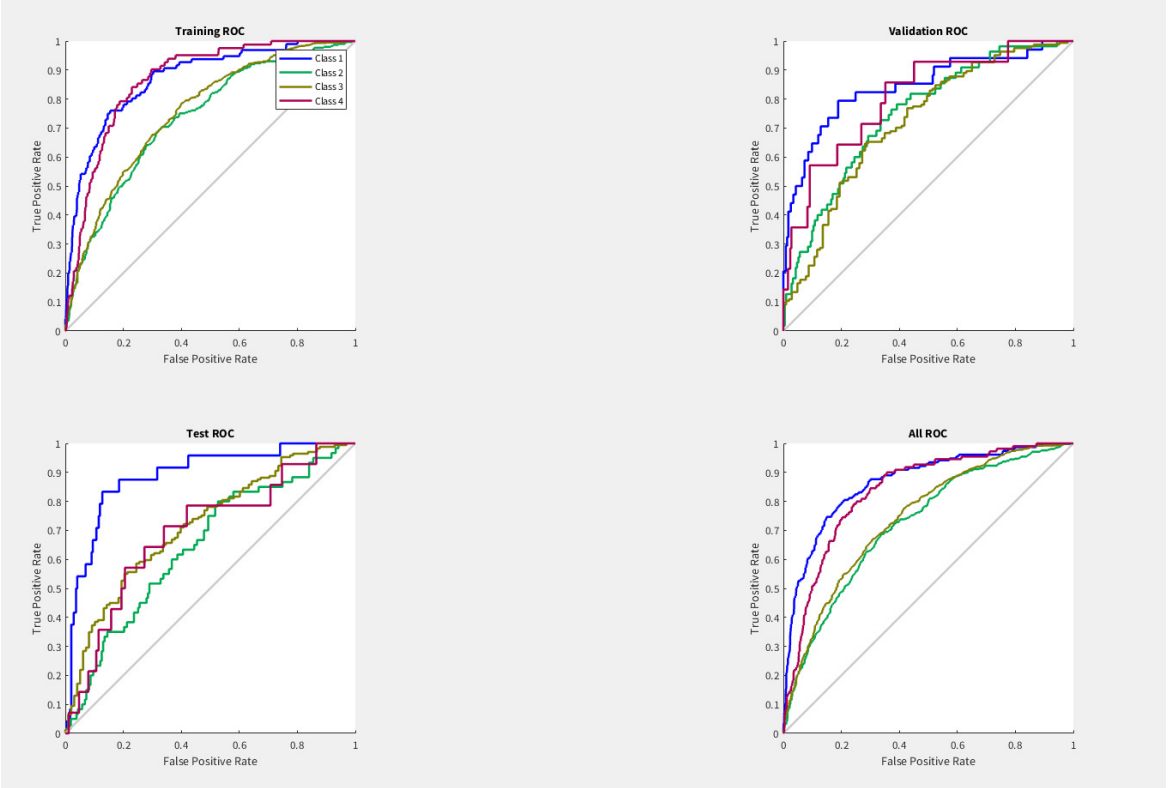


(B) ROC.

FIGURE C.29: Classification results of using a window size of 45x45 pixels, having the first 9 summations of the computed Fourier coefficients of the red and green components in the feature vector

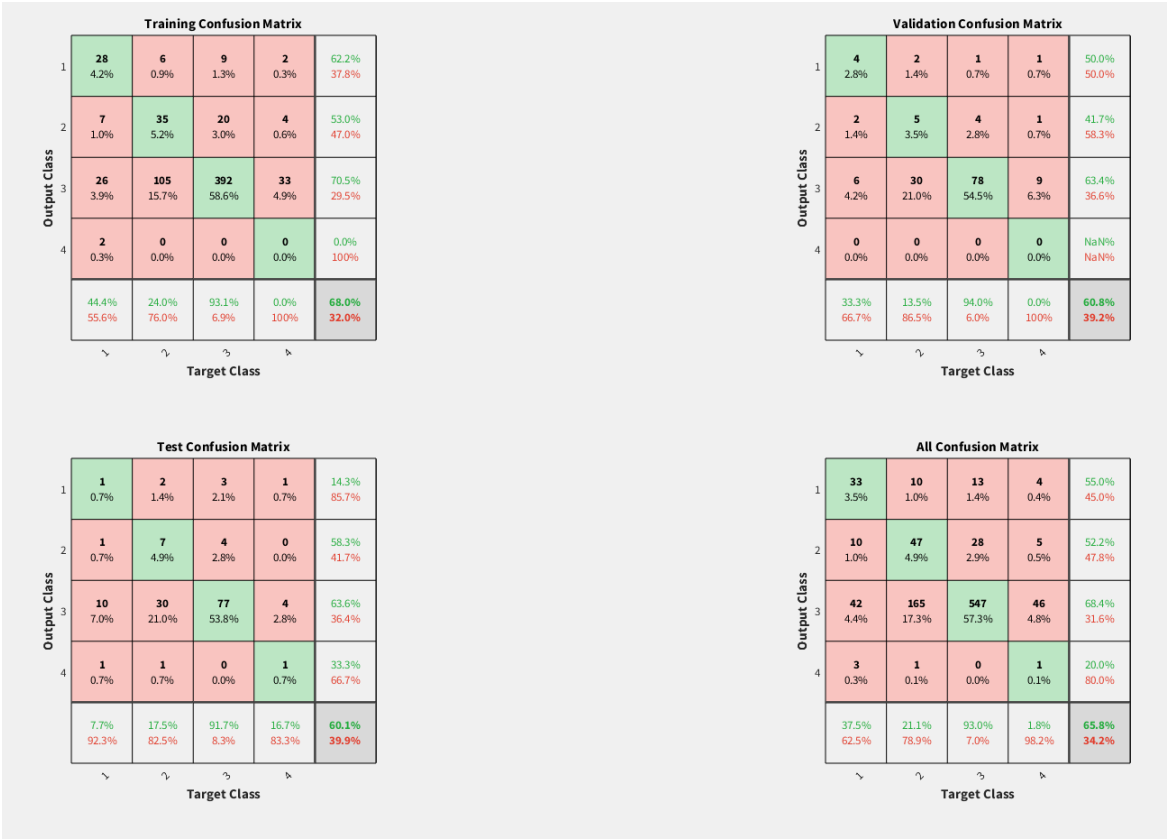


(A) Confusion matrix.

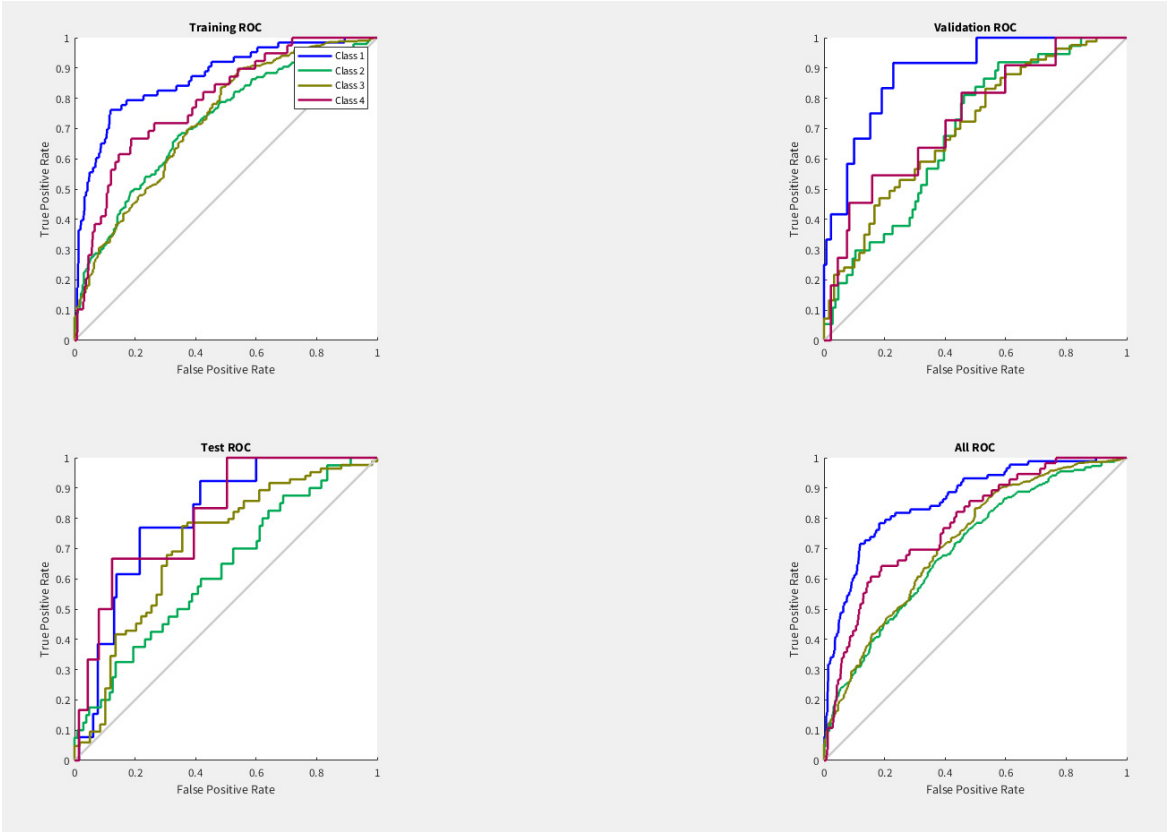


(B) ROC.

FIGURE C.30: Classification results of using a window size of 55x55 pixels, having the first 9 summations of the computed Fourier coefficients of the green component in the feature vector



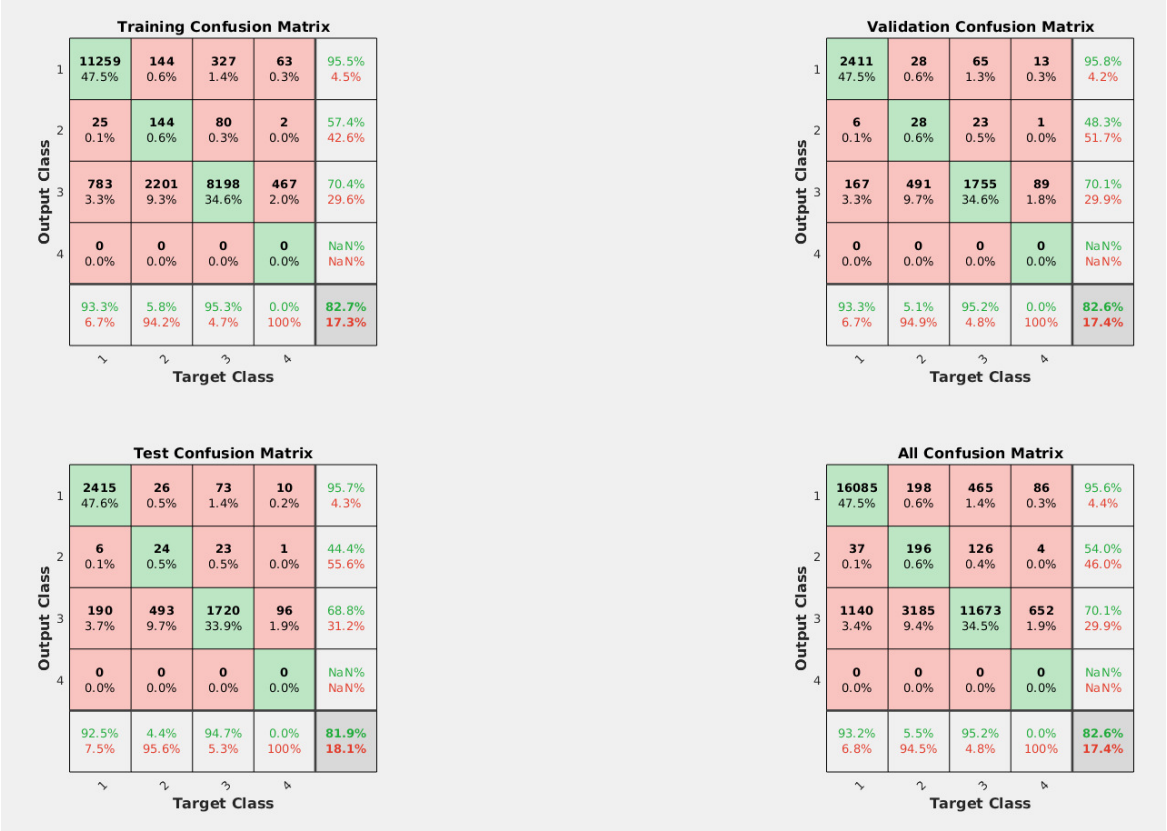
(A) Confusion matrix.



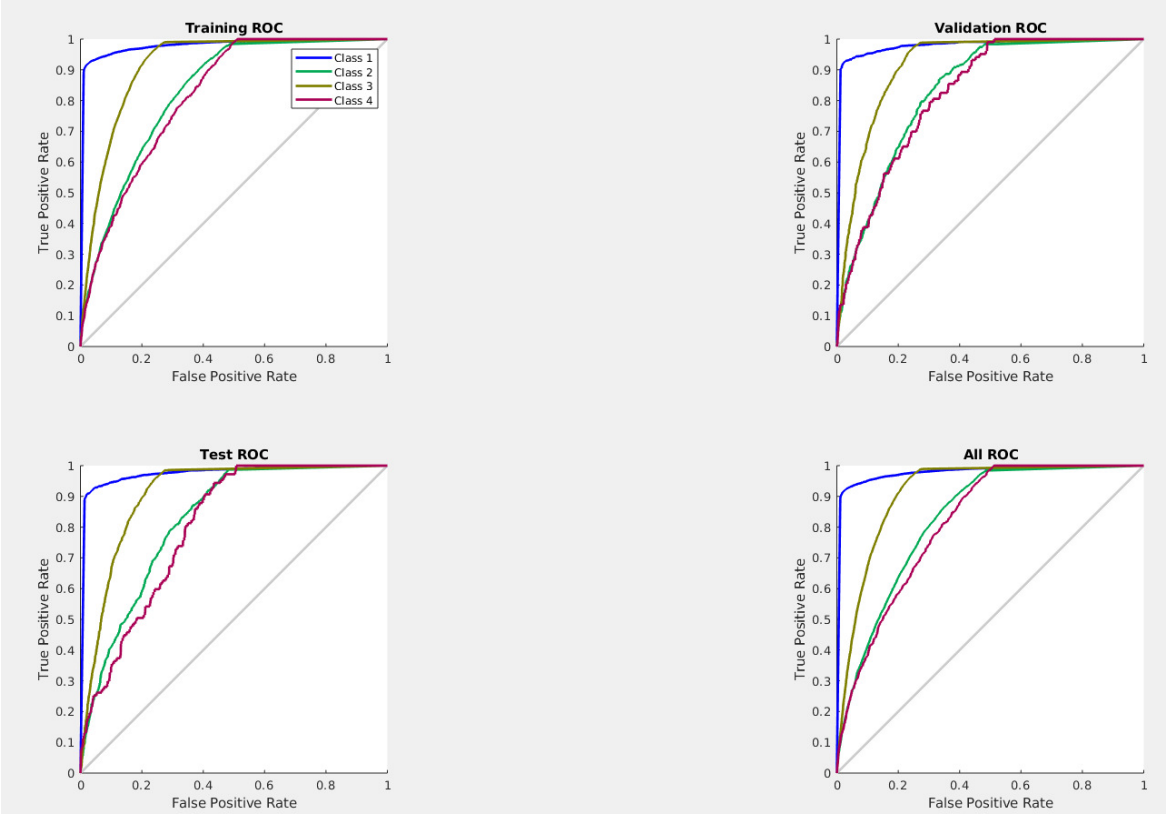
(B) ROC.

FIGURE C.31: Classification results of using a window size of 75x75 pixels, having the first 9 summations of Fourier coefficients of the green component in the feature vector

C.2 Stitched image classification results

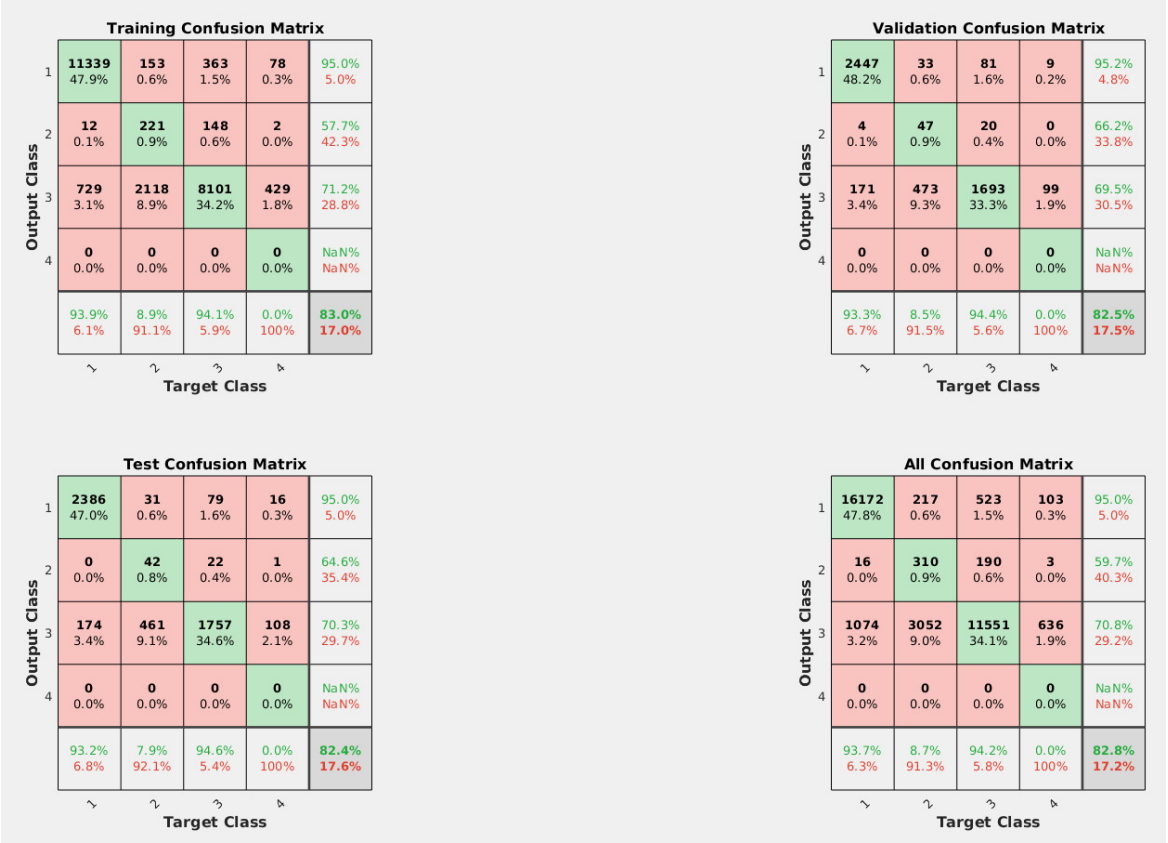


(A) Confusion matrix.

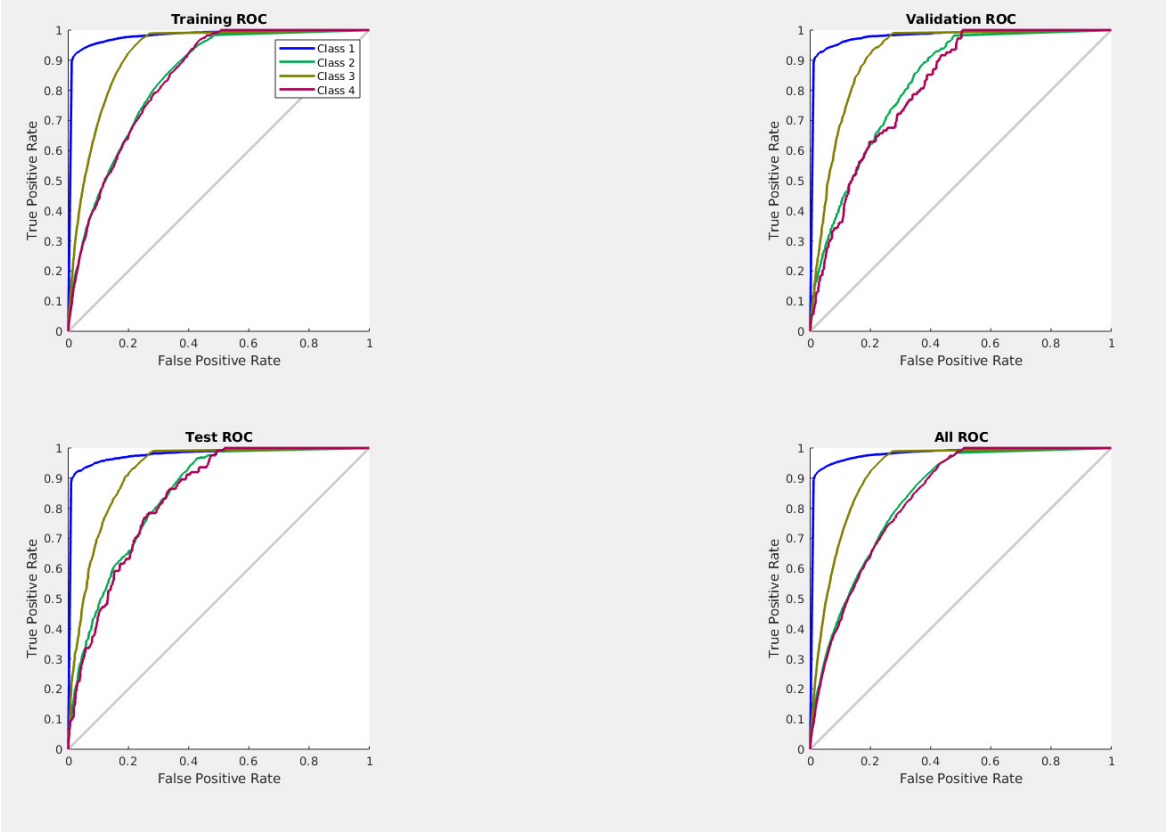


(B) ROC.

FIGURE C.32: Classification results of using a window size of 15x15 pixels, having the first 9 summations of the computed Fourier coefficients of the green component in the feature vector

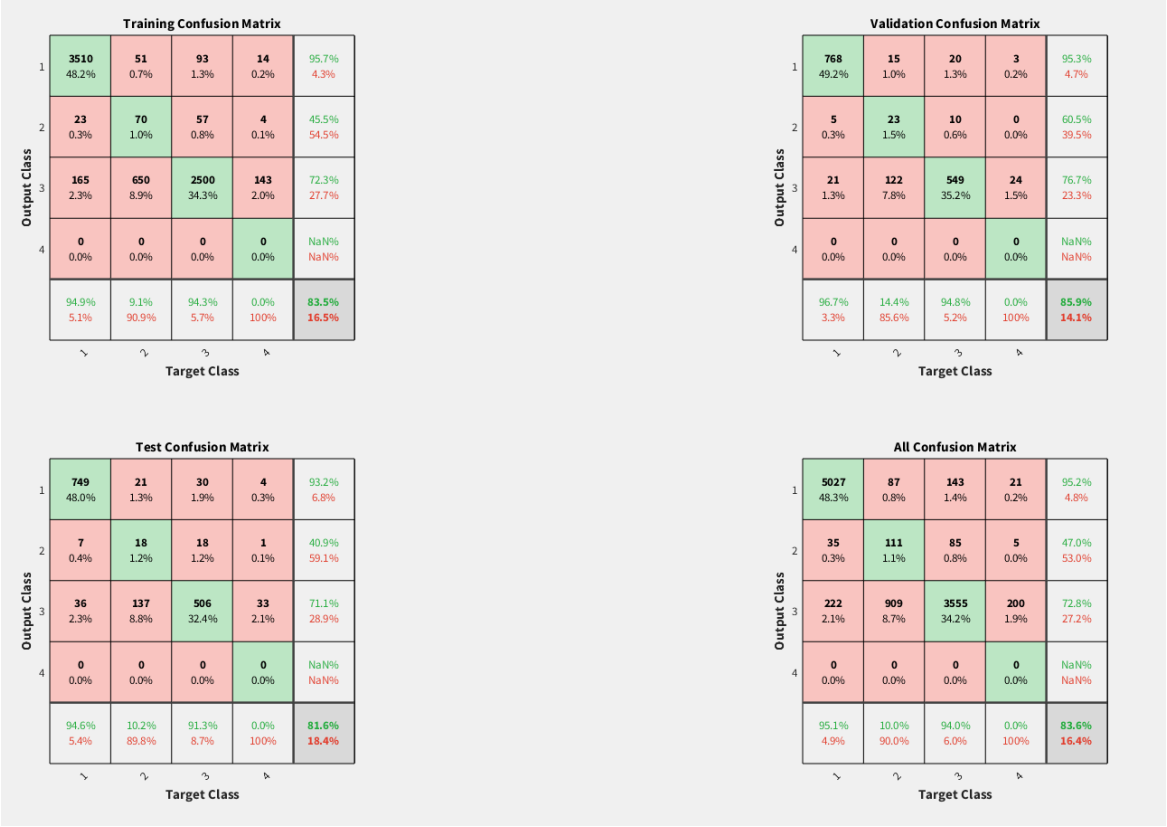


(A) Confusion matrix.

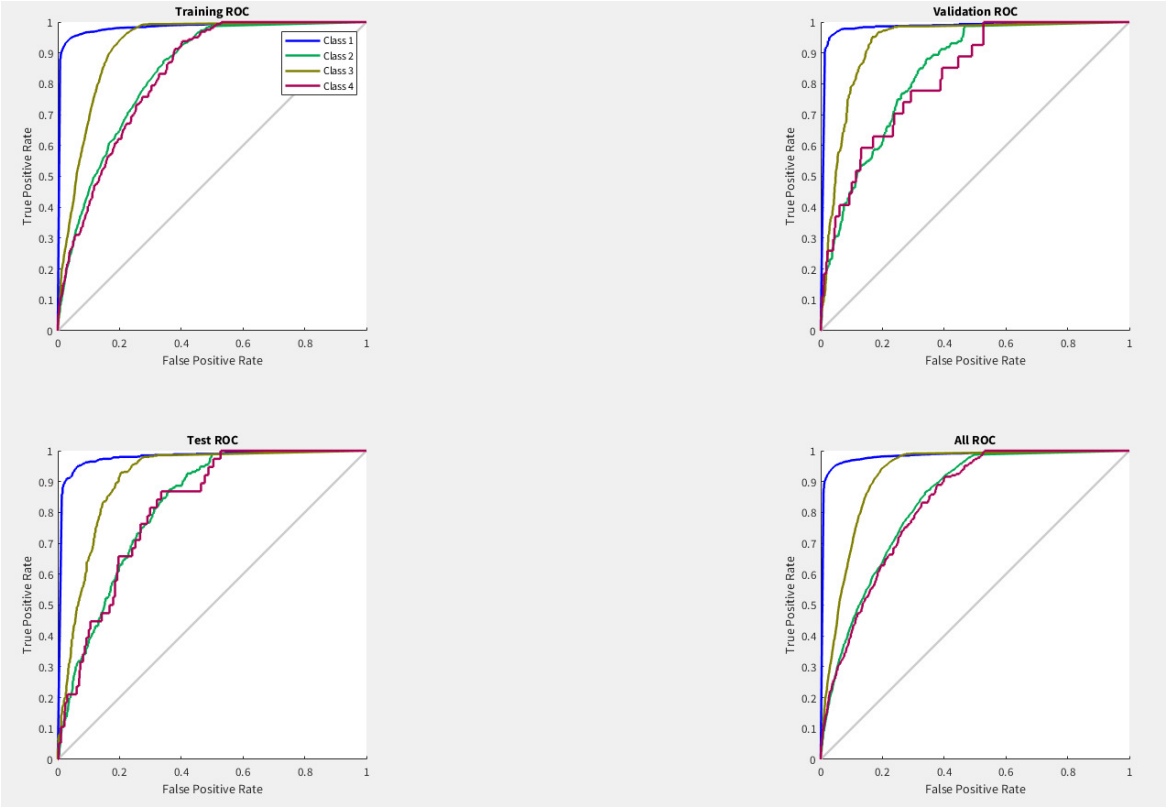


(B) ROC.

FIGURE C.33: Classification results of using a window size of 15x15 pixels, having the first 19 summations of the computed Fourier coefficients of the green component in the feature vector

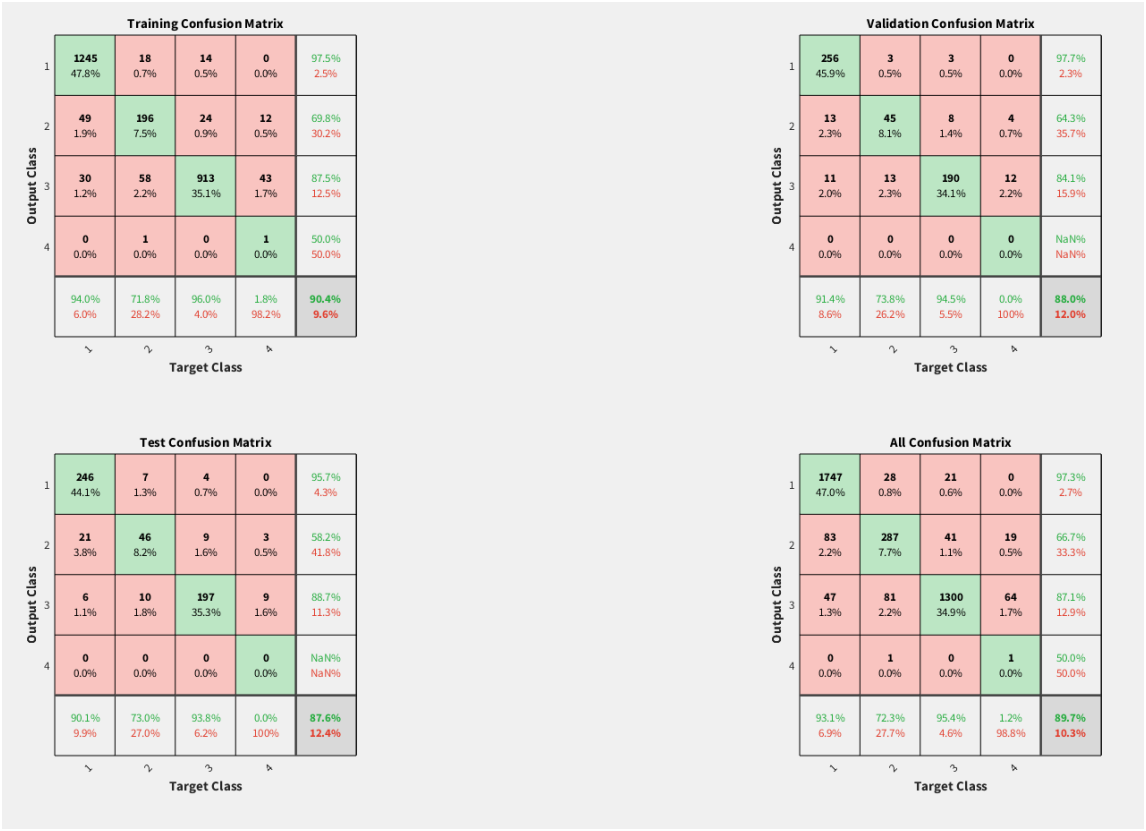


(A) Confusion matrix.

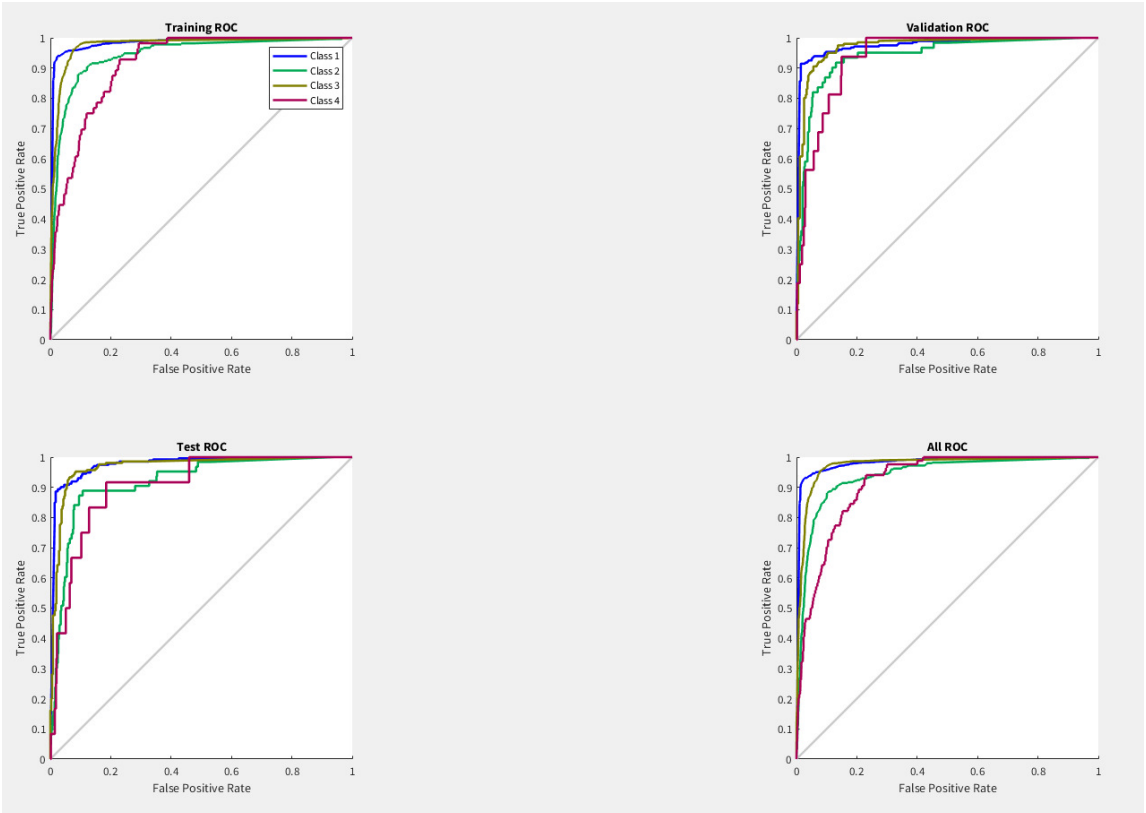


(B) ROC.

FIGURE C.34: Classification results of using a window size of 27x27 pixels, having the first 9 summations of the computed Fourier coefficients of the green component in the feature vector

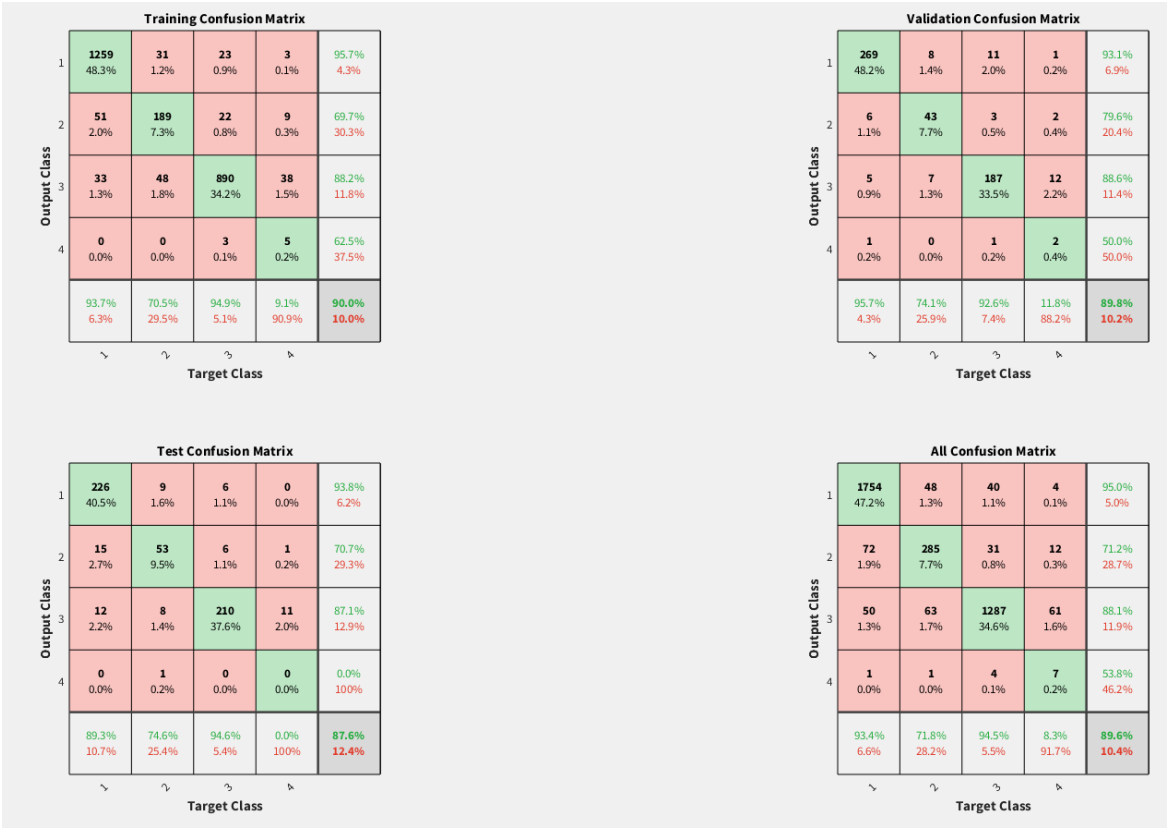


(A) Confusion matrix.

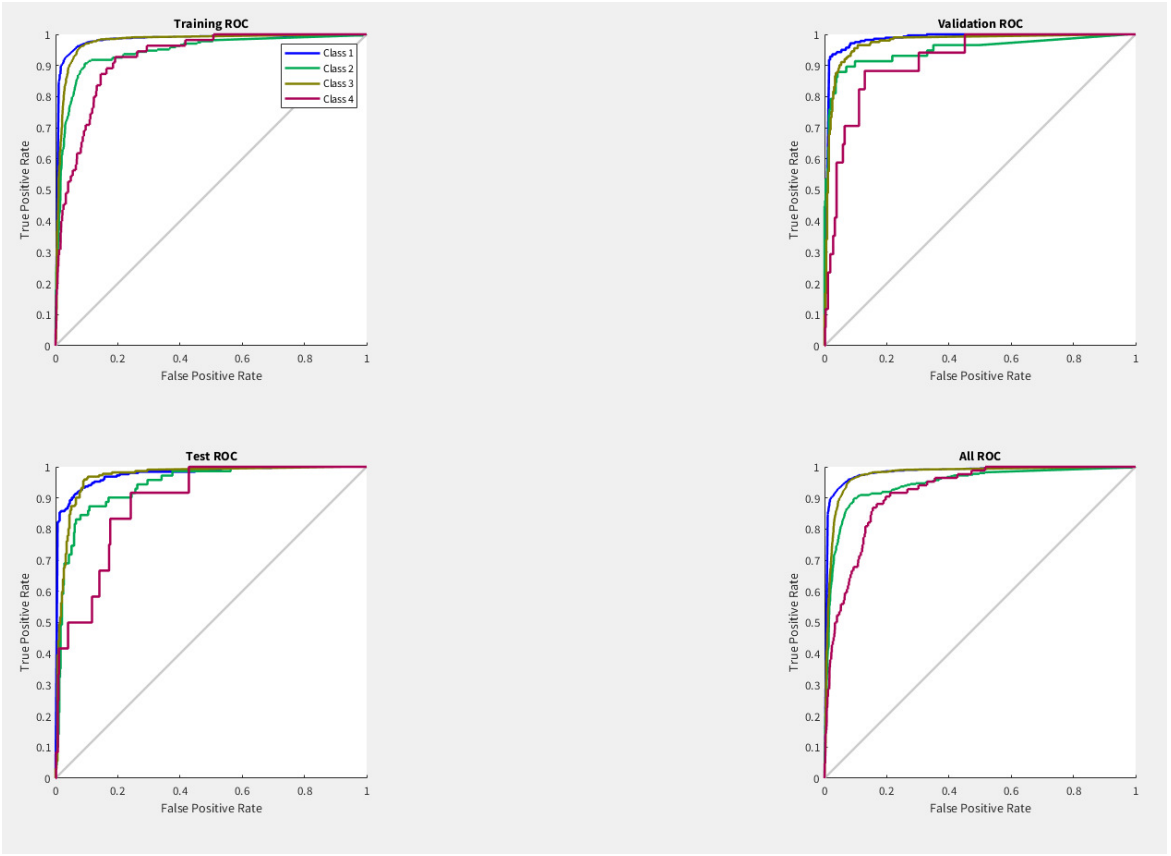


(B) ROC.

FIGURE C.35: Classification results of using a window size of 45x45 pixels, having the first 3 summations of the computed Fourier coefficients of the hue, saturation, value, red, green and blue components in the feature vector



(A) Confusion matrix.

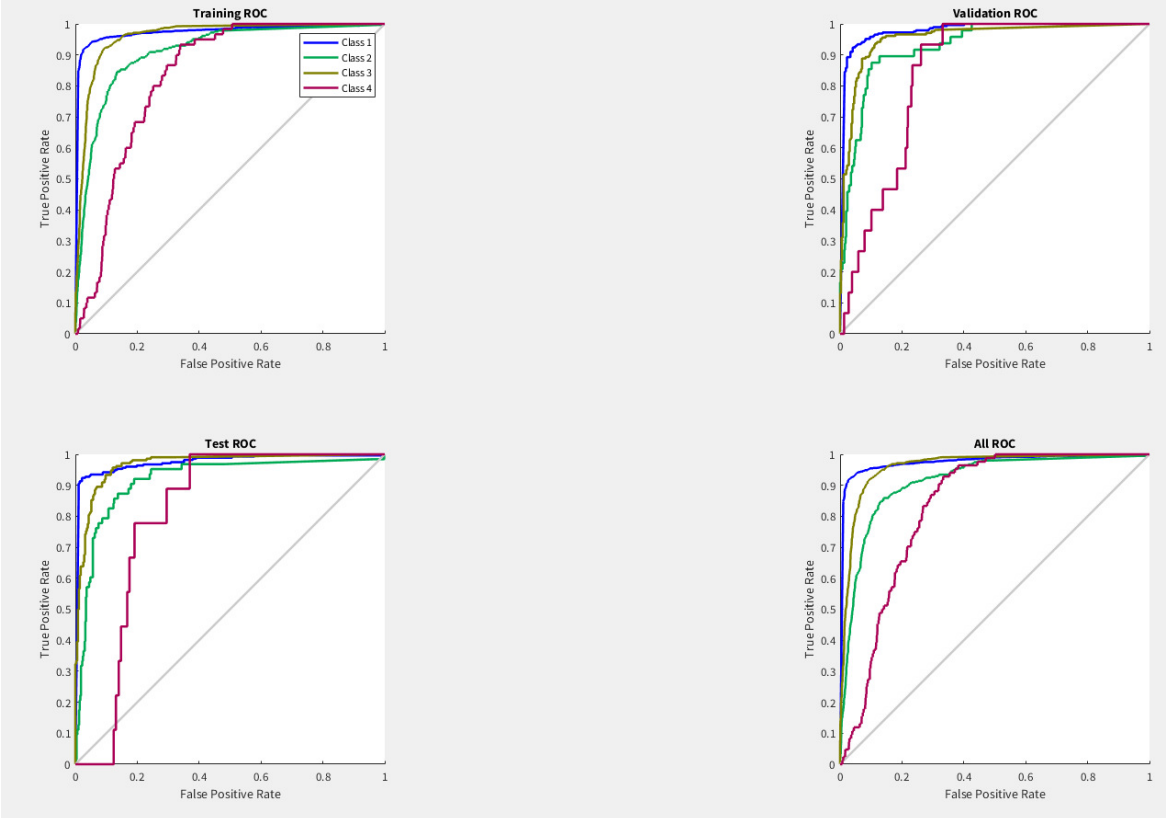


(B) ROC.

FIGURE C.36: Classification results of using a window size of 45x45 pixels, having the first 4 summations of the computed Fourier coefficients of the green and blue components, and the ExR index in the feature vector

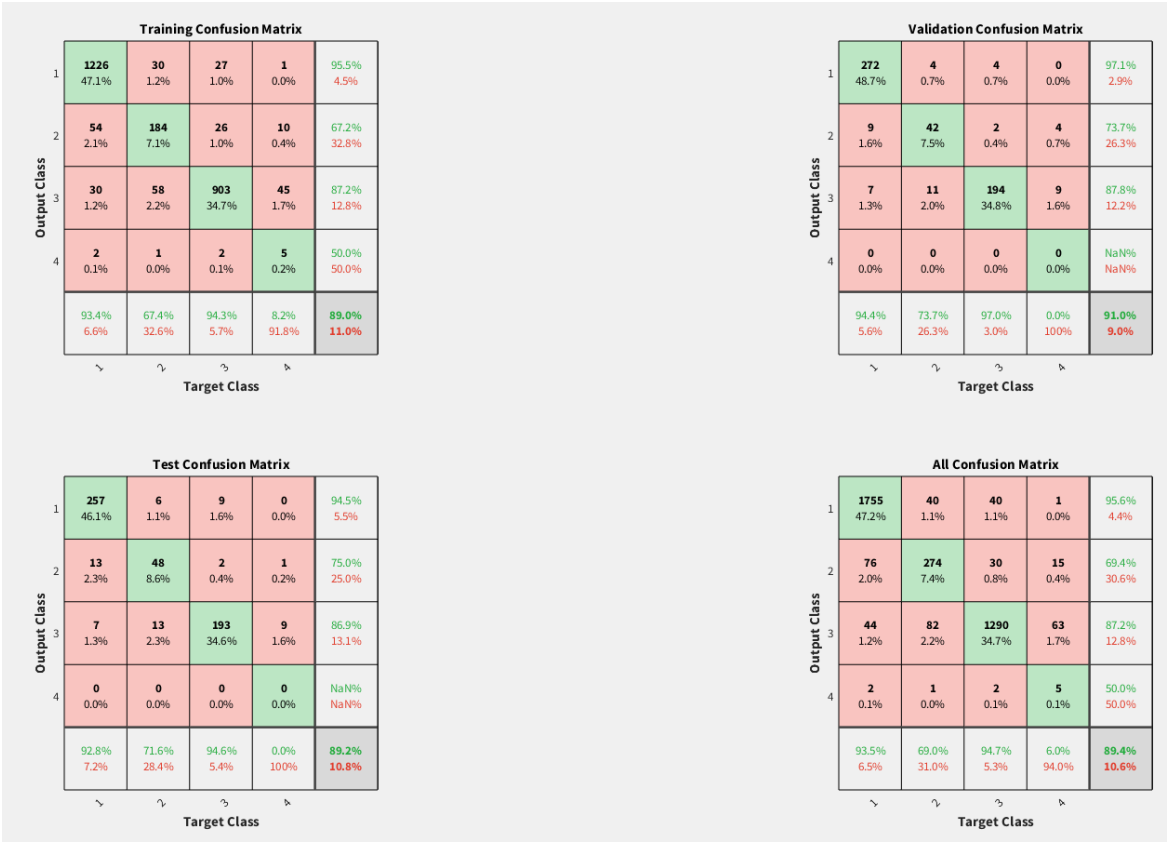


(A) Confusion matrix.

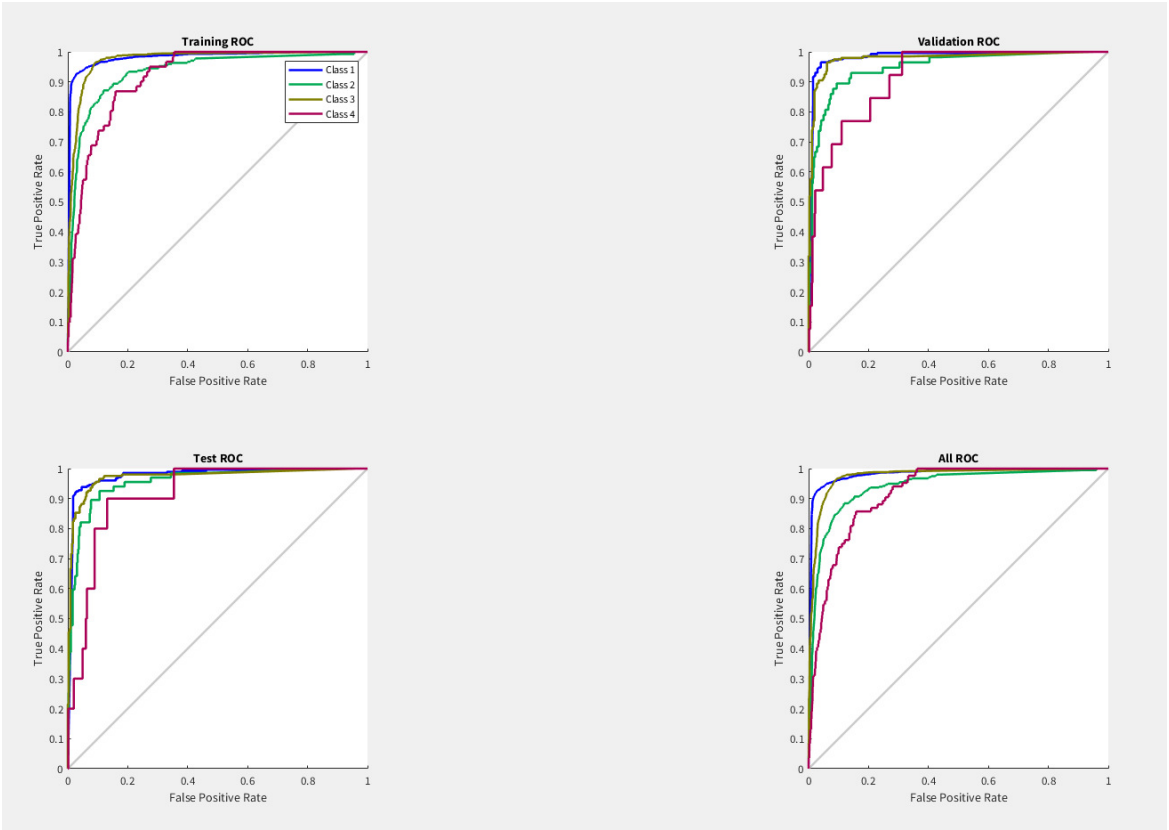


(B) ROC.

FIGURE C.37: Classification results of using a window size of 45x45 pixels, having the first 4 summations of the computed Fourier coefficients of the hue, saturation and value components in the feature vector

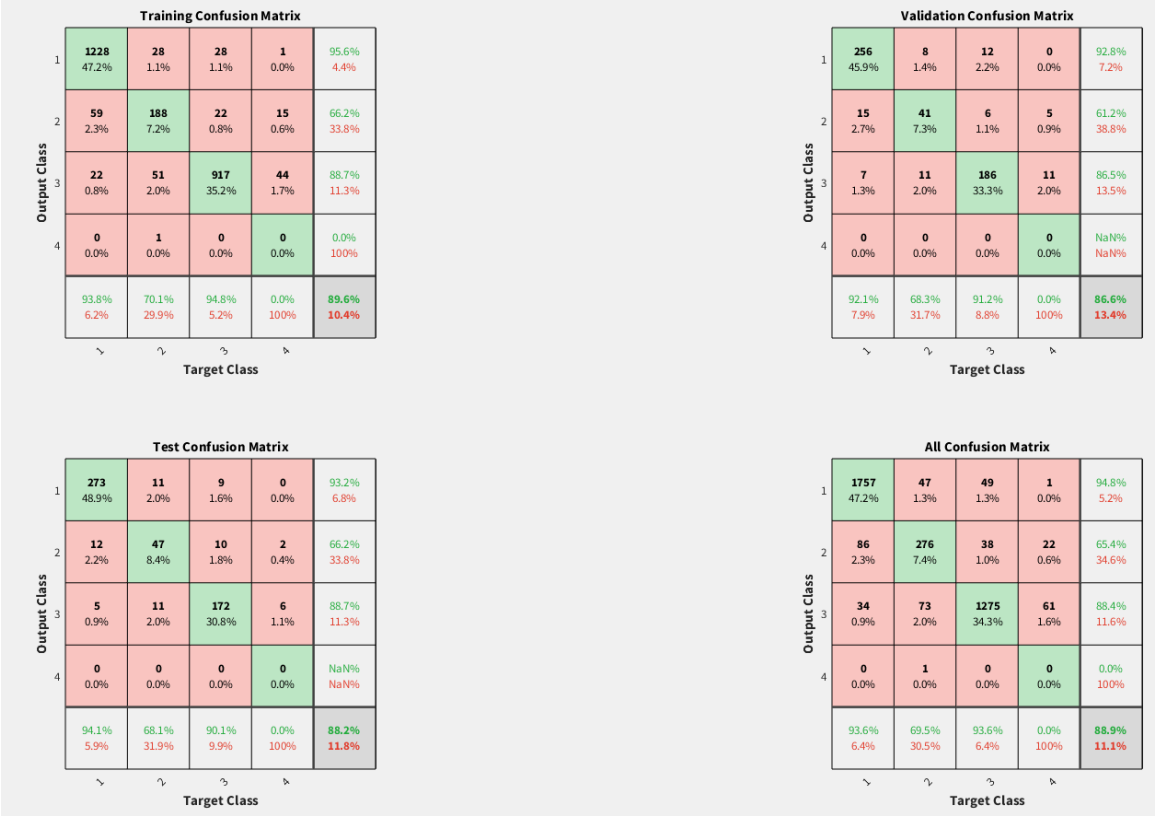


(A) Confusion matrix.

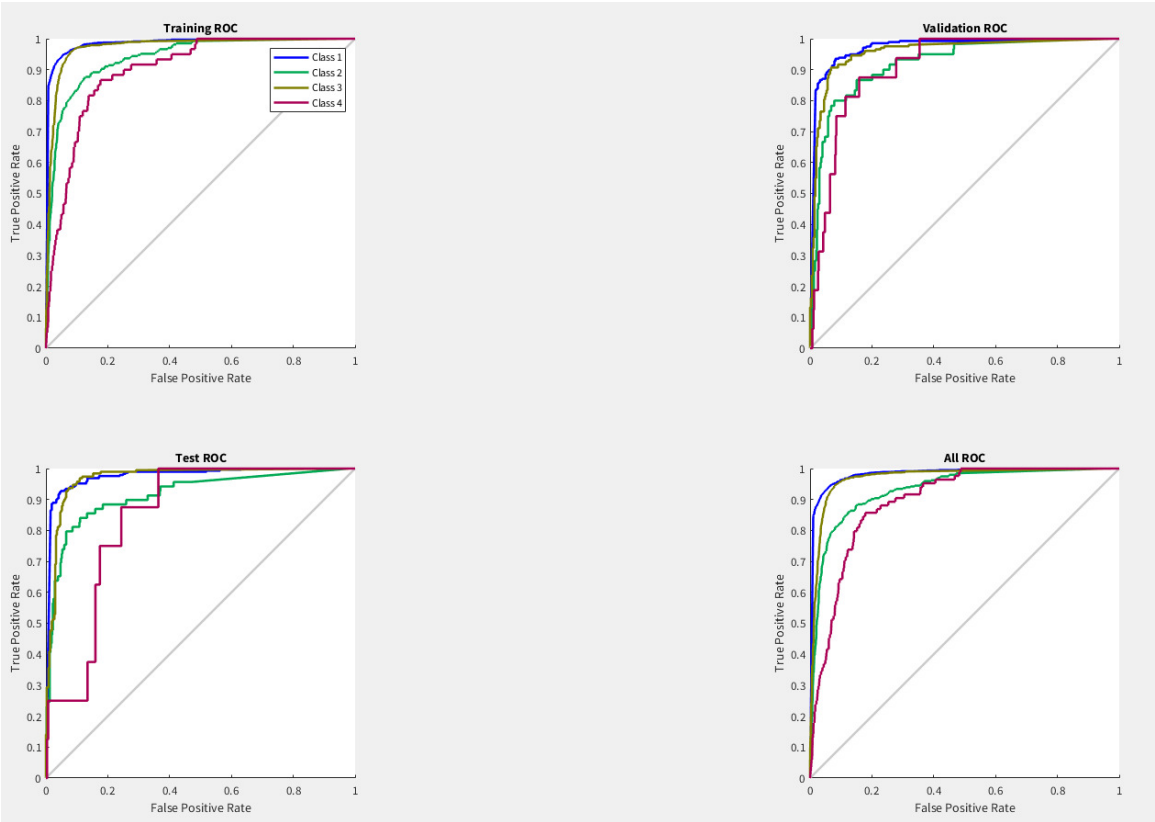


(B) ROC.

FIGURE C.38: Classification results of using a window size of 45x45 pixels, having the first 4 summations of the computed Fourier coefficients of the hue, saturation, value, red, green and blue components in the feature vector

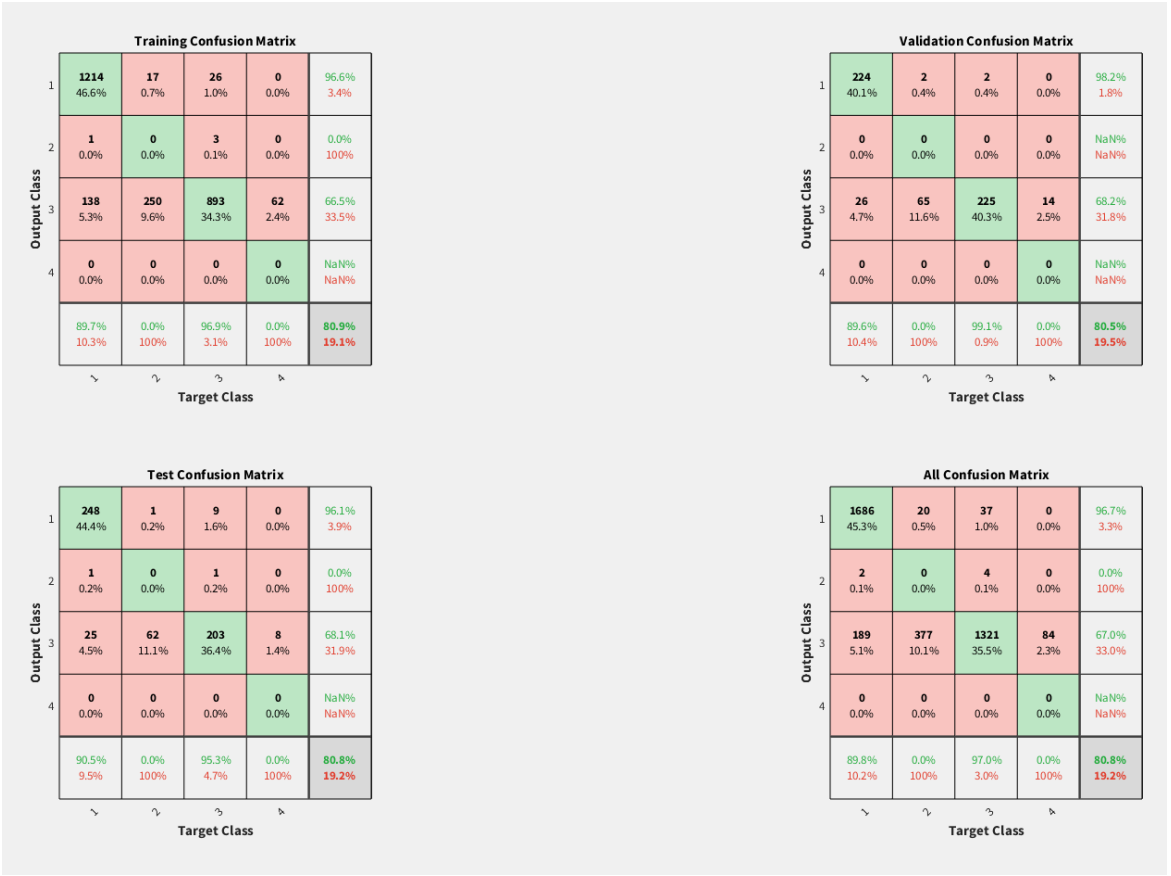


(A) Confusion matrix.

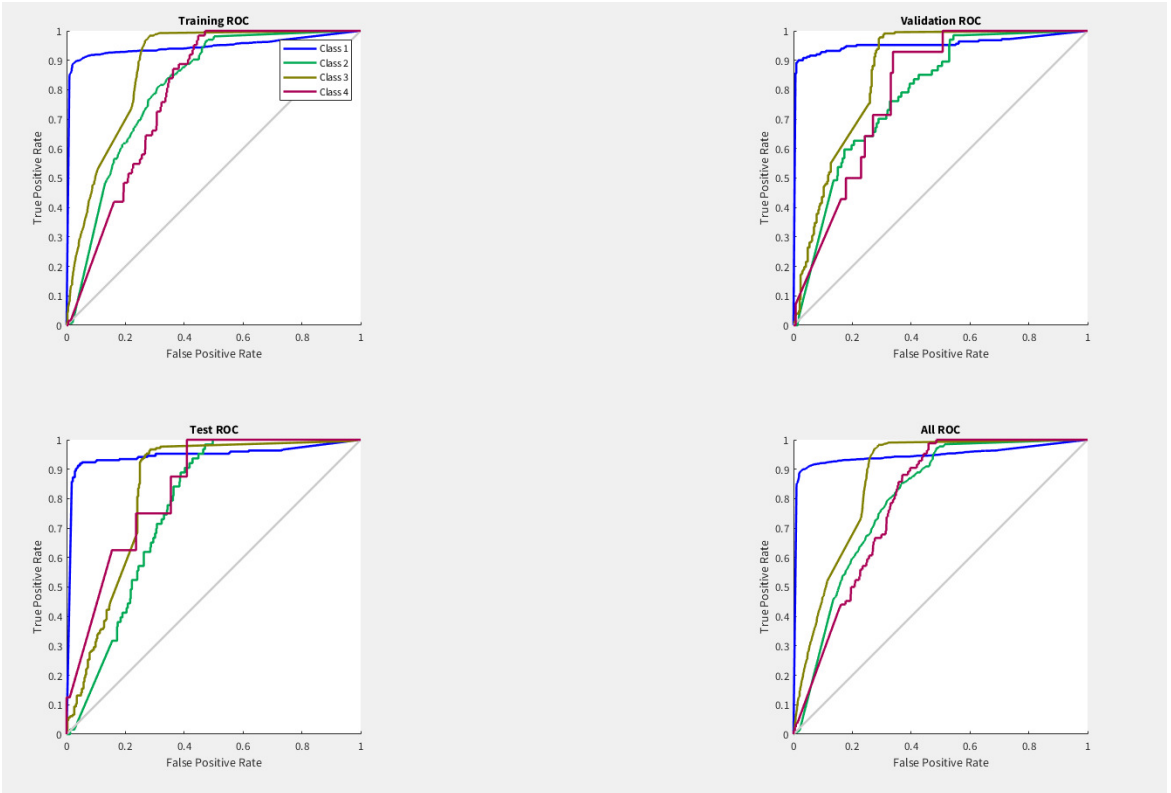


(B) ROC.

FIGURE C.39: Classification results of using a window size of 45x45 pixels, having the first 4 summations of the computed Fourier coefficients of the red, green and blue components in the feature vector

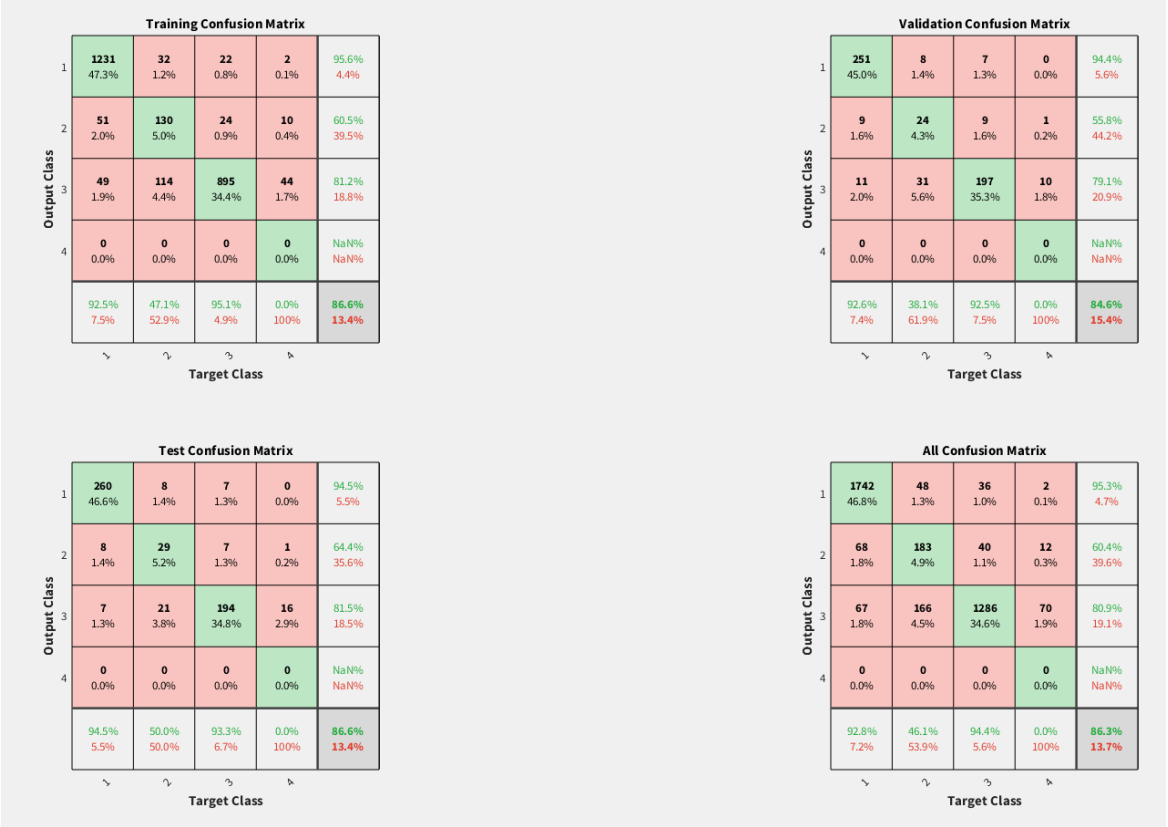


(A) Confusion matrix.

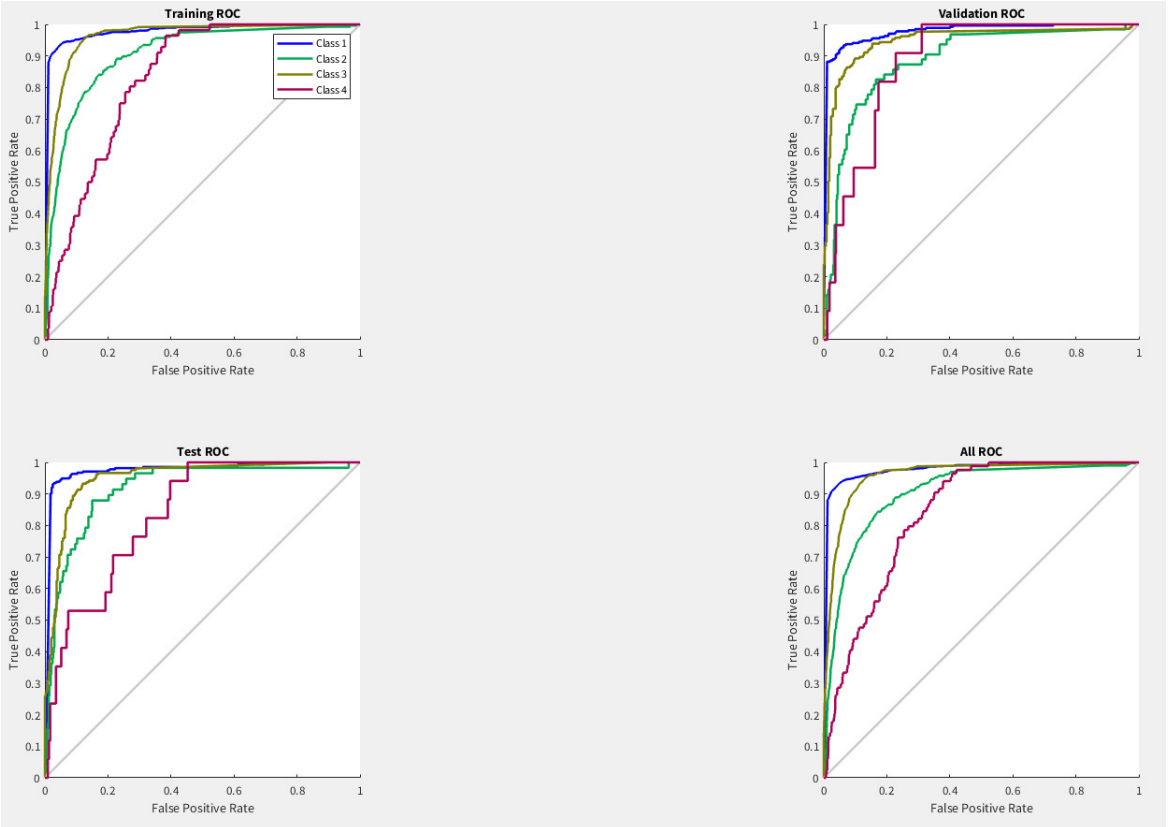


(B) ROC.

FIGURE C.40: Classification results of using a window size of 45x45 pixels, having the first 9 summations of the computed Fourier coefficients of the blue component in the feature vector

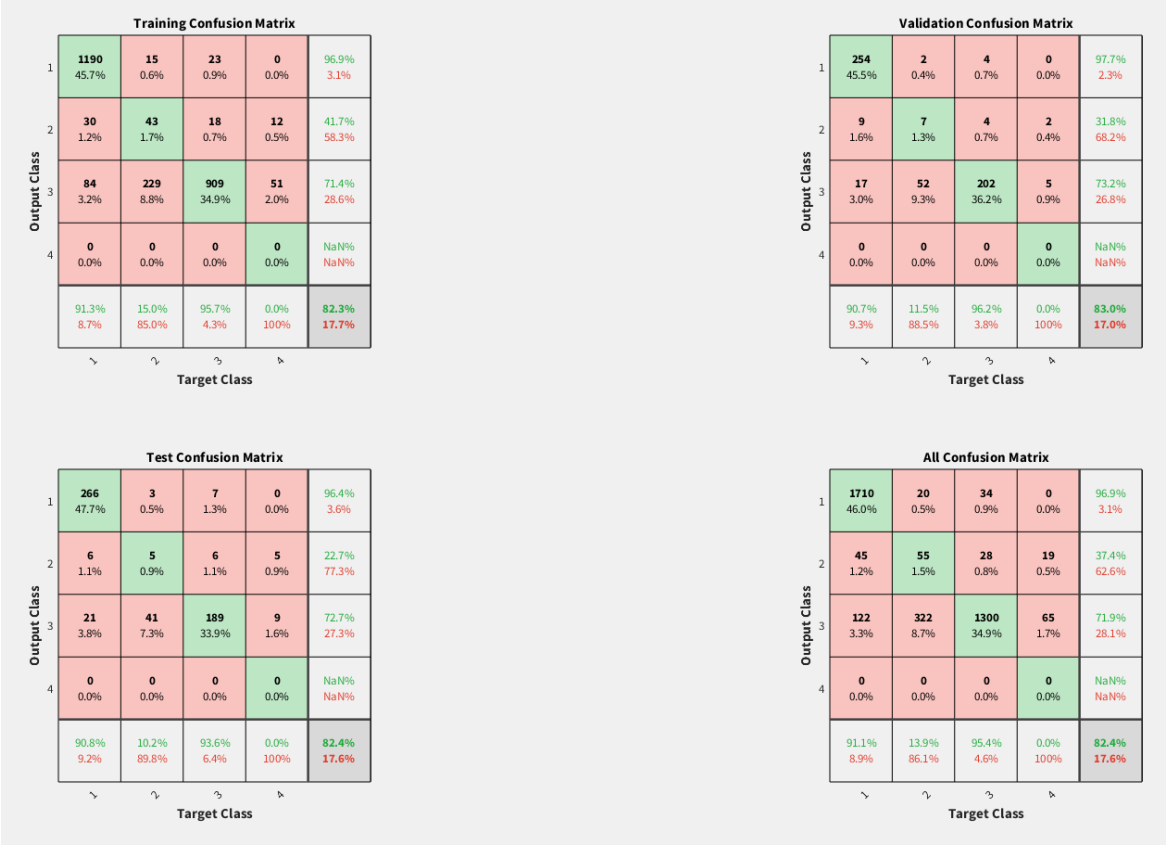


(A) Confusion matrix.

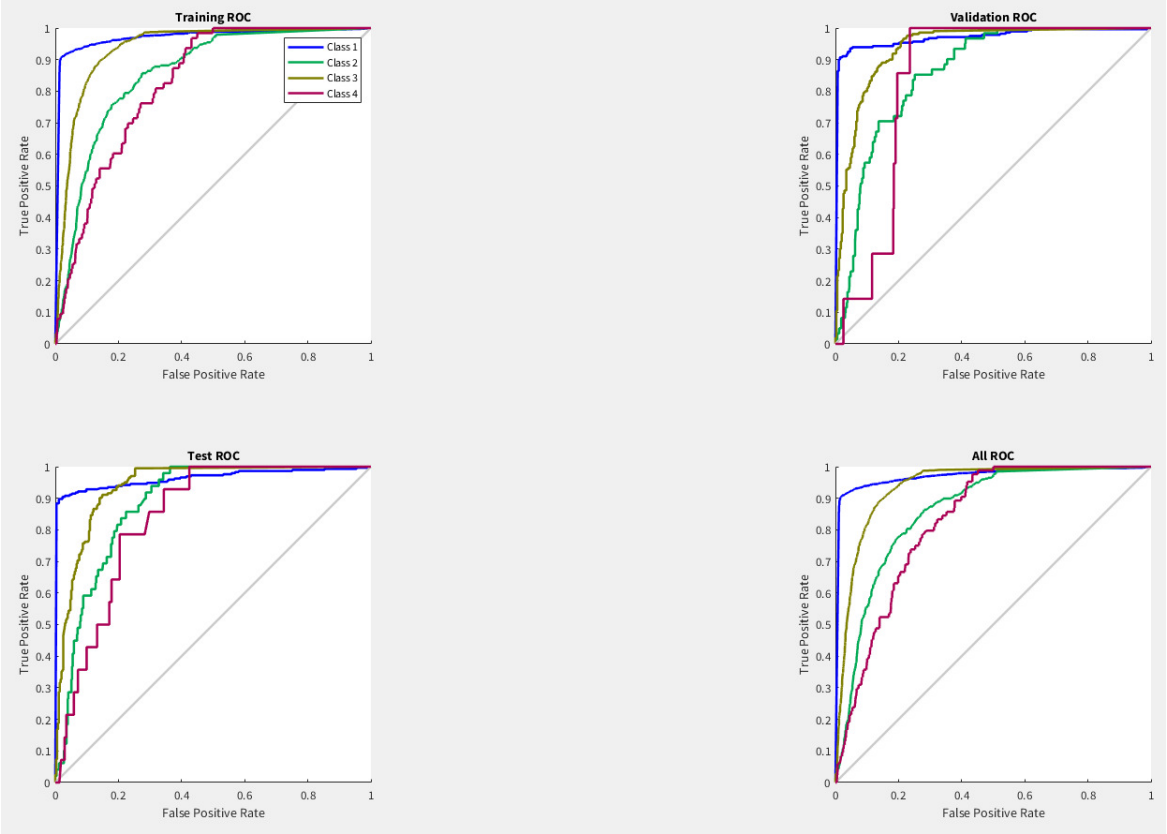


(B) ROC.

FIGURE C.41: Classification results of using a window size of 45x45 pixels, having the first 9 summations of the computed Fourier coefficients of the hue component in the feature vector

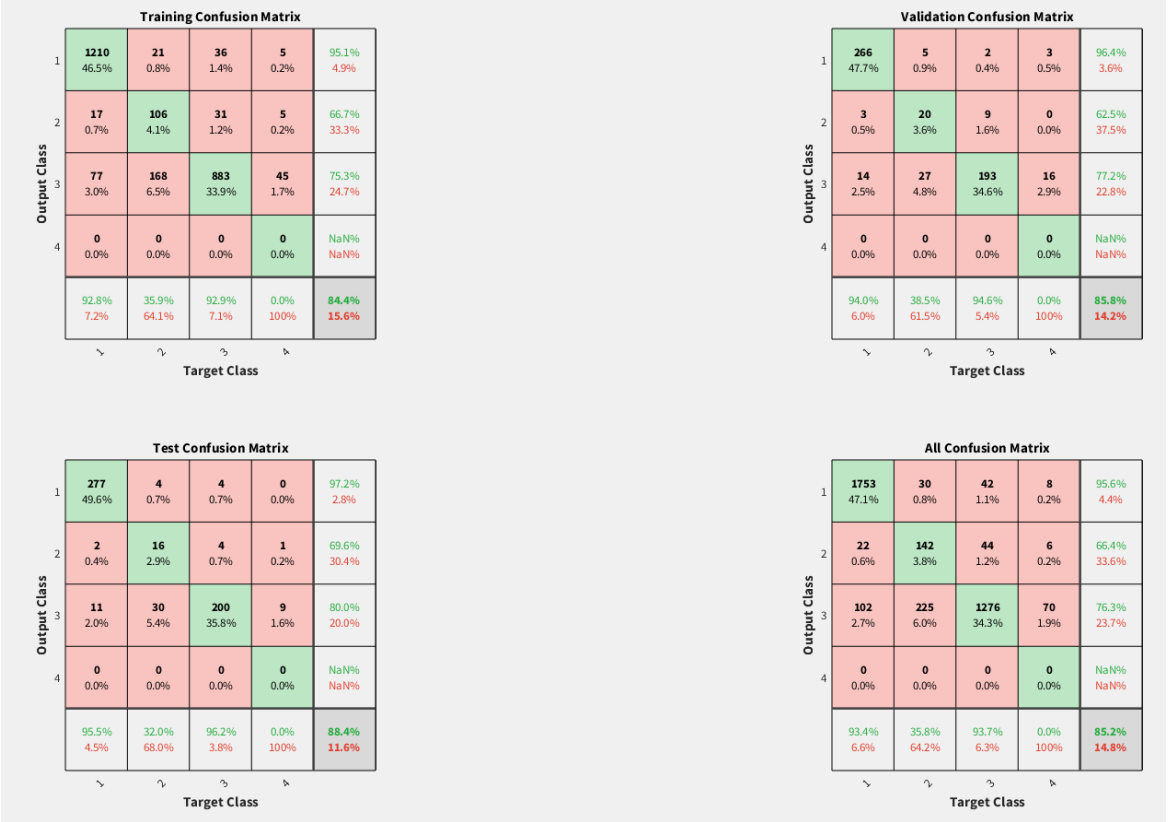


(A) Confusion matrix.

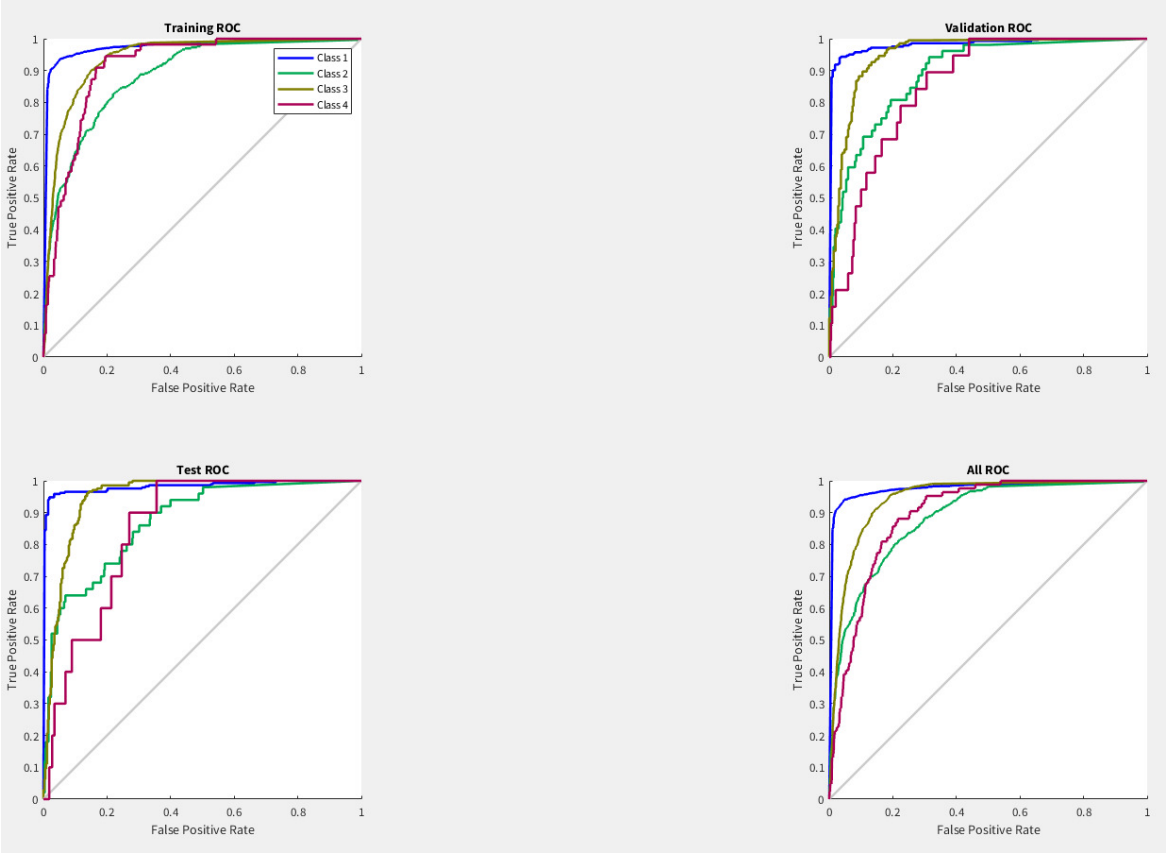


(B) ROC.

FIGURE C.42: Classification results of using a window size of 45x45 pixels, having the first 9 summations of the computed Fourier coefficients of the saturation component in the feature vector

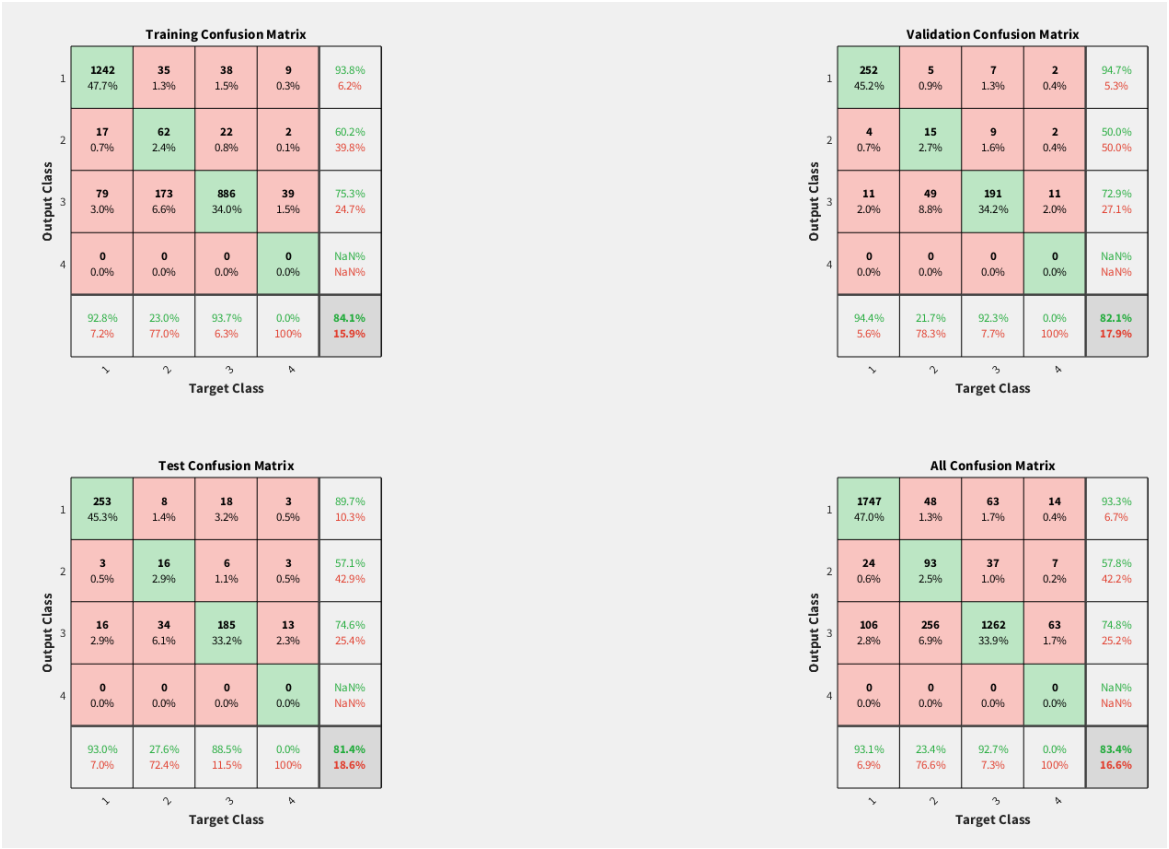


(A) Confusion matrix.

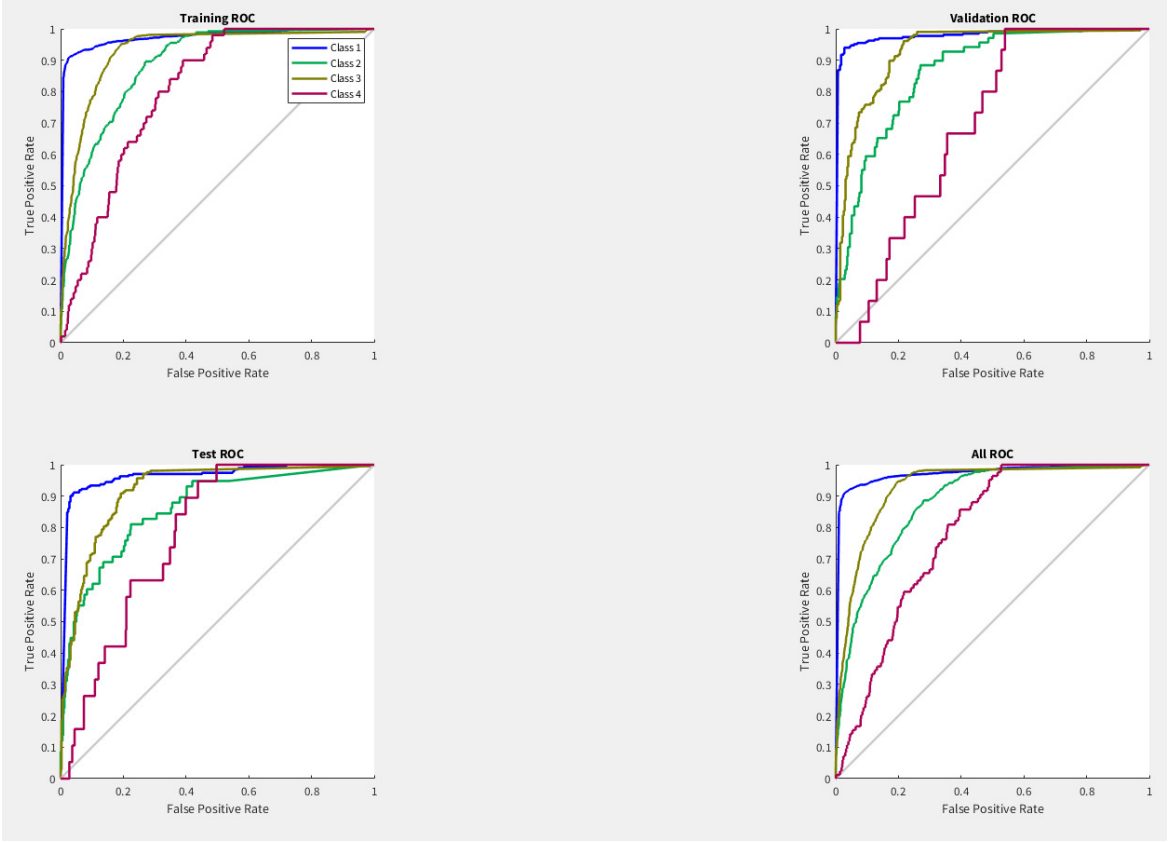


(B) ROC.

FIGURE C.43: Classification results of using a window size of 45x45 pixels, having the first 9 summations of the computed Fourier coefficients of the value component in the feature vector

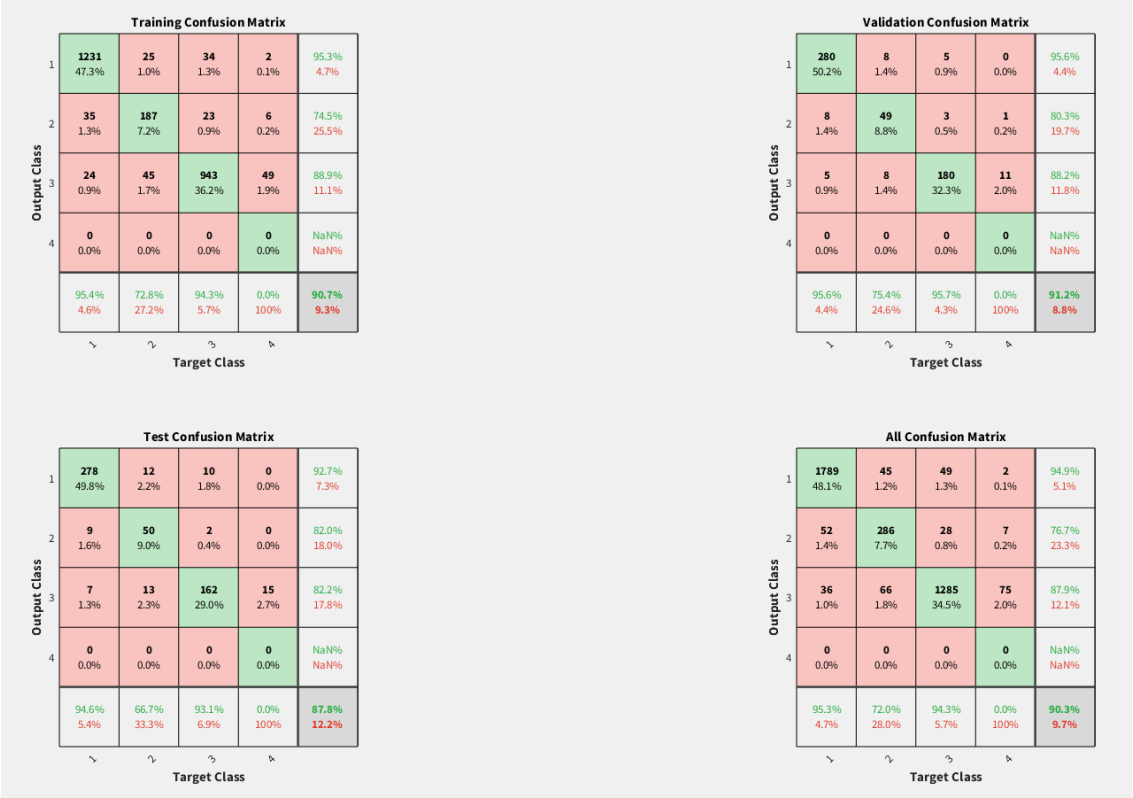


(A) Confusion matrix.

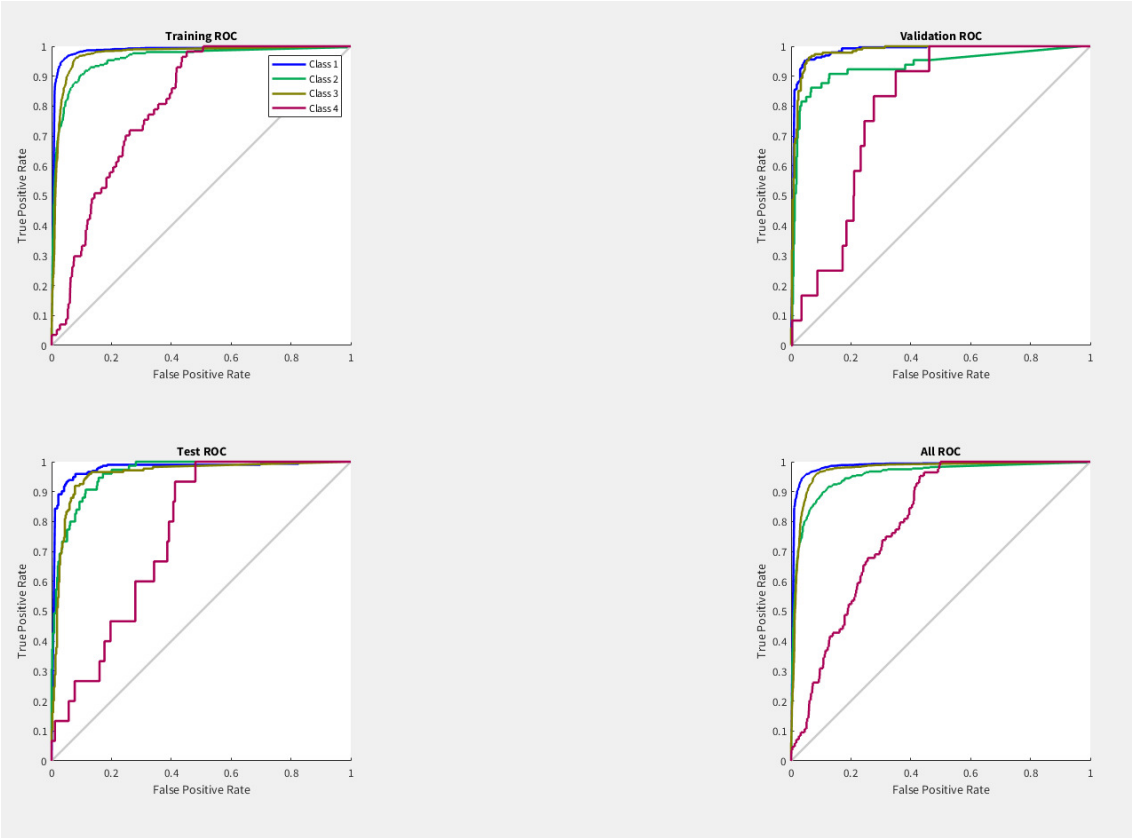


(B) ROC.

FIGURE C.44: Classification results of using a window size of 45x45 pixels, having the first 9 summations of the computed Fourier coefficients of the red component in the feature vector

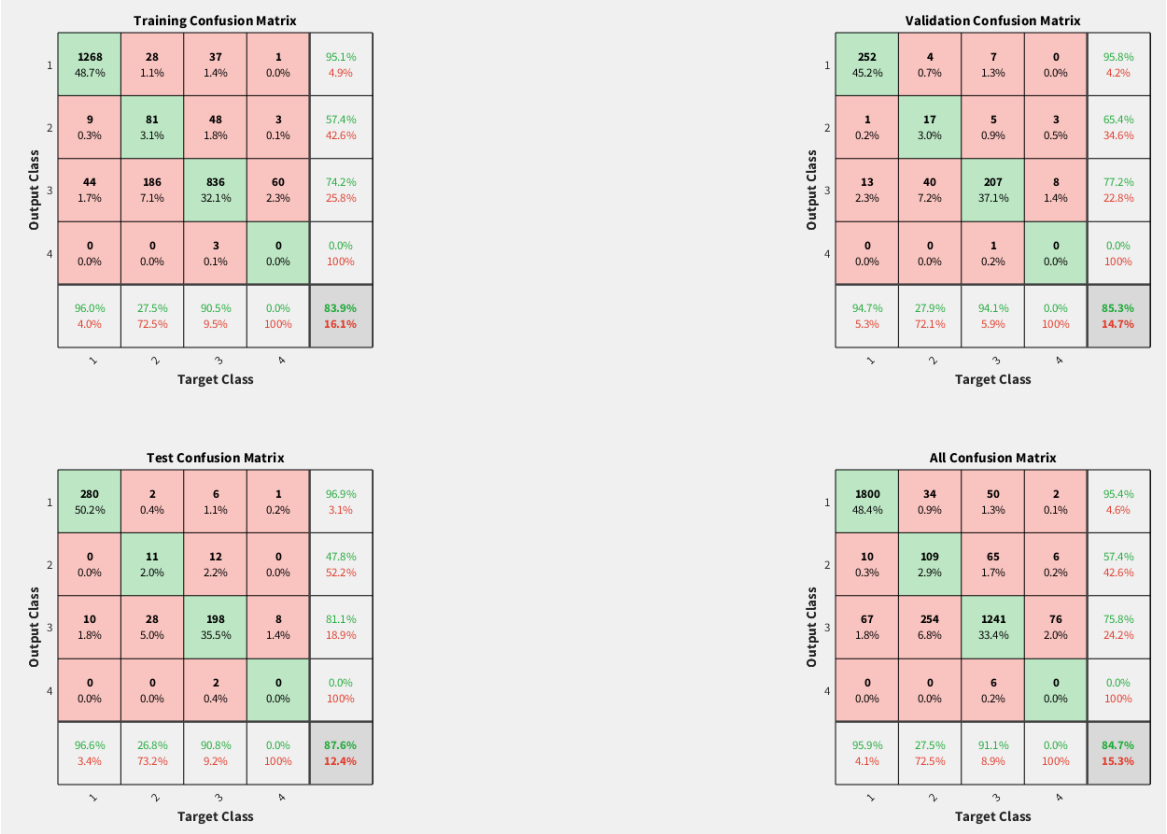


(A) Confusion matrix.

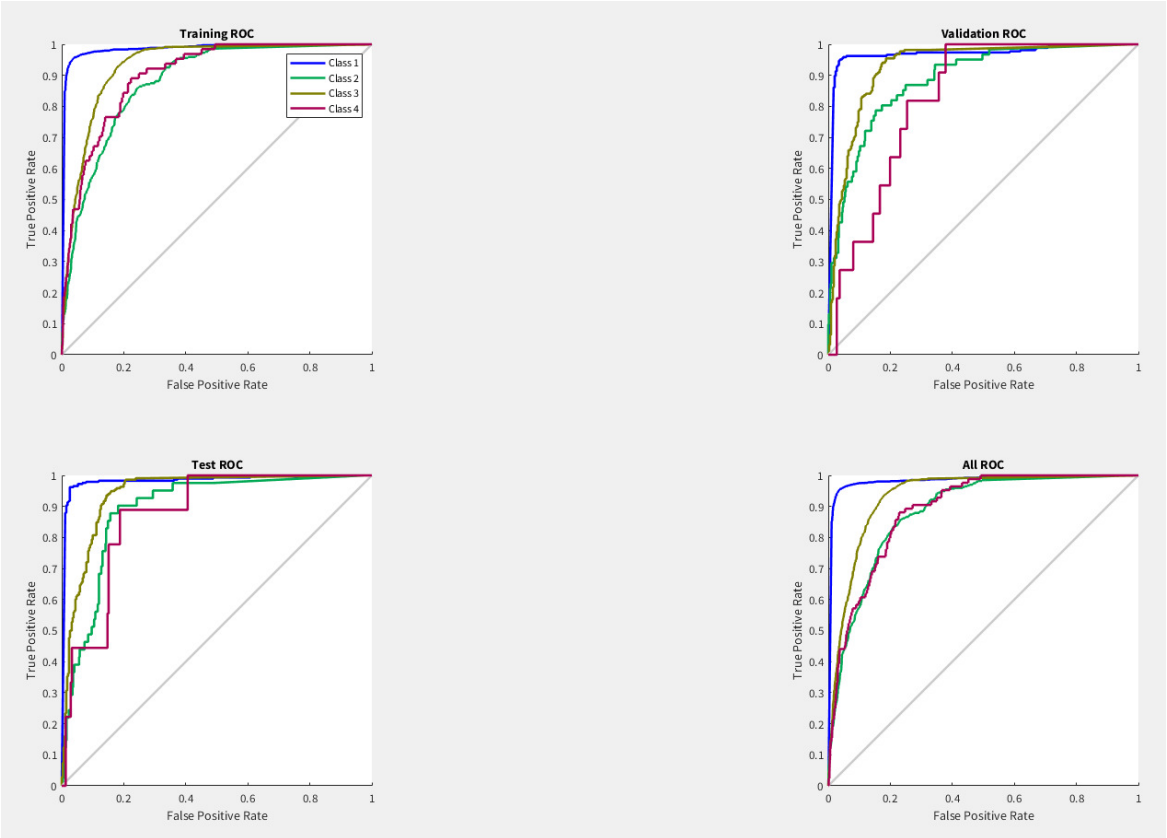


(B) ROC.

FIGURE C.45: Classification results of using a window size of 45x45 pixels, having the first 9 summations of the computed Fourier coefficients of the red, green and blue components in the feature vector

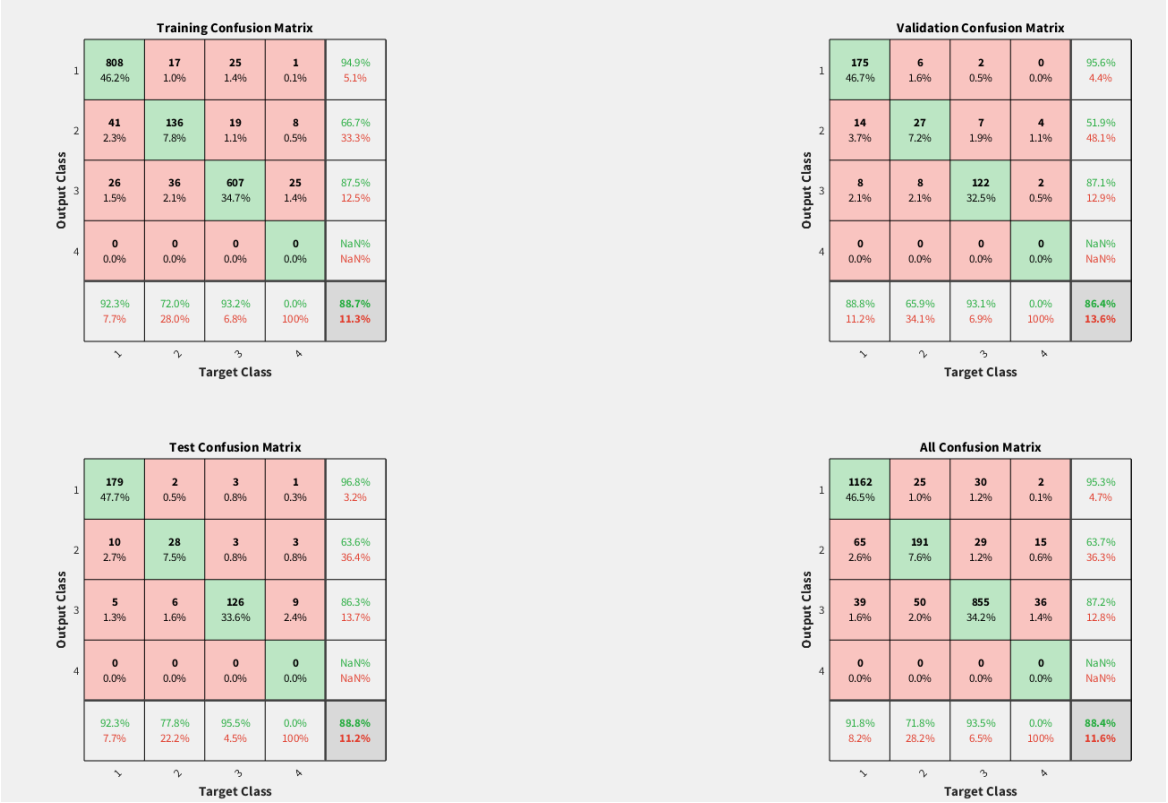


(A) Confusion matrix.

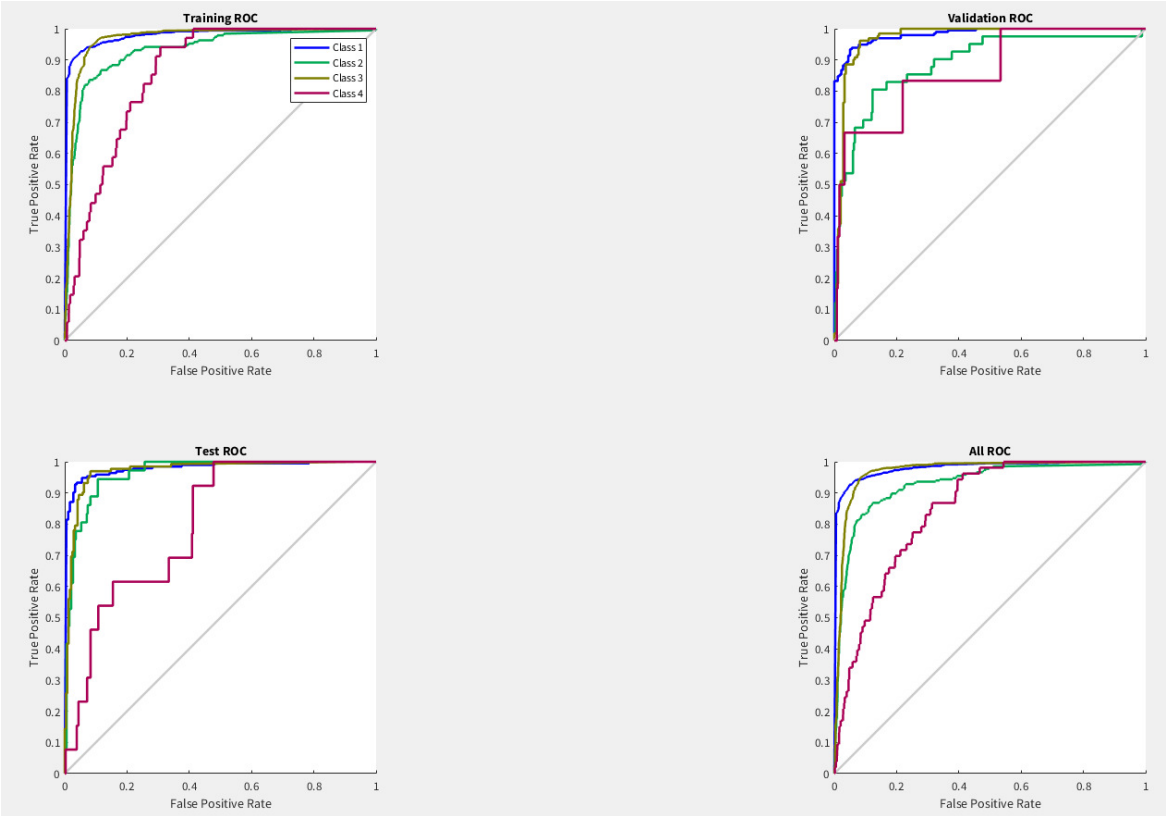


(B) ROC.

FIGURE C.46: Classification results of using a window size of 45x45 pixels, having the first 19 summations of the computed Fourier coefficients of the green component in the feature vector

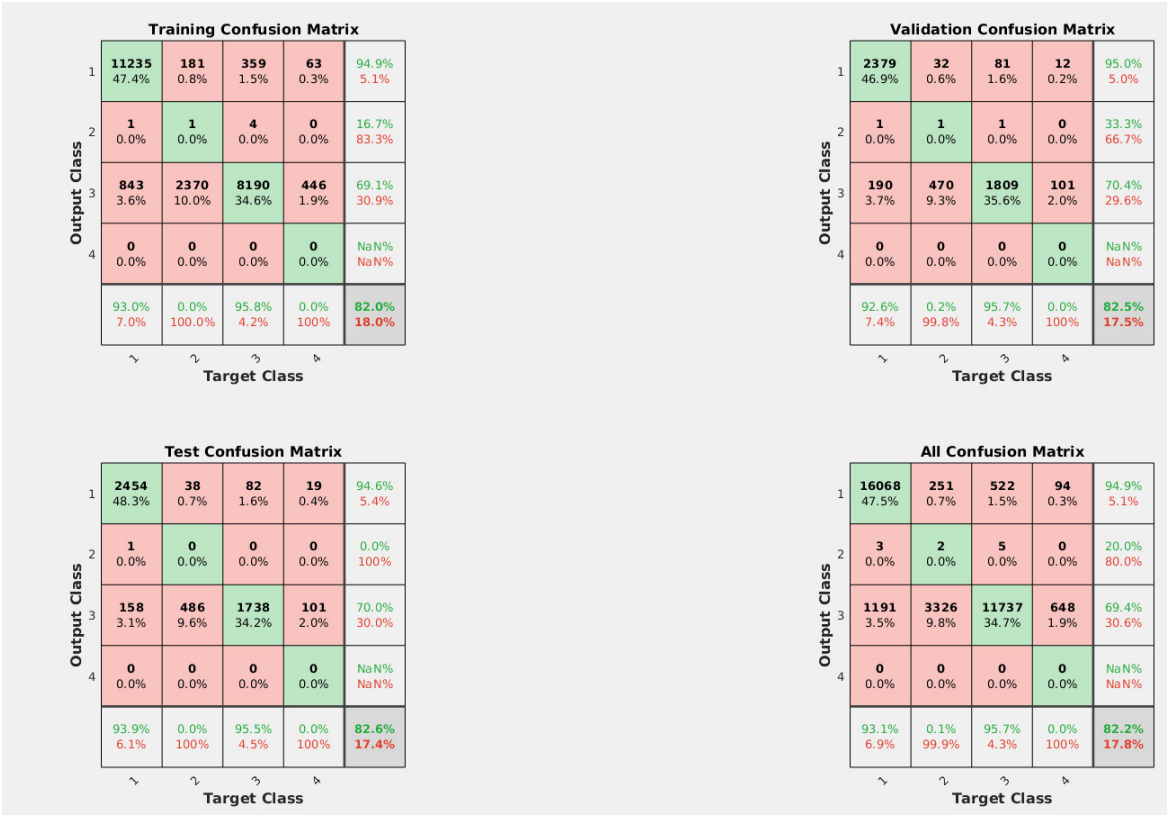


(A) Confusion matrix.

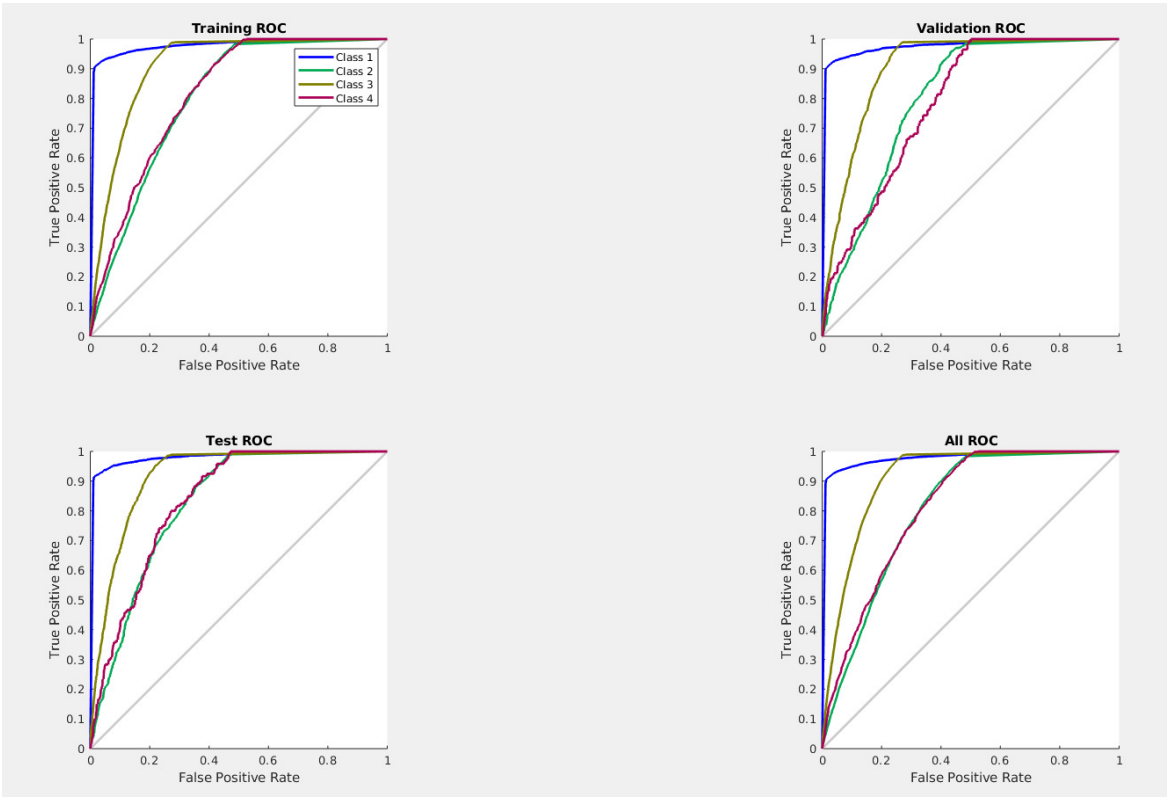


(B) ROC.

FIGURE C.47: Classification results of using a window size of 55x55 pixels, having the first 4 summations of the computed Fourier coefficients of the red and green components in the feature vector

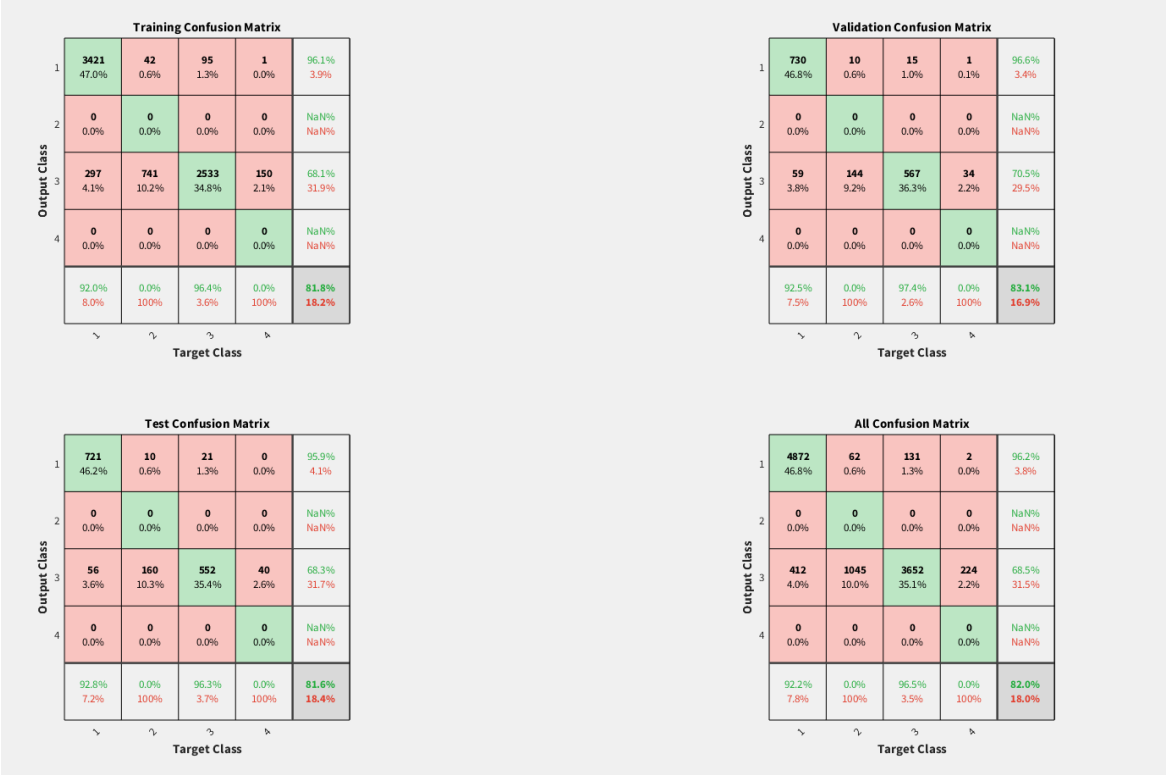


(A) Confusion matrix.

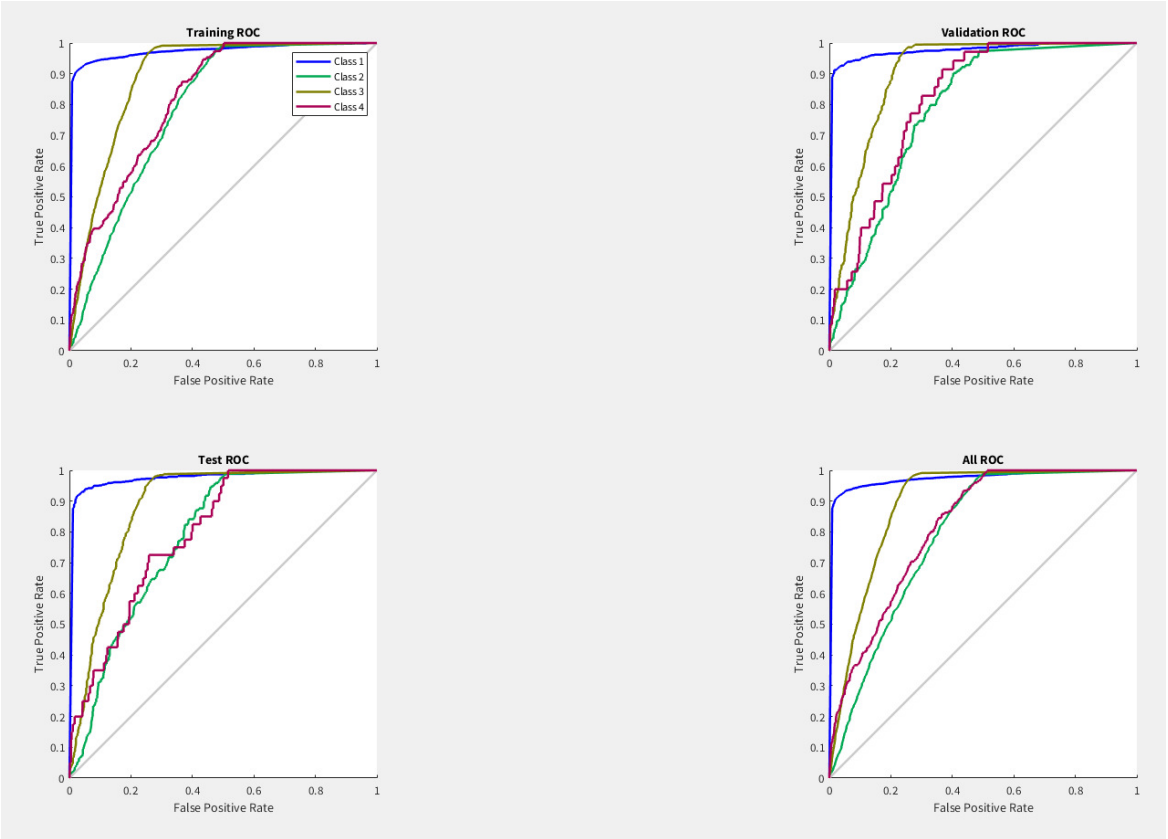


(B) ROC.

FIGURE C.48: Classification results of using a window size of 15x15 pixels, having the first 4 summations of the computed Fourier coefficients of the green component in the feature vector



(A) Confusion matrix.

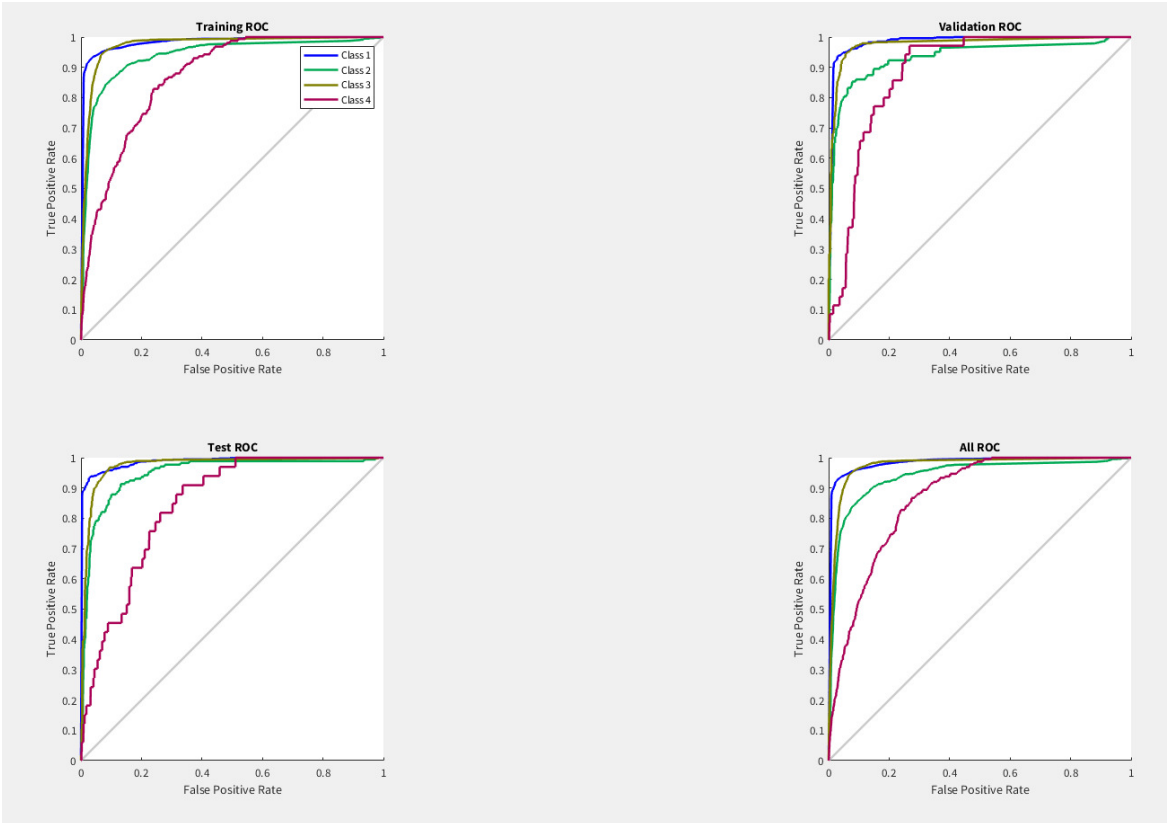


(B) ROC.

FIGURE C.49: Classification results of using a window size of 27x27 pixels, having the first 4 summations of the computed Fourier coefficients of the green component in the feature vector

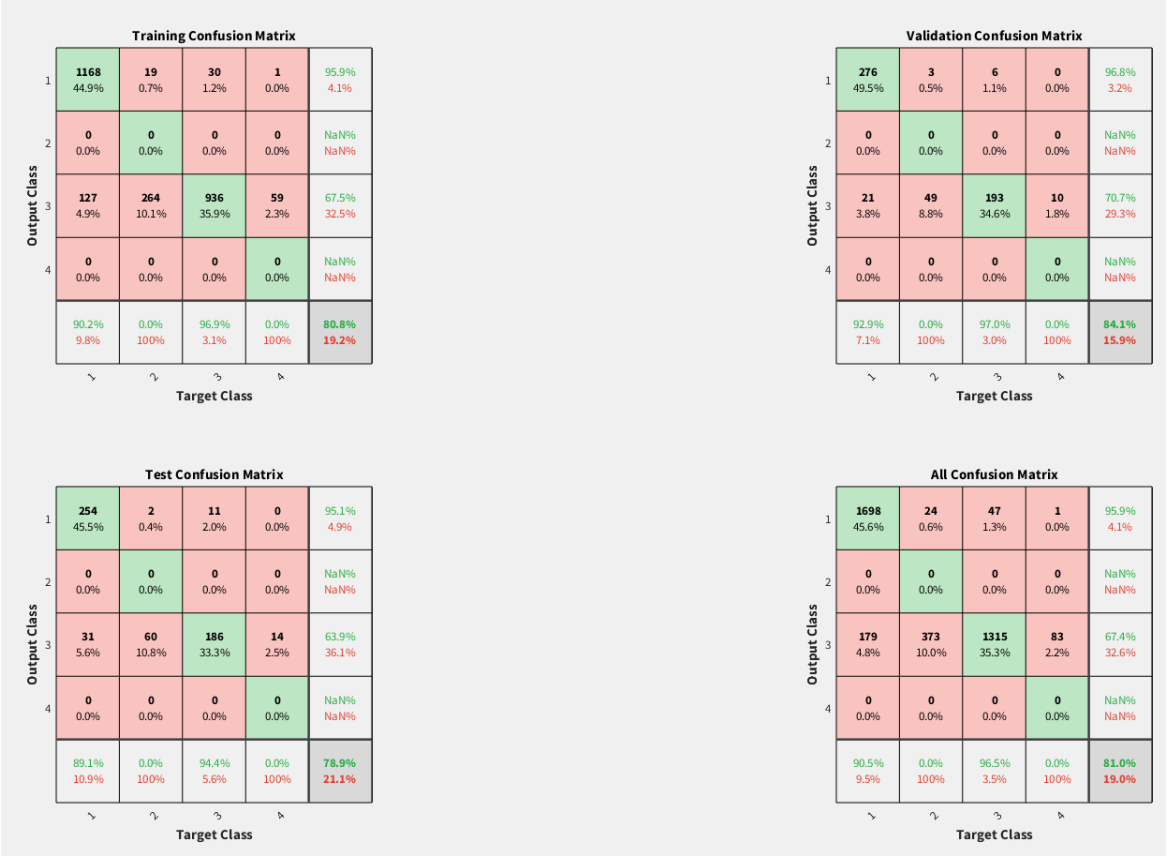


(A) Confusion matrix.

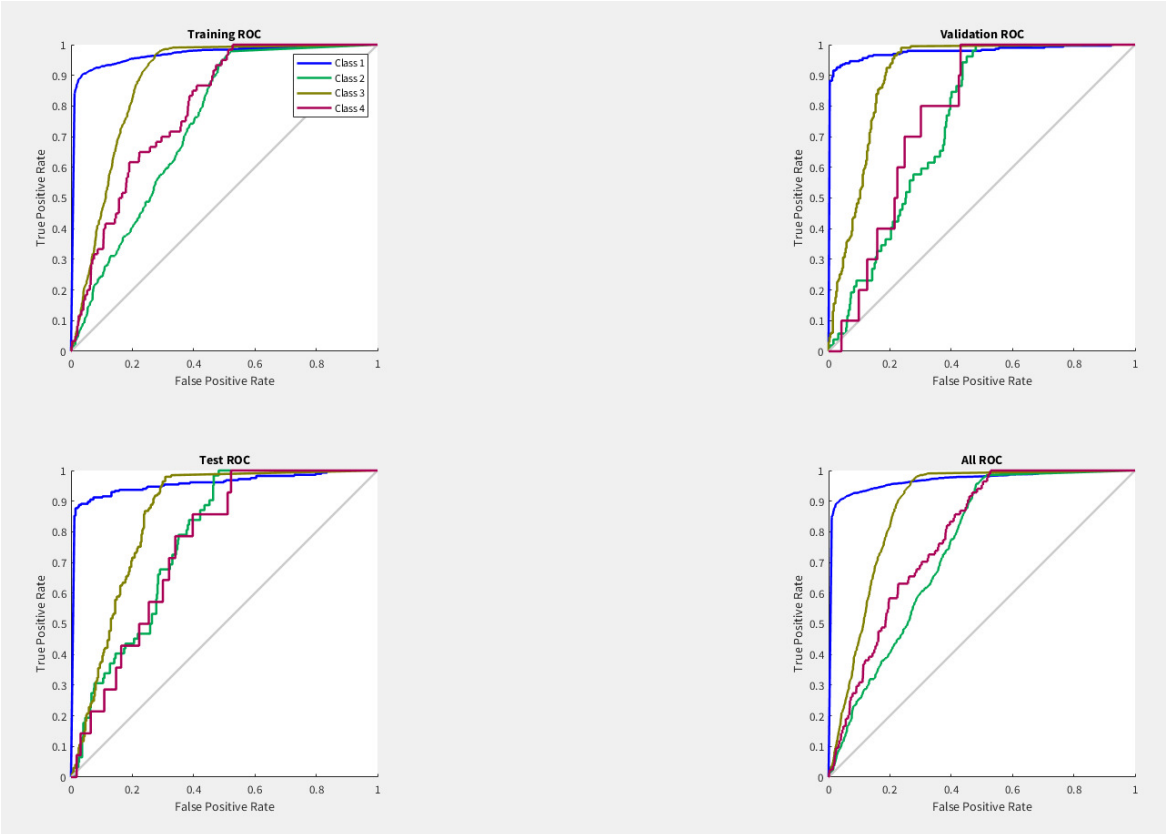


(B) ROC.

FIGURE C.50: Classification results of using a window size of 27x27 pixels, having the first 4 summations of the computed Fourier coefficients of the red and green components in the feature vector

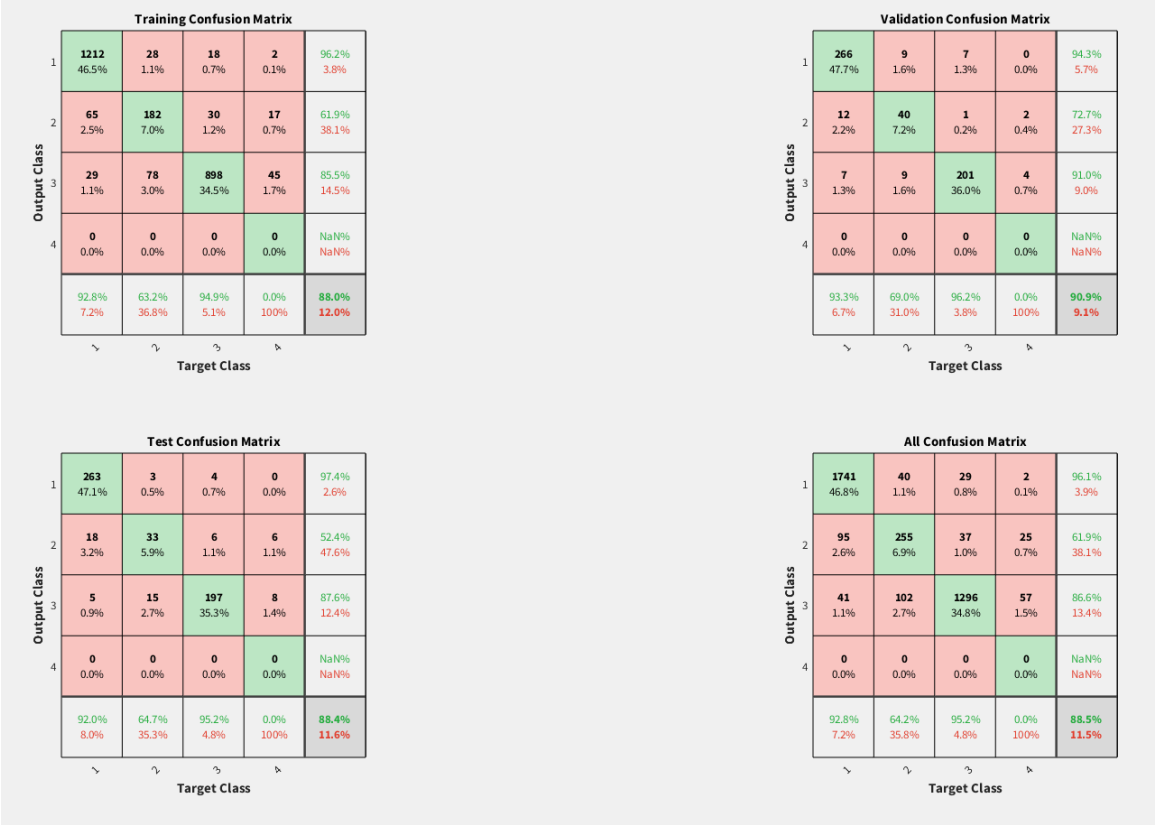


(A) Confusion matrix.

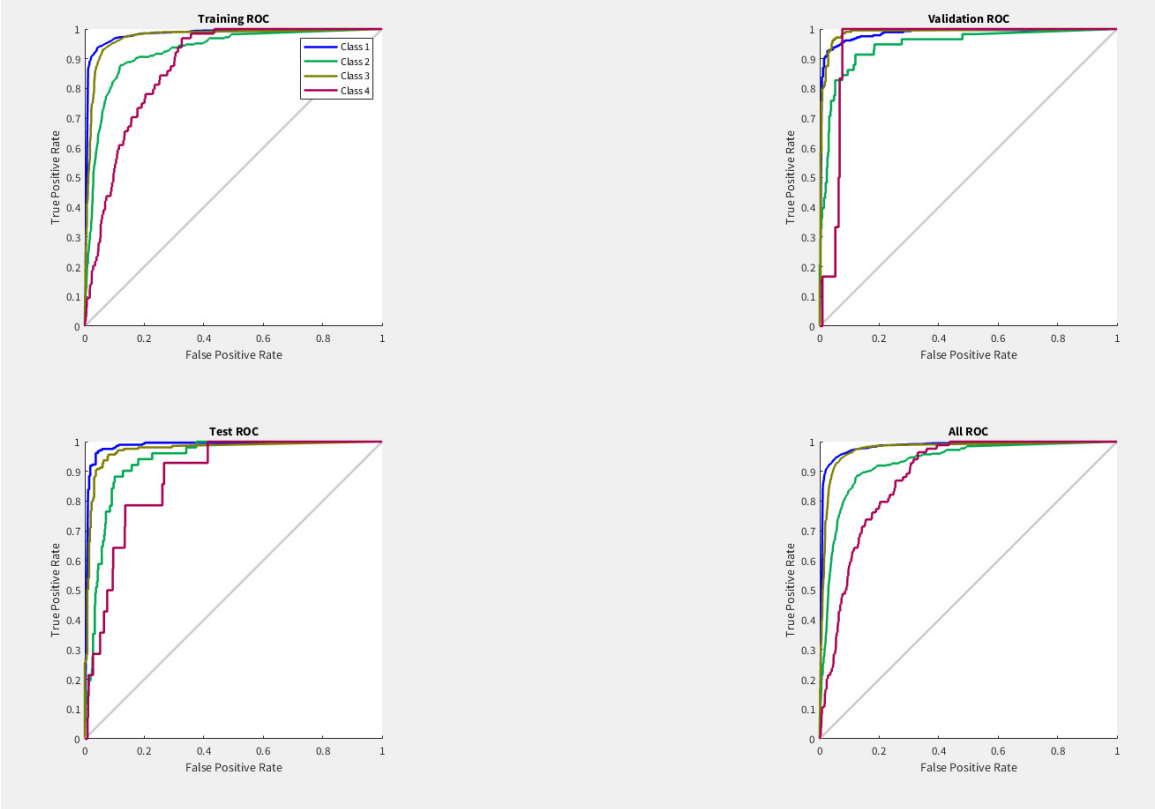


(B) ROC.

FIGURE C.51: Classification results of using a window size of 45x45 pixels, having the first 4 summations of the computed Fourier coefficients of the green component in the feature vector

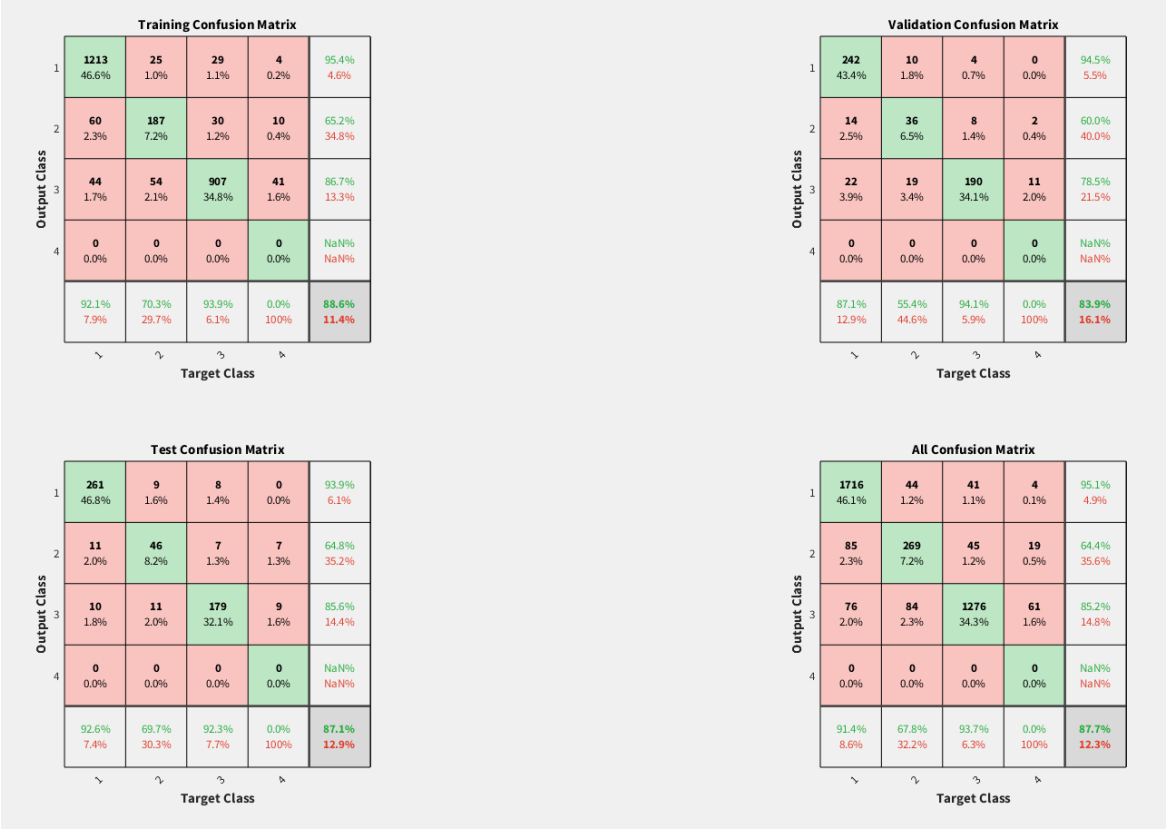


(A) Confusion matrix.

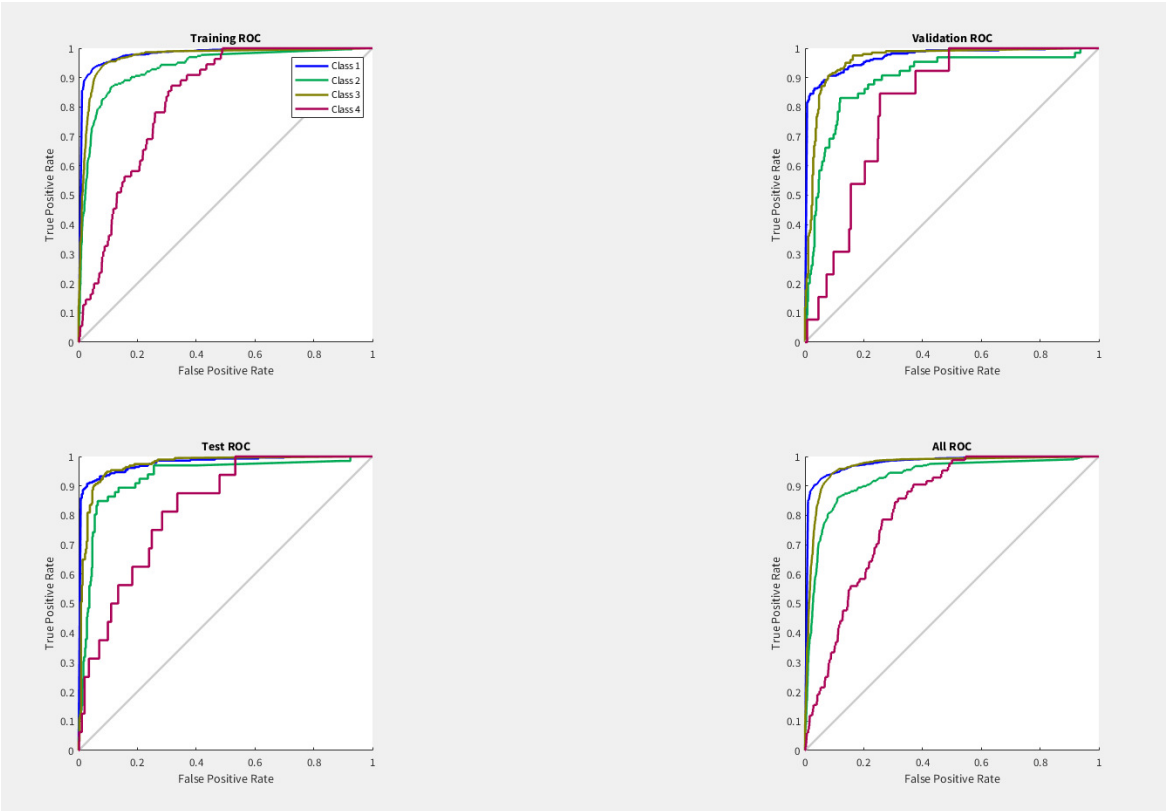


(B) ROC.

FIGURE C.52: Classification results of using a window size of 45x45 pixels, having the first 4 summations of the computed Fourier coefficients of the hue, saturation, value, red, green and blue components, and the ExR index in the feature vector

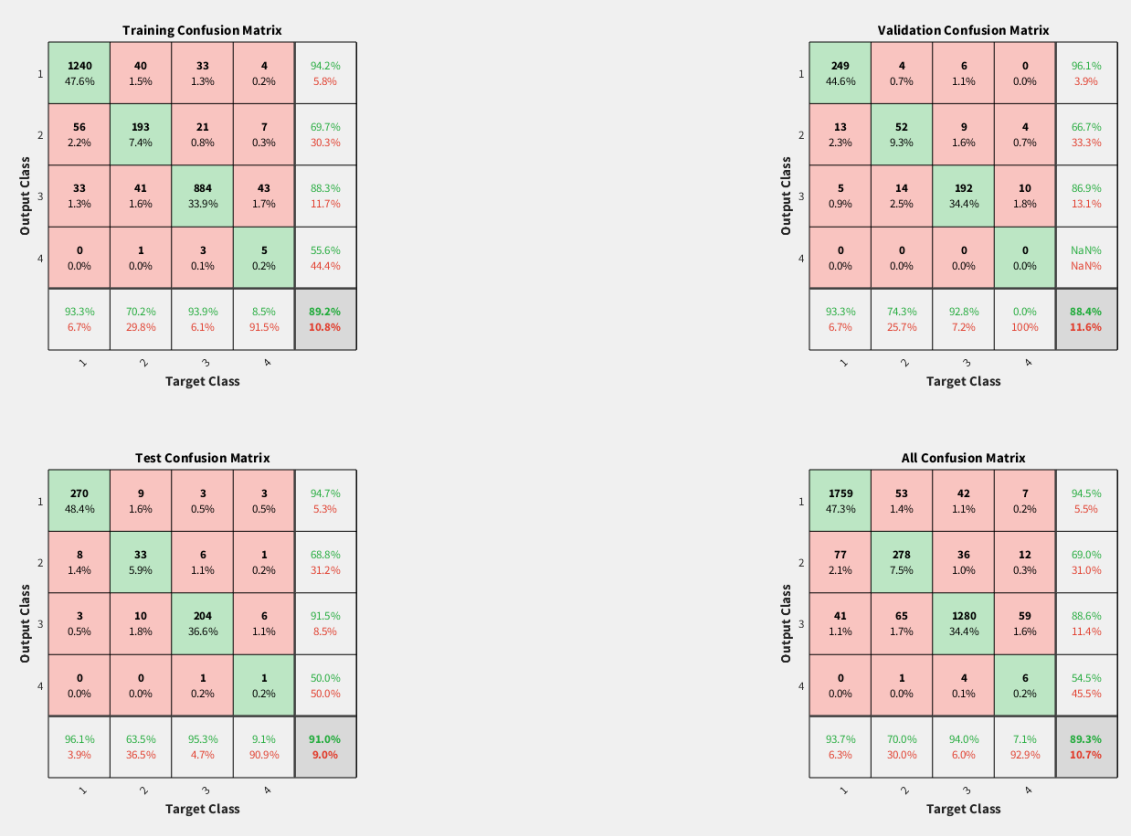


(A) Confusion matrix.

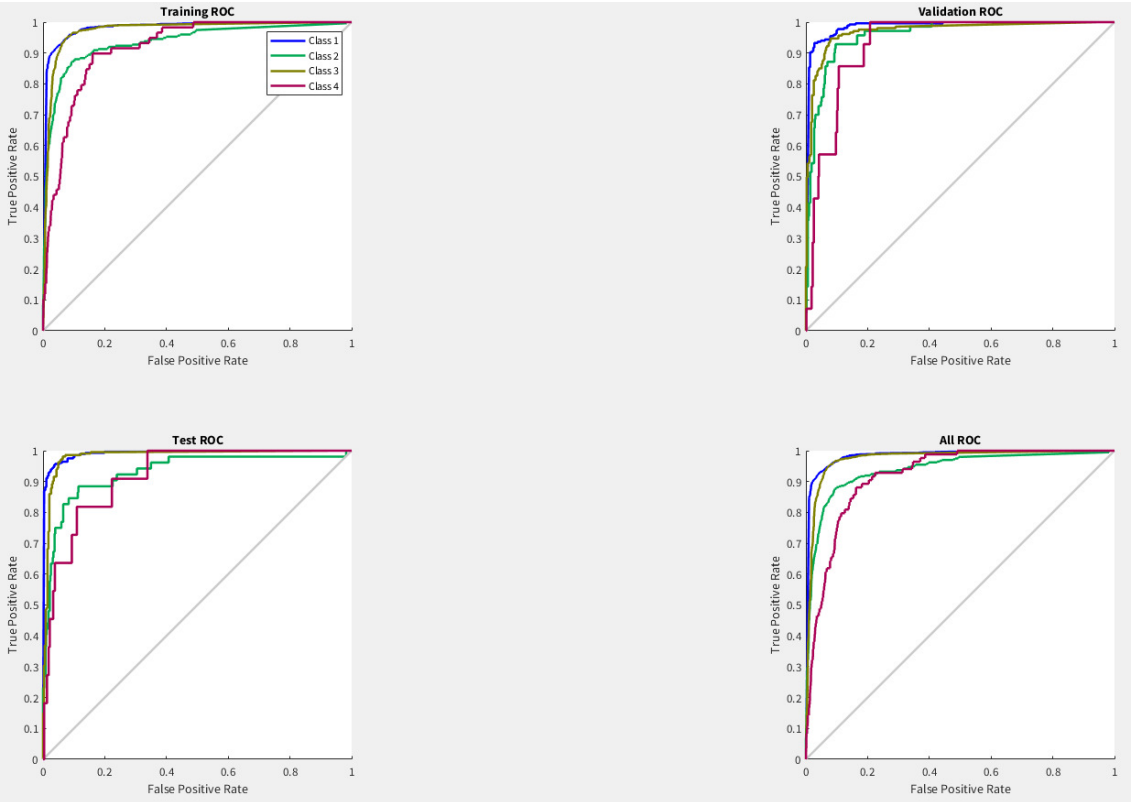


(B) ROC.

FIGURE C.53: Classification results of using a window size of 45x45 pixels, having the first 4 summations of the computed Fourier coefficients of the red and green components in the feature vector

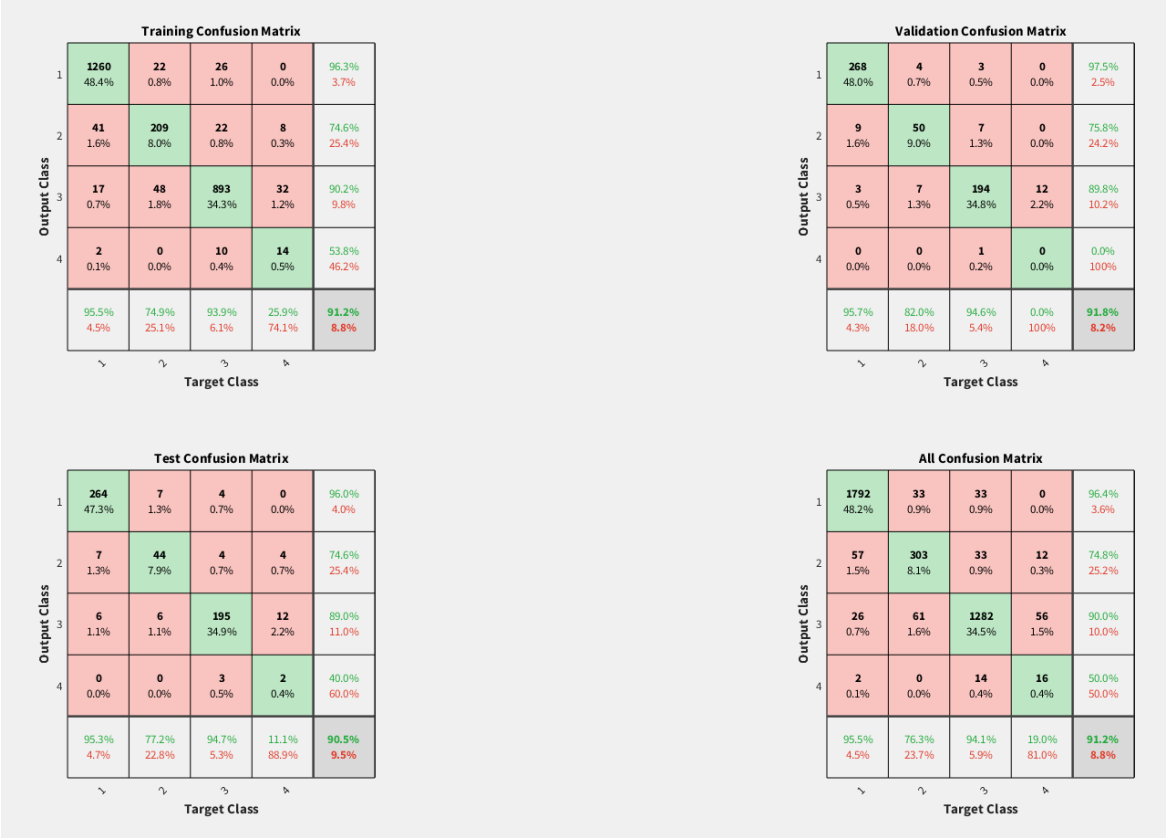


(A) Confusion matrix.

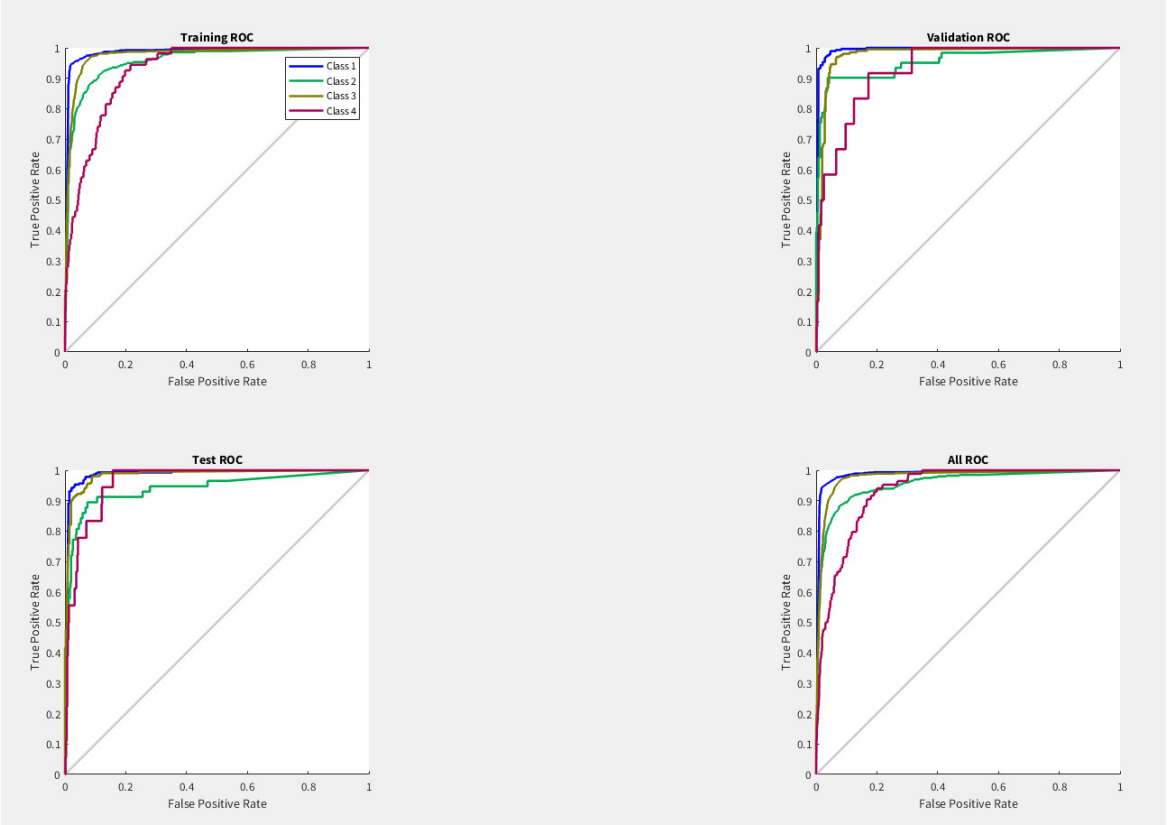


(B) ROC.

FIGURE C.54: Classification results of using a window size of 45x45 pixels, having the first 4 summations of the computed Fourier coefficients of the red, green and blue components, as well as the ExR in the feature vector



(A) Confusion matrix.

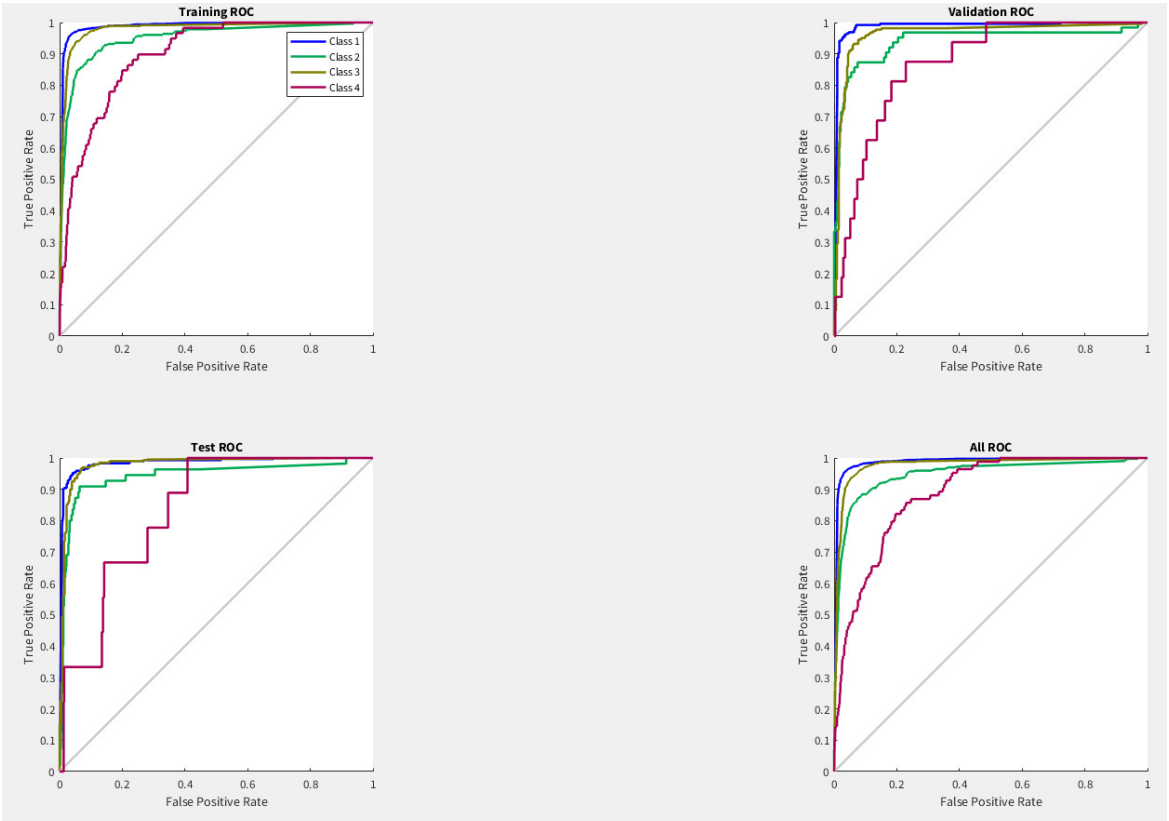


(B) ROC.

FIGURE C.55: Classification results of using a window size of 45x45 pixels, having the first 6 summations of the computed Fourier coefficients of the red, green, blue, hue, saturation and value components, as well as the ExR in the feature vector

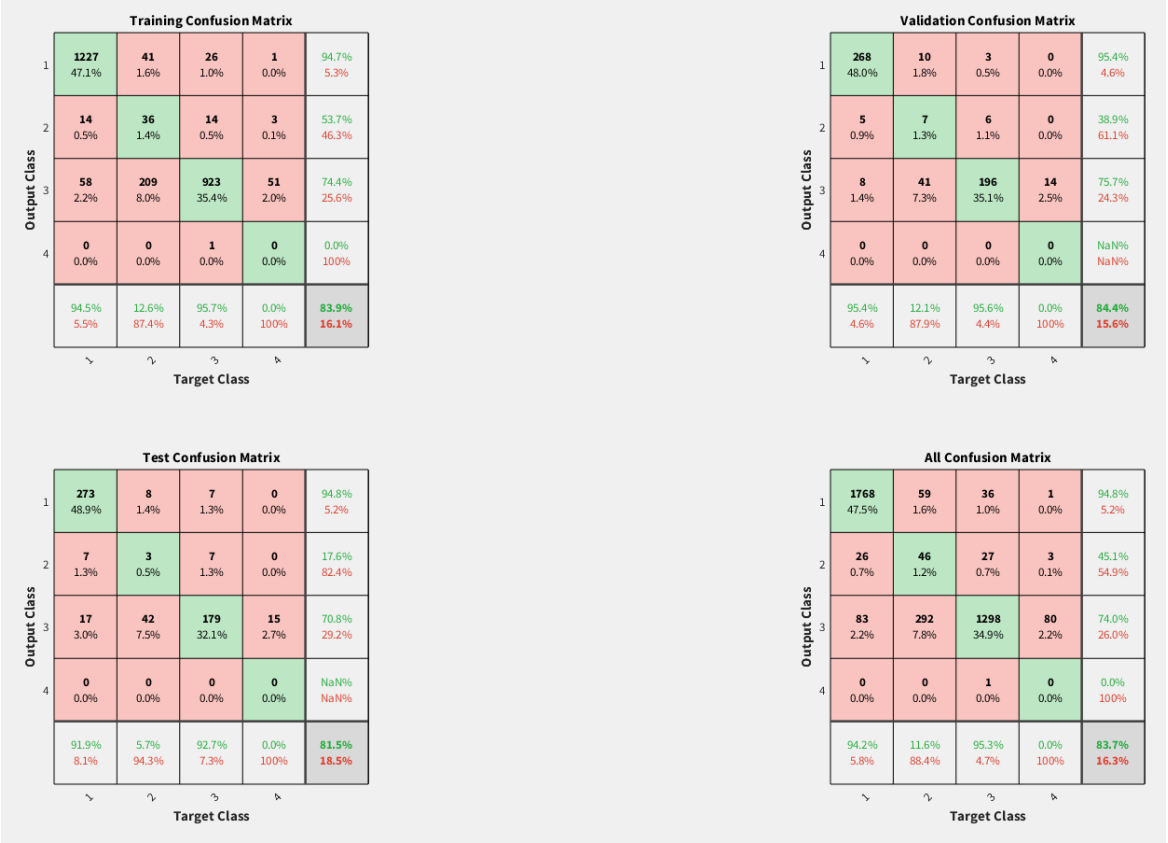


(A) Confusion matrix.

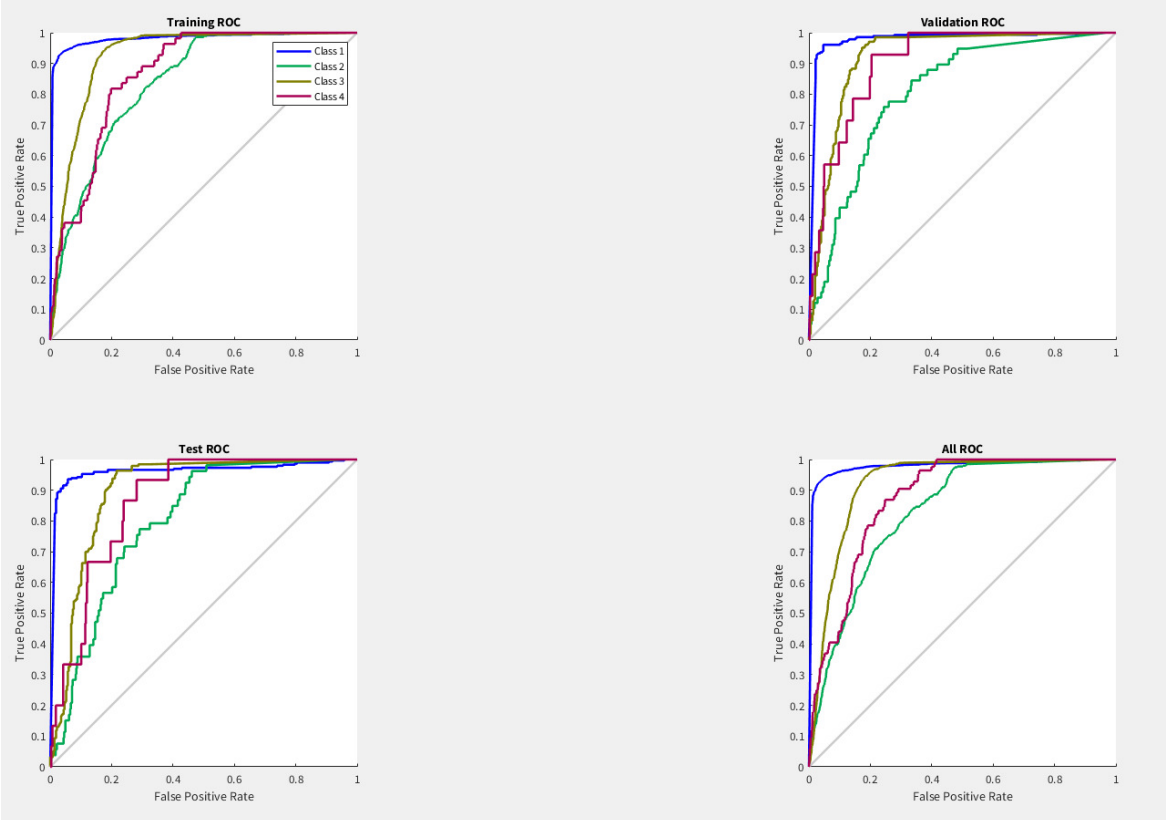


(B) ROC.

FIGURE C.56: Classification results of using a window size of 45x45 pixels, having the first 8 summations of the computed Fourier coefficients of the red, green, blue, hue, saturation and value components, as well as the ExR in the feature vector



(A) Confusion matrix.

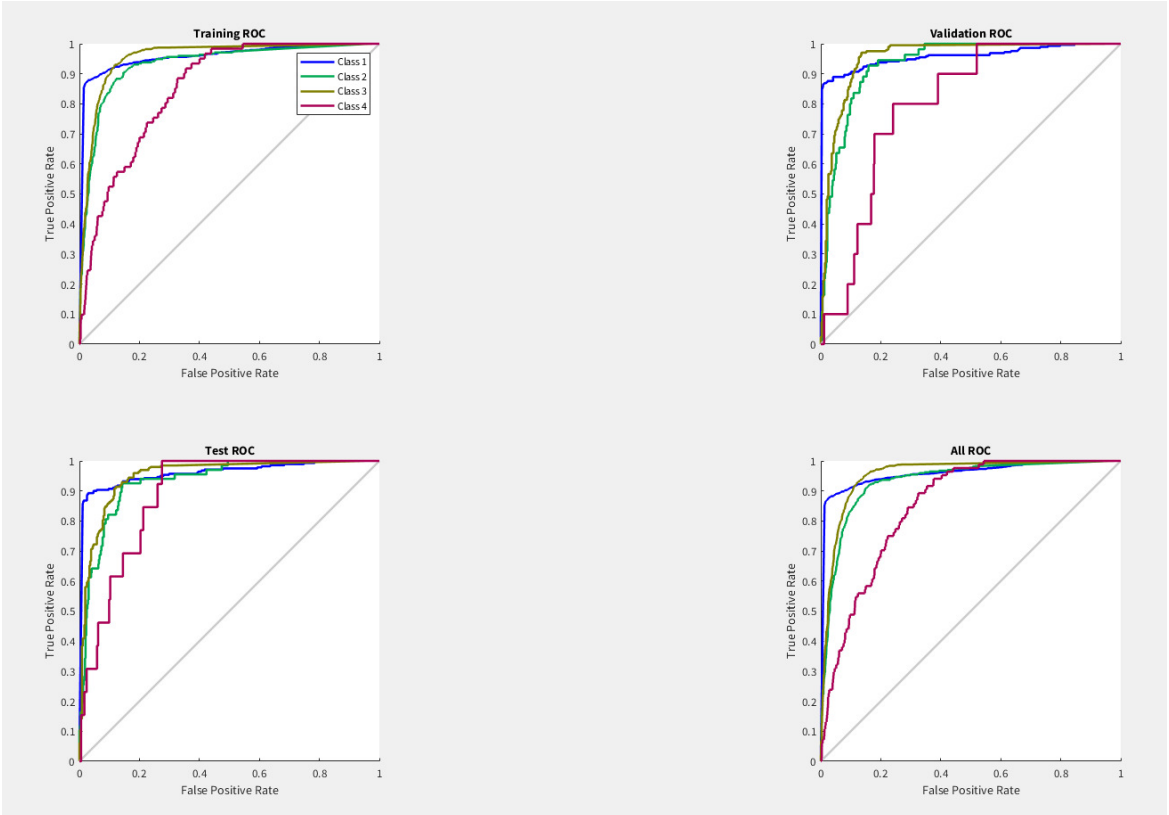


(B) ROC.

FIGURE C.57: Classification results of using a window size of 45x45 pixels, having the first 9 summations of the computed Fourier coefficients of the *ExG* index in the feature vector

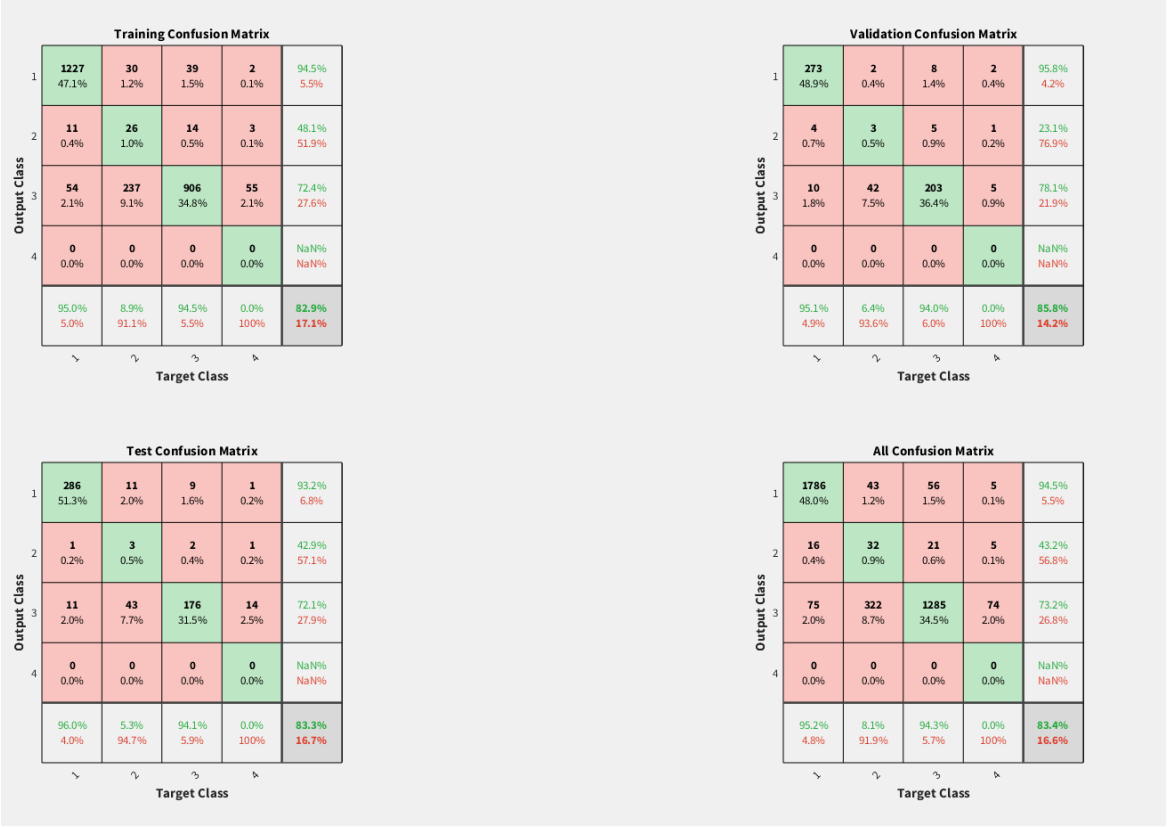


(A) Confusion matrix.

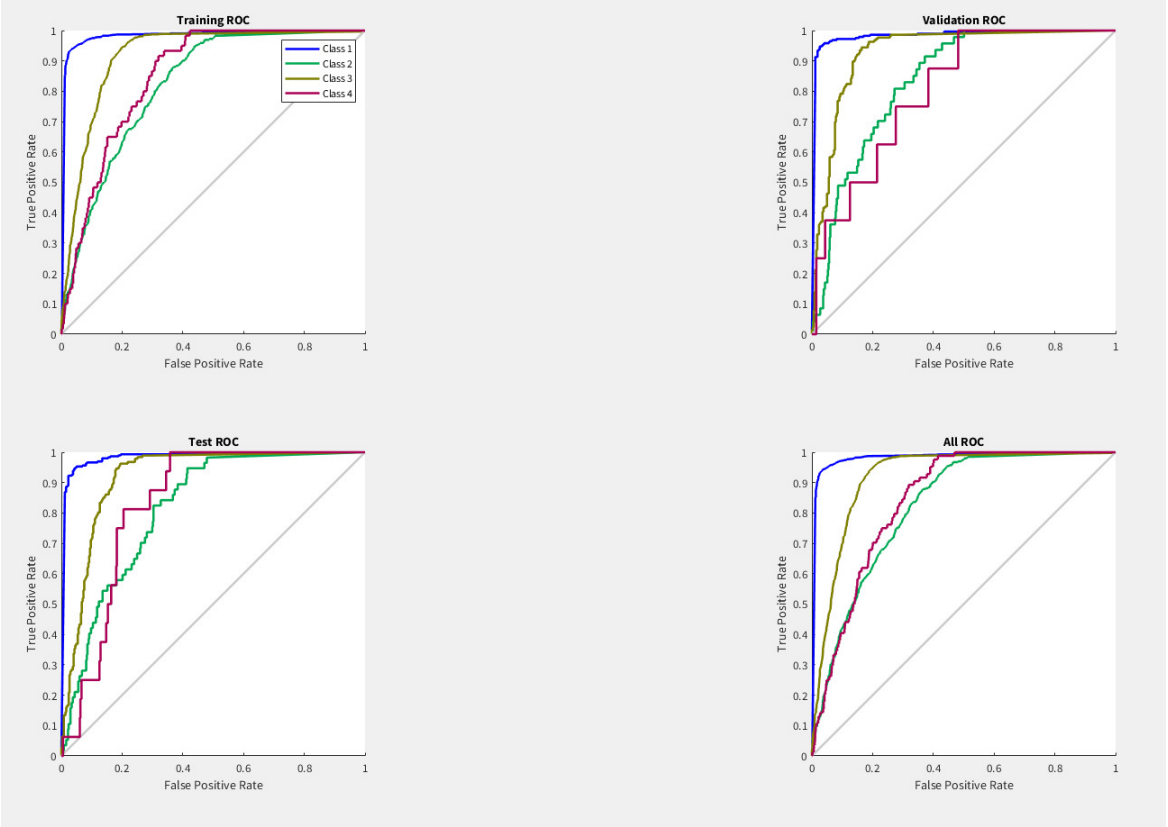


(B) ROC.

FIGURE C.58: Classification results of using a window size of 45x45 pixels, having the first 9 summations of the computed Fourier coefficients of the ExR index in the feature vector

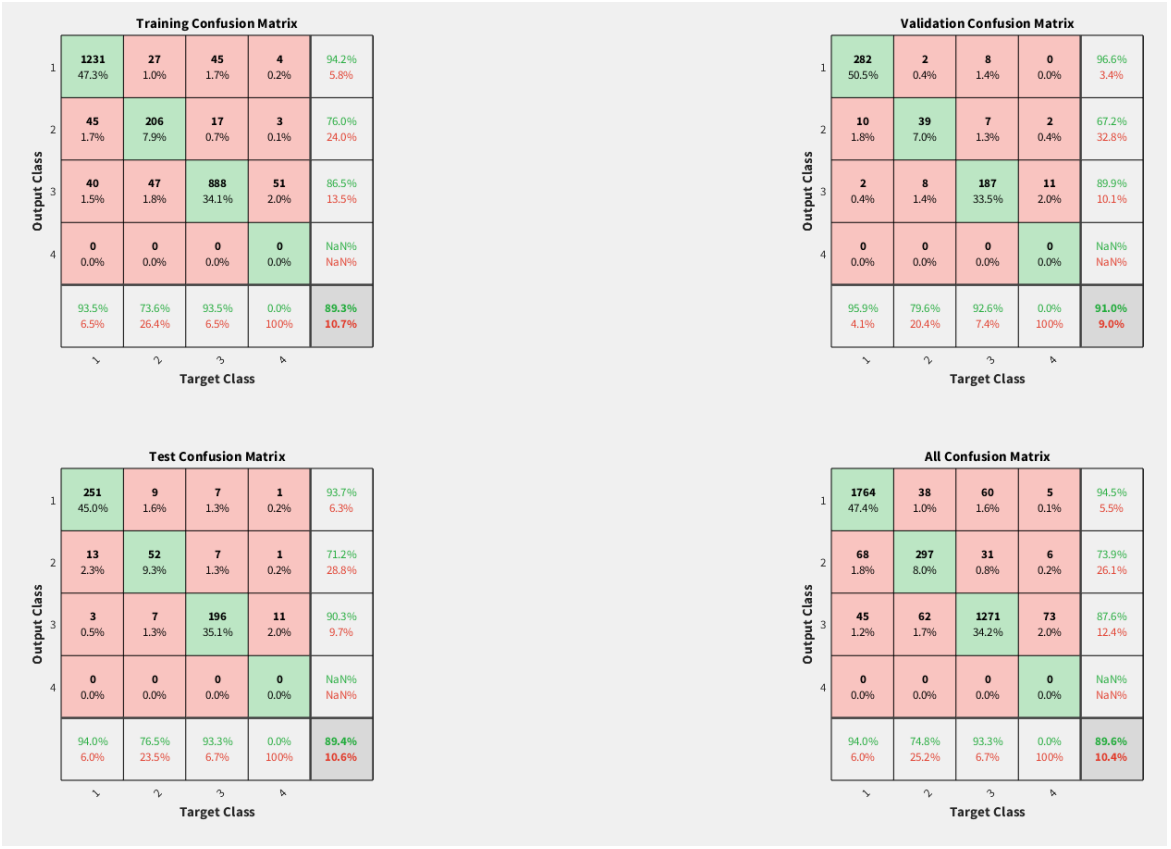


(A) Confusion matrix.

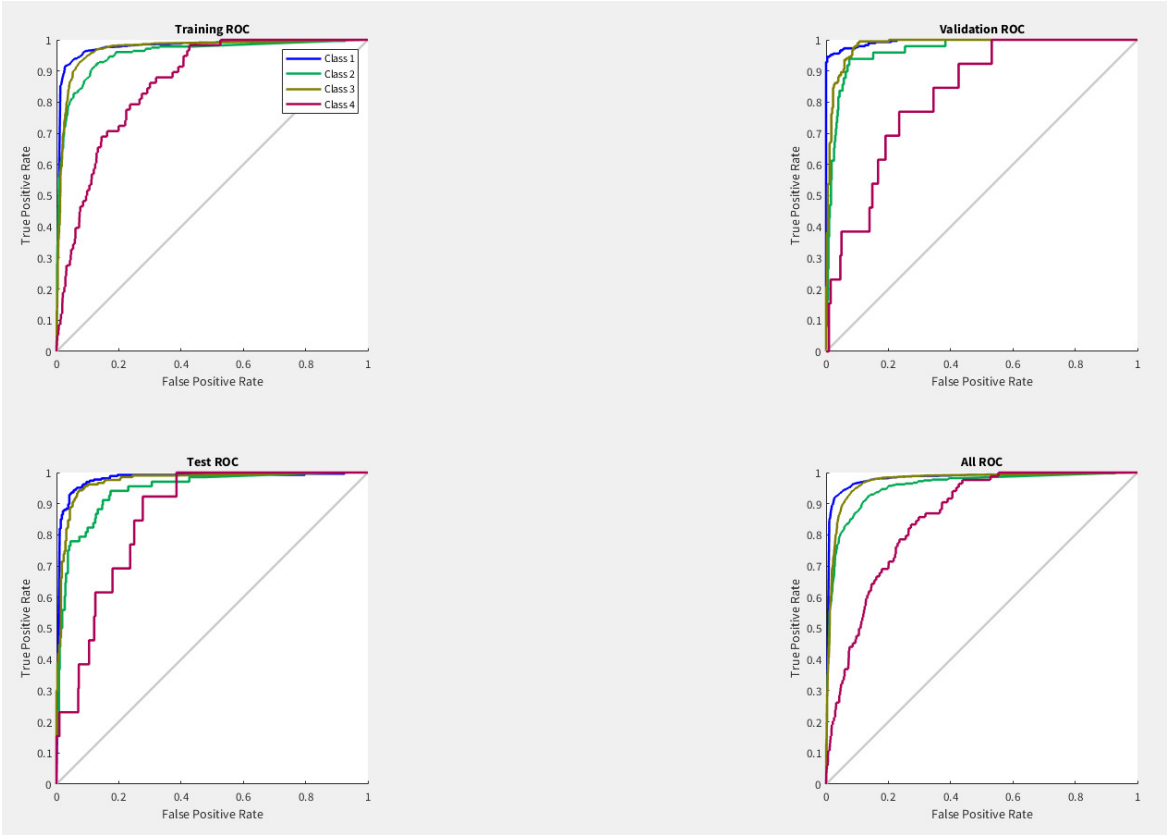


(B) ROC.

FIGURE C.59: Classification results of using a window size of 45x45 pixels, having the first 9 summations of the computed Fourier coefficients of the green component in the feature vector

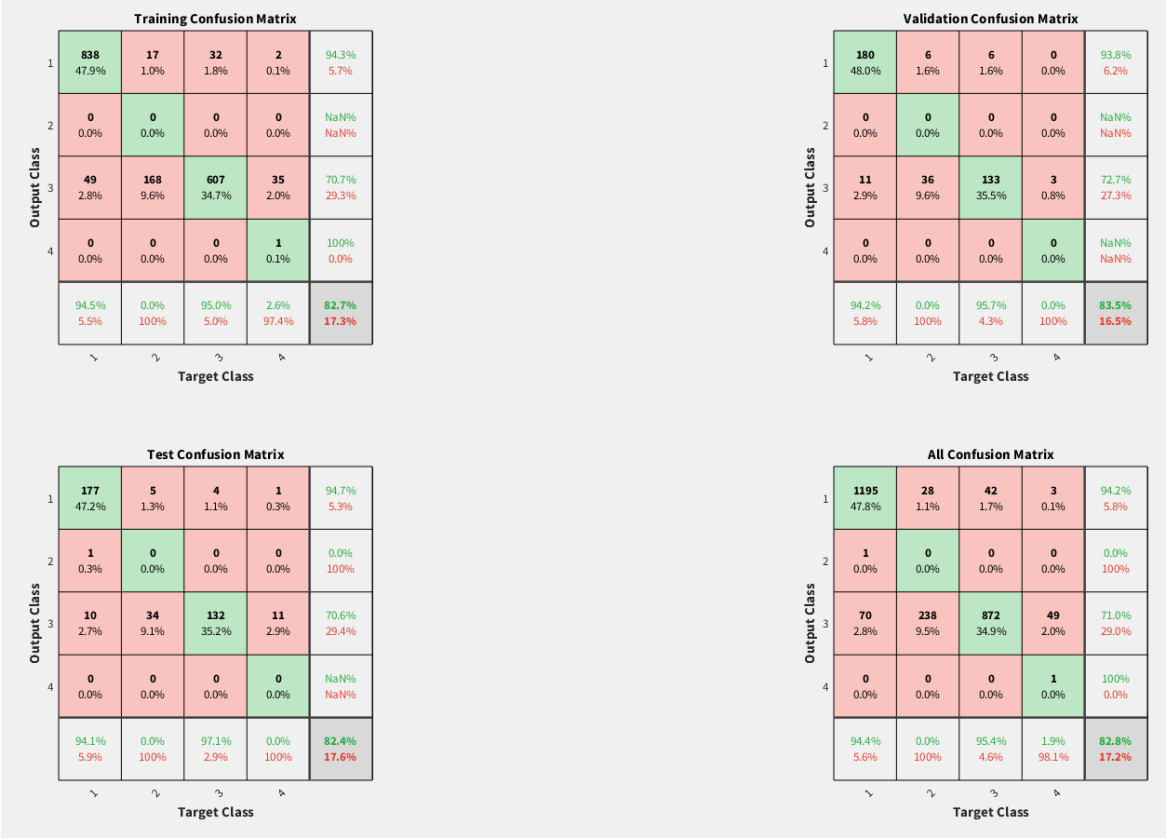


(A) Confusion matrix.

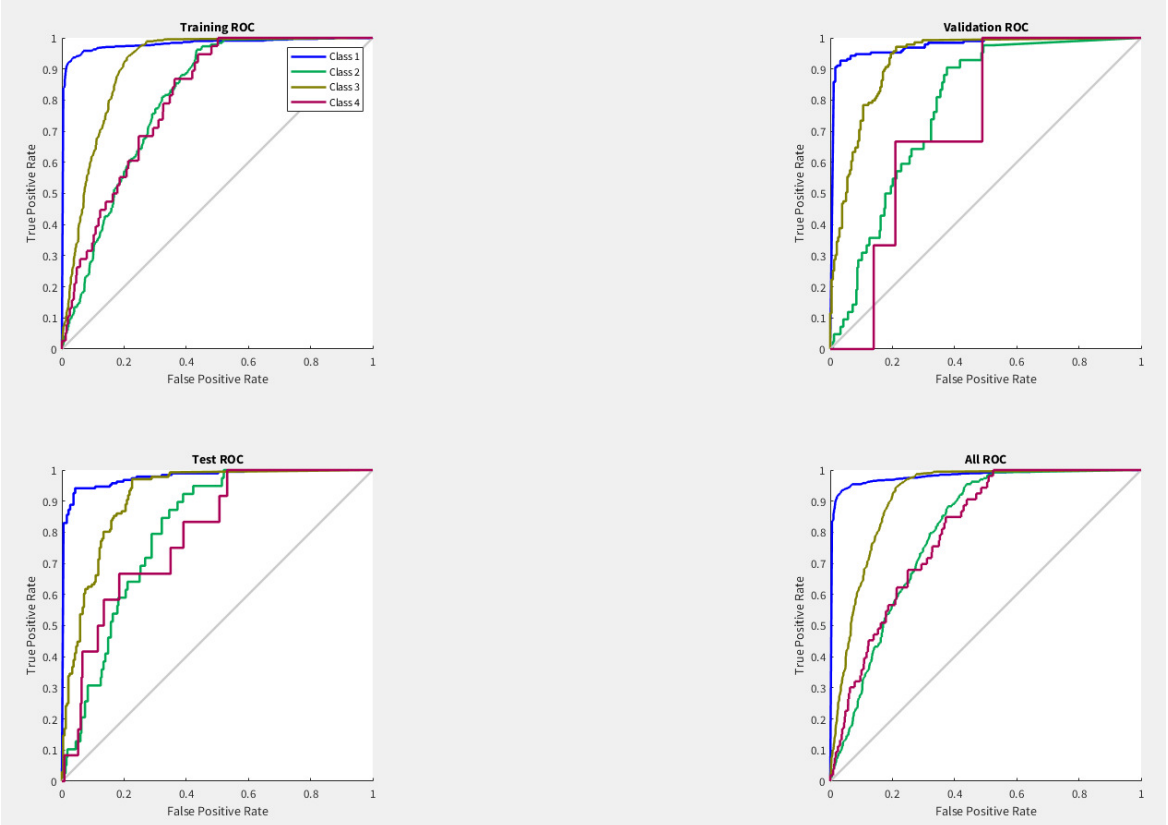


(B) ROC.

FIGURE C.60: Classification results of using a window size of 45x45 pixels, having the first 9 summations of the computed Fourier coefficients of the red and green components in the feature vector

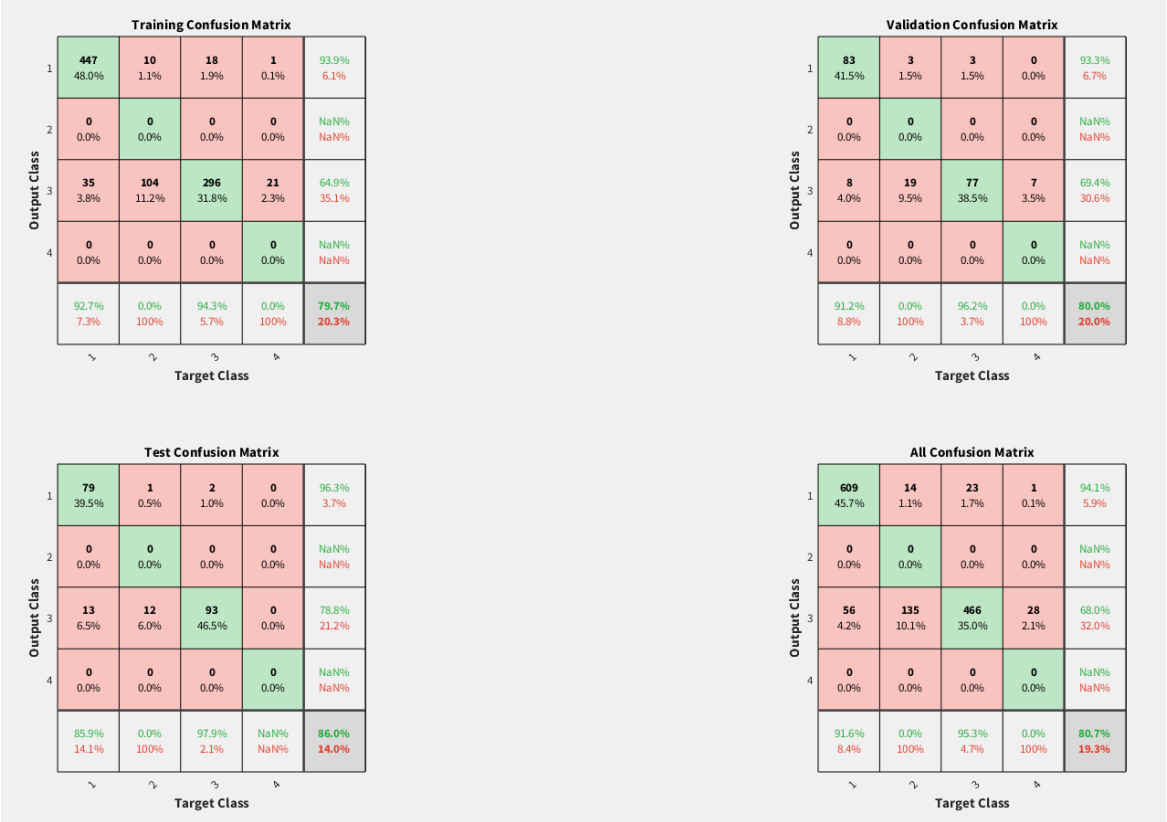


(A) Confusion matrix.

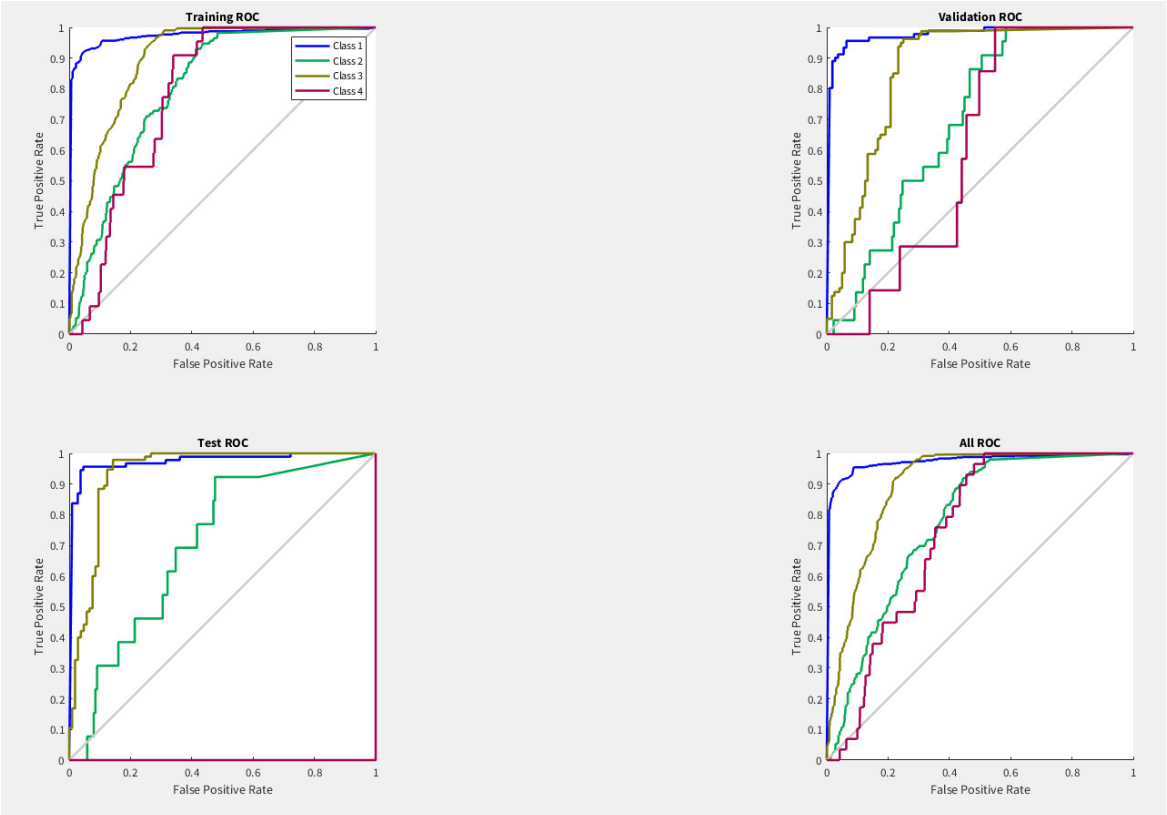


(B) ROC.

FIGURE C.61: Classification results of using a window size of 55x55 pixels, having the first 9 summations of the computed Fourier coefficients of the green component in the feature vector



(A) Confusion matrix.



(B) ROC.

FIGURE C.62: Classification results of using a window size of 75x75 pixels, having the first 9 summations of Fourier coefficients of the green component in the feature vector